GEOCHEMICAL INVESTIGATION AND QUANTIFICATION OF POTENTIAL CO_2 STORAGE WITHIN THE ARBUCKLE AQUIFER, KANSAS

by

BRENT D. CAMPBELL

B.S., Kansas State University, 2012
B.S., Kansas State University, 2012

A THESIS

submitted in partial fulfillment of the requirements for the degree

MASTER OF SCIENCE

Department of Geology
College of Arts and Sciences

KANSAS STATE UNIVERSITY
Manhattan, Kansas

2015

Approved by:

Major Professor
Saugata Datta

Copyright

BRENT CAMPBELL

2015

Abstract

With the ever-rising atmospheric concentrations of CO_2 there arises a need to either reduce emissions or develop technology to store or utilize the gas. Geologic carbon storage is a potential solution to this global problem. This work is a part of the U.S. Department of Energy small-scale pilot studies investigating different areas for carbon storage within North America, with Kansas being one of them. This project is investigating the feasibility for CO_2 storage within the hyper-saline Arbuckle aquifer in Kansas. The study incorporates the investigation of three wells that have been drilled to basement; one well used as a western calibration study (Cutter), and the other two as injection and monitoring wells (Wellington 1-28 and 1-32). Future injection will occur at the Wellington field within the Arbuckle aquifer at a depth of 4,900–5,050 ft. This current research transects the need to understand the lateral connectivity of the aquifers, with Cutter being the focus of this study.

Three zones are of interest: the Mississippian pay zone, a potential baffle zone, and the Arbuckle injection zone. Cored rock analyses and analyzed formation water chemistry determined that at Wellington there exists a zone that separated the vertical hydrologic flow units within the Arbuckle. This potential low porosity baffle zone within the Arbuckle could help impede the vertical migration of the buoyant CO_2 gas after injection. Geochemical analysis from formation water within Cutter indicates no vertical separation of the hydrologic units and instead shows a well-mixed zone. The lateral distance between Cutter and Wellington is approximately 217 miles. A well-mixed zone would allow the CO_2 plume to migrate vertically and potentially into potable water sources.

Formation brine from Cutter was co-injected with supercritical CO_2 into a cored rock from within the Arbuckle (7,098 ft.). Results show that the injected CO_2 preferentially preferred

a flow pathway between the chert nodules and dolomite. Post reaction formation chemistry of the brine showed the greatest reactivity occurring with redox sensitive species. Reactivity of these species could indicate that they will only be reactive on the CO_2 plumes front, and show little to no reactivity within the plume.

Table of Contents

List of Figures vii
List of Tables xiii
Acknowledgements xiv
Chapter 1 – Regional hydrochemical characterization for the determination of CO_2 storage in Kansas. 1
1.1 Introduction 1
1.2 Background 2
1.2.1 Historical Hydrogeology 6
1.3 Methods 9
1.3.1 Methods of water analyses at Wellington 11
1.3.2 Methods of water analyses at Cutter 13
1.3.3 Wellington experimental flow-through methods 17
1.4 Results 18
1.4.1 Results on Hydrogeochemistry of Wellington waters. 18
1.4.2 Results on Hydrogeochemistry of Cutter waters. 33
1.4.3 Wellington Flow-through results 53
1.5 Discussion 56
1.5.1 Ionic Species, Wellington 56
1.5.2 Ionic Species, Cutter 57
1.5.3 Brine Alteration, Wellington 58
1.5.4 Brine Alteration, Cutter 59
1.5.5 Vertical Connectivity, Wellington 61
1.5.6 Vertical Connectivity, Cutter 63
1.5.7 Flow-through experiment, Wellington 64
1.6 Conclusion 65
Chapter 2 – Experimental investigation for the characterization of CO_2-water-rock interactions utilizing cored rock and formation brine within a carbonate aquifer. 69
2.1 Introduction 69
2.2 Materials and Methods 71
2.2.1 Selection and mineralogy of cored rock plug 71
2.2.2 Swabbed brine chemistry 75

2.2.3 Cutter experimental flow-through methods 75
2.2.4 Cutter LLNL X-ray computed tomography analysis 80
2.2.5 Processing of X-ray computed tomography scans 80
2.3 Results 82
2.3.1 Cutter Flow-through analysis results 82
2.3.2 Cutter X-ray computed tomography analysis 96
2.4 Discussion 101
2.4.1 Flow-through experiment 101
2.5 Conclusion 109
Chapter 3 Conclusion 111
References 115
Appendix A 119
Appendix B 125

List of Figures

Figure 1.1 The four-major CO_2 trapping mechanisms (www.ICO2N.com)..... 5
Figure 1.2 Regional groundwater flow units and direction of major aquifer systems in Colorado, Kansas, and Missouri. (Jorgensen et al., 1989). 7
Figure 1.3 Stratigraphic column of Cutter KGS #1. Geologic units are labeled and their ages are shown. Water samples are highlighted to the right of the geologic ages of the formation units as blue, green, red boxes. 8
Figure 1.4 Isopach map indicating field locations and assessment areas of Cutter KGS #1 (Blue X), and Wellington Field KGS #1-32 & #1-28 wells (Purple X). Red lines indicate Arbuckle formation thickness. (Kansas Geological Survey)..... 9
Figure 1.5 Surrounding area around Cutter KGS #1 in southwest Kansas. 13
Figure 1.6 Cutter in-field sampling during the summer of 2013. 14
Figure 1.7 Cutter field equipment setup and analysis. A) Picture shows field setup with peristaltic pump, multiple probes, and filtration equipment. B) Photo shows data collection from HACH® Hydrolab. Spectrophotometer analysis was performed within the truck due to its sensitivity to light. 14
Figure 1.8 Wellington 1-32 and 1-28 piper diagram indicating a dominant Na-Ca-Cl brine. Wellington water increases in concentrations of Ca and Mg with depth. (Reproduced from Barker, 2012) 20
Figure 1.9 Depth profile of major cations and anions in Wellington. Circle symbols indicate DST samples, while diamonds indicate swab samples. Upper dashed line indicates top of Arbuckle, while lower dashed line indicates top of the Gunter Sandstone. (Reproduced from Barker, 2012) 21
Figure 1.10 Depth profile of redox sensitive species in Wellington. Circle symbols indicate DST samples, while diamonds indicate swab samples. Upper dashed line indicates top of Arbuckle, while lower dashed line indicates top of the Gunter Sandstone. (Reproduced from Barker, 2012) 22
Figure 1.11 Depth profile of Li and Si in Wellington. Circle symbols indicate DST samples, while diamonds indicate swab samples. Upper dashed line indicates top of Arbuckle, while lower dashed line indicates top of the Gunter Sandstone. (Reproduced from Barker, 2012) 23

Figure 1.12 Ionic species (Na, K, Ca, Mg) against Cl^- in Wellington. DST samples are shown in blue, and swab samples are shown in red. (Reproduced from Barker, 2012) 24
Figure 1.13 Ionic species (Br^-, SO_4, Sr, Li) against Cl^- in Wellington. DST samples are shown in blue, and swab samples are shown in red. (Reproduced from Barker, 2012) 25
Figure 1.14 Ca/Sr vs. Ca/Mg molar ratio plots in Wellington Upper intervals trend toward calcite recrystallization. Deeper depths, with the exception of the Mississippian interval, trend toward dolomitization. (McIntosh et al., 2004) (Reproduced from Barker, 2012) 26
Figure 1.15 Ca vs. SO_4 in Wellington. Circles indicate swabs and squares indicate DST samples. 26
Figure 1.16 $\delta^{18}O$ vs. $\delta^{2}H$ in Wellington. All depths plot below and are depleted in relation to the GMWL. (Replotted from Barker, 2012) 27
Figure 1.17 Depth wise profile of $\delta^{18}O$ vs. $\delta^{2}H$ in Wellington. Yellow-hatched box indicates the baffle zone, and the red-diagonal box indicates CO_2 injection zone. (Reproduced from Barker, 2012) 28
Figure 1.18 1/Sr vs. $^{87}Sr/^{86}Sr$ molar ratio in Wellington. Circles indicate swabs and squares indicate DST samples. 28
Figure 1.19 Cl^- vs. $\delta^{18}O$ and $\delta^{2}H$ in Wellington. DST samples are shown in blue, and swab samples are shown in red. Circles represent groupings of samples that correlate depth and Cl^- vs. isotope ratios. (Reproduced from Barker, 2012) 29
Figure 1.20 Cl/Br ratio against Cl^- in Wellington. Most of the depths, with the exception of the Mississippian interval, plot above the seawater evaporation curve. (Replotted from Barker, 2012) 30
Figure 1.21 Cl^- vs. Ca/Cl in Wellington. Circles indicate swabs and squares indicate DST samples. 31
Figure 1.22 Cl^- vs. K/Cl in Wellington. Circles indicate swabs and squares indicate DST samples. 31
Figure 1.23 Cl^- vs. Na/Cl in Wellington. Circles indicate swabs and squares indicate DST samples. 32
Figure 1.24 Cl/Br vs. Ca/Mg in Wellington. Circles indicate swabs and squares indicate DST samples. (McIntosh et al., 2004) 32
Figure 1.25 Piper diagram from Cutter water indicating a Na-Ca-Cl dominate brine. 35

Figure 1.26 Depth profiles of major cations in Cutter. Circles indicate swabs and squares indicate DST samples. A dashed line indicates the top of the Arbuckle, while the base of the Arbuckle is indicated by a dotted line. 37
Figure 1.27 Depth profile of redox sensitive species in Cutter. Circles indicate swabs and squares indicate DST samples. Fe is represented twice once with DST samples included, and the other only for swabbed waters to show greater variation with depth. A dashed line indicates the top of the Arbuckle, while the base of the Arbuckle is indicated by a dotted line. 38
Figure 1.28 Depth profile of anion species in Cutter. Circles indicate swabs and squares indicate DST samples. Fe and SO_4 are shown together to highlight possible microbial interactions. SO_4 concentration was divided by 100 in order to show a comparison to Fe. Br^- (KSU) represents analysis done at Kansas State University with a majority of Br^- samples below detection limits. Br^- (KGS) shows concentrations of Br^- in the same waters. A dashed line indicates the top of the Arbuckle, while the base of the Arbuckle is indicated by a dotted line. 39
Figure 1.29 Depth profiles of HCO_3 and pH in Cutter. Circles indicate swabs and squares indicate DST samples. Bicarbonate and lab pH was measured at KGS, with field pH measured at K-State. A dashed line indicates the top of the Arbuckle, while the base of the Arbuckle is indicated by a dotted line. 40
Figure 1.30 Ionic species (Ca, Mg, Sr, Na) vs. chloride in Cutter. Circles indicate swabs and squares indicate DST samples. Dashed line indicates the seawater evaporation curve. 41
Figure 1.31 Ionic species (K, Li, SO_4, Br^-) vs. chloride in Cutter. Circles indicate swabs and squares indicate DST samples. Dashed line indicates the seawater evaporation curve. 42
Figure 1.32 Ca/Sr vs. Ca/Mg in Cutter. Circles indicate swabs and squares indicate DST samples. Upper Arbuckle trends towards a calcite recrystallization trend, while the majority of the other samples show no trend or a trend towards dolomitization. 43
Figure 1.33 Ca vs. SO_4 in Cutter. Circles indicate swabs and squares indicate DST samples. 44
Figure 1.34 Ca vs. HCO_3 in Cutter. Circles indicate swabs and squares indicate DST samples.. 44
Figure 1.35 Chloride vs. Cl/Br in Cutter. Circles indicate swabs and squares indicate DST samples. Dashed line indicates the seawater evaporation curve..... 45
Figure 1.36 Cl^- vs. Ca/Cl in Cutter. Circles indicate swabs and squares indicate DST samples. Dashed line indicates the seawater evaporation curve. 46

Figure 1.37 Cl^- vs. K/Cl in Cutter. Circles indicate swabs and squares indicate DST samples. Dashed line indicates the seawater evaporation curve. 46
Figure 1.38 Cl^- vs. Na/Cl in Cutter. Circles indicate swabs and squares indicate DST samples. Dashed line indicates the seawater evaporation curve. 47
Figure 1.39 Cl/Br vs. Ca/Mg in Cutter. Circles indicate swabs and squares indicate DST samples. Dashed line indicates halite dissolution or calcite precipitation. (McIntosh et al., 2004) 47
Figure 1.40 Chloride vs. $\delta^{13}C$ (DIC), $\delta^{18}O$, and $\delta^{2}H$ in Cutter. Circles indicate swabs. 48
Figure 1.41 $\delta^{18}O$ vs. $\delta^{2}H$ in Cutter. Circles indicate swabs. All samples plot below the Global Meteoric Water Line (GMWL-solid black line) and are depleted in relation to it. 49
Figure 1.42 Depth profiles of $\delta^{13}C$ (DIC), $\delta^{18}O$, and $\delta^{2}H$ in Cutter. A dashed line indicates the top of the Arbuckle, while the base of the Arbuckle is indicated by a dotted line. Circles indicate swabs. 50
Figure 1.43 $\delta^{13}C$ (DIC) vs. HCO_3 in Cutter. Circles indicate swabs. 51
Figure 1.44 1/Sr vs. $^{87}Sr/^{86}Sr$ in Cutter. Circles indicate swabs. 52
Figure 1.45 $\delta^{13}C$ (DIC) vs. $^{87}Sr/^{86}Sr$ in Cutter. Circles indicate swabs. 52
Figure 1.46 Wellington flow-through pH and alkalinity change through time. (Reproduced from Barker, 2012) 54
Figure 1.47 Wellington flow-through ionic species and alkalinity change through time. (Reproduced from Barker, 2012) 55
Figure 1.48 Wellington flow-through ionic species and alkalinity change through time. (Reproduced from Barker, 2012) 55
Figure 2.1 Basic and overly simplified LLNL experimental setup and directional flow chart. Flow goes from right to left. 70
Figure 2.2 Rotational views of Cutter Core 20-9 (7,098 ft.). E) Side of injection. F) Side of outlet. Chert nodule seen in (B) is the same as seen in (E). 72
Figure 2.3 Thin sections of Core 20-9 (7,098 ft.). A) (4x in Plain Light) Heterogeneous contact between large chert nodule and fine grained dolomite packstone. Large chert nodule in upper portion of image exhibiting microporous chert matrix. Accumulation of argillaceous materials along porous fracture boundary. Moderate intergranular porosity within dolomite packstone matrix. B) 4x in Cross-Polarized Light) Heterogeneous contact between large chert nodule and fine grained dolomite packstone. Pore spaces in microporous siliceous

matrix along right side of image infilled with radiating chalcedony. Medium grained dolomite rhomb present in silica matrix. Note argillaceous accumulation along fracture boundary. (Mike Vega)..... 72
Figure 2.4 Cutter stratigraphic column. Stratigraphic column is abbreviated in relation to the entire well and sample depths collected and analyzed. Red squares indicated swab depths. Gray cylinder indicates core 20-9 used in the experiment. Red line indicates full extent of the Arbuckle group. (Modified from Kansas Geological Survey) 74
Figure 2.5 A) LLNL reactor end-cap. B) LLNL latter with black Viton® wrapped core. (Images courtesy of Lawrence Livermore National Laboratories). 76
Figure 2.6 LLNL core flooding reactor experimental setup. (Images courtesy of Lawrence Livermore National Laboratories) 78
Figure 2.7 TIC analysis using a gastight glass syringe. (Images courtesy of Lawrence Livermore National Laboratories) 79
Figure 2.8 Cutter LLNL threshold differences indicating porosity. Images show differentiation between threshold values. Threshold values are: A=20, B=30, C=40, and D=50. All thresholds were taken from the same image slice. 81
Figure 2.9 Cutter LLNL pressure change through time. 86
Figure 2.10 Variation of Ba^{2+} concentration through time. 86
Figure 2.11 Variation of Br^{-} concentration through time. 87
Figure 2.12 Variation of Ca^{2+} concentration through time. 87
Figure 2.13 Variation of Cl^{-} concentration through time. 88
Figure 2.14 Variation of Cu^{2+} concentration through time.. 88
Figure 2.15 Variation of Fe concentration through time. 89
Figure 2.16 Variation of K^{+} concentration through time. 89
Figure 2.17 Variation of Li^{+} concentration through time. 90
Figure 2.18 Variation of Mg^{2+} concentration through time. 90
Figure 2.19 Variation of Mn concentration through time. 91
Figure 2.20 Variation of Na^{+} concentration through time. 91
Figure 2.21 Variation of NO_2^{-} concentration through time. 92
Figure 2.22 Variation of SO_4^{2-} concentration through time. 92
Figure 2.23 Variation of Sr^{2+} concentration through time. 93

Figure 2.24 Variation of $\delta^{13}C$ (DIC) concentration through time. 93
Figure 2.25 Variation of $\delta^{18}O$ concentration through time. 94
Figure 2.26 Variation of $\delta^{2}H$ concentration through time. 94
Figure 2.27 Variation of total inorganic carbon (TIC) concentration through time. 95
Figure 2.28 Cutter 20-9 core and 3D XRCT images. All (A) pictures indicate inlet side, all (B) pictures indicate same point of view along with flow direction, all (C) images indicate outlet side, and all (D) images indicate backside of (B). All x1 images indicate pre-injection pore space, all x2 images indicate low threshold pore space, and all x3 images indicate high threshold pore space. The chert is outlined in black in photos A, B, and C. 99
Figure 2.29 Post XRCT image of the inlet side of the core. Fluid flow preferentially followed the darker gray areas, especially between mineral boundaries as can be seen in the center of the image. Chert is the lighter of the gray colors and occurs in the bottom right of the image in a half oval outline. 99
Figure 2.30 Post XRCT image of a middle slice of core looking towards the outlet. Chert is outlined as the lighter color occurring in the right half of the image. 100
Figure 2.31 Post XRCT image of the outlet side of the core. Chert is outlined as the lighter color occurring in the left side of the image. 101
Figure A.3.1 Cutter vs. Wellington comparison of $\delta^{18}O$ vs. $\delta^{2}H$. 119

List of Tables

Table 1.1 Wellington 1-32 and 1-28 swab and DST samples, date sampled, depth ranges of sample, and corresponding formations. 10
Table 1.2 Cutter swab and DST samples, date sampled, depth ranges of sample, and corresponding formations. 10
Table 1.3 Wellington 1-32 and 1-28, analyzed ionic species concentrations, their corresponding depths and well locations. ICP-OES was used for DST and swab 1 cation analysis, while swabs 2-5 cations were analyzed using HR-ICP-MS. 19
Table 1.4 Wellington 1-32 and 1-28, analyzed isotopic concentrations, their corresponding depths and well locations. $^{87}Sr/^{86}Sr$ analysis was selected for a few depths based on the other two isotopic concentrations. 19
Table 1.5 Ionic species concentrations and their corresponding depths from Cutter. All cations were analyzed by ICP-OES. 34
Table 1.6 Isotopic concentrations and their corresponding depths from Cutter. 34
Table 2.1 Water chemistry of swabs 3-5 from Cutter. 75
Table 2.2 Cutter LLNL cation analysis of pre and post experimental flow through eluent. CO_2 started at day 5.11, sample A6. Apre1-2 is from the first brine-mixing vessel. Apre 3-4 is from the open Nalgene/pre-CO_2 flow. Apre5-6 is from the second brine-mixing vessel. Amq is MilliQ water. Apost 1-2 is from the first brine-mixing vessel. Apost 3-4 is from the second brine-mixing vessel. Aextra is from the reactor vessel confining water. Apre 7-8 is from the third brine-mixing vessel. 83
Table 2.3 Cutter LLNL anion analysis of pre and post experimental flow through formation water. CO_2 started at day 5.11, sample B6. Bpre1-2 is from the first brine-mixing vessel. Bpre 3-4 is from the open Nalgene/pre-CO_2 flow. Bpre5,8 is from the second brine-mixing vessel. Bmq is MilliQ water. Bpost 1 is from the first brine-mixing vessel. Bpost 3 is from the second brine-mixing vessel. Bpost 5 is from the third brine-mixing vessel. B1xtr2 is from the reactor vessel confining water. 84
Table 2.4 Cutter LLNL analysis total inorganic carbon (TIC), δ^2H, $\delta^{18}O$, and $\delta^{13}C$ (DIC). CO_2 flow started at day 5.11, sample C6. BCCpre1-2 is from the first brine-mixing vessel. 85

Acknowledgements

I would like to express my sincere appreciation to everyone who has helped me get through the last two years, and to where I am today.

Firstly, I would like to thank Kansas State University for the opportunity to attend graduate school, along with the surrounding district to the southwest for helping me get through it. I would like to thank the college of Arts and Sciences and the Graduate School for their generous financial support in the form of research travel grants and student travel grants, those of which have allowed me to travel and present at multiple conferences.

I would like to thank Paul and Deana Strunk for their generous scholarship along with Paul's engaging and lively talks when he is in the department or at conferences. I also would like to thank the American Association of Petroleum Geologists for their financial support in the form of the Barrett Family named grant. I would like to thank Jason Bruns for being a huge help in the field when few others were. Dr. Masato Ueshima for his kindness and help in laboratory analysis at the University of Kansas.

I would like to thank Lawrence Livermore National Laboratories for the chance to conduct research. I would like to thank Dr. Susan Carroll for the fantastic opportunity to do the research, along with her kindness and generosity throughout the wonderful experience. I would like to especially thank Dr. Megan Smith for putting up with me during the summer and to this day; and for her immense amount of help and knowledge shared over the last year.

I would like to thank the following faculty within the department. Dr. George Clark for the numerous opportunities he has given others and myself within the department for travel and scholarship, along with his help in printing multiple posters at the last minute. Dr. Allen Archer for always keeping things lively and fun. Dr. Matthew Kirk for his engaging conversations and

work done within the department. Finally Dr. Matthew Totten for all the help over the last two years, and for the great opportunity to be on the IBA team.

I would like to thank all my friends in and outside of the department. Mike Vega for his help in the field and laboratory. Finally I would like to thank my good friend Shovon Barua for our innumerous talks about politics, drama, life and everything else over the last two years.

To my committee members: I would like to dearly thank Dr. Lynn Watney for always having the calmest of demeanors in many situations where most wouldn't, and for his unfailing sense of humor. I would also like to thank him for his generous support over the last two years, and for his immense amount of knowledge shared. Dr. Sambhudas Chaudhuri for his long and engaging discussions and for always trying to ensure that work was kept too a minimum. Finally Dr. Matthew Brueseke for being a phenomenal person and professor, and for his help with thin sections and use of his microscope and camera system.

I would like to thank my advisor and good friend Dr. Saugata Datta for the opportunity of working on this large and rewarding research project. I would especially like to thank him for his high standards that of which always drove me to achieve better; and for the push to always present at national and international conferences.

Finally I would like to deeply thank my loving family, those of whom have always showed continual support of me no matter my choices. I would like to especially thank my parents Ron and Julie Campbell for pushing me and providing me the innumerous opportunities throughout life; also Lesli, Scott, and Gus Campbell for all the help and frustrations over the years. Lastly my dear Kyleen Kelly for her enduring support and companionship, and for helping me get through the last two years, those of which have been the best years of my life.

Chapter 1 – Regional hydrochemical characterization for the determination of CO_2 storage in Kansas.

1.1 Introduction

Carbon dioxide storage in deep geologic formations has arisen to be one of the greatest potential approaches to feasibly decrease global atmospheric greenhouse gas levels. The first step in these projects is the identification of appropriate and safe repositories within the subsurface for the storage of this anthropogenic greenhouse gas. Carbon dioxide is chosen as the injectate due to its relative ease of capture from point sources that burn fossil fuels. The gas when combined with other ionic constituents that are usually found within the proposed geologic formation can form minerals and be safely trapped for millennia.

Three wells have been drilled in Kansas to investigate the feasibility of CO_2 storage within the regional carbonate Arbuckle aquifer. One of the wells, Wellington KGS #1-28 located in south-central Kansas in Wellington Field, Sumner County will be used for CO_2 injection and monitoring, while the other well in Wellington Field (KGS #1-32) and the well located in Cutter Field, Cutter KGS #1, in southwest Kansas will be used as a western calibration site. Swabs and drill stem tests have been taken from all three wells from 26 varying depths. Each sample depth has been analyzed for major and trace chemical concentrations, and varying isotopes. Vertical connectivity of the two locations is evaluated using the hydrochemical data. Lateral connectivity from the two study areas will be inferred, due to Cutter and Wellington Fields being 217 miles apart, by cross comparison of chemical data of each stratigraphic unit. Connectivity of the system will have implications for the migration of injected CO_2.

Experimental core-flooding tests were completed on individual cores within the Arbuckle from both Wellington and Cutter. The core-flooding simulated a small-scale injection scenario, utilizing cored rock and formation water, at formation temperatures and pressures. Analyzing formation water injected into the core will give insight into what minerals are dissolving and precipitating, and how the CO_2 will affect the aqueous environment at depth. Pre and post X-ray computed tomography scans were completed on the Cutter core before and after the core-flooding experiment to determine flow pathways through the core.

Geochemical and hydrochemical characterization of the environment within the aquifer is needed to establish baseline conditions in order to evaluate the affects of CO_2 injection on the pre-existing environment. Characterization can help determine the potential volume of CO_2 that can be injected, and how the CO_2 will interact through either dissolution or precipitation reactions. Hydrochemistry can determine the connectivity of the system, and can determine the direction and extent of flow of the CO_2 once it is injected.

1.2 Background

In order to curb the rising concentrations of greenhouse gases, carbon capture and storage (CCS) will be an essential component for global CO_2 reduction (IPCC, 2005) while fossil fuels are still being used. To achieve net neutrality or further reduction of CO_2 emissions, large volumes of gas will need to be stored, or a reduction in fossil fuel consumption made. Deep saline aquifers are an attractive repository for CCS due to their large capacity for storage and extensive abundance (US DOE, 2010). The DOE regional carbon storage partnerships estimate CO_2 storage within saline aquifers found in the

United States and Canada to be as low as 2,102 billion metric tons to as much as 22,043 billion metric tons of CO_2. These estimates are based on total area, gross formation thickness, total porosity, and in-situ pressure and temperature conditions. However, not all locations are suitable for storage (Bachu, 2003). Feasibility is determined by formation thickness, porosity, permeability, caprock integrity, and geologic stability, along with other geographical and economical considerations. Many other types of geologic formations are being considered for CO_2 storage (Leung et al., 2014). Projects around the world are currently investigating and injecting into saline aquifers. Much of the current scientific knowledge comes from these small and large-scale injection projects and the experience gained by the petroleum industry (Michael et al., 2010) in enhanced oil recovery (EOR) where CO_2 has been utilized since the 1970's. Combining the well-established science of EOR with the emerging CCS industry will allow for both increased hydrocarbon production and a decreased carbon footprint (Hill et al., 2013).

Carbon dioxide is stored at depth by four trapping mechanisms, all of which operate on varying time-scales (Figure 1.1) (Benson & Cole, 2008; Romanak et al., 2013; Burnside & Naylor, 2014). These mechanisms must all be effective to prevent significant leakage (Benson & Cook, 2005). Introduction of CO_2 gas into the subsurface and the subsequent acidification due to proton enrichment to the environment is shown in equations 1, 2, and 3 (Zekri et al., 2009). The acid (H_2CO_3) will disassociate into H^+ ions and bicarbonate (HCO_3^-), equation 3. Dissolution of the host rock in the form of a carbonate with the introduction of CO_2 can be seen in equations 4 and 5 (Golubev et al., 2009). In equations 4 and 5 "Me" is Ca and Mg. pH buffering occurs through the

dissolution of carbonates. pH change within the environment is determined by the buffering capacity of that environment. Equation 6 shows the final stage of precipitation.

1) $CO_2(g) \rightarrow CO_2(aq)$
2) $CO_2(aq) + H_2O \leftrightarrow H_2CO_3(aq)$
3) $H_2CO_3(aq) \leftrightarrow H^+ + HCO_3^-$
4) $MeCO_3(s) + H^+ \rightarrow Me^{2+} + HCO_3^-$
5) $MeCO_3(s) \leftrightarrow Me^{2+} + CO_3^{2-}$
6) $Me^{2+} + CO_3^{2-} \leftrightarrow MeCO_3(s)$

Injection of CO_2 into a stable environment at depth has profound effects on the existing chemical equilibrium (Kampman et al., 2014; Black et al., 2014). CO_2 injection creates a dry dehydrated zone around the well, which subsequently increases the total dissolved content of the ionic species found within the formation water (Peysson et al., 2014). This increase can allow for premature precipitation of minerals or salts that can cause a localized reduction in porosity and permeability (Ott et al., 2015). As the CO_2 dissolves into the formation brine it causes acidification due to the formation of carbonic acid. The integrity of wellbores and caprocks can be affected and their capacity, potentially, diminished due to the lower pH. Caprock integrity is paramount as it is typically the first barrier of flow to the vertically buoyant gas (Wollenweber et al., 2010). Formation pressure must be monitored and injection pressure must not cause over-pressurization of the existing system, as it could detrimentally degrade the caprock and allow for leakage to occur (Song & Zhang, 2012). Leakage can also occur through existing faults systems and fracture networks that breach caprock and allow CO_2 to escape from the reservoir. Injection into sedimentary basins can be of concern from CO_2

leakage through abandoned or improperly sealed wells, especially oil and gas wells that penetrate the caprock and reservoir. These old wells are commonly lined with Portland cement, less resistant than modern cement mixtures to detrimental reactions when pH changes. This old type of cement can dissolve under low pH conditions and allow fracture pathways to develop. Pathways for fluid migration through cement can either be CO_2 induced or be already present, formed by improper cementation of the well. In contrast, fracture pathways can be filled thereby reducing permeability and leakage potential if cement carbonation occurs (Carey, 2013).

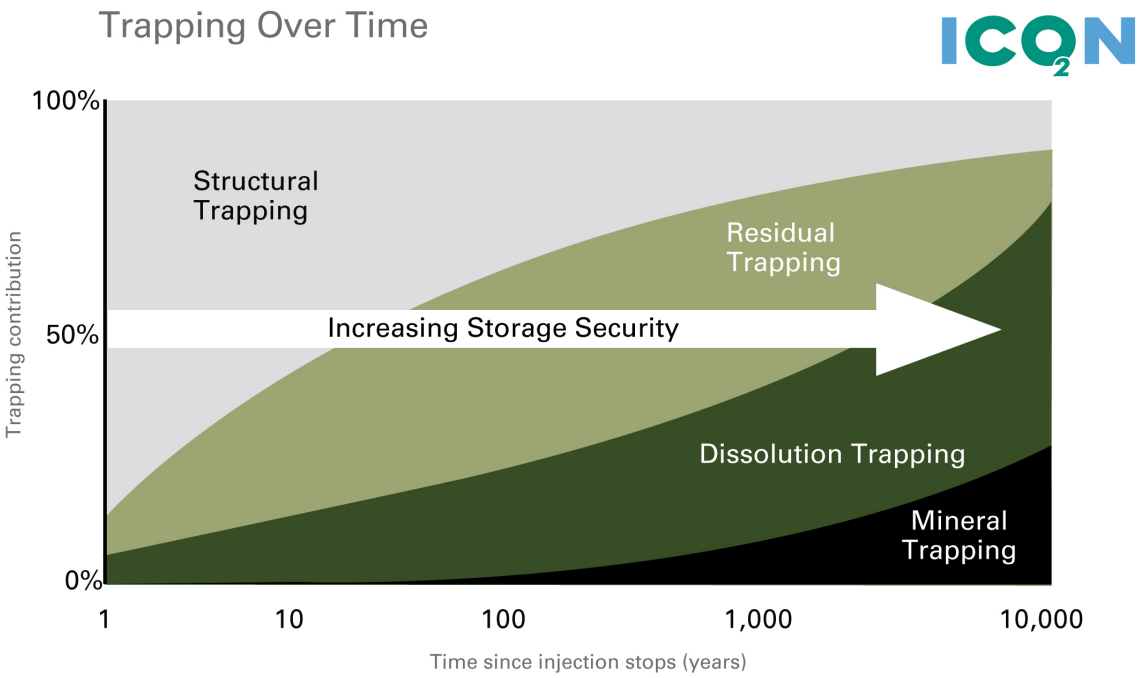


Figure 1.1 The four-major CO_2 trapping mechanisms (www.ICO2N.com).

Within the injection interval mineral dissolution caused by pH decrease could also allow for mobilization of metals or other toxic elements. Dissolution pathways develop through the caprock or wellbores and could result in extensive contamination of CO_2 and

any mobilized metals into freshwater resources or to the surface (Kharaka, et al., 2009; Humez, 2013).

Three experimental wells were drilled to investigate the feasibility for enhanced oil recovery (EOR) and CO_2 storage in the Mississippian and Lower Pennsylvanian reservoirs and carbon storage in the underlying Arbuckle Group in Kansas. Two wells, KGS 1-28 and 1-32, drilled in Wellington Field and the Berexco Cutter KGS #1 in Cutter Field are part of the regional evaluation of carbon storage in south-central Kansas. The main focus is on the Western Interior Plains Aquifer System. This system encompasses the oil and gas rich Mississippian carbonates and the Chester and Morrow sandstones, along with the underlying saline Arbuckle Group aquifer. Utilizing one of the largest aquifer systems in the United States with the estimated capacity to store 2.7 billion tons of CO_2 (Carr, et al., 2005), this aquifer system has a great potential to help Kansas in reducing global greenhouse gas concentrations.

1.2.1 Historical Hydrogeology

The Arbuckle aquifer, located throughout western and central Kansas is a target formation for CO_2 injection. The Arbuckle is part of the Paleozoic-age Western Interior Plains Aquifer System covering much of Kansas and the surrounding states. Within this system the carbonate Arbuckle aquifer is sufficiently deep (>3,500 ft.) and thick (>800 ft.), consisting of predominantly dolomitic strata (Figure 1.3). Multiple caprocks lie above to help insure confinement of the Arbuckle aquifer. Interbedded shales are reported throughout the Arbuckle and could allow for greater impedance to vertical CO_2 flow, while also allowing CO_2 to interact with the residual brine for longer periods of time. Total dissolved solids within the Arbuckle range from less than 10,000 to greater than

250,000 ppm (Carr et al., 2005). Groundwater flow within the OPAS is generally topographically controlled; flow is to the east from Colorado and northeast from Nebraska into the lowland areas toward the Missouri and Mississippi Rivers (Figure 1.2) (Carr et al, 1986; Jorgensen, 1989).

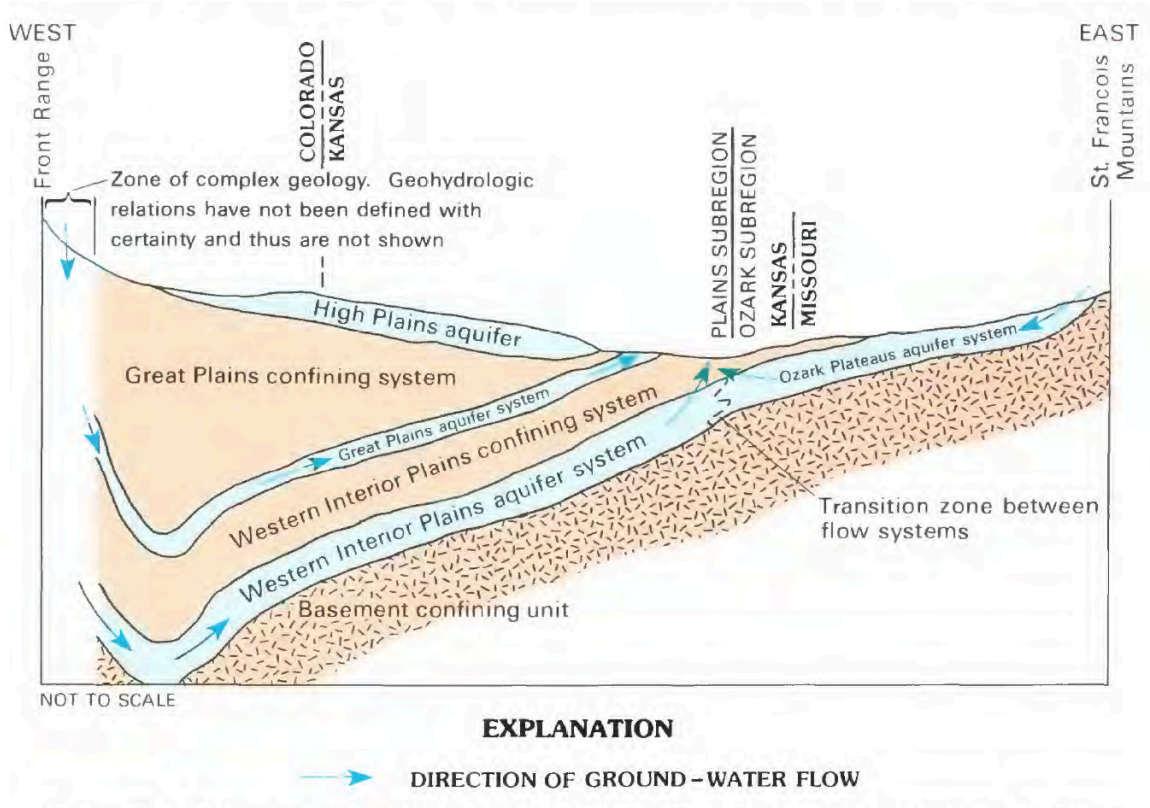


Figure 1.2 Regional groundwater flow units and direction of major aquifer systems in Colorado, Kansas, and Missouri. (Jorgensen et al., 1989).

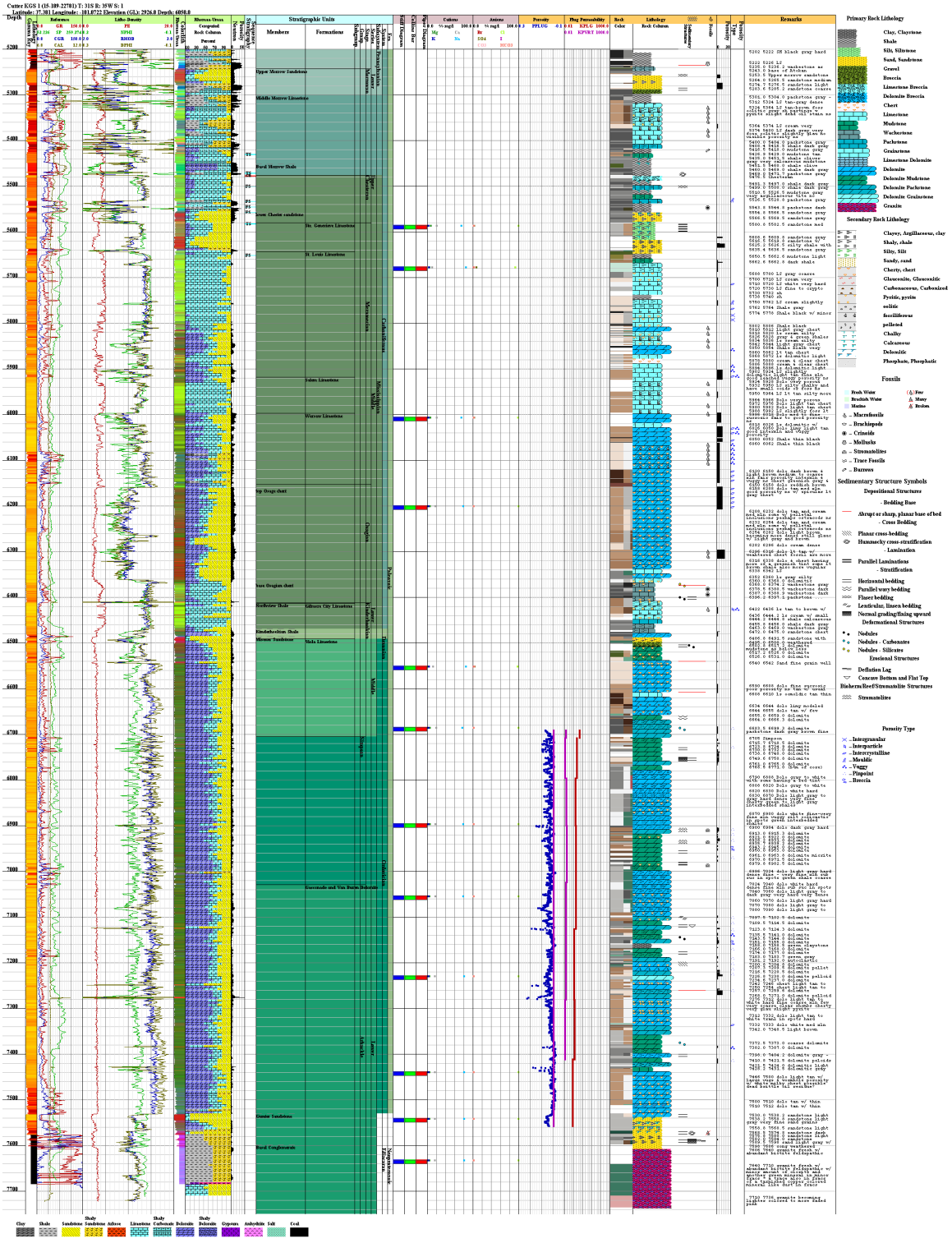


Figure 1.3 Stratigraphic column of Cutter KGS #1. Geologic units are labeled and their ages are shown. Water samples are highlighted to the right of the geologic ages of the formation units as blue, green, red boxes.

1.3 Methods

KGS 1-28 and 1-32 are located in the Wellington Field near the town of Wellington, Sumner County, Kansas. KGS 1-32 is located 2,835 ft. to the southwest of KGS 1-28 (Figure 1.4). Cutter is located in Stevens County, Kansas near the town of Moscow. Cutter is located 217 miles to the west of wells 1-28 and1-32 (Figure 1.4). The Wellington KGS #1-32 and Cutter KGS #1 wells were cored with 1,628 ft. of core retrieved in #1-32, and 1,042 ft. of core retrieved at Cutter KGS #1. A total of 8 drill stem tests (DST's) and 5 swabs were taken at Wellington (Table 1.1) and a total of 2 DST's and 11 swabs were taken at Cutter (Table 1.2). Formation waters were analyzed for some in-field parameters. The majority of water samples were analyzed for major cations and anions, along with $\delta^{2}H$, $\delta^{18}O$, $\delta^{13}C$ (DIC), and $^{87}Sr/^{86}Sr$ (Table 1.3, Table 1.4, Table 1.5, Table 1.6).

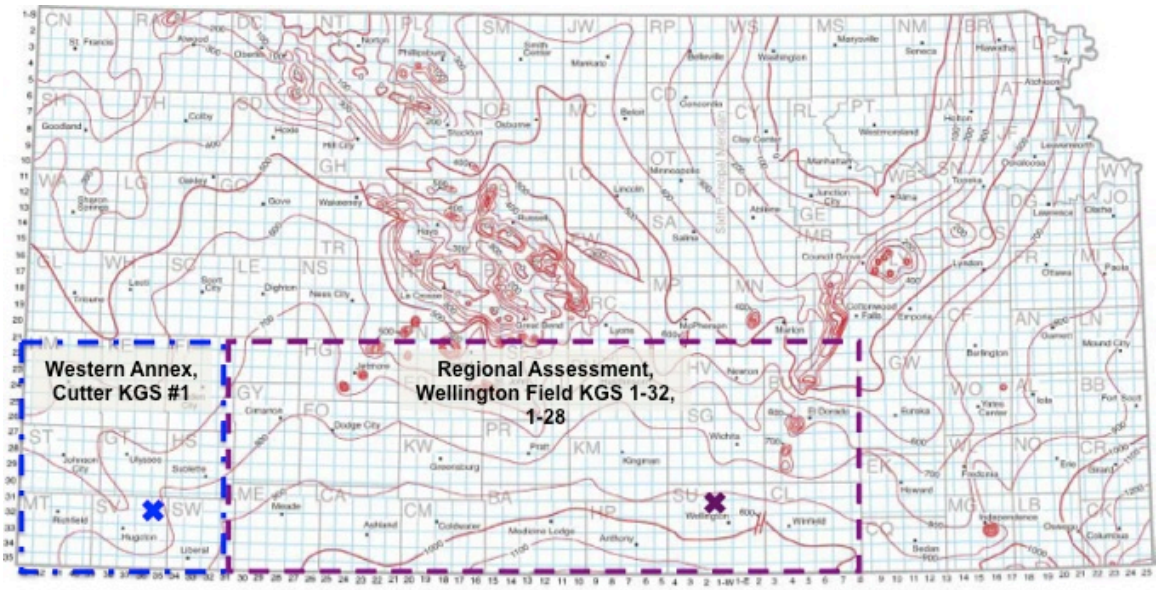


Figure 1.4 Isopach map indicating field locations and assessment areas of Cutter KGS #1 (Blue X), and Wellington Field KGS #1-32 & #1-28 wells (Purple X). Red lines indicate Arbuckle formation thickness. (Kansas Geological Survey)

Wellington	Date	Well #	Depth Interval (ft.)	Formation
DST 1	1/9/11	KGS 1-32	3,664 – 3,690	Mississippian
DST 4	1/25/11	KGS 1-32	4,175 – 4,190	Arbuckle
DST 3	1/24/11	KGS 1-32	4,280 – 4,390	Arbuckle
Swab 5	6/14/12	KGS 1-32	4,374 – 4,386	Arbuckle
DST 2	1/23/11	KGS 1-32	4,465 – 4,575	Arbuckle
Swab 4	6/12/12	KGS 1-32	4,872 – 4,878	Roubidoux
DST 8	3/6/11	KGS 1-28	4,866 – 4,885	Roubidoux
DST 7	3/6/11	KGS 1-28	4,917 – 4,937	Gasconade
Swab 3	6/11/12	KGS 1-32	4,924 – 4,932	Gasconade
Swab 1	7/29/11	KGS 1-28	4,995 – 5,015	Gasconade
Swab 2	8/11/11	KGS 1-32	5,000 – 5,020	Gasconade
DST 6	3/5/11	KGS 1-28	5,026 – 5,047	Gasconade
DST 5	3/5/11	KGS 1-28	5,133 – 5,233	Gunter – Basement

Table 1.1 Wellington 1-32 and 1-28 swab and DST samples, date sampled, depth ranges of sample, and corresponding formations.

Cutter	Date	Well #	Depth Interval (ft.)	Formation
Swab 11	7/26/13	Cutter KGS #1	5,545 – 5,622	Chester
Swab 10	7/25/13	Cutter KGS #1	5,670 – 5,680	St. Louis
Swab 9	7/23/13	Cutter KGS #1	6,000 – 6,010	Warsaw
Swab 8	7/22/13	Cutter KGS #1	6,194 – 6,204	Osage
Swab 7	7/22/13	Cutter KGS #1	6,543 – 6,558	Viola
Swab 6	7/16/13	Cutter KGS #1	6,676 – 6,686	Simpson
Swab 5	7/10/13	Cutter KGS #1	6,880 – 6,904	Jeff City – Cotter
Swab 4	7/9/13	Cutter KGS #1	7,046 – 7,056	Jeff City – Cotter
Swab 3	7/1/13	Cutter KGS #1	7,218 – 7,234	Gasconade
DST 2	7/3/13	Cutter KGS #1	7,218 – 7,234	Gasconade
Swab 2	6/26/13	Cutter KGS #1	7,430 – 7,442	Gasconade
Swab 1	6/25/13	Cutter KGS #1	7,532 – 7,543	Gunter
DST 1	6/28/13	Cutter KGS #1	7,522 – 7,735	Gunter

Table 1.2 Cutter swab and DST samples, date sampled, depth ranges of sample, and corresponding formations.

Swab tests, were performed by perforating the casing of the well and allowing formation fluid to enter the well. Removable inflatable packers were placed above and below the targeted formation depth to limit contamination from surrounding waters and allow for fluid entry from the targeted formation. The flow of water into the well varied by location and formation, and sometimes required a couple of days to get sufficient fluid

volume. Once the fluid was available a bailer retrieved the water for sample collection. Drill stem tests are similar to swab tests except for the manner in which fluid is retrieved and that no well casing is present when perforating. DST's measure formation pressures while also allowing fluid recovery for testing. Fluid retrieved for both tests was generally the dirtiest near the top of the fluid column and required sampling to occur as cleaner water surfaced.

Using the analyzed formation waters and cored sections, experimental core flooding was performed later in the laboratory. Cores from both KGS 1-32, and Cutter were experimentally investigated by simultaneously injecting formation brine and CO_2 into a chosen core plug drilled from each well. These experiments investigated the relationships between porosity and permeability change that would occur with the introduction and injection of CO_2 by creating an in-situ injection scenario. X-Ray Computed Tomography (XRCT) scans taken of the cores, pre and post experimental injection, were used to determine fluid flow pathways and if preferential pathways of dissolution developed. Preferential pathways are shown by increases in porosity seen in the post-experimental scans. Mineral precipitation and dissolution is shown by decreases or an increase in pore space, represented by the color black on the XRCT scans. XRCT scans are used to compliment the solution chemistry that was monitored throughout the experiment and allow for an understanding of a larger scale injection scenario.

1.3.1 Methods of water analyses at Wellington

KGS wells 1-28 and 1-32 were completed and sampled in 2012 to a depth of ~5,200'. All water samples were collected via drill stem tests and swabbing (Table 1.1). Water was allowed to freely flow from the well to permit the cleanest and clearest water

possible for sampling. Water was collected in 5 gallon buckets and immediate sample collection took place in the following containers: one 2 gallon Thermo Scientific® clear HDPE jug (Cat. No. 02- 923K); two 500 mL Fisherbrand® clear HDPE bottles (Cat. No. 02-912-323); one 250 mL Fisherbrand® clear glass bottle (Cat. No. 02911760); two 125 mL Thermo Scientific® amber HDPE bottles (Cat. No. 02-923-5C); one 60 mL Fisherbrand® glass bottle (Cat. No. 02-911-757); and two 50 mL Fisherbrand® clear centrifuge tubes (Cat. No. 06-443-20). Upon completion of sampling all sample containers were sealed with electrical tape and kept on ice. All samples were taken while wearing gloves, and all equipment was cleaned with deionized water (DI). All samples were filtered through a 0.45 μm Milipore® filter. Half of the samples were acidified with Optima grade HNO_3 (65-70%) for major cation analysis, and the other half were unacidified for major anion analysis. Water was monitored utilizing a HACH® Hydromet Hydrolab® MS5® Water Quality Multiprobe (Cat. No. 003078HY) connected to the hand-held Trimble® Recon® handheld PDA (400 64/256 Yellow BT/802; Cat. No. 69670). The Hydrolab was used to measure conductivity (μS/cm), dissolved oxygen (DO) (mg/L), oxidation-reduction potential (ORP) (mV), pH, resistivity, salinity (ppt), and temperature (°C). Utilizing a HACH® DR2800 spectrophotometer total iron, ferrous iron, and alkalinity were measured. Total iron was measured using the FerroVer® iron reagent AccuVac® ampules (Prod. #2507025) with a range of 0.02-3.00 mg/L Fe, HACH® method 8008. Ferrous iron was measured using the Ferrous iron reagent AccuVac® ampules (Prod. #2514025) with a range of 0.02-3.00 mg/L Fe^{2+}, HACH® method 8146. Total alkalinity was measured using the alkalinity TNTplus reagent set (Prod. #TNT870) with a range of 25-400 mg/L $CaCO_3$, HACH® method 10239. Inductively Coupled

Plasma-Optical Emission Spectroscopy (ICP-OES) analyzed major cation data for each DST, and for swab 1. High Resolution Inductively Coupled Plasma Mass Spectroscopy (HR-ICP-MS) analyzed swabs 2-5. Analyses were performed at Activation Laboratories®, CA. ICP-OES samples were run through a Varian® 730-ES Axial ICP, and the ICP-MS were run through an Element2®. IC analyses were run on a Dionex® 120 with a Dionex® IonPac® AS9-HC Column. 12 of the brine samples were analyzed for δ^2H, $\delta^{18}O$ and were analyzed by stable isotope mass spectrometry (SIMS) using a Picarro G1301. A few samples were analyzed for $^{87}Sr/^{86}Sr$ and selected based off of the δ^2H, $\delta^{18}O$ analysis and interpretation. $^{87}Sr/^{86}Sr$ isotopic ratios were analyzed on a Triton multi-collector mass-spectrometer. Rb and Sr were separated by extraction chromatography. During the analysis the ratios $^{87}Sr/^{86}Sr$ of NBS 987 standard was 0.710246+/-0.000007. Analysis was performed by Activation Laboratories®.

1.3.2 Methods of water analyses at Cutter

Cutter KGS #1 was sampled and completed in July 2013 to a depth of 7,742'. 11 swabs and 2 DST's were taken from various depths (Table 1.2).



Figure 1.5 Surrounding area around Cutter KGS #1 in southwest Kansas.



Figure 1.6 Cutter in-field sampling during the summer of 2013.



Figure 1.7 Cutter field equipment setup and analysis. A) Picture shows field setup with peristaltic pump, multiple probes, and filtration equipment. B) Photo shows data collection from HACH® Hydrolab. Spectrophotometer analysis was performed within the truck due to its sensitivity to light.

The same sampling procedure and protocols were followed as were done at Wellington, unless otherwise noted. Water samples were collected in the following: two 2 gallon Thermo Scientific® clear HDPE jugs (Cat. No. 02- 923K), two 500 mL Fisherbrand® clear HDPE bottles (Cat. No. 02-912-323), two 250 mL Fisherbrand® clear glass bottles (Cat. No. 02-911-760), two 125 mL Thermo Scientific® amber HDPE bottles (Cat. No.02-923-5C), three 60 mL Fisherbrand® clear glass bottles (Cat. No. 02-911-757), and two 50 mL Fisherbrand® clear centrifuge tubes (Cat. No. 06-443-20). Utilizing gloves, all samples were filtered through a 0.45 μm Milipore® filter. Half of the samples were acidified with Optima grade HNO_3 (65-70%) for major cation analysis, and the other half were unacidified for major anion analysis. Oil was filtered out utilizing an initial 0.10 μm filter followed by the aforementioned 0.45 μm filtration. The HACH® Hydromet Hydrolab® MS5® Water Quality Multiprobe was used and measured the same parameters as was done at Wellington. In addition to the Hydrolab three different probes were added and include: Mettler Toledo SevenGo meter, Mettler Toledo SevenGo Pro meter, and a HACH® HQ40d Multi meter. The Mettler Toledo SevenGo SG3 meter measures conductivity (μS/cm), and the SevenGo pro SG6 measures DO (%). The HACH® HQ40d measures pH, ORP (mV), temperature (°C), resistivity (MΩ-cm), salinity (ppt), and total dissolved solids (TDS) (mg/LΩ). Again using the HACH® DR2800 spectrophotometer additional new tests were added, including the three mentioned previously, and include: Nitrate TNT Plus reagent (Prod. #TNT835) with a high range 1.0-60 mg/L NO_3, and low range of 0.23-13.5 mg/L NO_3-N, HACH® method 10206; Sulfate TNTplus, High range (Prod. #TNT865) with a range of 150-900 mg/L SO_4, HACH® method 10227; Ammonia TNTplus, HR (Prod. #TNT832) with a range of

2-47 mg/L NH_3-N, HACH® method 10205; and Iron TNTplus reagent (Prod. #TNT858) with a range of 0.2-6.0 mg/L Fe, HACH® method 10229. Not all of these tests were run on each swab as new tests were progressively added throughout field sampling. Analyses of field test kits were completed after sample collection and electronic measurements were recorded. CHEMetrics® and HACH® test kits were used. CHEMetrics® kits that were used include: Oxygen (Dissolved) (Cat. No. K-7540) with a range of 0-40 ppb, method RhodazineD; Nitrate (Cat. No. K-6909D) with a range of 0-30 ppm as N, method Cadmium Reduction; Nitrite (Cat. No. K-7004) with a range of 0-2.2 ppm as N, method Azo Dye Formation; Phosphate (Cat. No. K-8510) with a range of 0-1 & 1-10 ppm, method Stannous Chloride; and Silica (Cat. No. K-9010) with a range of 0-1 & 1-10 ppm, method Heteropoly Blue. HACH® test kits included: Alkalinity (Prod. #20637-00) with a range of 10-4,000 mg/L, method Digital Titrator/Sulfuric Acid; Chloride (Prod. #208601) with a range of 5,000-100,000 mg/L Cl^-, method Drop count titration/Silver nitrate; and Sulfate (Prod. #2251-00) with a range of 50-200 mg/L, method Extinction/Turbidimetric. Water samples were processed for major cation and anion analysis, and were analyzed at Activation Laboratories®. Major cations were determined using a Spectro® Cirros (ICP-OES) that included a 36 elemental suite. Major anions were analyzed using a Dionex® DX-120 IC for a determination of seven anions. Isotech Laboratories Inc., Champaign, IL, analyzed the samples from Cutter for light isotopes and included δ^2H, $\delta^{18}O$, $\delta^{13}C$ (DIC). δ^2H and $\delta^{18}O$ were analyzed on a Picarro® CRDS model L1102-i. $\delta^{13}C$ (DIC) was performed on a Thermo® GasBench II interfaced with a Thermo® Delta V Plus IRMS. $^{87}Sr/^{86}Sr$ isotopic ratios were analyzed on a Triton multi-collector mass-spectrometer. Rb and Sr were separated by extraction chromatography. During the analysis the ratios

$^{87}Sr/^{86}Sr$ of NBS 987 standard was 0.710246+/-0.000007. Analysis was performed by Activation Laboratories®.

1.3.3 Wellington experimental flow-through methods

Supercritical flow-through experiments were undertaken at the National Energy Technology Laboratory (NETL) in Pittsburgh, PA. A flow-through Core Flow System 839Z was used with a Hassler type core holder. This Hassler cell allows for injection conditions to be recreated by allowing for controlled temperatures and confining pressures. This experiment injects brine and CO_2 independently and relies on mixing to occur within the core. The brine and CO_2 are housed in different accumulators. Brine temperatures were set to 40°C to mimic Arbuckle formation temperatures. CO_2 was kept in a liquid state at 4°C. Confining pressure of the core was set to 2,100 psi. A dual piston pump injects both CO_2 and brine simultaneously, and during that process CO_2 becomes supercritical. All flow rates, temperatures, and pressures are regulated and controlled. Flow rates are not only determined by the pumps, but by the porosity and permeability of the core. Sample 31-19 (4,977') was chosen. The core was light to medium grey; autoclastic breccia; open fractures; large, sparry pink dolomite; strongly brecciated; vugs, fractures with fluid enhancement; and Fe oxides present (2mm). Equilibrium conditions were established by allowing the core to be saturated with brine for 12 hours. After 12 hours CO_2 was injected in order to simulate the dehydration phase that occurs after injection. This phase occurs when the injected CO_2 pushes out all formation waters creating a dehydrated zone around the well. Injection of CO_2 occurred for a couple minutes, and then simultaneous brine-CO_2 flow was initiated at a rate of 1mL/min. Post flow-through water was collected and sampled every hour for major cation and anion

analysis. Alkalinity and pH were monitored and measured by a HACH® DR2800 spectrophotometer at every sampling interval. Major cation and anion analysis was performed by Activation Laboratories® with the same instruments and methods as stated previously.

1.4 Results

The following series of graphs are arranged sequentially, first for Wellington wells and later for Cutter. Comparison graphs between Cutter and Wellington that display data presented below are combined into more detailed graphs and are included in Appendix A.

1.4.1 Results on Hydrogeochemistry of Wellington waters.

Swabs and DST's were analyzed for major and trace ionic species and isotope compositions (Table 1.3, and Table 1.4). Individual ions are plotted to represent a vertical depth profile of their concentrations for both swabbed and DST waters (Figure 1.9, Figure 1.10, and Figure 1.11). Formation waters are predominantly a Na-Ca-Cl brine (Figure 1.8), with TDS varying from 54,002 mg/L within the shallowest depths, to 191,717 mg/L within the deepest depths. $Ca^{2+}$and Mg^{2+} show increased enrichment with depth, as seen on the Piper diagram and individual depth plots. Alkalinity values vary between 124 mg/L and 378 mg/L HCO_3^- within the Arbuckle.

Wellington			K^+	Mg^{2+}	Mn	Si	Ca^{2+}	Fe	Na^+	S	Sr^{2+}	Br^-	Cl^-	SO_4^{2-}
Sample Name	Well #	Depth (ft.)	mg/L`	mg/L	mg/L	mg/L	mg/L	mg/L	mg/L	mg/L	mg/L	mg/L	mg/L	mg/L
DST 1	KGS 1-32	3,664 – 3,690	702	1890	0.89	3.3	11300	0.29	58000	233	417	464	119000	703
DST 4	KGS 1-32	4,175 – 4,190	834	880	1.1	14	5030	0.05	31500	345	158	120	65800	1060
DST 3	KGS 1-32	4,280 – 4,390	424	460	0.59	12.9	2150	0.07	17400	553	71.3	75.9	32000	1610
Swab 5	KGS 1-32	4,374 – 4,386	398	933	3.80	5.9	3907	12.844	25585		132.34	97	47598	986
DST 2	KGS 1-32	4,465 – 4,575	347	347	1.17	8.3	1500	0.09	15900	271	55.4	79.7	30500	873
Swab 4	KGS 1-32	4,872 – 4,878	900	1764	2.21	8.4	10527	1.772	50565		324.04	191	103326	543
DST 8	KGS 1-28	4,866 – 4,885	1080	1160	2.2	12.1	7310	0.2	38300	136	253	190	84400	346
DST 7	KGS 1-28	4,917 – 4,937	1430	1630	0.81	11.4	10300	0.09	54300	148	334	235	118000	336
Swab 3	KGS 1-32	4,924 – 4,932	907	1802	3.06	4.8	10550	10.972	49842		330.61	196	104390	478
Swab 1	KGS 1-28	4,995 – 5,015	1160	1790	0.2	5	10600	0.03	57500	136	335	235	114000	425
Swab 2	KGS 1-32	5,000 – 5,020	961	1910	1.27	4.8	11784	8.677	54791		383.47	226	106013	389
DST 6	KGS 1-28	5,026 – 5,047	1280	1430	0.7	11.6	8820	0.08	48600	208	274	198	103000	3140
DST 5	KGS 1-28	5,133 – 5,233	1280	1450	0.61	10.2	8670	0.16	48400	247	262	176	102000	3320

Table 1.3 Wellington 1-32 and 1-28, analyzed ionic species concentrations, their corresponding depths and well locations. ICP-OES was used for DST and swab 1 cation analysis, while swabs 2-5 cations were analyzed using HR-ICP-MS.

Wellington			$\delta D\ H_2O$	$\delta^{18}O\ H_2O$	$^{87}Sr/^{86}Sr$
Sample Name	Well #	Depth (ft.)	(‰)	(‰)	(Molar)
DST 1	KGS 1-32	3,664 – 3,690	-15	-0.1	
DST 4	KGS 1-32	4,175 – 4,190	-44	-5.1	0.712677
DST 3	KGS 1-32	4,280 – 4,390	-66	-6.9	0.716239
Swab 5	KGS 1-32	4,374 – 4,386	-59	-6.8	
DST 2	KGS 1-32	4,465 – 4,575	-46	-5	0.717626
Swab 4	KGS 1-32	4,872 – 4,878	-30	-3.9	
DST 8	KGS 1-28	4,866 – 4,885	-30	-3.7	0.716381
DST 7	KGS 1-28	4,917 – 4,937	-27	-3.3	
Swab 3	KGS 1-32	4,924 – 4,932	-34	-3.1	0.717796
Swab 1	KGS 1-28	4,995 – 5,015	-26	-3.1	
DST 6	KGS 1-28	5,026 – 5,047	-25	-3.1	0.717457
DST 5	KGS 1-28	5,133 – 5,233	-19	-2.2	

Table 1.4 Wellington 1-32 and 1-28, analyzed isotopic concentrations, their corresponding depths and well locations. $^{87}Sr/^{86}Sr$ analysis was selected for a few depths based on the other two isotopic concentrations.

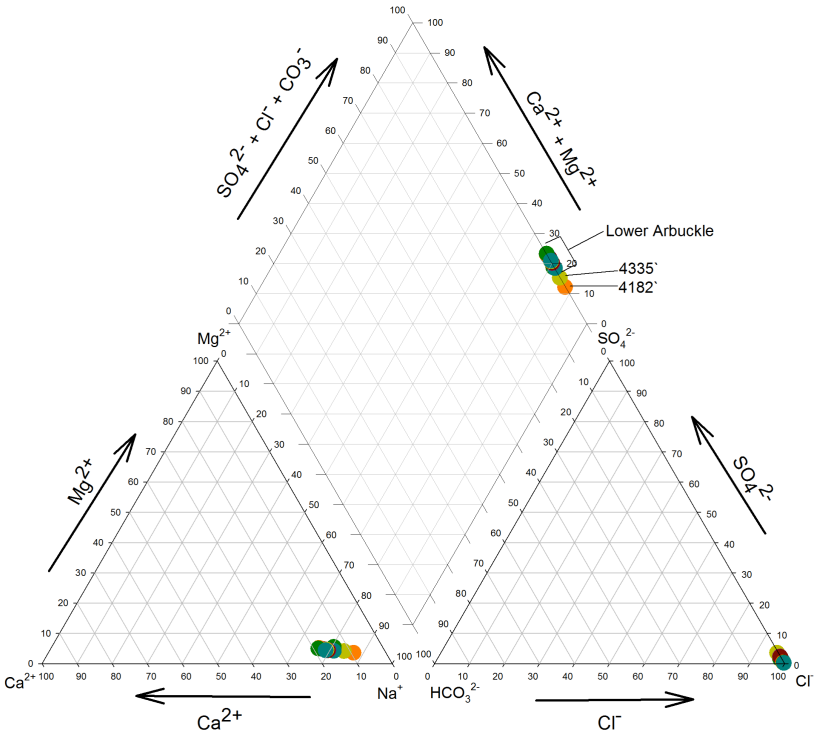


Figure 1.8 Wellington 1-32 and 1-28 piper diagram indicating a dominant Na-Ca-Cl brine. Wellington water increases in concentrations of Ca and Mg with depth. (Reproduced from Barker, 2012)

Individual major elemental concentrations plotted against depth show the majority of the elements increase with depth (Ca^{2+}, Mg^{2+}, Na^{+}, K^{+}, Sr^{2+}, Cl^{-}) with redox sensitive elements indicating no general trend with depth as seen in (Fe, Mn, P, S, SO_4^{2-}). Only below 5,036 ft. do the majority of elemental concentrations start to decrease. The decrease in concentration is due to the granite wash or Gunter Sandstone contact, which exhibits a different chemical composition than the overlying Arbuckle. The redox sensitive species and their depth wise concentration graphs show disagreement with swab and DST data, and is likely due to differences in HR-ICP-MS and ICP-OES analysis (Figure 1.9, Figure 1.10, and Figure 1.11). Large differences in analyzed concentrations between HR-ICP-MS and ICP-OES can be seen for: Mn, Fe, Li^{+}, Si^{2+}, and SO_4^{2-}. These differences could be due to the sampling procedures of DST and swabbed samples, or

due to the differences in analysis as detection limits for individual elements are different for both methods. ICP-OES is generally better used for major element concentrations while HR-ICP-MS is better used for determining trace element concentrations.

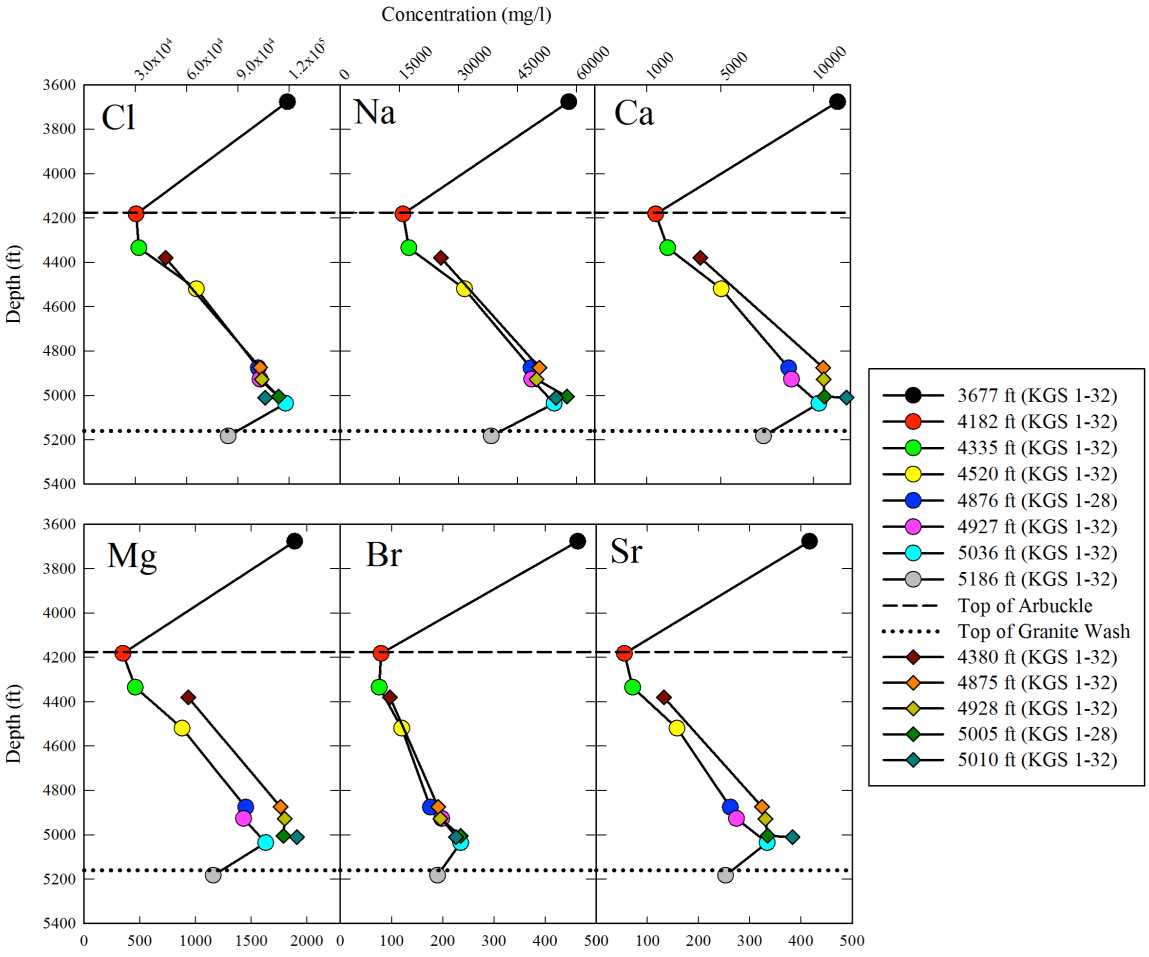


Figure 1.9 Depth profile of major cations and anions in Wellington. Circle symbols indicate DST samples, while diamonds indicate swab samples. Upper dashed line indicates top of Arbuckle, while lower dashed line indicates top of the Gunter Sandstone. (Reproduced from Barker, 2012)

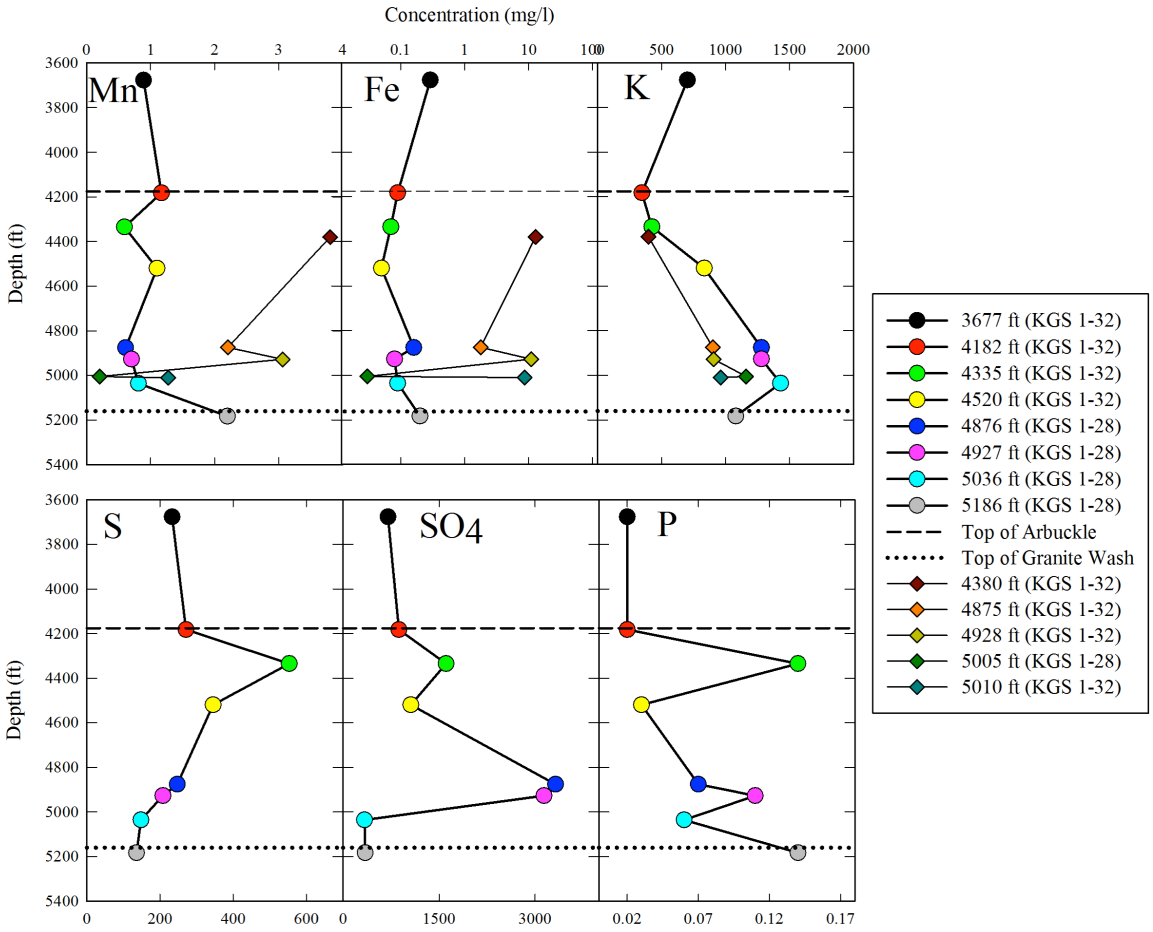


Figure 1.10 Depth profile of redox sensitive species in Wellington. Circle symbols indicate DST samples, while diamonds indicate swab samples. Upper dashed line indicates top of Arbuckle, while lower dashed line indicates top of the Gunter Sandstone. (Reproduced from Barker, 2012)

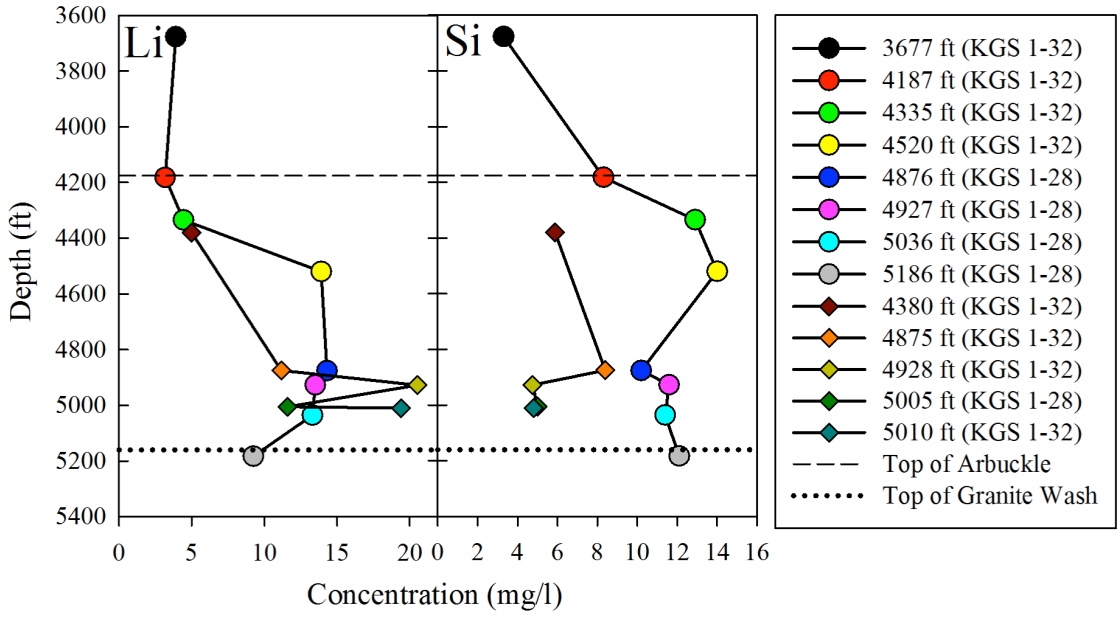


Figure 1.11 Depth profile of Li and Si in Wellington. Circle symbols indicate DST samples, while diamonds indicate swab samples. Upper dashed line indicates top of Arbuckle, while lower dashed line indicates top of the Gunter Sandstone. (Reproduced from Barker, 2012)

Major elements were plotted against chloride to investigate diagenetic alterations of brines (Figure 1.12, and Figure 1.13). Seawater evaporation curves were added to show depletion or enrichment in relation to seawater. Ca^{2+} and Sr^{2+} show similar trends with linear enrichment, while Mg^{2+} shows semi-linear depletion in relation to the evaporation curve. Na^{+} plots along most of the evaporation curve while K^{+} shows depletion and a strong relationship relative to the evaporation curve. Br^{-} is slightly depleted in relation to the evaporation cure with the one DST in the Mississippian showing enrichment. SO_4^{2-} is largely depleted, with two DST's within the Arbuckle showing distinct separation. Li^{2+} is enriched in relation to the seawater evaporation curve, and shows two possible groupings.

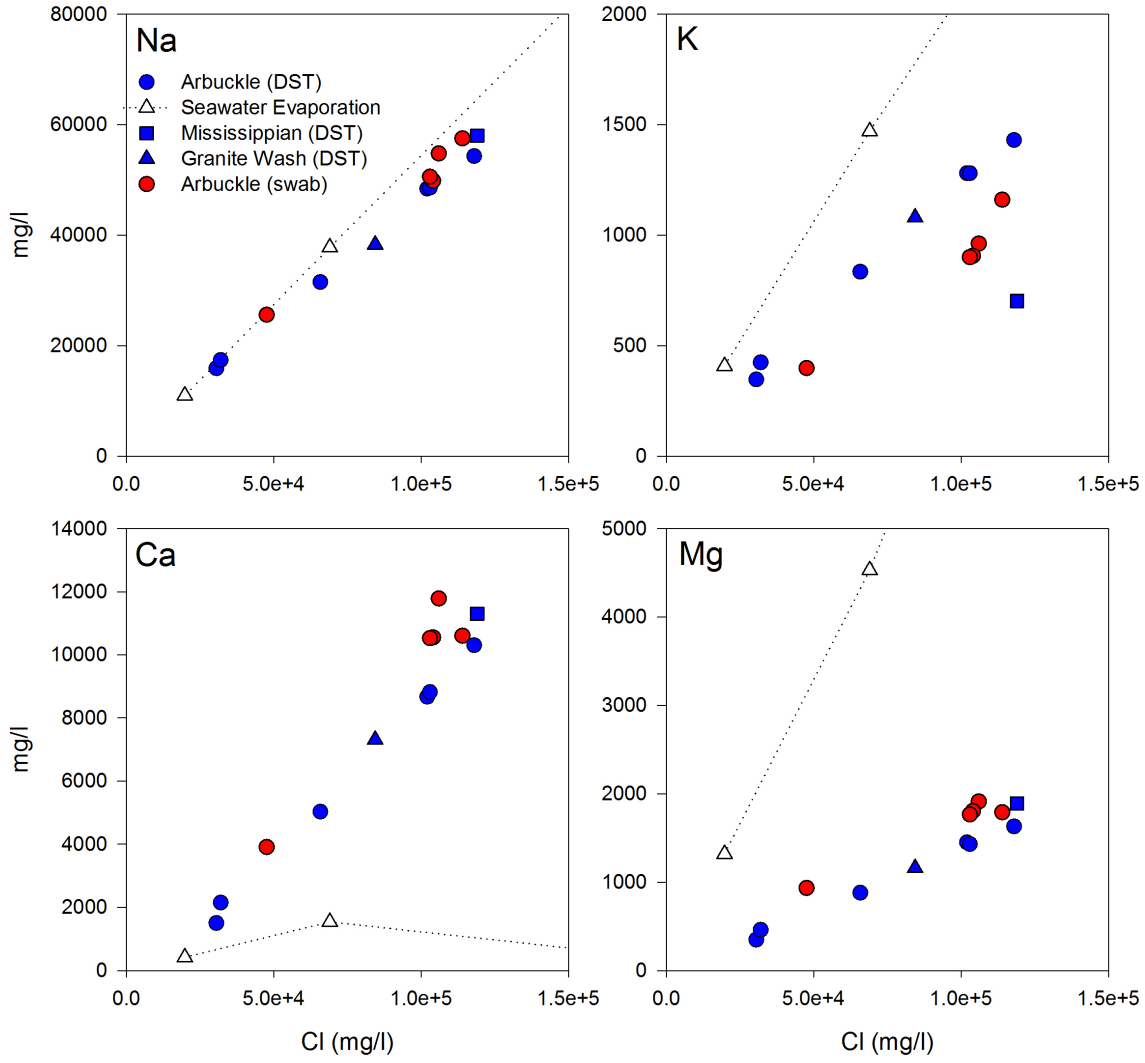


Figure 1.12 Ionic species (Na, K, Ca, Mg) against Cl^- in Wellington. DST samples are shown in blue, and swab samples are shown in red. (Reproduced from Barker, 2012)

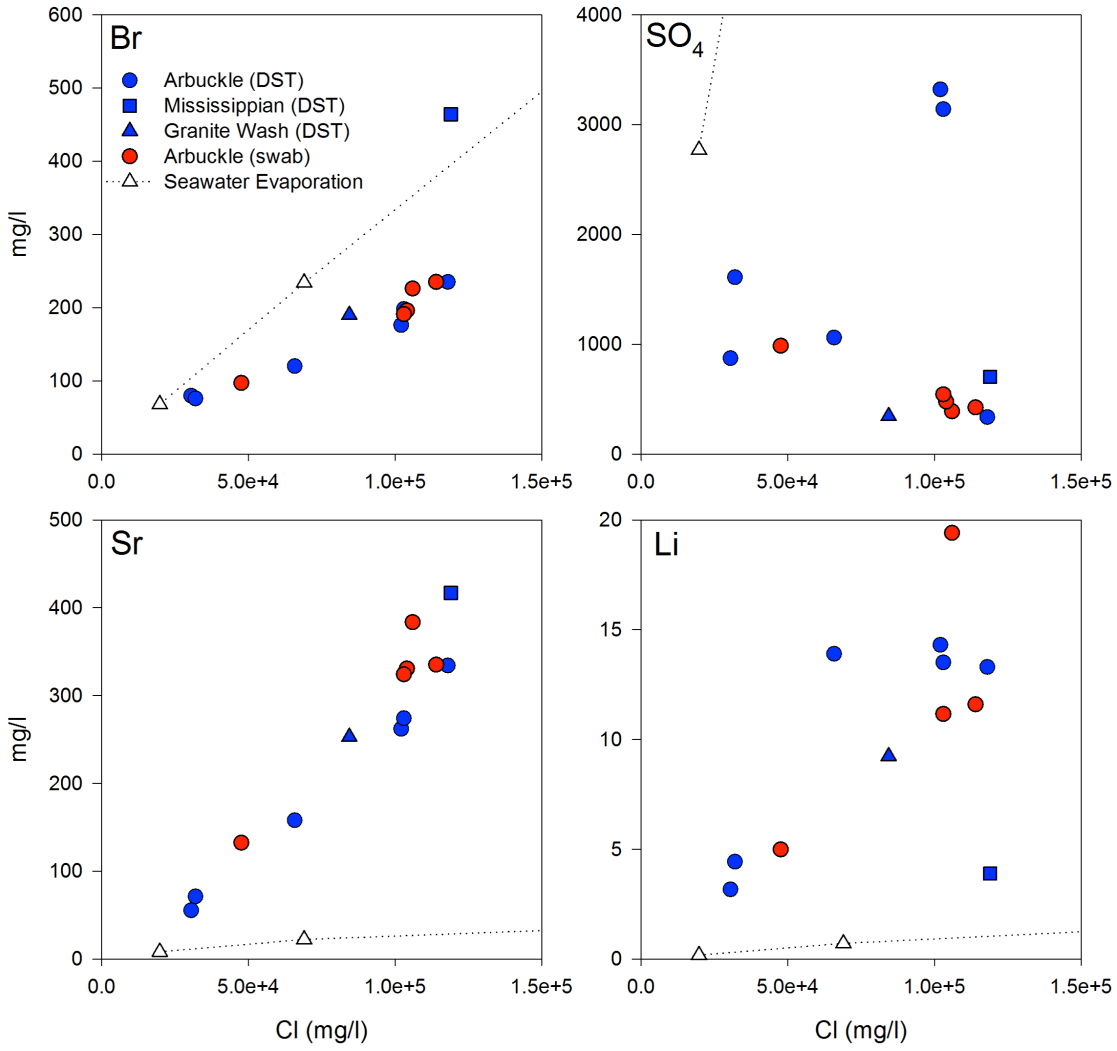


Figure 1.13 Ionic species (Br^-, SO_4, Sr, Li) against Cl^- in Wellington. DST samples are shown in blue, and swab samples are shown in red. (Reproduced from Barker, 2012)

Plots using molar ratios of Ca/Sr vs. Ca/Mg (Figure 1.14), demonstrate that the upper Arbuckle plots along the calcite recrystallization line, while the lower Arbuckle plots along the dolomitization trend line. Ca^{2+} vs. SO_4^{2-} was plotted to investigate any correlations between one another (Figure 1.15).

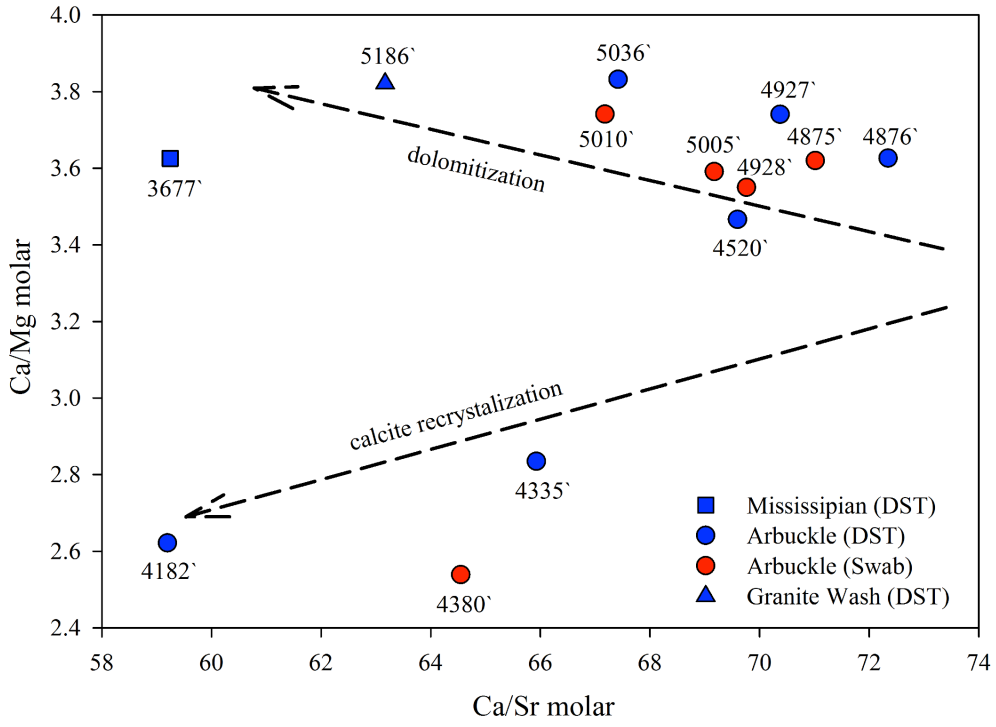


Figure 1.14 Ca/Sr vs. Ca/Mg molar ratio plots in Wellington Upper intervals trend toward calcite recrystallization. Deeper depths, with the exception of the Mississippian interval, trend toward dolomitization. (McIntosh et al., 2004) (Reproduced from Barker, 2012)

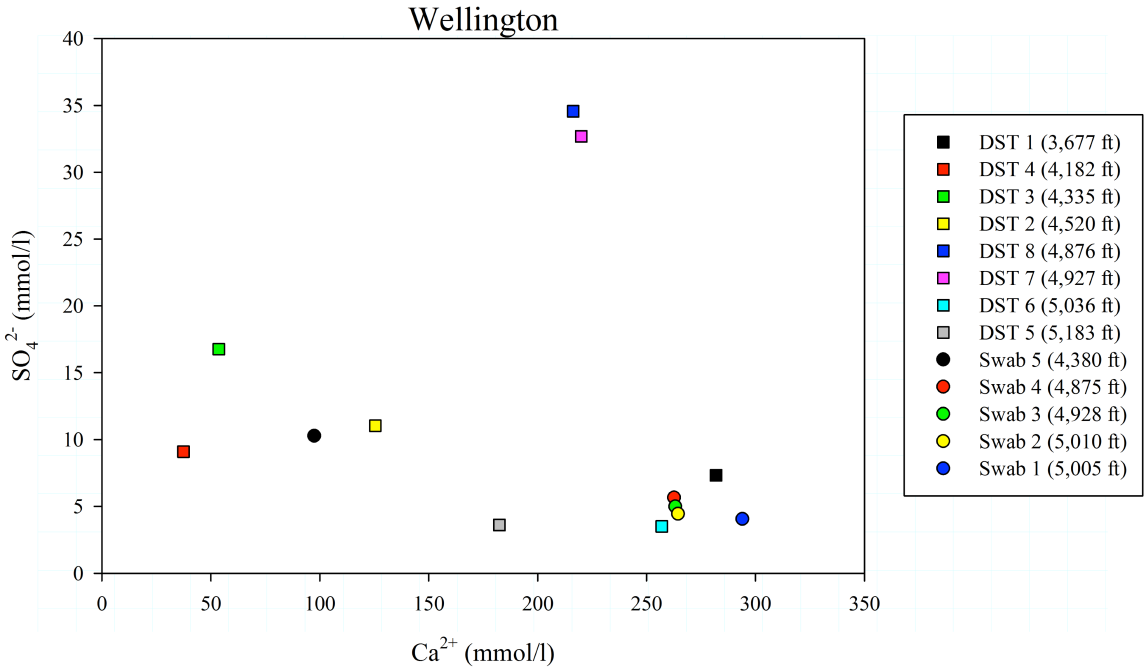


Figure 1.15 Ca vs. SO_4 in Wellington. Circles indicate swabs and squares indicate DST samples.

Vertical connectivity can be determined using δ^2H and $\delta^{18}O$ values and Cl/Br ratios. Isotopes were plotted against the global meteoric water line (GMWL) to indicate enrichment or depletion depending on if they plot above or below the GMWL line (Figure 1.16).

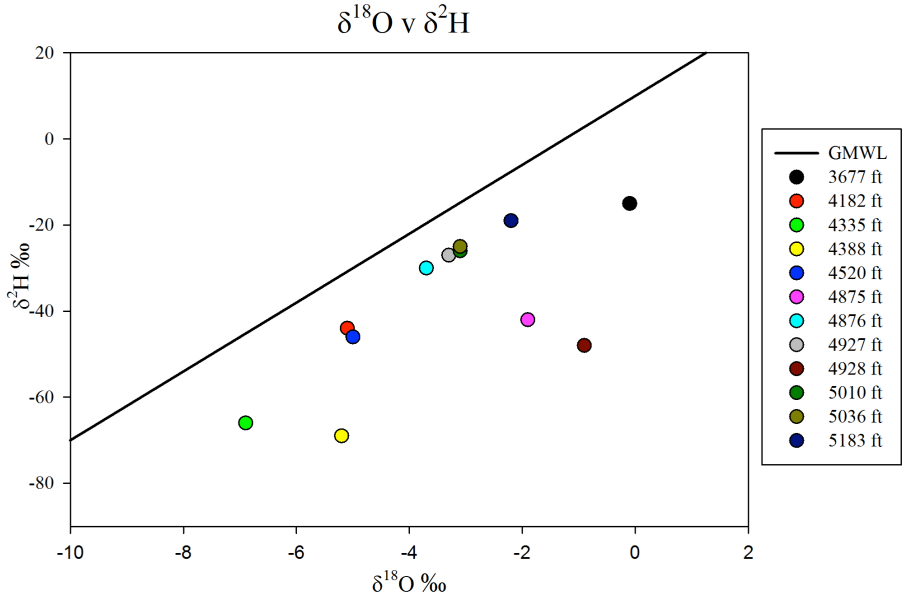


Figure 1.16 $\delta^{18}O$ vs. δ^2H in Wellington. All depths plot below and are depleted in relation to the GMWL. (Replotted from Barker, 2012)

The isotopes are all depleted with a close linear proximity in relation to the GMWL, with the lower Arbuckle being more enriched than the upper Arbuckle waters. Depth wise variation of individual isotopes indicate greatest enrichment within the Mississippian followed by depletion at depths 4,335' and 4,388', and then increasing in enrichment towards the Gunter Sandstone (Figure 1.17). 1/Sr vs. $^{87}Sr/^{86}Sr$ plots shows agreement between swab 3 and DST 6 (Figure 1.18). The samples show similar variation as the depth wise plot of $\delta^{18}O$ vs. δ^2H. This indicates separation between DST 3 and DST 2 with DST 3 lying above the baffle zone and DST 2 lying below it.

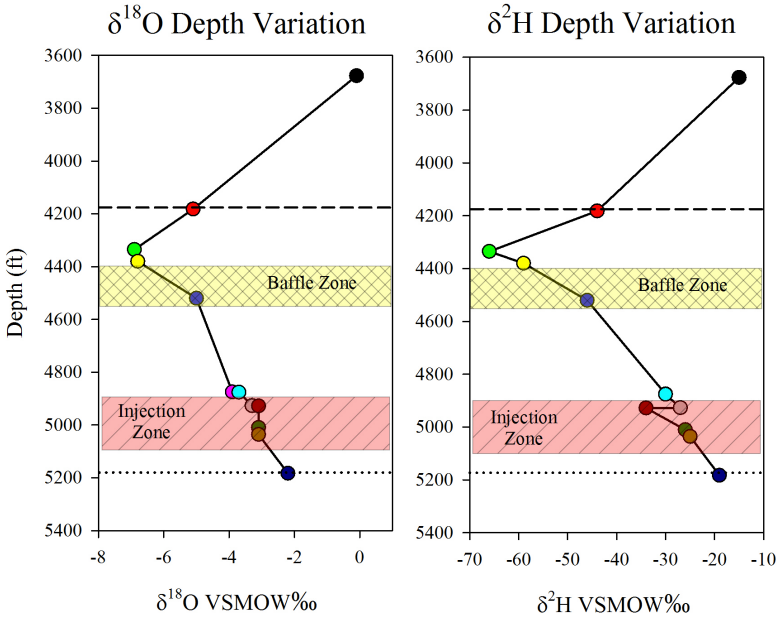


Figure 1.17 Depth wise profile of $\delta^{18}O$ vs. $\delta^{2}H$ in Wellington. Yellow-hatched box indicates the baffle zone, and the red-diagonal box indicates CO_2 injection zone. (Reproduced from Barker, 2012)

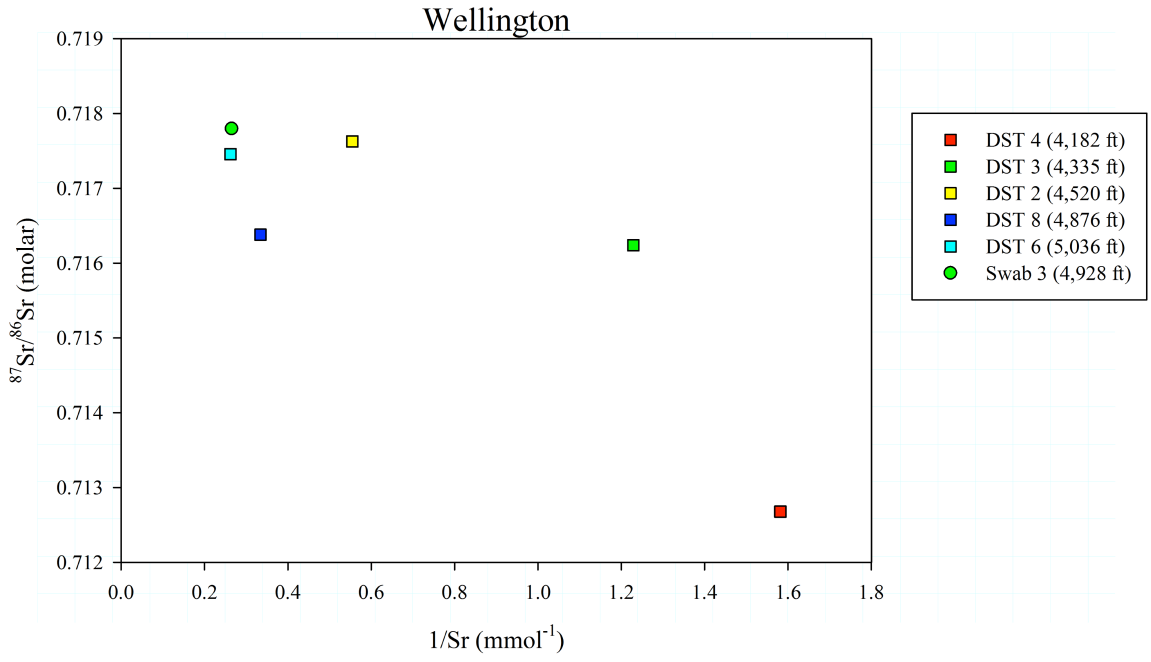


Figure 1.18 1/Sr vs. $^{87}Sr/^{86}Sr$ molar ratio in Wellington. Circles indicate swabs and squares indicate DST samples.

Isotopes ($\delta^{18}O$, and $\delta^{2}H$) were plotted against Cl^- to further investigate connectivity (Figure 1.19). This comparison shows distinct groupings of waters. Hypothetical mixing lines are shown to represent mixing between the Mississippian and the upper Arbuckle (line "A"), and the upper and lower Arbuckle (line "B"). Two clear groupings can be seen: the upper and lower Arbuckle. Connectivity between these zones however is limited, which is indicated by the distinct groupings. If groupings of similar depths are seen it can indicate vertical separation and limited connectivity.

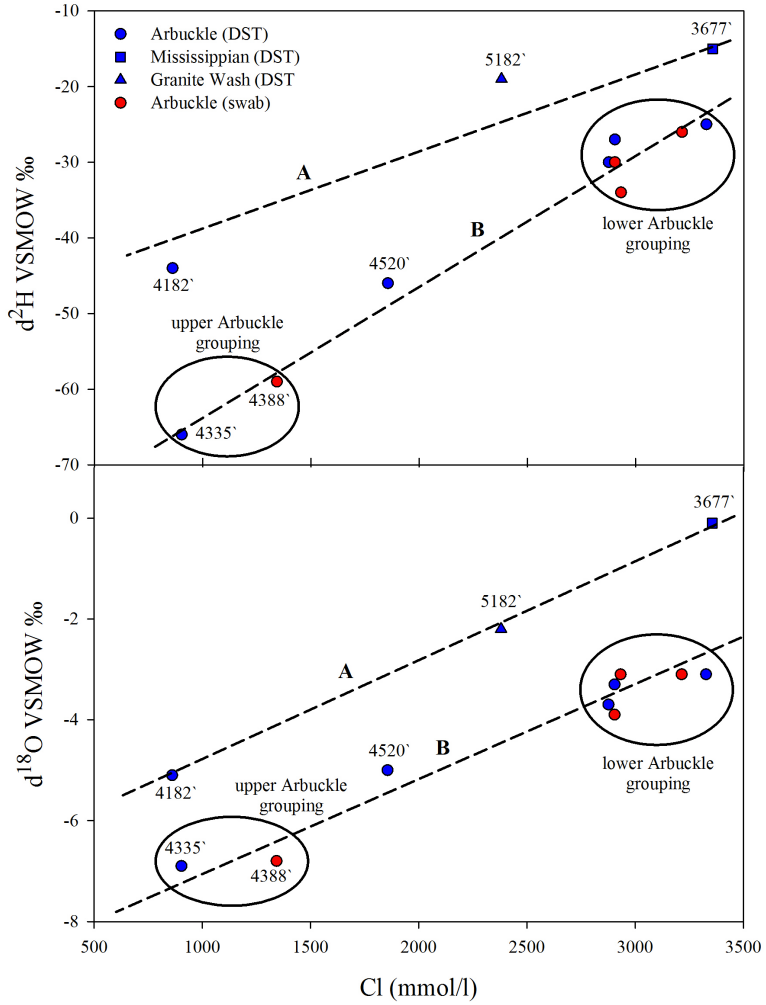


Figure 1.19 Cl^- vs. $\delta^{18}O$ and $\delta^{2}H$ in Wellington. DST samples are shown in blue, and swab samples are shown in red. Circles represent groupings of samples that correlate depth and Cl^- vs. isotope ratios. (Reproduced from Barker, 2012)

Cl/Br ratios are used to indicate mixing of waters, as they are both conservative species/tracers during the evaporation of seawater. The same groupings seen within the upper and lower Arbuckle of the isotopic data are seen here with the Cl/Br ratios plotted against Cl^- (Figure 1.20). Figures (Figure 1.21, Figure 1.22, and Figure 1.23) show the same groupings and separation of the upper and lower Arbuckle water. DST's 2 and 5 always segue the upper and lower Arbuckle groupings. In Figure 1.24 plots Cl/Br vs. Ca/Mg to investigate halite dissolution or calcite precipitation reactions. This figure indicates that the majority of the waters have been influenced by dolomitization of limestone and from halite dissolution.

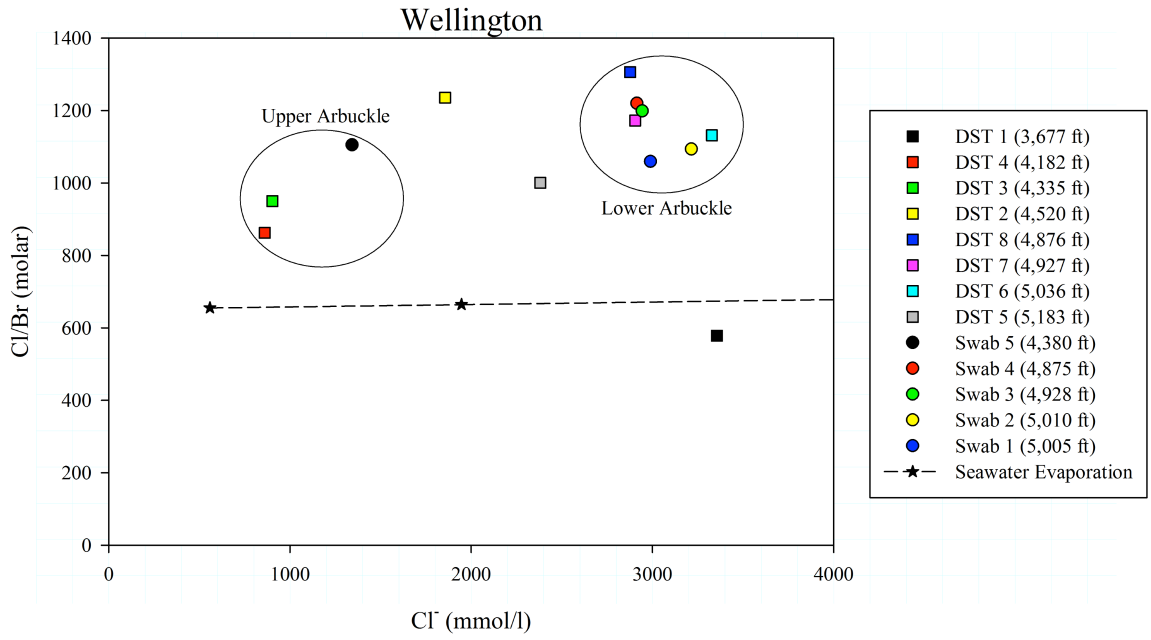


Figure 1.20 Cl/Br ratio against Cl^- in Wellington. Most of the depths, with the exception of the Mississippian interval, plot above the seawater evaporation curve. (Replotted from Barker, 2012)

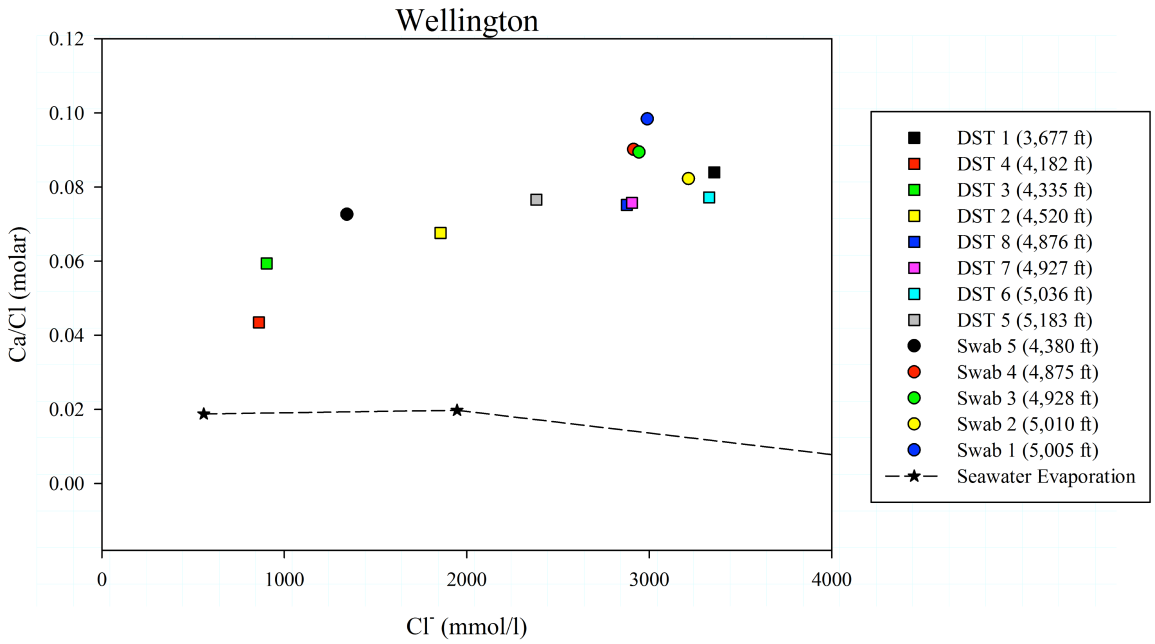


Figure 1.21 Cl- vs. Ca/Cl in Wellington. Circles indicate swabs and squares indicate DST samples.

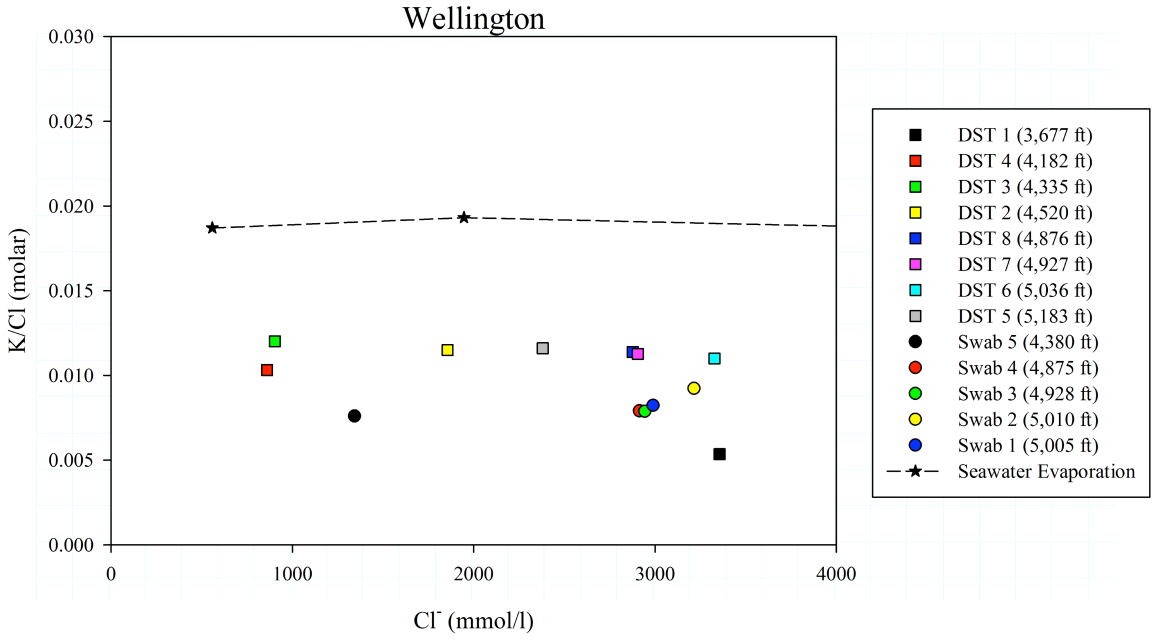


Figure 1.22 Cl- vs. K/Cl in Wellington. Circles indicate swabs and squares indicate DST samples.

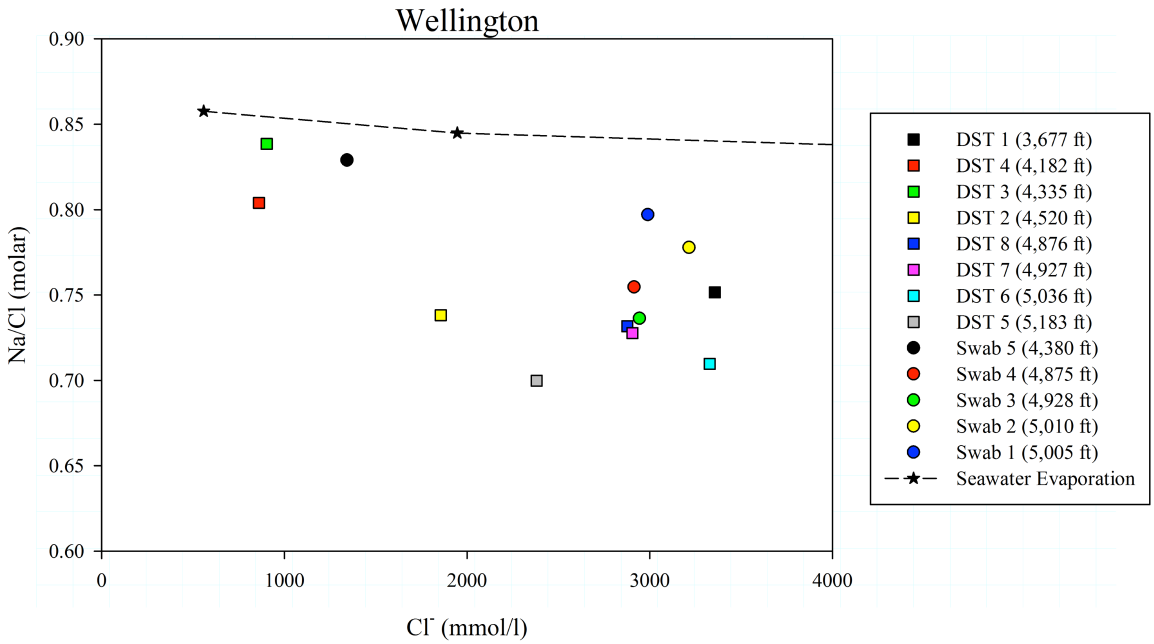


Figure 1.23 Cl⁻ vs. Na/Cl in Wellington. Circles indicate swabs and squares indicate DST samples.

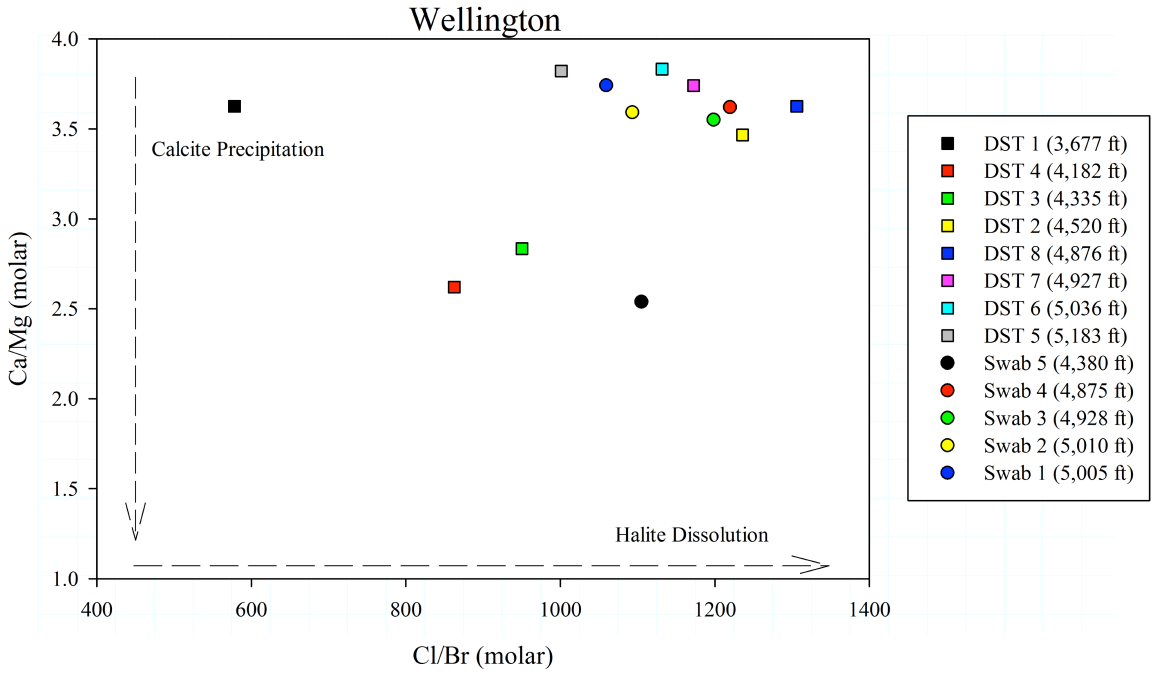


Figure 1.24 Cl/Br vs. Ca/Mg in Wellington. Circles indicate swabs and squares indicate DST samples. (McIntosh et al., 2004)

1.4.2 Results on Hydrogeochemistry of Cutter waters.

Due to the high TDS values of these waters, some elements were extremely difficult to analyze due to the large background noise created by the high salinity. Bromide was under detection limits when measured by KSU, but was above detection limits when measured by the KGS. Both data sets are shown to identify the similarity of concentration. Bromide data analyzed by the KGS is used in all of the figures for Cutter unless otherwise stated. Laboratory pH and alkalinity (HCO_3^-) of the water samples that was used in the following figures was measured by the KGS. Major elements that were above detection limits are shown in (Table 1.5), and isotopes are shown in (Table 1.6).The water is predominantly a Na-Ca-Cl type brine (Figure 1.25), with TDS values ranging from a low of 49,000 mg/L (swab 10) to a high of 172,000 mg/L (swab 1). Sample depths are all indicated with the same color in every figure for the following graphs of Cutter.

Cutter		K^+	Mg^{2+}	Mn	Si	Ca^{2+}	Fe	Na^+	S	Sr^{2+}	Br^-	Br^{-*}	Cl^-	SO_4^{2-}
Sample Name	Depth (ft.)	mg/L	mg/L	mg/L	mg/L	mg/L	mg/L	mg/L	mg/L	mg/L	mg/L	mg/L	mg/L	mg/L
Swab 11	5,545 – 5,622	930	1290	0.63	9.6	6950	1.05	29700	268	189	0	149.3	67300	1070
Swab 10	5,670 – 5,680	830	363	2.33	28.9	1650	4.13	15900	731	51.4	0	43.4	27400	2560
Swab 9	6,000 – 6,010	803	1020	0.7	16.8	5420	7.34	23700	277	146	121	115.4	53200	1100
Swab 8	6,194 – 6,204	814	865	0.93	16.9	5410	8.82	28700	196	140	0	97.9	61100	832
Swab 7	6,543 – 6,558	1060	247	5.29	0	2430	1.2	19800	446	73.4	0	51.5	37900	1400
Swab 6	6,676 – 6,686	1250	1300	1.58	6.2	8810	7.85	40000	194	232	0	152.8	89800	734
Swab 5	6,880 – 6,904	1410	1470	1.41	0	9100	4.43	47600	178	229	0	164.4	103000	475
Swab 4	7,046 – 7,056	1100	898	2.13	13.2	6510	0	34700	264	139	161	106.2	72300	705
Swab 3	7,218 – 7,234	987	896	2.01	20.2	6090	2.85	35600	192	155	0	115.1	78600	557
DST 2	7,218 – 7,234	963	858	3.37	11.6	5640	53	34300	201	145	0	112.9	73800	930
Swab 2	7,430 – 7,442	1360	1140	2.85	8.2	8400	0	49700	206	213	159	153.2	103000	603
Swab 1	7,532 – 7,543	1460	1190	4.4	0	9010	0	52600	203	223	0	157.5	107000	714
DST 1	7,522 – 7,735	1280	1070	4.12	0	7820	44.3	46600	189	200	117	161.6	100000	750

Table 1.5 Ionic species concentrations and their corresponding depths from Cutter. All cations were analyzed by ICP-OES.

Cutter		$\delta D\ H_2O$	$\delta^{18}O\ H_2O$	$\delta\ ^{13}C$ DIC	$^{87}Sr/^{86}Sr$
Sample Name	Depth (ft.)	(‰)	(‰)	(‰)	(Molar)
Swab 11	5,545 – 5,622	-42.9	-6.30	-5.9	0.722246
Swab 10	5,670 – 5,680	-60.4	-7.46	-10.8	0.72225
Swab 9	6,000 – 6,010	-47.4	-7.02	-17.3	0.722753
Swab 8	6,194 – 6,204	-50.0	-7.23	-18.2	0.721898
Swab 7	6,543 – 6,558	-59.4	-6.68	-33.4	0.719475
Swab 6	6,676 – 6,686	-41.4	-5.76	-8.4	0.720212
Swab 5	6,880 – 6,904	-36.3	-5.36	-7.5	0.721598
Swab 4	7,046 – 7,056	-47.8	-6.44	-18.7	0.721409
Swab 3	7,218 – 7,234	-48.3	-6.54	-10.7	0.721237
Swab 2	7,430 – 7,442	-38.4	-5.47	-6.2	0.720426
Swab 1	7,532 – 7,543	-36.6	-5.21	-7.2	0.720577

Table 1.6 Isotopic concentrations and their corresponding depths from Cutter.

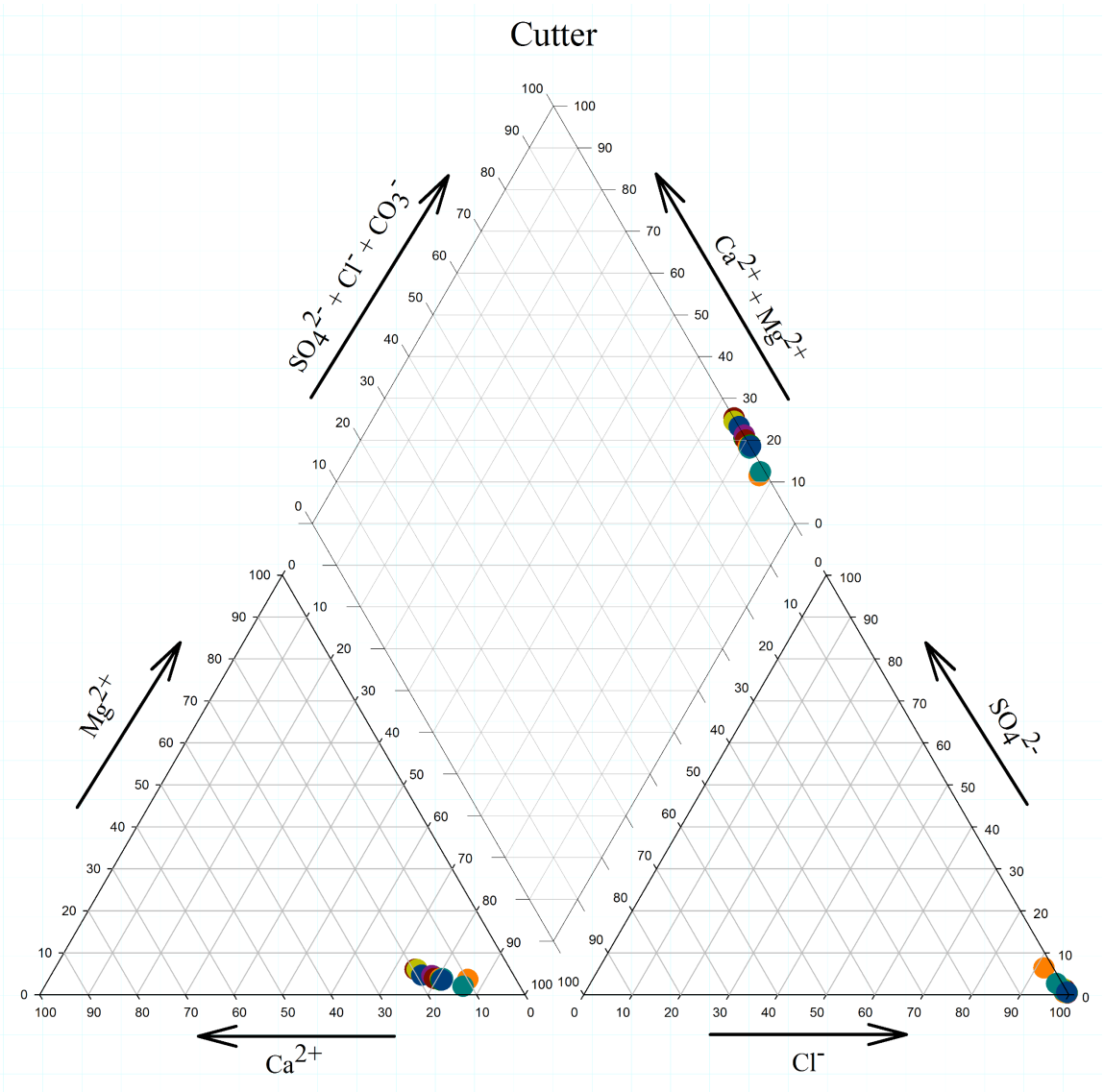


Figure 1.25 Piper diagram from Cutter water indicating a Na-Ca-Cl dominate brine.

Individual ions along with pH and bicarbonate were analyzed and are shown with varying concentrations with depth (Figure 1.26, Figure 1.27, Figure 1.28, and Figure 1.29). A general increase in concentration with depth occurs with the majority of elements (Mn, Sr^{2+}, Na^+, K^+, Cl^-, Ca^{2+}). There generally is a high concentration of each element within the Mississippian, with concentrations showing a general decreasing trend down to the Arbuckle. Tables (Table 1.5, and Table 1.6) and figures (Figure 1.26, Figure

1.27, Figure 1.28, and Figure 1.29) show that ions are in high concentrations within the lower Chester (swab 11), and then generally decrease within the St. Louis and Viola (swabs 10, 7). An increase in concentration is seen in the Simpson and Jefferson City (swabs 6,5), followed by a common decrease within the lower Jefferson City and middle Gasconade (swabs 4,3). Maximum, or near maximum, concentrations of each element are found within the Gunter Sandstone (swab 1). Exceptions to this are ions that either showed no trend (Br^-, Mg^{2+}, Si) or had a decrease in concentration with depth (Fe, Li^+). Swabs 7 and 10 show distinct similarities in these plots, and usually indicate the highest or lowest concentrations.

In relation to the Chester on the shelf margin (swab 11), it is believed that sulfate nodules found within the unit came from brine derived from the shelf. The evaporite precipitation may be to some extent derived from Cutter water chemistry since Cl^-, Ca, and Mg show enrichment while SO_4 shows depletion at that depth.

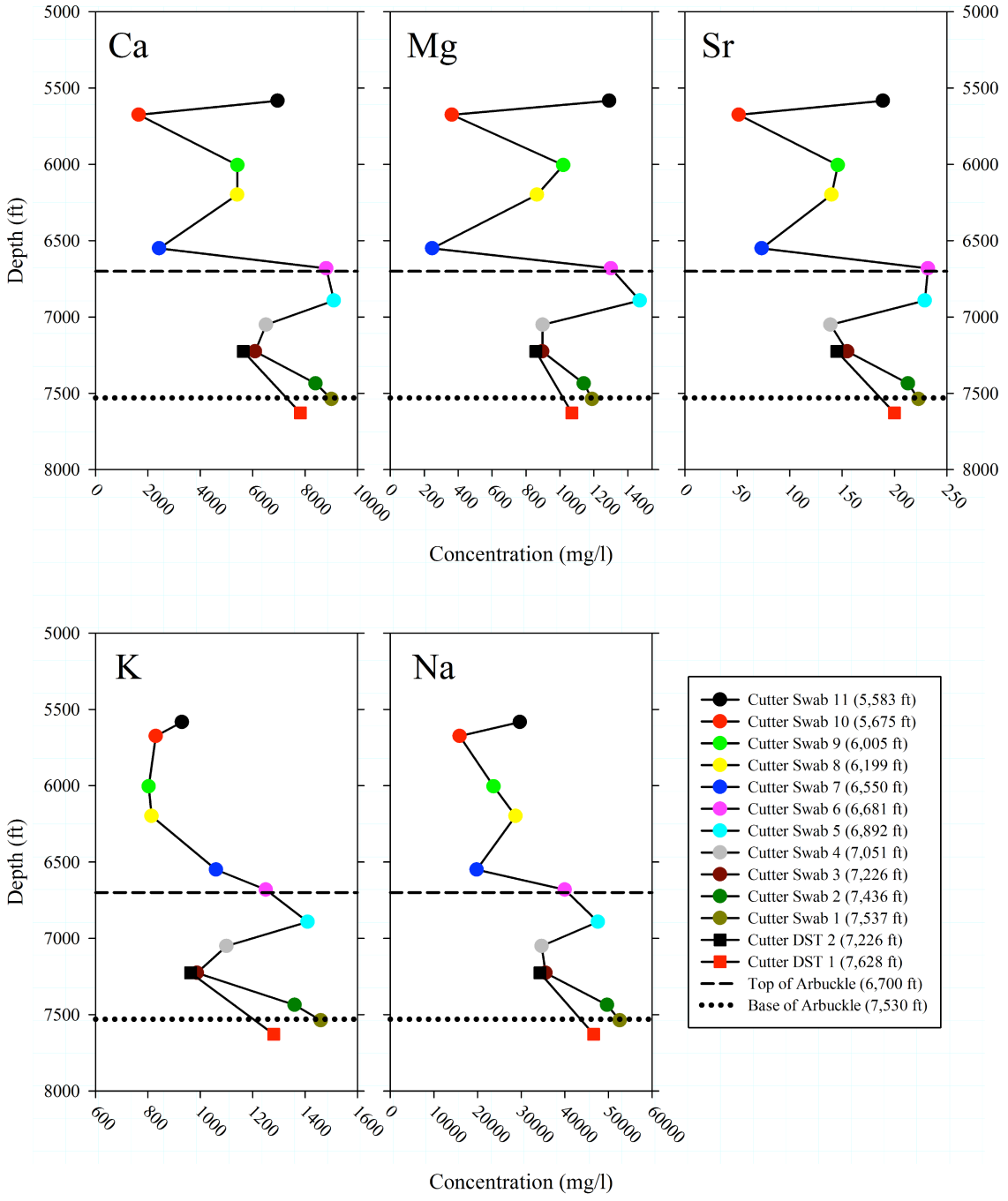


Figure 1.26 Depth profiles of major cations in Cutter. Circles indicate swabs and squares indicate DST samples. A dashed line indicates the top of the Arbuckle, while the base of the Arbuckle is indicated by a dotted line.

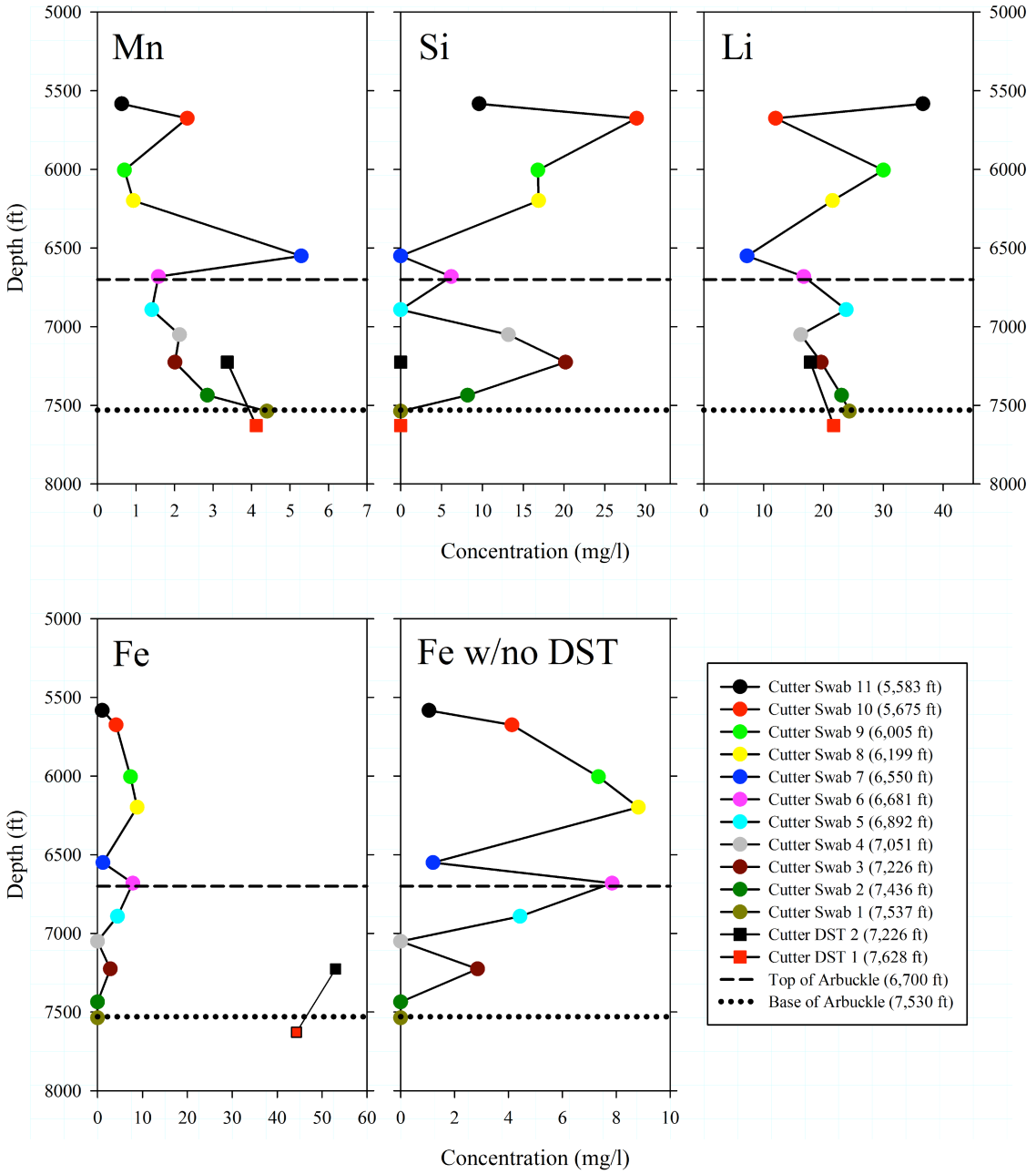


Figure 1.27 Depth profile of redox sensitive species in Cutter. Circles indicate swabs and squares indicate DST samples. Fe is represented twice once with DST samples included, and the other only for swabbed waters to show greater variation with depth. A dashed line indicates the top of the Arbuckle, while the base of the Arbuckle is indicated by a dotted line.

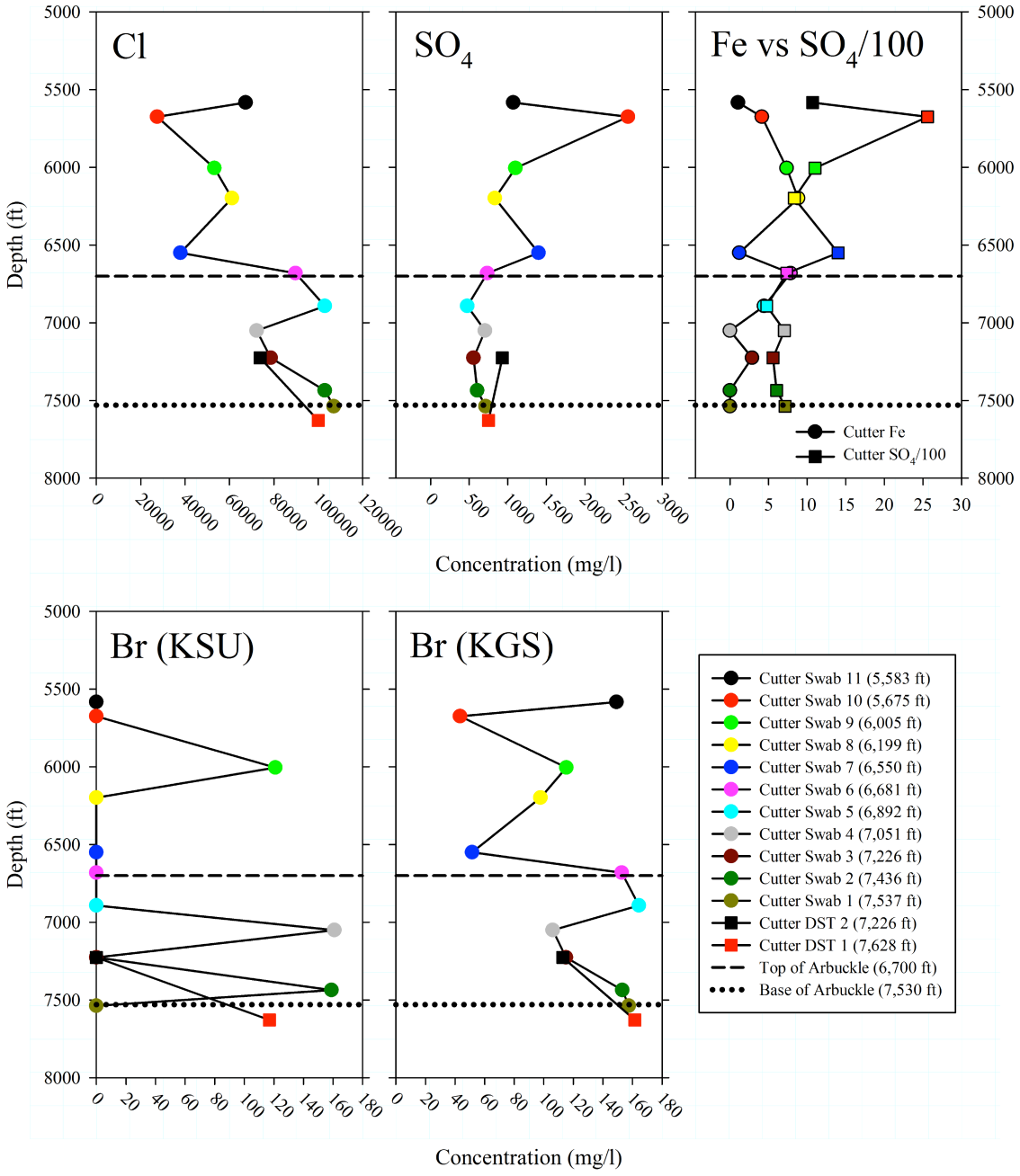


Figure 1.28 Depth profile of anion species in Cutter. Circles indicate swabs and squares indicate DST samples. Fe and SO_4 are shown together to highlight possible microbial interactions. SO_4 concentration was divided by 100 in order to show a comparison to Fe. Br^- (KSU) represents analysis done at Kansas State University with a majority of Br^- samples below detection limits. Br^- (KGS) shows concentrations of Br^- in the same waters. A dashed line indicates the top of the Arbuckle, while the base of the Arbuckle is indicated by a dotted line.

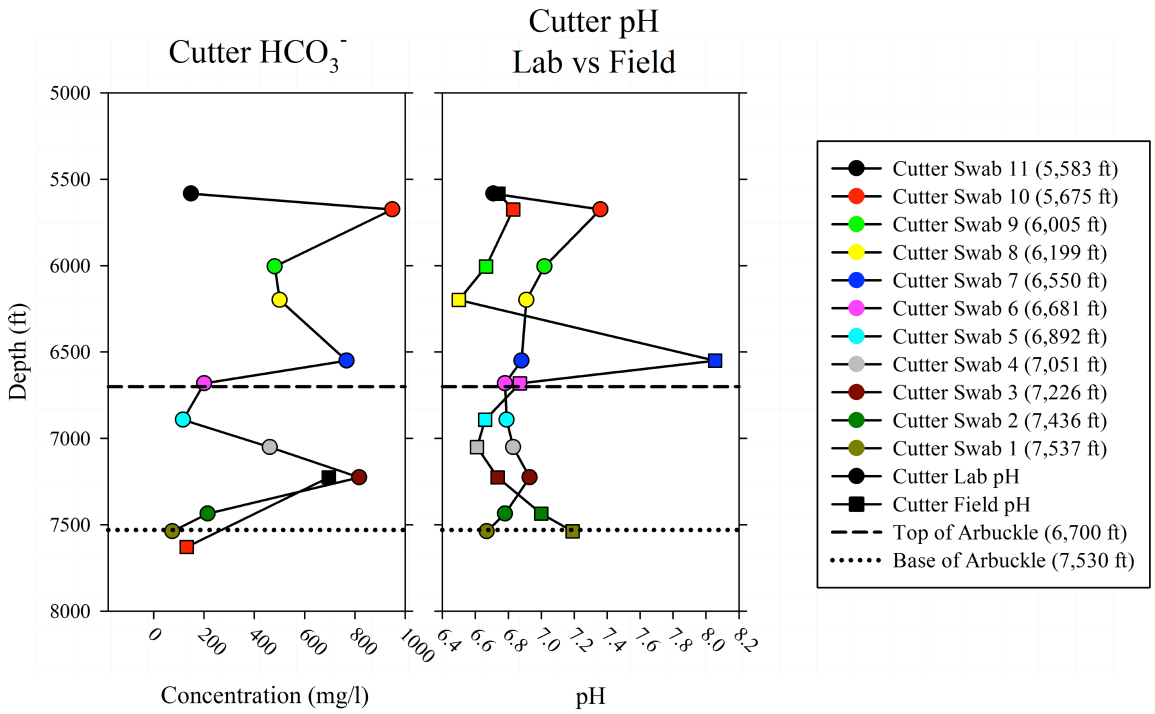


Figure 1.29 Depth profiles of HCO_3 and pH in Cutter. Circles indicate swabs and squares indicate DST samples. Bicarbonate and lab pH was measured at KGS, with field pH measured at K-State. A dashed line indicates the top of the Arbuckle, while the base of the Arbuckle is indicated by a dotted line.

Molar ratios plotted against Cl^- were used to determine diagenetic alteration of the brines (Figure 1.30, and Figure 1.31). Ca^{2+} is highly enriched, while Mg^{2+} is highly depleted in relation to the seawater evaporation curve. Sr^{2+} is heavily enriched in relation to the evaporation curve. Li^+ is greatly enriched, while K^+ is slightly depleted in relation to the evaporation curve. Na^+ follows the evaporation curve and is only slightly depleted in relation to it with SO_4^{2+} being heavily depleted. Br^- is slightly depleted in relation to the seawater evaporation curve. Swabs 7 and 10 again show distinct variations in these plots (Figure 1.30, and Figure 1.31).

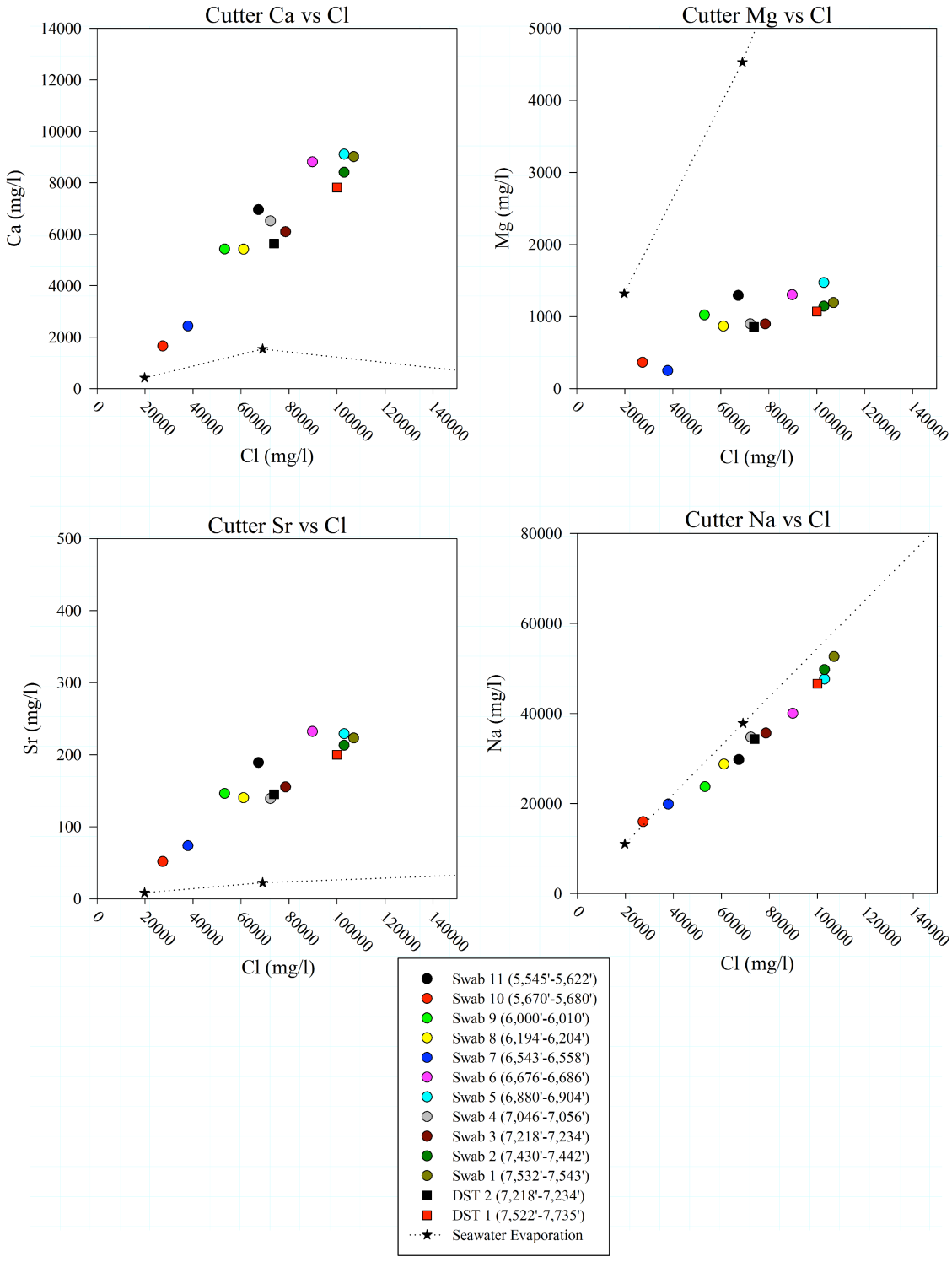


Figure 1.30 Ionic species (Ca, Mg, Sr, Na) vs. chloride in Cutter. Circles indicate swabs and squares indicate DST samples. Dashed line indicates the seawater evaporation curve.

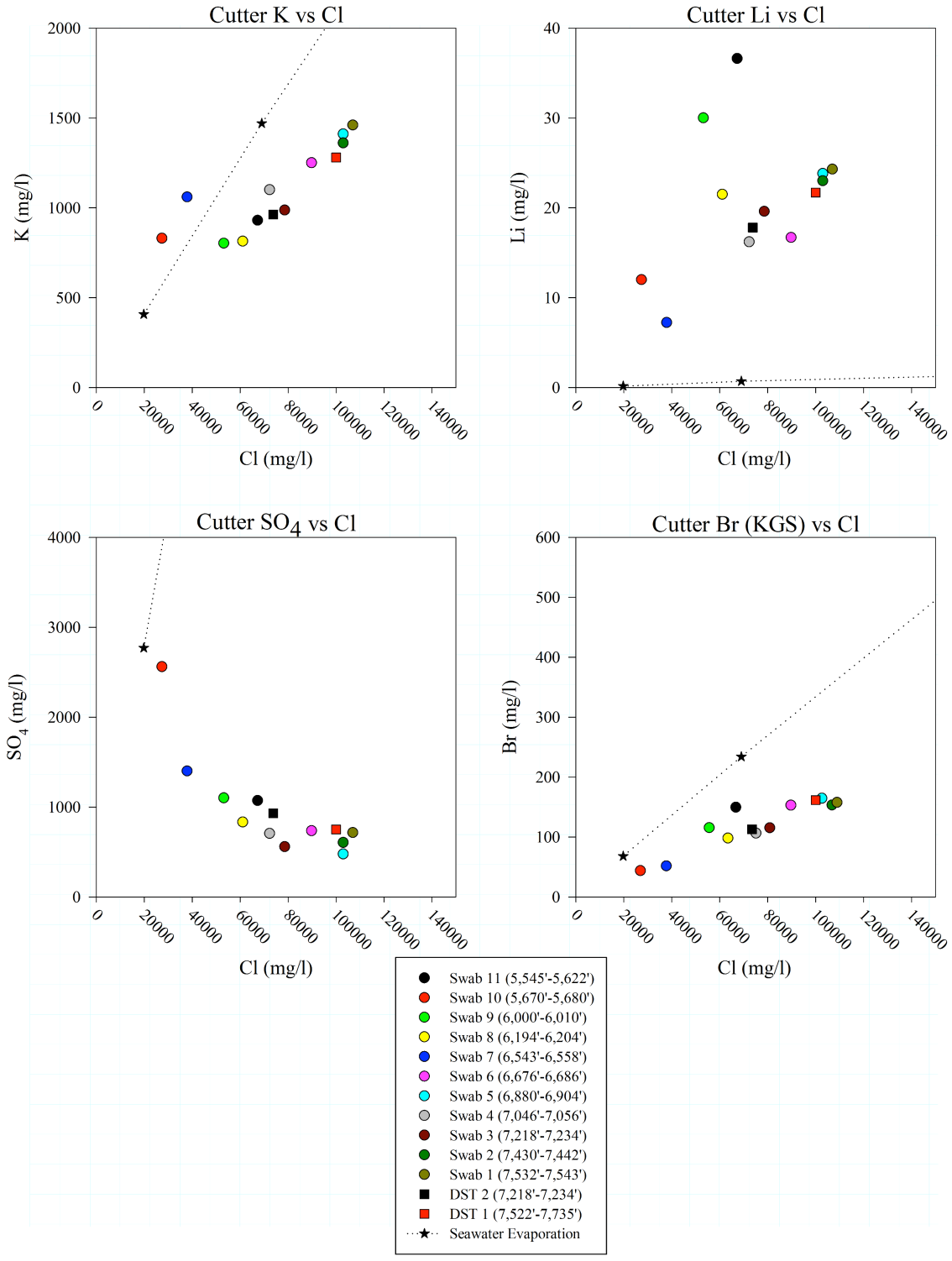


Figure 1.31 Ionic species (K, Li, SO_4, Br^-) vs. chloride in Cutter. Circles indicate swabs and squares indicate DST samples. Dashed line indicates the seawater evaporation curve.

Ca/Mg molar ratios were plotted against Ca/Sr (Figure 1.32). In Cutter a dominant dolomitization trend can be seen, and is due to the excess Ca^{2+}, and Sr^{2+}, and the depleted Mg^{2+}. Ca^{2+} vs. SO_4^{2-} and Ca^{2+} vs. HCO_3^- both show no distinct groupings, but do show swabs 7 and 10 as distinct outliers (Figure 1.33, and Figure 1.34). Both figures can further determine the extent to which carbonate dissolution has affected the brines.

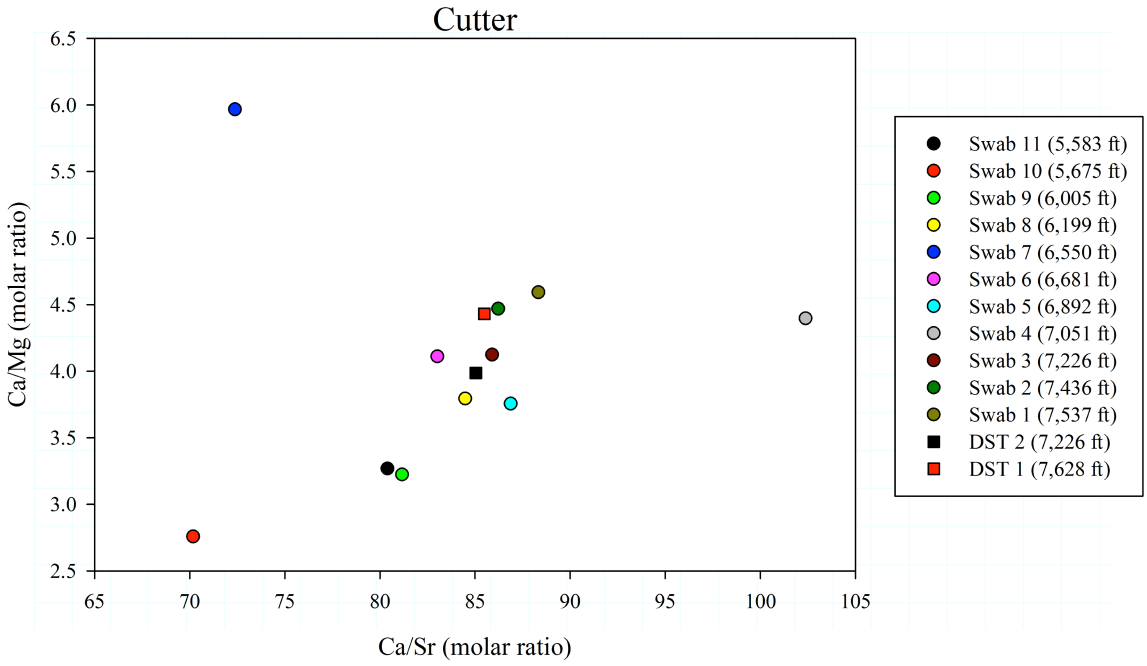


Figure 1.32 Ca/Sr vs. Ca/Mg in Cutter. Circles indicate swabs and squares indicate DST samples. Upper Arbuckle trends towards a calcite recrystallization trend, while the majority of the other samples show no trend or a trend towards dolomitization.

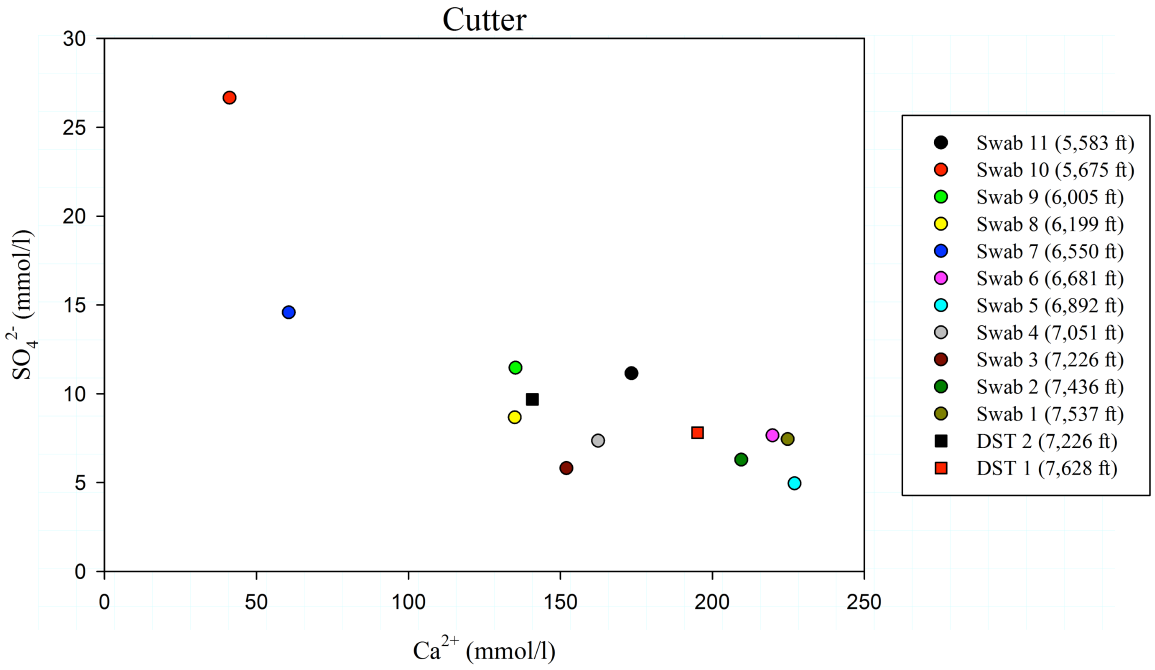


Figure 1.33 Ca vs. SO_4 in Cutter. Circles indicate swabs and squares indicate DST samples.

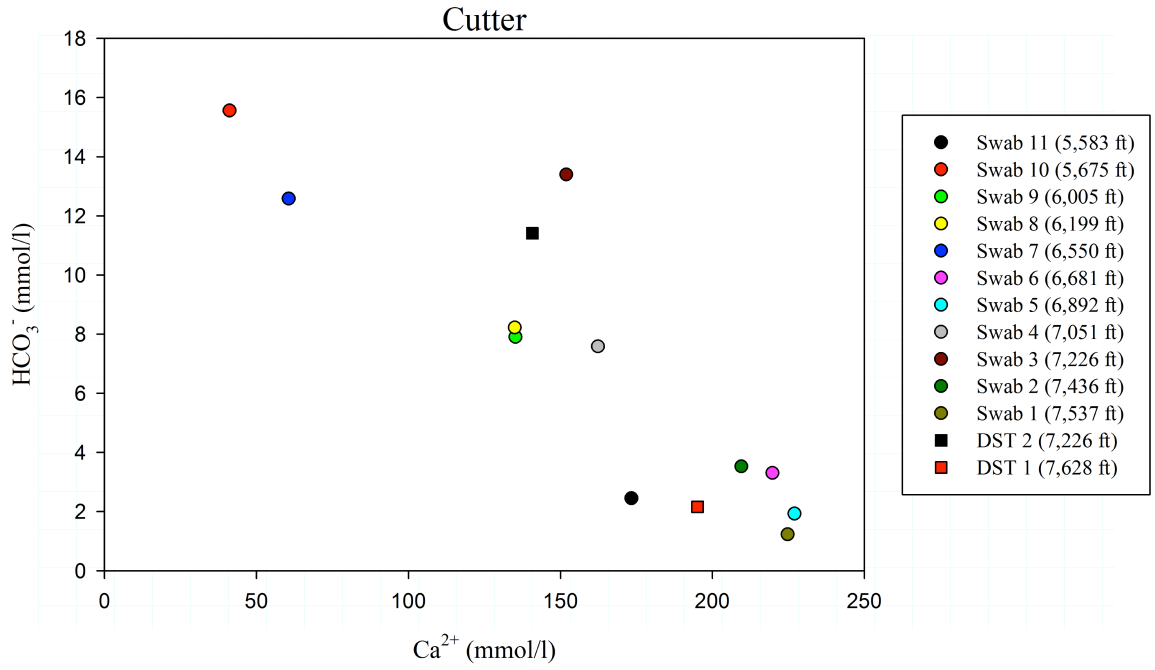


Figure 1.34 Ca vs. HCO_3 in Cutter. Circles indicate swabs and squares indicate DST samples.

Stable isotopes ($\delta^{13}C$ (DIC), $\delta^{18}O$, $\delta^{2}H$, and $^{87}Sr/^{86}Sr$) and Cl/Br vs. Cl^- ratios were used to determine vertical connectivity. Swabs 7 and 10 show distinct depletion in Cl^- and plot in the top left corner of the graph with the rest of the samples all plotting above the seawater evaporation curve (Figure 1.35).

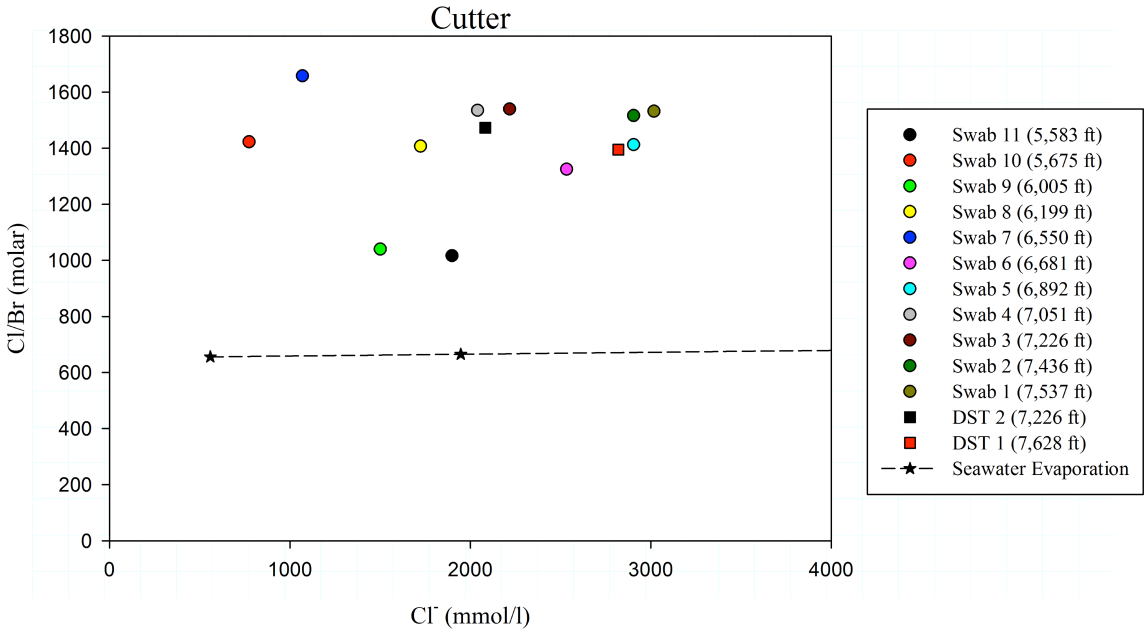


Figure 1.35 Chloride vs. Cl/Br in Cutter. Circles indicate swabs and squares indicate DST samples. Dashed line indicates the seawater evaporation curve.

Cl^- vs. ionic ratios can define reactions that have affected the brine. Cl^- vs. Ca/Cl indicates that the formation waters have been affected by rock weathering and carbonate dissolution due to the high Ca/Cl values (Figure 1.36). Cl^- vs. K/Cl indicates that rock weathering has not affected the brine, and carbonate dissolution is the dominant process (Figure 1.37). Figure 1.38 confirms that rock weathering is not a dominant process affecting the brines due to low Na/Cl ratios. Cl/Br vs. Ca/Mg plots show that halite dissolution has strongly affected the brines (Figure 1.39).

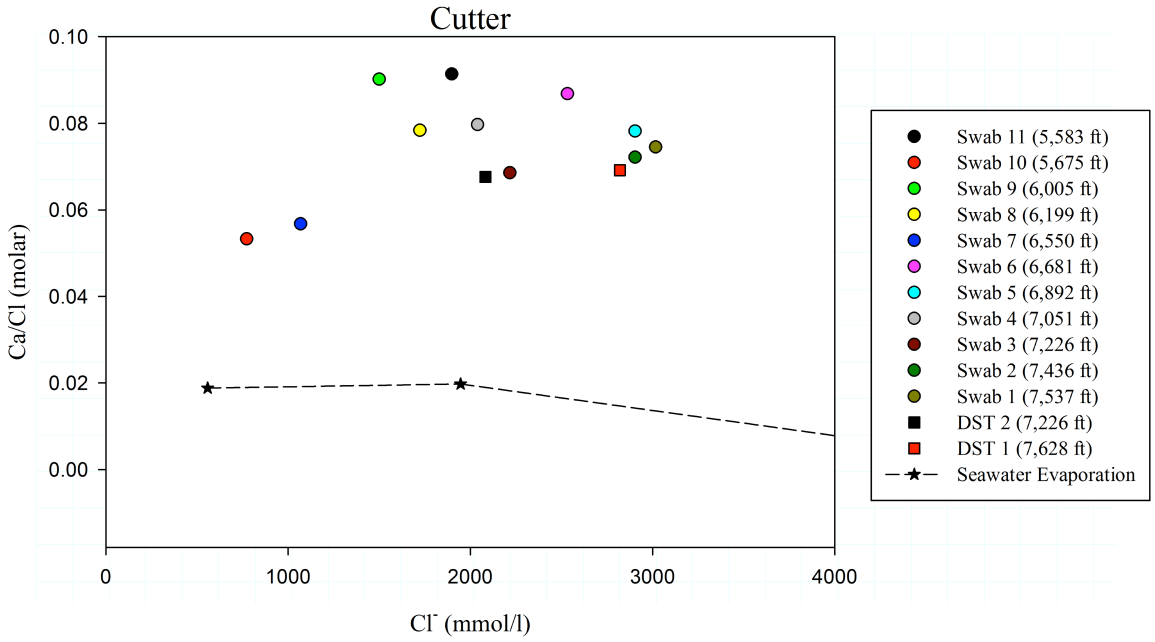


Figure 1.36 Cl- vs. Ca/Cl in Cutter. Circles indicate swabs and squares indicate DST samples. Dashed line indicates the seawater evaporation curve.

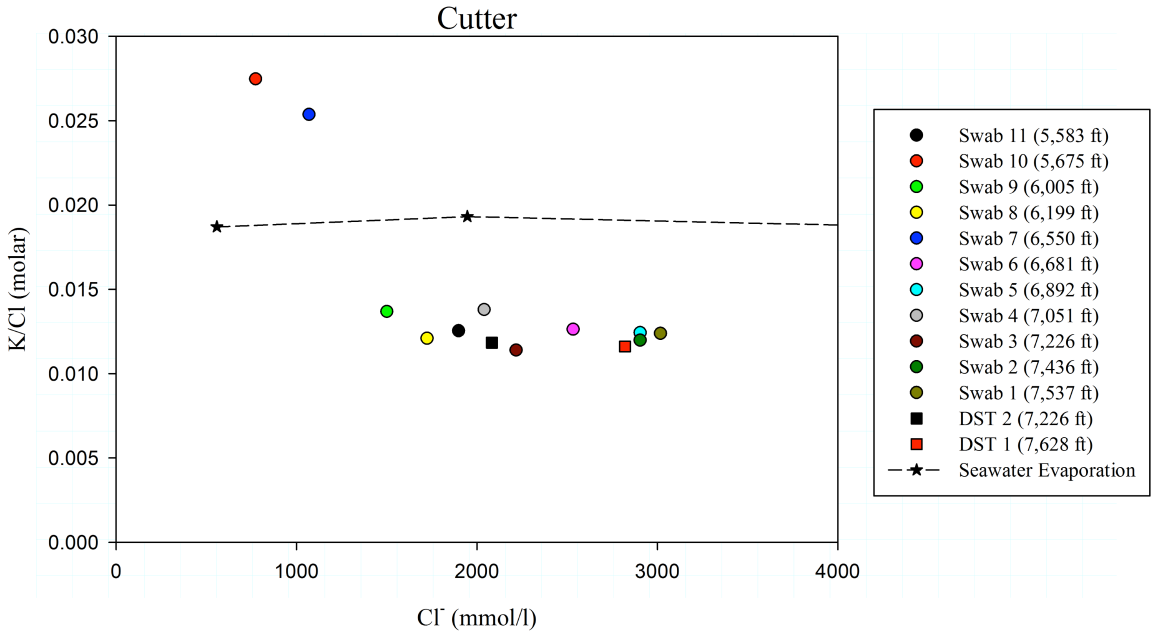


Figure 1.37 Cl- vs. K/Cl in Cutter. Circles indicate swabs and squares indicate DST samples. Dashed line indicates the seawater evaporation curve.

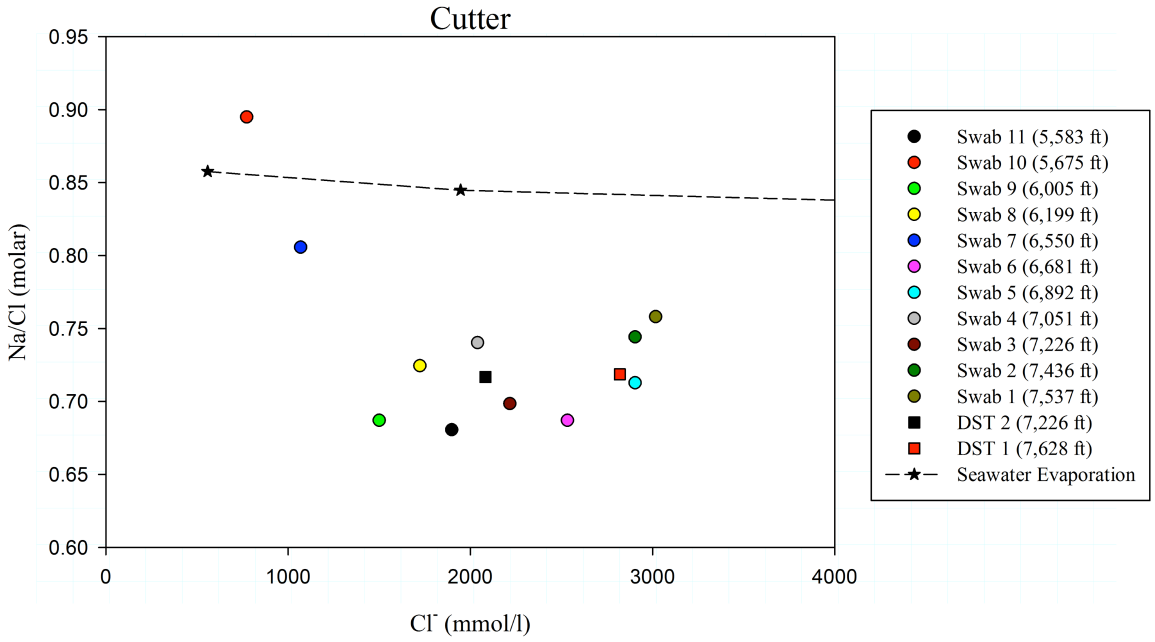


Figure 1.38 Cl⁻ vs. Na/Cl in Cutter. Circles indicate swabs and squares indicate DST samples. Dashed line indicates the seawater evaporation curve.

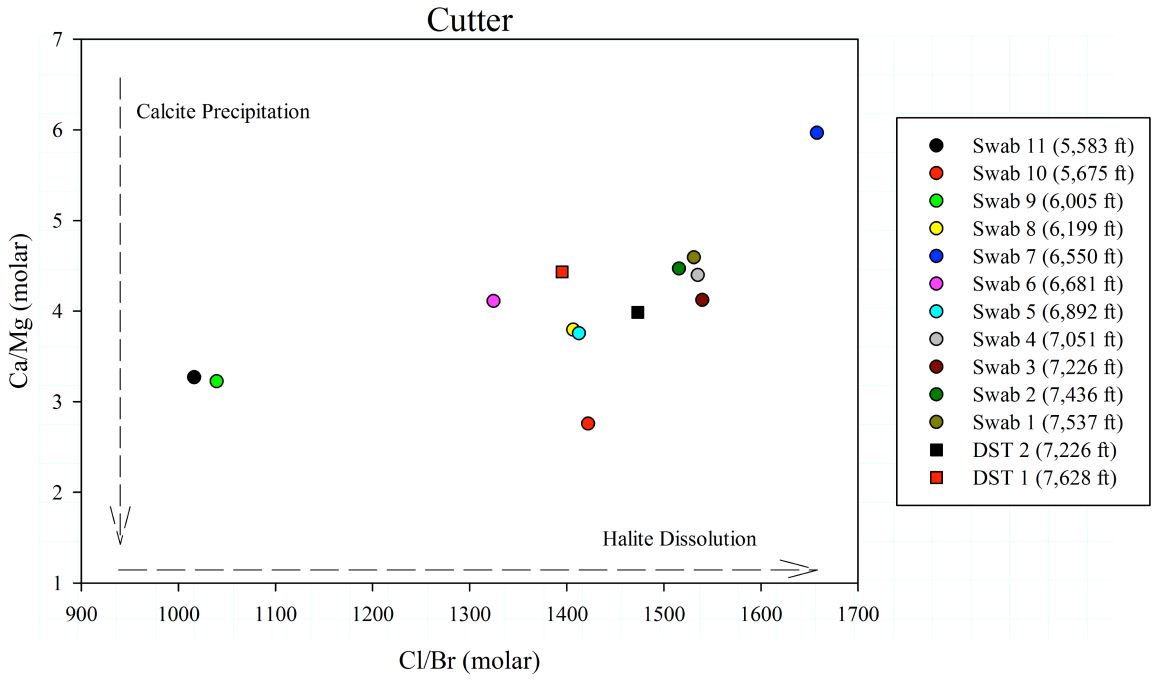


Figure 1.39 Cl/Br vs. Ca/Mg in Cutter. Circles indicate swabs and squares indicate DST samples. Dashed line indicates halite dissolution or calcite precipitation. (McIntosh et al., 2004)

$\delta^{13}C$ (DIC), $\delta^{18}O$, and $\delta^{2}H$ vs. Cl^- in general shows little to no vertical separation within Cutter, with the exception of swabs 7 and 10. Both $\delta^{2}H$ and $\delta^{18}O$ show a constant linear increase above 1,500 mmol/L of Cl^- indicating little vertical separation, swabs 7 and 10 again show distinct variations in relation to the other samples (Figure 1.40). $\delta^{18}O$, and $\delta^{2}H$ plots along a somewhat linear trend.

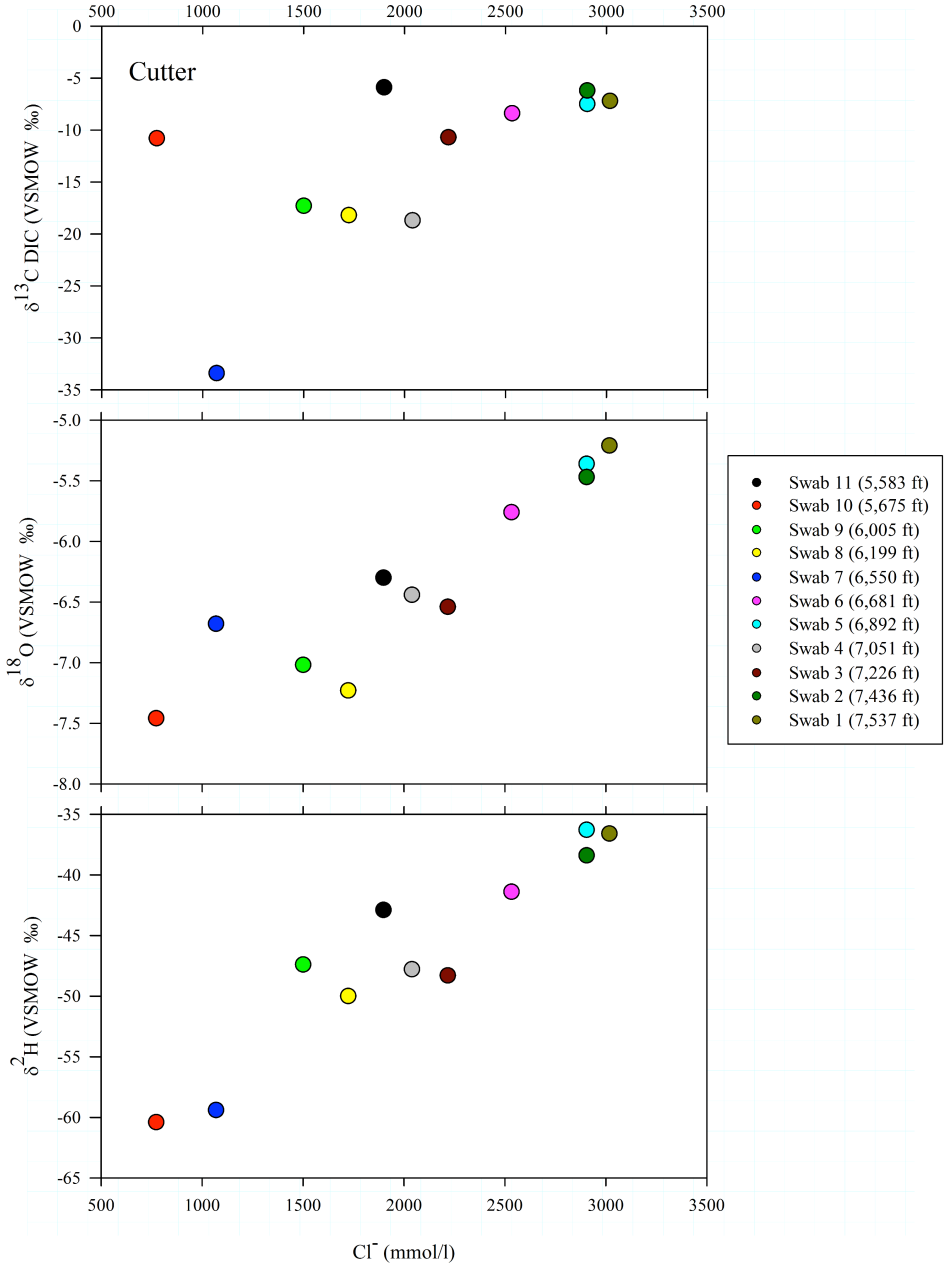


Figure 1.40 Chloride vs. $\delta^{13}C$ (DIC), $\delta^{18}O$, and $\delta^{2}H$ in Cutter. Circles indicate swabs.

$\delta^{18}O$ vs. $\delta^{2}H$ shows a tight cluster of the majority of samples plotting within the range of -7.5‰ to -5‰ (Figure 1.41). Swabs 7 and 10 are greatly depleted in relation to the other samples, especially with respect to $\delta^{2}H$.

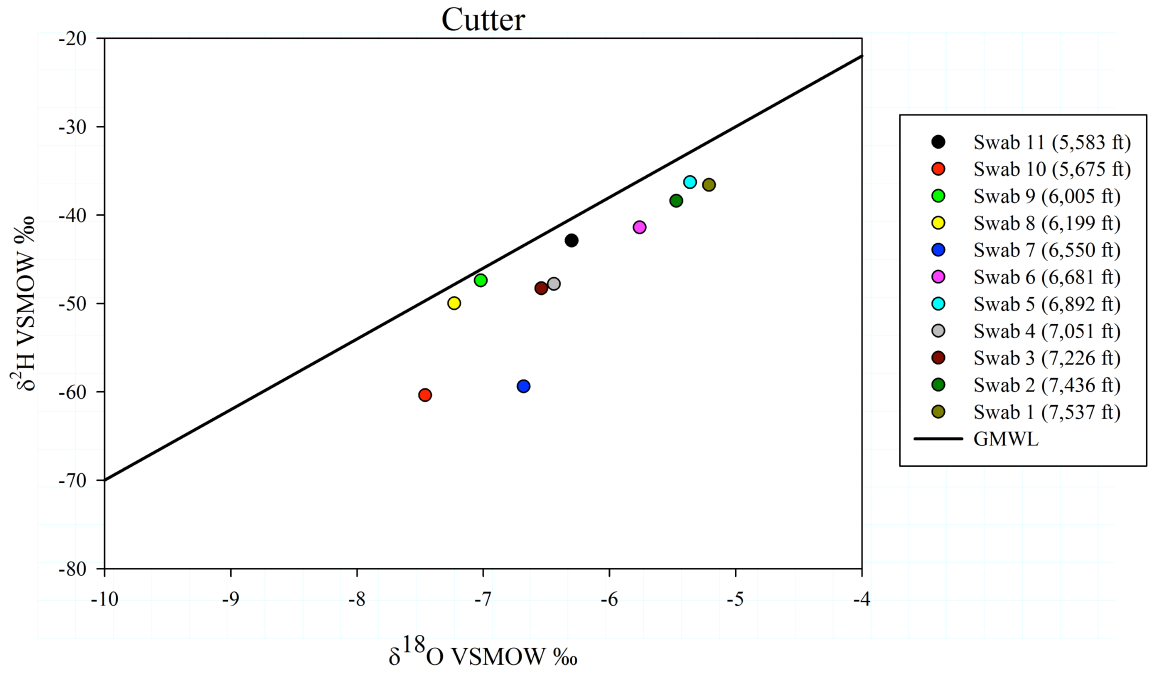


Figure 1.41 $\delta^{18}O$ vs. $\delta^{2}H$ in Cutter. Circles indicate swabs. All samples plot below the Global Meteoric Water Line (GMWL-solid black line) and are depleted in relation to it.

Depth wise concentrations of these isotopes further highlight the differences of other swabbed waters from swabs 7 and 10 (Figure 1.42). $\delta^{2}H$ vs. depth indicates both swabs 7 and 10 having the greatest depletion. With $\delta^{18}O$ vs. depth, only swab 10 shows significant deviation with respect to the rest of the samples, and is the most depleted. For $\delta^{13}C$ (DIC), swab 7 shows the greatest depletion at -35‰.

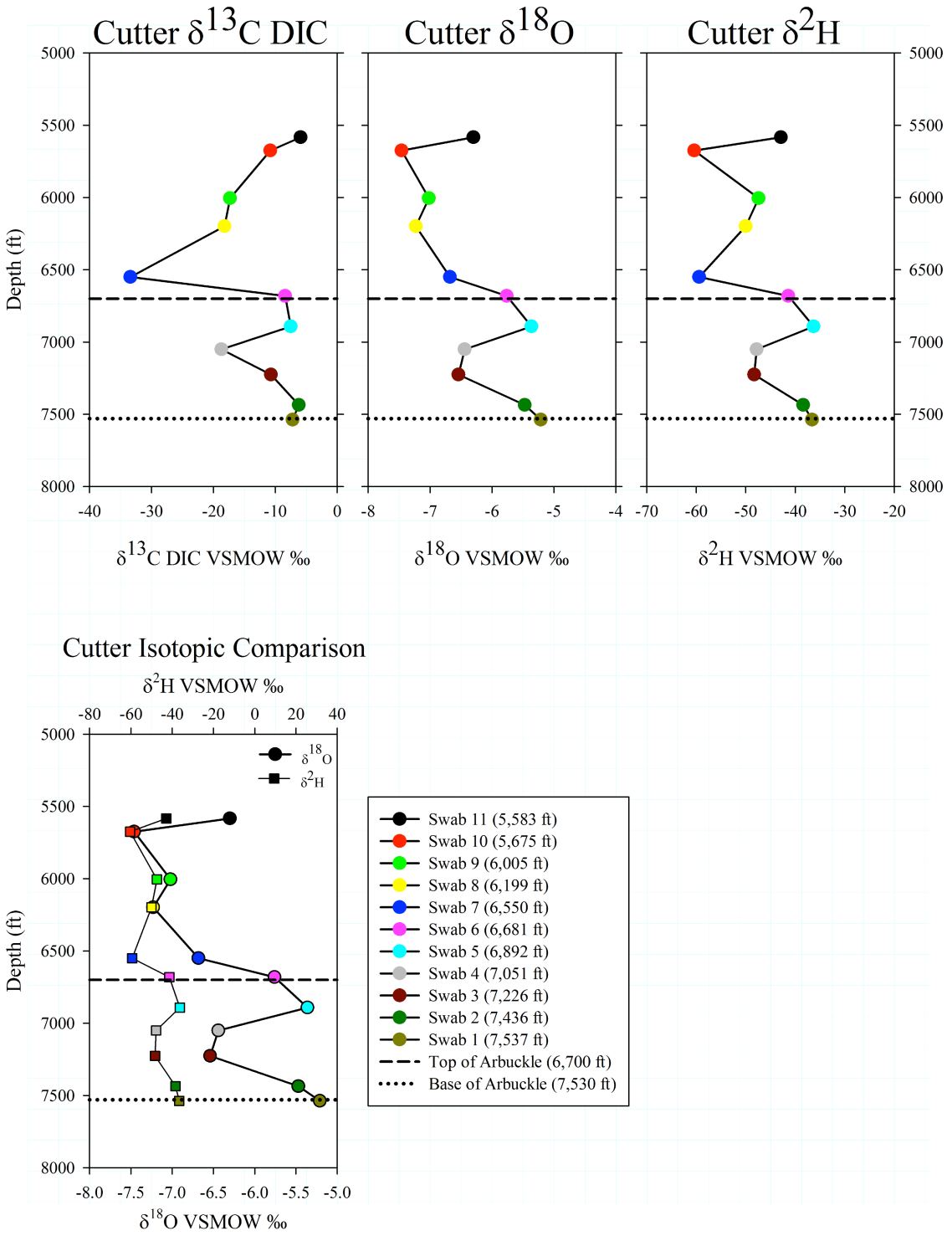


Figure 1.42 Depth profiles of $\delta^{13}C$ (DIC), $\delta^{18}O$, and $\delta^{2}H$ in Cutter. A dashed line indicates the top of the Arbuckle, while the base of the Arbuckle is indicated by a dotted line. Circles indicate swabs.

$\delta^{13}C$ (DIC) vs. HCO_3 shows possible microbial influences on the formation brines. Groupings show clusters with distinct variability (Figure 1.43). Figure 1.44 shows no correlations or groupings of swabbed waters based off of depth. Samples all plot above 0.702, with the exception of swab 7, indicating a possible silicate weathering influence on the brine. $\delta^{13}C$ (DIC) vs. $^{87}Sr/^{86}Sr$ can also show silicate weathering influences on brine (Figure 1.45). This figure again shows no groupings, however does show that silica weathering has affected the brines. Swab 7 is the most by far the most depleted in both $^{87}Sr/^{86}Sr$ and $\delta^{13}C$ (DIC).

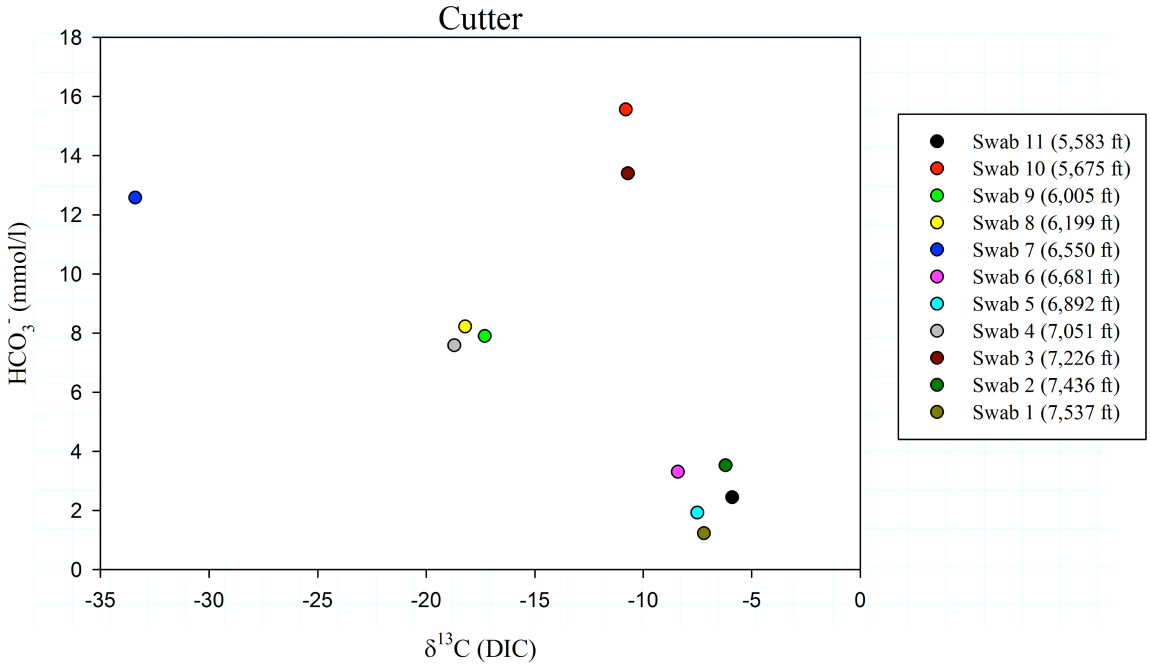


Figure 1.43 $\delta^{13}C$ (DIC) vs. HCO_3 in Cutter. Circles indicate swabs.

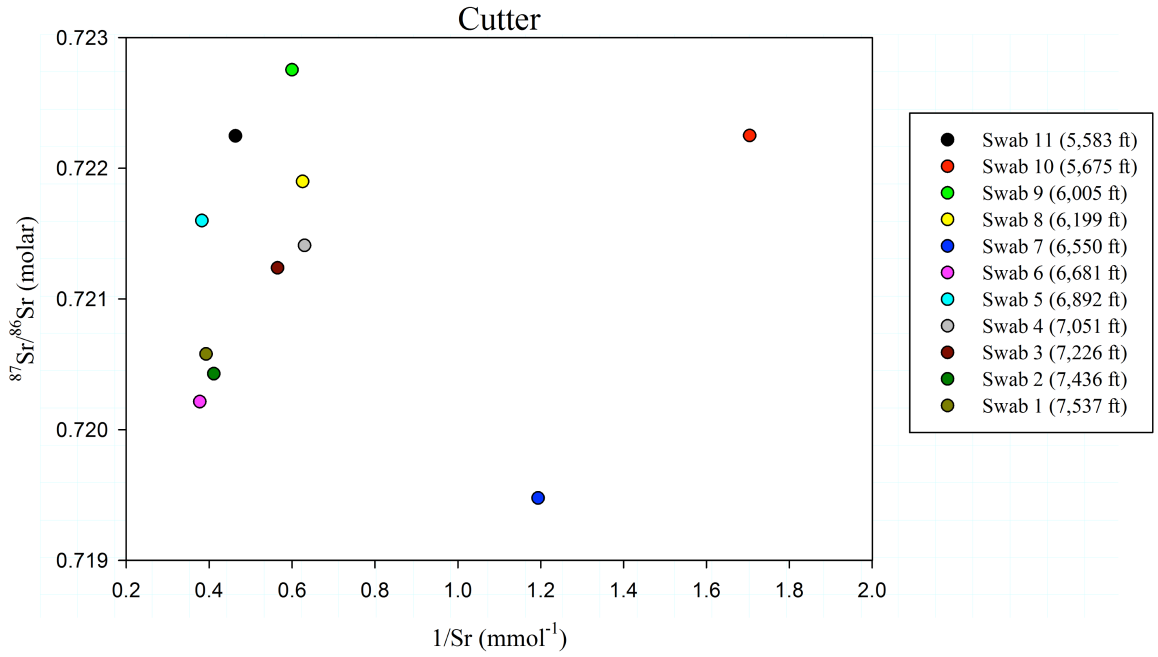


Figure 1.44 1/Sr vs. $^{87}Sr/^{86}Sr$ in Cutter. Circles indicate swabs.

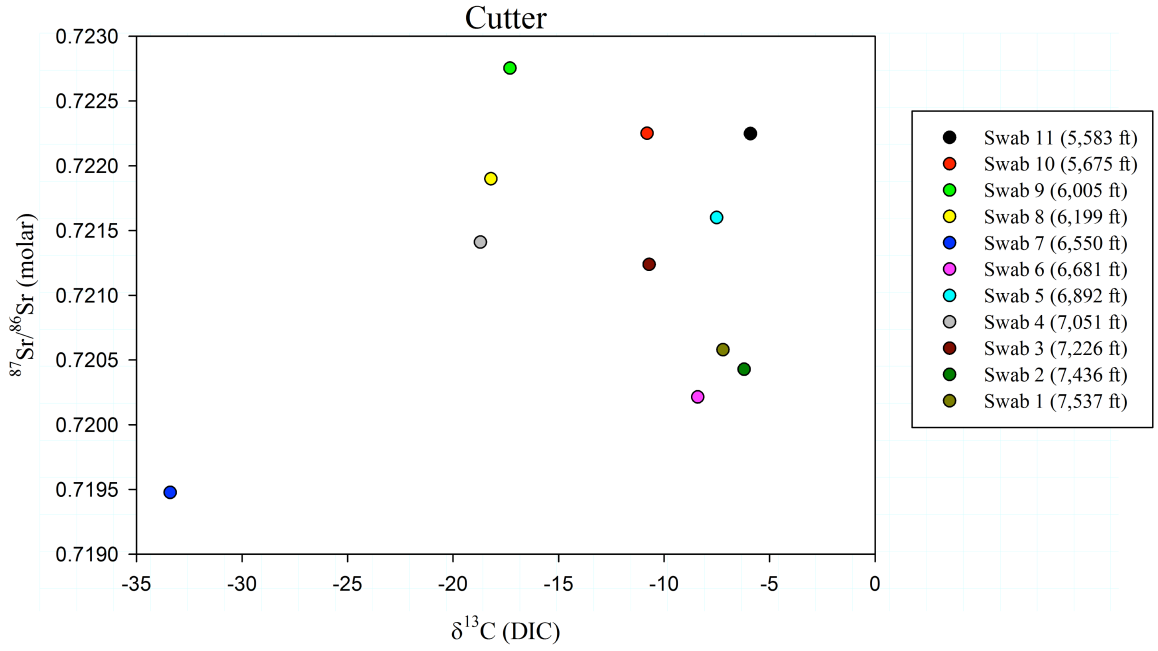


Figure 1.45 $\delta^{13}C$ (DIC) vs. $^{87}Sr/^{86}Sr$ in Cutter. Circles indicate swabs.

1.4.3 Wellington Flow-through results

Initial saturation phase waters showed the following changes in elemental chemistry during the first 13 hours: Ca^{2+}(-7%), Fe (+23,200%), Mg^{2+} (-11%), Mn (+835%), Na^{+} (-6%), P (+350%), S (+1%), Cl^{-} (-6%), and SO_4^{2-} (-13%).

After the saturation phase, CO_2 was introduced and caused Ca^{2+}, Mg^{2+}, Mn, Na^{+}, Cl^{-}, and SO_4^{2-} to increase, and Fe, P, and S to decrease in solution within the first 5 hours of injection. SO_4^{2-} and Mn varied in concentration while the other trends were stable up to hour 10 of CO_2 injection. During the last 8 hours of the experiment Ca^{2+}, Mg^{2+}, Na^{+}, and Cl^{-} decrease in concentration while Fe, P, S, and SO_4^{2-} increased.

pH and alkalinity were measured with every sample collection. These two measurements show an inverse relationship over the course of the first 7 hours of the experiment (Figure 1.46). An initial pH decrease, due to CO_2 injection, along with an alkalinity increase shows carbonate dissolution taking place. Carbonate dissolution reactions cause the cyclic movements of increasing then decreasing pH and alkalinity values. Equilibrium appears to have been established past hour 21 of the experiment. However this is hard to establish due to CO_2 degassing. Degassing of CO_2 could be the reason for the large increase in pH. With CO_2 leaving thereby causing pH to increase, it should allow for carbonate precipitation to occur.

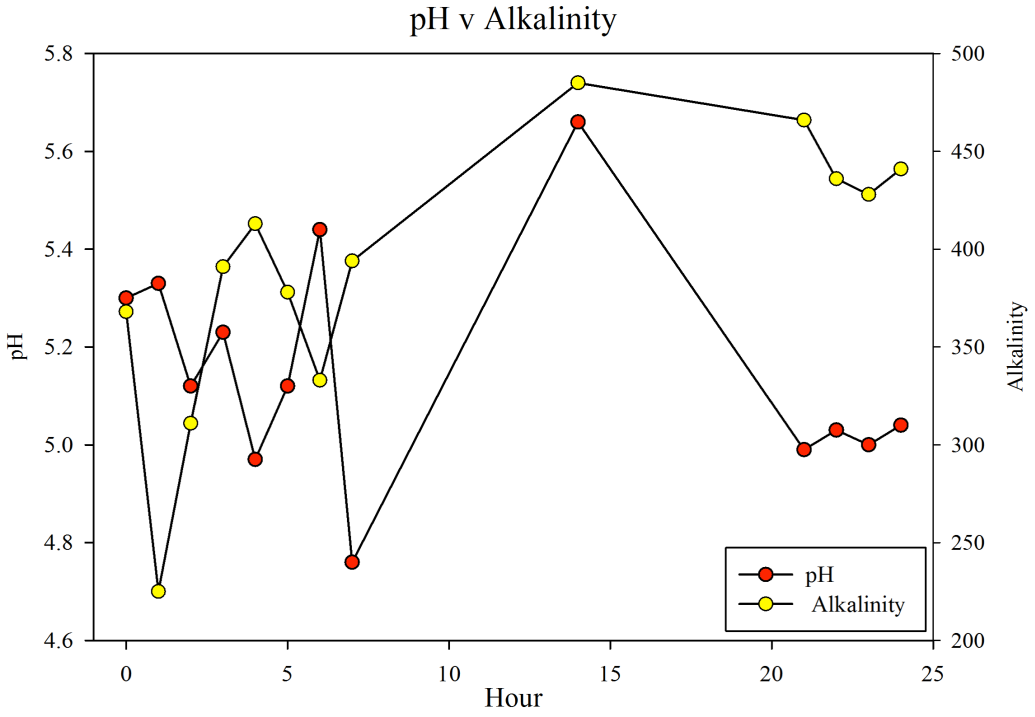


Figure 1.46 Wellington flow-through pH and alkalinity change through time. (Reproduced from Barker, 2012)

Individual major elements and alkalinity are plotted against time (Figure 1.47, and Figure 1.48). With the introduction of CO_2 into a carbonate rock, Ca, Mg and CO_3 should increase in aqueous concentrations due to dissolution, and this is shown. Alkalinity values in general follow each elements concentrations throughout the experiment. Initial increases in concentration are seen with Ca^{2+}, Na^{+}, Mg^{2+}, and Cl^{-}. Decreases are seen with Fe, Mn, S, and P with SO_4^{2-} fluctuating throughout the experiment. Alkalinity follows the same general trend as Ca^{2+}, Mg^{2+}, Cl^{-}, Na^{+}, Mn, and SO_4^{2-}, while showing an inverse trend with S, and no trend with Fe.

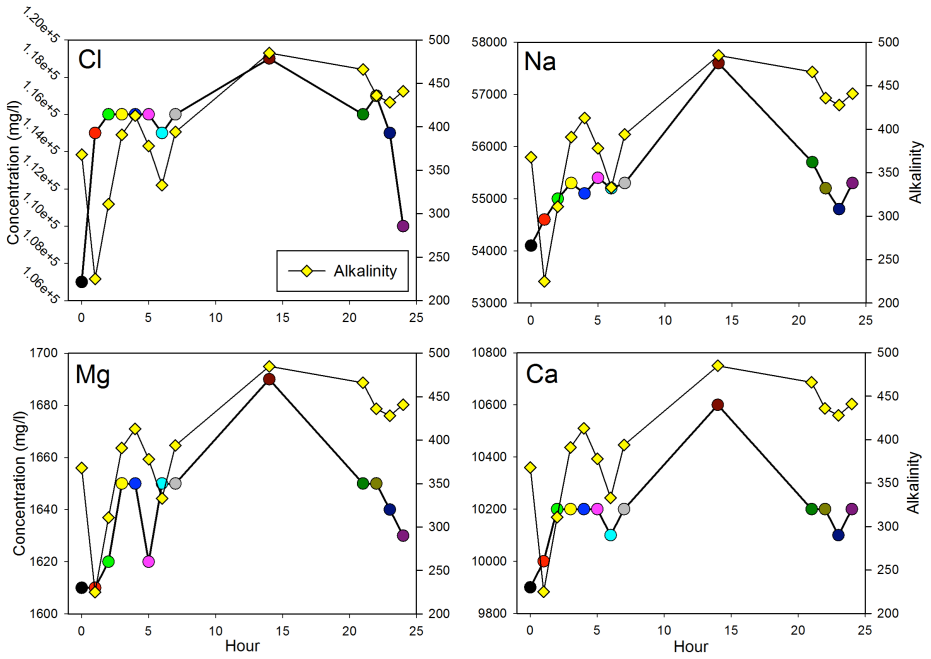


Figure 1.47 Wellington flow-through ionic species and alkalinity change through time. (Reproduced from Barker, 2012)

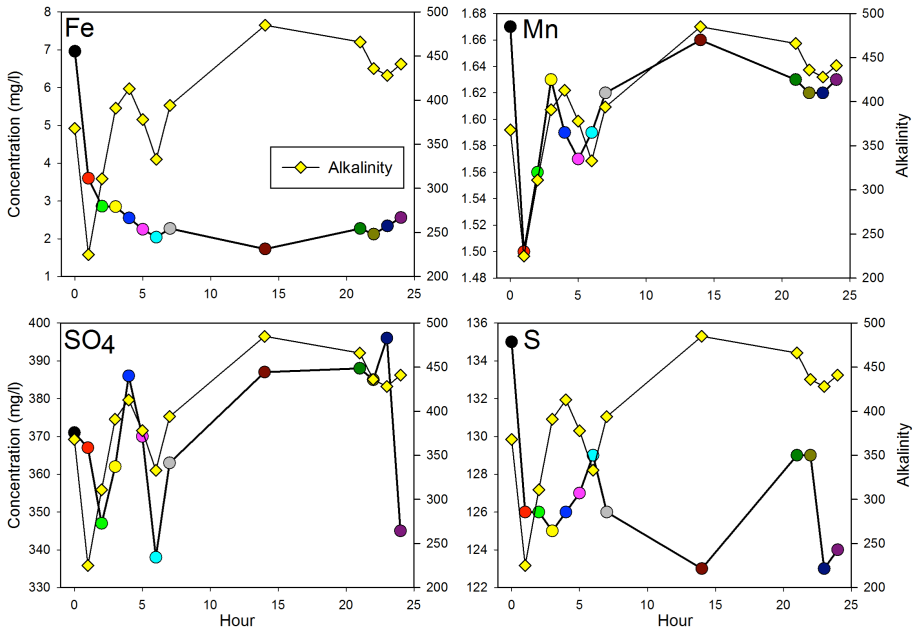


Figure 1.48 Wellington flow-through ionic species and alkalinity change through time. (Reproduced from Barker, 2012)

1.5 Discussion

1.5.1 Ionic Species, Wellington

Wellington was drilled and sampled from 3,677 ft. to 5,010 ft. Most elemental (Cl^-, Na, Ca, Mg, Br^-, Sr, K, Li) concentrations increase with depth from the top to the base of the Arbuckle. Increasing TDS with depth and within the Arbuckle will allow for greater chemical reactivity to help aid in the dissolution and precipitation of CO_2, and will affect the solubility of CO_2 into the formation brine. Redox sensitive species (Mn, Fe, SO_4,) show greater variability with depth. The variability of iron and sulfur is likely due to microbial stratification of iron and sulfur reducing bacteria.

One particular pair of elements is of interest are Fe and S. These two elements can cohabitate with one another and be consumed and altered by microbes. Usually one type of microbe dominates the other, with roles changing depending on the environment. Iron is an important species due to its reactivity and ability to precipitate as siderite. Precipitation of siderite requires the reduced form of Fe to be present. However reduced Fe species thermodynamically favors the formation of pyrite. Within Wellington Fe increases and S decreases with depth. Due to the high affinity of Fe to sulfur this inverse relationship of concentration with depth could allow for the formation of siderite if excess sulfide is co-injected along with CO_2. Excess sulfide could be injected in the forms of either H_2S or SO_2. By injecting excess sulfide it would allow for the reduction of iron (III) oxyhydroxides to the reduced form needed to precipitate siderite. Trapping of CO_2 by mineralization is the end goal for CO_2 storage; however if precipitation occurs too quickly it could cause decreased porosity and permeability thereby limiting the amount of CO_2 that could be injected (Ott et al., 2015;).

1.5.2 Ionic Species, Cutter

Cutter was cored intermittently from 5,095 ft. to 7,589.5 ft. and then drilled to TD at 7,735 ft. Unlike at Wellington; Cutter was drilled and sampled from the basal Pennsylvanian, Mississippian, Devonian, and Upper Ordovician that lie above the Arbuckle. The Arbuckle was not continuously cored as at Wellington. At Cutter the hydrochemistry indicates that the majority of the ions increase in concentration with depth except for SO_4, S, Si, and Li, all of which show decreasing trends. Two anomalous swabs, 7 (Upper Viola Ls) and 10 (St. Louis Limestone), show strong deviation from the trend of any particular species; meaning they exhibit, usually, the highest concentrations on a generally decreasing concentration trend with depth, or the lowest concentrations on a generally increasing concentration trend with depth (Figure 1.26, Figure 1.27, and Figure 1.28). Swabs 7 and 10 exhibit this same distinction when $\delta^{13}C$ (DIC), $\delta^{18}O$, $\delta^{2}H$, and $^{87}Sr/^{86}Sr$ are plotted against with depth, along with HCO_3^- and laboratory and field pH values (Figure 1.42), and Figure 1.29). Swab 10, sampled from the St. Louis (5,670 – 5,680 ft.) was recovered with a significant amount of oil. The oil recovered could have had an effect on the analysis. Swab 7, sampled within the Viola (6,543 – 6,558 ft.), required overnight recovery for enough water for sampling. This zone was tight with only 3.3 barrels of water (BW) recovered after overnight filling. Drilling mud and other contaminants could have been recovered with the water and could account for the distinct concentration at these depths.

Fe and S again are of interest at Cutter for the same reasons as stated above for Wellington. Wellington has lower average S and Fe concentrations than Cutter, and there was no H_2S gas measured at Cutter. With higher amounts of S and Fe at Cutter, injection

of H_2S gas could allow for a significant amount of Fe reduction to occur. Without the presence of H_2S the sub-surficial environment would not be equilibrated with the gas, and could allow for the precipitation of siderite.

1.5.3 Brine Alteration, Wellington

Brine alterations due to diagenetic changes are investigated using Cl^- ratios (Figure 1.12, Figure 1.13). Deviation from the seawater evaporation curve indicates diagenetic alteration has occurred. Na^+ closely follows the evaporation curve indicating little or no alteration. K^+ is depleted in relation to the seawater evaporation curve. K^+ depletion could be explained by the formation of illite and K-feldspar (Wilson and Long, 1993). Argillaceous zones, observed within the Wellington core, could account for the K^+ depletion. Ca^{2+} and Sr^{2+} follow the same trend and are strongly enriched while Mg^{2+} is slightly depleted. This relationship is largely due to the dolomitization of calcite. Extensive dolomite is found within KGS 1-32, and the process of dolomitization has had significant influence on brine at depths 4,520 ft. and below, with the exception of DST 1 (3,677 ft.) which also shows a trend of dolomitization. Within the upper Arbuckle and Mississippian formations, calcite recrystallization has occurred. Calcite recrystallization can partially explain the lack of Ca^{2+} within these formations, and can be seen with the presence of limestone within the lithological profile.

Dolomitization and calcite recrystallization can be further confirmed using Ca/Mg vs. Ca/Sr molar ratio plots. Figure 1.14, further confirms the influence of dolomitization and calcite recrystallization of the brine while also indicating separation of the upper and lower intervals at Wellington. SO_4^{2-} is heavily depleted and shows no trend with depth. The depletion could be due to either microbial communities, or diagenetic alterations.

With the presence of high amounts of H_2S gas, microbial influences on the brine could account for the SO_4^{2-} depletion due to microbial reduction of sulfate to sulfide. Scheffer, (2012) did find that sulfate was being reduced to sulfide within the Arbuckle. Within the upper Arbuckle SO_4^{2-} concentrations were between 8.4 – 15.3 mmol/L and steadily decreased down with depth to 2.8 mmol/L indicating sulfate reduction.

1.5.4 Brine Alteration, Cutter

Figures (Figure 1.30 and Figure 1.31) plot individual ionic species against Cl^-. Ca^{2+} shows a linear trend of enrichment in relation to the seawater evaporation curve, which could be due to dolomitization of carbonate minerals. Sr^{2+} is nearly identical in this enrichment trend of Ca^{2+}, while Mg^{2+} is strongly depleted. Sr^{2+} enrichment could be due to possible mineral recrystallization. This enrichment of Ca^{2+} and Sr^{2+} along with a depletion of Mg^{2+} again indicates dolomitization has significantly affected the brines. Loss of Mg^{2+} following seawater evaporation could be from the conversion of calcite to dolomite. There are no depth wise trends for depletion or enrichment as seen at Wellington. The two anomalous swabs, 7 and 10, again plot very differently from the rest of the samples. These two swabs tend to plot much closer to the seawater evaporation line, and are actually both enriched in K^+ while the rest of the samples are depleted. Argillaceous zones could again account for the depletion of K^+ (Wilson and Long, 1993). The enriched swabs 7 and 10 could suggest lack of argillaceous sinks for K^+ or is being incorporated from other possible sources in these two zones.

Ca/Sr vs. Ca/Mg ratios indicate that the main alteration of the brines is from dolomitization (Figure 1.32). There is a greater abundance of Ca^{2+} in relation to Sr^{2+} at Cutter, than there is at Wellington, and makes Cutters water plot more explicitly in the

dolomitization area of alteration. Again at Cutter there are no groupings of swabs by depth, as in comparison to Wellington where the top and lower Arbuckle showed different brine alterations. Swab 7 shows a significant abundance of Ca^{2+} to Mg^{2+} and plots at the top of the graph, while swab 10 shows significant depletion. These two swabs plot at the extremes of the ratio plots along the y-axis, meaning they have inverse concentrations of Ca^{2+} to Mg^{2+} in relation to one another. These plots correlate to the dominant limestone found at swab 10, and the dolomite found at swab 7.

Dolomitization of carbonate minerals may be a plausible reason for detecting excess of Ca^{2}, in relation to Cl^{-} ratio plots (Figure 1.30, Figure 1.31). (Carpenter, 1978). Loss of Mg^{2+} following seawater evaporation may be due to conversion of calcite to dolomite, equation 7.

7) $2CaCO_3 + Mg^{2+} \rightarrow CaMg(CO_3)_2 + Ca^{2+}$.

Sr^{2+} enrichment, in relation to Cl^{-} ratio plots, may be due to possible carbonate mineral recrystallization of aragonite to calcite and then to dolomite (Stueber and Walter, 1991). The depletion of sulfate in relation to the seawater evaporation curve could be caused by either biological sulfate reduction, or the precipitation of $CaSO_4$ (Wilson and Long, 1993.) While there was little to no H_2S gas detected, and was not measured, biological sulfate reduction could be a minimal cause of the sulfate depletion at least within the carbonate units. The process of dolomitization can allow for the precipitation of $CaSO_4$ as anhydrite, which would sequentially cause a depletion of sulfate within the carbonate aquifer units.

1.5.5 Vertical Connectivity, Wellington

δ^2H and $\delta^{18}O$ were used to help determine vertical connectivity (Figure 1.16). These two isotopes were plotted and compared to the GMWL in order to determine hydraulic communication and connectivity of the varying formations. This comparison highlighted similarities within the lower Arbuckle, and small groupings in the upper depths. The sample from within the Mississippian is very enriched in comparison to the samples within the Arbuckle. The two most depleted samples, 4,335 ft. & 4,388 ft., are grouped together and coincide with the two of the three outliers on the Ca/Mg vs. Ca/Sr plot (Figure 1.14). These two outliers could indicate that the upper and lower depths within the Arbuckle are not hydraulically connected. The sample directly below these two outliers shows enrichment, from -7‰ to -5‰, indicating a possible zone of separation due to a significant ‰ increase. A depth wise plot of each of these isotopes shows greater clarity into this possible zone of separation as seen in Figure 1.17.

Musgrove and Banner (1993) descried three brine end members from within the midcontinent with implications for groundwater mixing. These three end members originate from: 1. meteoric waters, 2. dissolution of halite, 3. from an evolved seawater. Each of these end members is based on the brines concentrations of major elements and isotopes. Within Wellington most brines indicate an evolved seawater origin, group 3, with a couple of exceptions. These exceptions are again at 4,335 ft. & 4,388 ft., which show the highest depletion in δ^2H and $\delta^{18}O$.

Cl/Br vs. Cl^- plots can be used to indicate mixing. Both Cl^- and Br^- are conservative anions that remain in solution during evaporation. Figure 1.20, shows that all samples within the Arbuckle plot above the seawater evaporation curve, indicating

mixing from secondary brine formed from the dissolution of halite (Fontes and Matray, 1993). The Mississippian sample plots below the line indicating greater abundance of Br^-, and a different mixing of waters. The upper and lower Arbuckle again shows distinct separation. Figure 1.24 further shows the extent that halite dissolution has had an effect on the brines.

δ^2H and $\delta^{18}O$ against Cl^- shows further zonation of brines found within the Arbuckle (Figure 1.19). These plots again show the distinct separation of the upper and lower Arbuckle. The upper Arbuckle is greatly depleted in both isotopic ‰ and Cl^- concentrations, while the lower Arbuckle is enriched in both. This plot further confirms the vertical separation occurring within the Arbuckle. Figure 1.18 shows the distinct variations in 1/Sr data of the samples above and below the baffle: DST 2 and 3.

Microbial evidence for vertical separation within Wellington field was studied (Scheffer, 2012). It was found that different microbial zones exist above and below this low porosity baffle zone. Individual bacteria were examined and showed two different microbial communities above and below the baffle zone. Redox sensitive species were analyzed to help determine microbial activity. Sulfate and reduced iron (Fe^{2+}) both increased down to the top of the baffle zone and then deceased below it. These differences in redox species concentrations and microbial communities suggest vertical separation of the upper and lower Arbuckle.

There is strong evidence for a low porosity baffle zone that separates the upper and lower Arbuckle. This baffle zone is an effective connectivity barrier found near the top of the Arbuckle, and above the zone of CO_2 injection. While still found within this carbonate aquifer, it could be an effective trap for the vertical migration of the CO_2

plume. Even if this baffle zone vertically separates dissolved ionic species, it may not effectively seal the upper and lower Arbuckle upon the introduction of CO_2 and the consequential reduced pH environment.

1.5.6 Vertical Connectivity, Cutter

δ^2H and $\delta^{18}O$ are plotted to investigate zones of separation (Figure 1.41). Most of the swab waters from Cutter plot along the GMWL and show slight depletion in relation to the GMWL. There are three sets of swabs that plot near one another. However one set, swabs 7 and 10, show distinct depletion in relation to the others, and plot much lower and further from the GMWL. Only two other groupings are seen and are of swabs 8 and 9, and swabs 3 and 4 with the other swabs showing no zonation or grouping. This lack of separation could indicate a well-mixed environment throughout the varying intervals, with the exception of swabs 7 and 10. $\delta^{18}O$ vs. δ^2H at Cutter shows an overall tight grouping in relation to Wellington which shows a much wider spread and areas of separation based on depth (Figure A.3.1). At Wellington the two swabs that define the baffle zone show the same depletion, and plot close to swabs 7 and 10 from Cutter. A well-mixed and vertically connected system will have greater implications for CO_2 migration and contamination.

All of Cutter samples on the Cl^- vs. Cl/Br graph plot above the seawater evaporation curve (Figure 1.35). Br^- concentrations were replicated and analyzed at the KGS, as many of the original Br^- concentrations were below detection limits when measured at K-state. There are two groups, one being of swabs 7 and 10 with the rest showing no relation. Swabs 7 and 10 are the most depleted in Cl^- concentrations, with

swab 7 having the highest concentration of Br^-. Figure 1.39 shows that like at Wellington, halite dissolution has strongly affected the brines.

Isotopic values plotted against Cl^- further define the differences in the hydrochemistry of swabs 7 and 10 (Figure 1.40). For δ^2H and $\delta^{18}O$, swabs 7 and 10 again show the greatest depletion in comparison to the rest of the samples collected. Both swab 8 and 9 plots the closest to swabs 7 and 10, and lie stratigraphically between them. Due to the stratigraphic location and where swabs 8 and 9 plot could be caused by swabs 7 and 10 limiting vertical connectivity, and segregating swabs 8 and 9 from the rest of the system. While swabs 8 and 9 are the nearest plots to swabs 7 and 10, they are not nearly as depleted and plot near the rest of the samples. This infers that while swabs 7 and 10 do separate swabs 8 and 9 from the system by limiting vertical connectivity, the separation is weak. Strontium isotopes show no indication of vertical separation and again swabs 7 and 10 plot as outliers.

1.5.7 Flow-through experiment, Wellington

The core 31-19 was allowed to initially be saturated with brine before CO_2 injection. During this saturation phase the majority of ionic species (Ca, Na, Mg, Cl^-, SO_4, S) decreased from their initial concentrations, while redox sensitive species increased (Fe, Mn, P). The initial brine concentration and the concentration at time zero are not the same. This difference could possibly be due to the core being allowed to dry and be exposed to the environment, and the brine being re-pressurized to near formation pressures and temperatures. Initial pre and post pressurization analyses of the ionic species should differ because of this reestablishment of formation conditions.

Ionic species varied in concentration in the post injection samples. Initial increases in Ca, Na, Mg, Mn, Cl^- and SO_4 occur over the first 5 hours, while S and Fe decrease at the same time. At hour 5 there is a distinct decrease in all of these species, except S, which shows an increase in concentration.

Alkalinity and pH were measured with the same effluent along with the other ionic constituents, and do not represent experimental conditions. A correlation can be seen between the three parameters, with the best correlation being with the ionic species and alkalinity. Alkalinity closely follows the same trend as Ca, Mg, Na, Cl^-, Mn, and SO_4. S shows a near inverse relation to alkalinity, and Fe shows no reliable correlation. The similar Ca and Mg trends along with alkalinity is expected due to the dissolution of the carbonate core with the introduction of CO_2 followed by the sequential decrease in pH that drives the dissolution. Alkalinity and pH display a near inverse relationship for the majority of the experiment up till hour 15, thereafter they follow the same general trend (Figure 1.46). As the pH decreases due to the introduction of CO_2 it dissolves the carbonate rock. This dissolution caused by the decrease in pH inversely increases alkalinity. Fluctuation of these two parameters over the course of the first couple of hours is when the system was trying to reestablish equilibrium. Since only one sample was taken between hours 7 and 21 for the entirety of the experiment, it is difficult to determine trends accurately. Overall, during the last hours of the experiment it appears that pH and alkalinity may be nearing equilibrium due to the less variable trends.

1.6 Conclusion

Coal, natural gas, and fossil fuels have become staples of our society. Our advancement in the use of these non-renewable energy resources has thrust us into the

modern age. However this rapid journey has caused, and will continue to cause, major changes to our planet. Geologic carbon storage (GSC) is the most likely solution to the problem, without the decrease in consumption of fossil fuels or alternative energy growth. Not every location is suitable for GCS, and each location must be studied extensively to ensure containment for generations. Sedimentary basins, particularly deep saline aquifers hold the potential for the largest amount of prospective storage. This work is investigating the potential feasibility for storage in a deep saline aquifer within a carbonate unit in south-central Kansas.

The Wellington field has been studied extensively, with it being the location of injection. Cutter is being investigated and used as a western calibration study to Wellington. At both locations three zones are of interest; the uppermost Mississippian interval which will be used for enhanced oil recovery, and not highlighted in this work; a low porosity zone, or baffle zone found within the Arbuckle at Wellington; and the Arbuckle injection zone.

Within Wellington NMR logs and porosity measurements along with isotope and ionic analyses demonstrate a low porosity zone at the top of the Arbuckle. This zone could inhibit the vertical migration of the CO_2 plume and allow for greater CO_2-water-rock interactions to occur. $^{87}Sr/^{86}Sr$ analysis, further confirmed the disconnect between the upper and lower units of the Arbuckle. Microbial work (Scheffer, 2012) confirmed vertical separation within the Arbuckle that correlated with the baffle zone. Hydrochemical analysis shows that the upper Arbuckle is limestone rich and the lower depths dominantly dolomite, with core data confirming this (Barker, 2012). Ca/Sr vs. Ca/Mg demonstrates that dolomitization has had significant effect on the lower depths,

while calcite recrystallization has affected the upper depths of the Arbuckle. Diagenetic alterations to the brine appear to have been driven by halite dissolution, as seen in Cl/Br vs. Ca/Mg.

Cutter hydrochemistry indicated a well-mixed zone. Hydrochemical data showed no distinctions or groupings of depth to indicate limited vertical connectivity. However swabs 7 and 10 could be the exception. Both of these intervals plot as distinct outliers in the majority of the figures. These intervals could have different flow regimes, or be anomalous due to sampling conditions. Swab 7 was sampled from a very dense interval, with recovery of only a few barrels, while swab 10 had extensive amounts of oil present. Both of these sampling conditions could be, or partially be, the reason for their distinctiveness. The two intervals between, swabs 8 and 9, generally plot the closest to the outliers, swabs 7 and 10. This could indicate that swabs 7 and 10 are distinct hydrological flow units within Cutter that partially separate the upper intervals. However due to the general intermediary position of swabs 8 and 9 to the rest of the samples, it could mean that the vertical separation caused by swabs 7 and 10 is weak. Like Wellington, the upper intervals of Cutter show a calcite recrystallization trend, while the deeper depths show a stronger dolomitic influence. Halite dissolution is again the major diagenetic influence on the brine.

Hydrochemical analysis can only give partial insight into the feasibility of CO_2 storage, and its interpretation should always be used in conjunction with other analyses. From the results of this work, it can be concluded that Wellington field would be fully suited as a geologic carbon storage site. The connectivity of the Arbuckle, with multiple overlying caprocks, along with the presence of the baffle zone could ensure the security

and storage capacity needed for successful injection and storage thereafter. However at Cutter, it appears that storage capacity and security would be diminished by the connectivity of the entire system.

Acknowledgements and Disclaimer

This work was performed under the U.S. Department of Energy and National Energy Technology Laboratory Contract #FE0002056. Experimental work and analysis was conducted at Lawrence Livermore National Laboratory. Further analysis was completed at Kansas State University, University of Kansas, and the Kansas Geological Survey.

A version of this Chapter is intended for publication in the journal American Association of Petroleum Geologists Bulletin.

Chapter 2 – Experimental investigation for the characterization of CO_2-water-rock interactions utilizing cored rock and formation brine within a carbonate aquifer.

2.1 Introduction

Geologic carbon storage is one potential solution to reduce the global atmospheric concentration of carbon dioxide. Storage can occur in a variety of underground formations through four trapping mechanisms. These trapping mechanisms operate on varying time scales and security of storage. Among these different formations, saline aquifers, basaltic sequences, and sedimentary basins are the most likely of candidates for CO_2 storage. Reactivity will vary between sites and will depend on: 1) pre-existing reservoir mineralogy; 2) rates and mechanisms of CO_2 emplacement; 3) variations in the temperature and pressure conditions of the reservoir and its effect on CO_2 and mineral solubility; 4) variable reaction rates (Kampman et al., 2014). Proximity of the point source to the injection site will be crucial as transportation costs can render a project uneconomical. Injection into these formations alters the existing chemical equilibrium with the extent of alteration depending on the type of formation. Of these formations, saline aquifers hold the potential for the greatest capacity for storage. CO_2 solubility into the brine will be determined by pressure, temperature, and salinity of the formation brine (Dubacq et al., 2013). Carbonate units with high salinity formation water could exhibit the greatest change in chemical equilibria as CO_2 injected into these environments will acidify the water and cause dissolution of the host rock to occur. Injection of CO_2 into the formation brine affects the existing chemical environment in three general ways; 1) initially injection causes acidification of the formation brine; 2) this is followed by pH

buffering by the dissolution of host rock; 3) re-precipitation of secondary minerals (Black et al., 2014). Dissolution of the host rock, and the potential for alteration to overlying caprocks, can be studied through experimental core flooding.

Most experimental studies on core flooding have used a combination of three different conditions. The first one uses actual cored rock from the potential GCS field and floods it with synthetic brine that should mimic in-situ brine. The second uses cored rock that mimics the potential GCS field formation rock while also using synthetic brine. The third and more rare study utilizes cored rock and sampled formation brine from the potential GCS site. This work is an investigation into the dissolution of a carbonate bearing rock using cored rock and formation brine from the CO_2 injection zone.

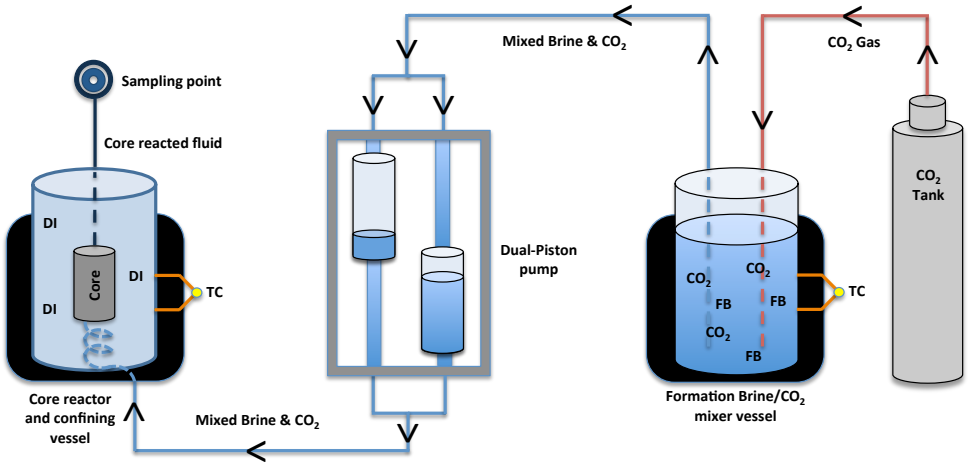


Figure 2.1 Basic and overly simplified LLNL experimental setup and directional flow chart. Flow goes from right to left.

2.2 Materials and Methods

2.2.1 Selection and mineralogy of cored rock plug

The basis for which samples were chosen was essentially four-fold: 1) high permeability (Kmax, Kvert, K90); 2) high yet not unreasonably high porosity (ideally <10%); 3) any relative heterogeneity in both the mineralogical and petrophysical realms (i.e. vuggy porous zones, convoluted fracture pathways, secondary dolomite/argillaceous infillings, etc.); and 4) a strong preexisting data set pertaining to the depth at which a sample was chosen (i.e. thin sections, swab/DST water chemistry, isotope data, etc.). All samples for this experiment were collected from within the Arbuckle. Utilizing these parameters, 3 samples were chosen and taken to LLNL for further examination. With further inspection and assessment core 20-9 was chosen due to its variable mineralogy, lack of vugs, and the closest swab water chemistry.

Core 20-9 (7,098') was chosen for its depth, high relative permeability (2.849 mD), and high relative porosity (3.6%) (Figure 2.2). The mineralogy of the core is believed to be representative of the target depth of CO_2 injection. The core was a light gray fine-grained dolomite mudstone with a large (2.5 x 2x2cm) chert nodule along one side, with a similar (2.5 x 1cm) chert nodule along the other side. Pinpoint vugs were found throughout the plug, with a white powdery carbonate material found along the chert-dolomite boundaries and as fracture/vug infilling on both ends. The core was also intact and void of large vugs or large fractures that would normally relinquish its feasibility for selection. Thin sections of the core was taken and described in Figure 2.3.

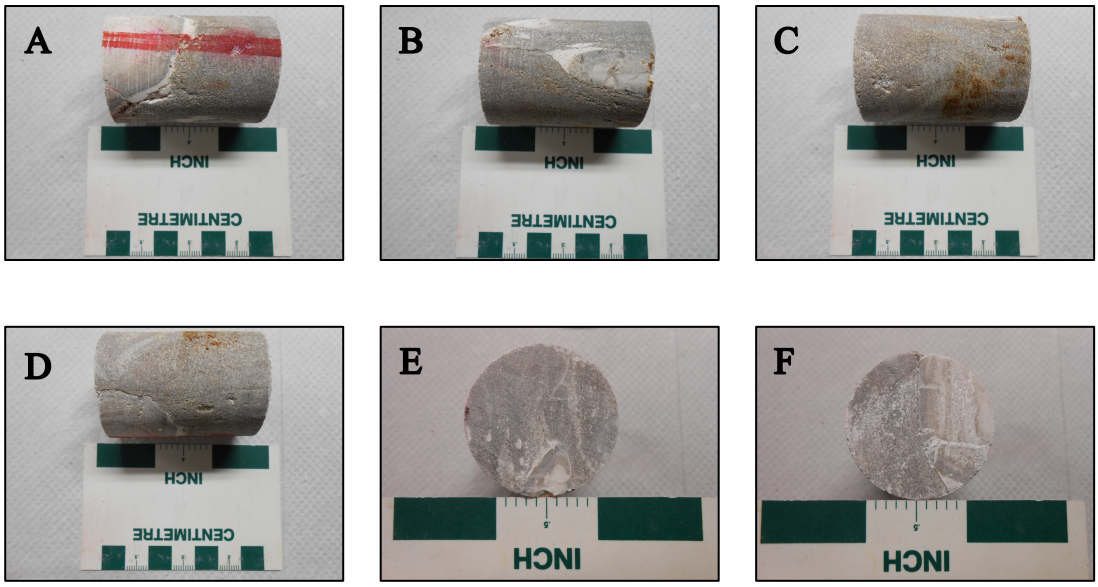


Figure 2.2 Rotational views of Cutter Core 20-9 (7,098 ft.). E) Side of injection. F) Side of outlet. Chert nodule seen in (B) is the same as seen in (E).

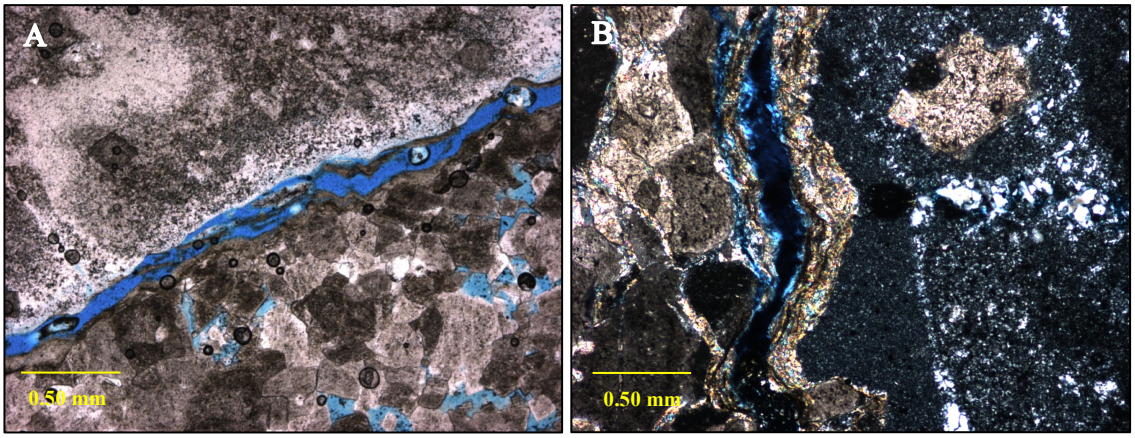


Figure 2.3 Thin sections of Core 20-9 (7,098 ft.). A) (4x in Plain Light) Heterogeneous contact between large chert nodule and fine grained dolomite packstone. Large chert nodule in upper portion of image exhibiting microporous chert matrix. Accumulation of argillaceous materials along porous fracture boundary. Moderate intergranular porosity within dolomite packstone matrix. B) 4x in Cross-Polarized Light) Heterogeneous contact between large chert nodule and fine grained dolomite packstone. Pore spaces in microporous siliceous matrix along right side of image infilled with radiating chalcedony. Medium grained dolomite rhomb present in silica matrix. Note argillaceous accumulation along fracture boundary. (Mike Vega)

The Arbuckle group is a thick sequence found throughout Kansas entirely in the subsurface except in the structurally high areas of the regional uplifts. The group is dominantly dolomite with interbedded shaly aquitards (Merriam, 1963). The depth of the group ranges from 500 feet in the southeast to 7,000 feet in the southwestern parts of Kansas (Franseen, 2003). The unit thickens from the north to the south with a maximum thickness of near 1,400 feet. The group contains rocks that are late Cambrian to early Ordovician in age. The group usually contains five different units, however with the complexity and similarity of some of the units the group is classified as being below the overlying Simpson Group and the lower Reagan Sandstone. The Arbuckle is a prime candidate for CO_2 storage due to its high total dissolved solids, thickness, depth, overlying caprocks, and its detachment from freshwater resources.

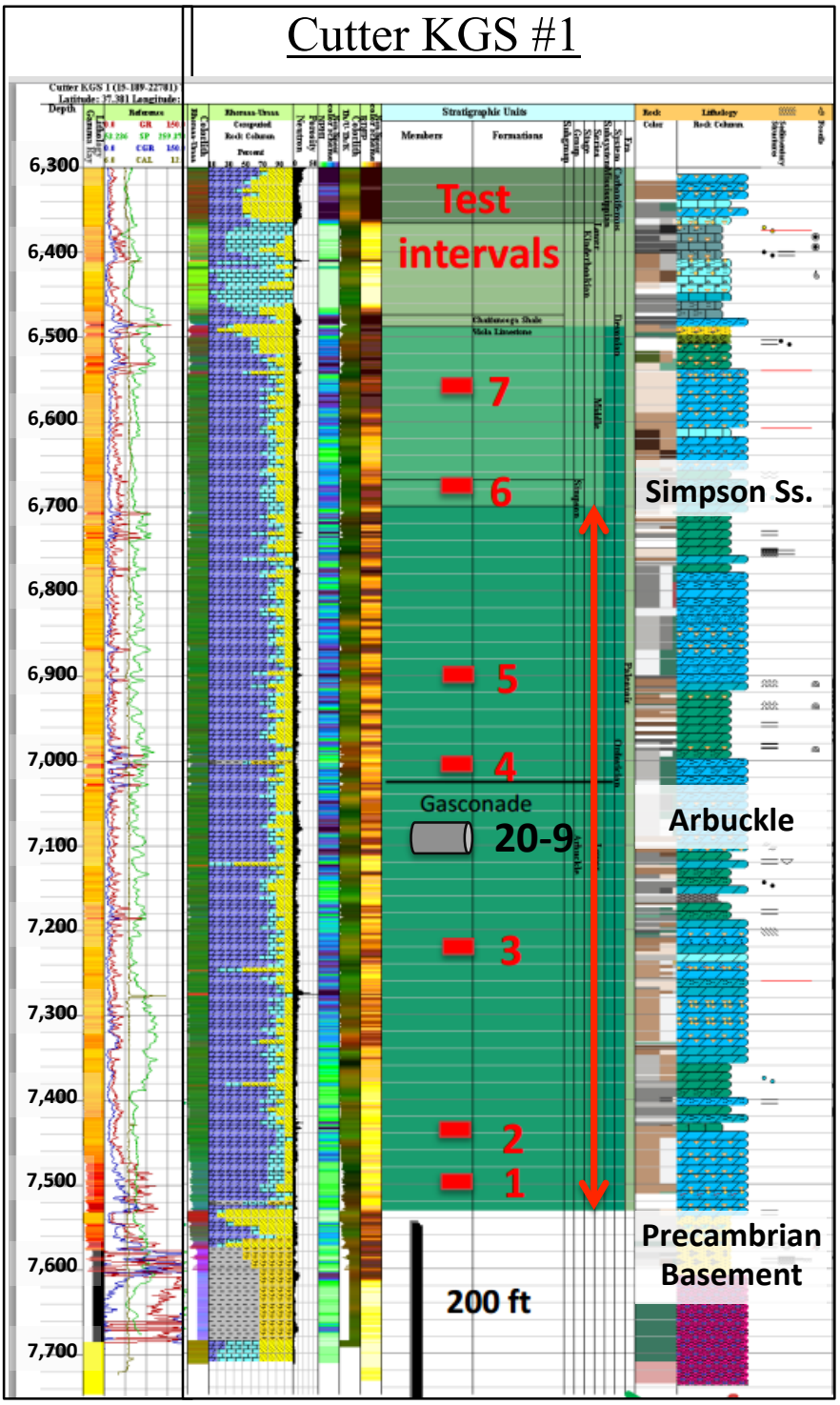


Figure 2.4 Cutter stratigraphic column. Stratigraphic column is abbreviated in relation to the entire well and sample depths collected and analyzed. Red squares indicated swab depths. Gray cylinder indicates core 20-9 used in the experiment. Red line indicates full extent of the Arbuckle group. (Modified from Kansas Geological Survey)

2.2.2 Swabbed brine chemistry

Swab 4 (7,046-7,056') was chosen as the brine to be injected, ~3M NaCl. Swab 4 was the closest water sample to the core and would most likely be in near-equilibrium with the core plug upon experimental saturation. The formation brine from Cutter is predominantly a Na-Ca-Cl type brine with TDS values ranging from 49,000 mg/L to 172,000 mg/L. There is a general depth wise increase in ionic concentration of the brine. Swab 4 had a near average ionic concentration of the major species and didn't contain extremely high or low concentrations of species that were of interest (Table 2.1). The turbidity of the water was low and was therefor of lesser concern for injection into the core flooding apparatus, as there was a concern for precipitation of the brine inside the piping.

Cutter		pH	HCO_3^-	K^+	Mg^{2+}	Mn	Ca^{2+}	Fe	Na^+	S	Sr^{2+}	Br*	Cl^-	SO_4^{2-}
Sample Name	Depth (ft.)		mg/L	mg/L	mg/L	mg/L	mg/L	mg/L	mg/L	mg/L	mg/L	mg/L	mg/L	mg/L
Swab 5	6,880 – 6,904	6.79	117	1410	1470	1.41	9100	4.43	47600	178	229	164.4	103000	475
Swab 4	**7,046 – 7,056**	**6.83**	**462**	**1100**	**898**	**2.13**	**6510**	**0**	**34700**	**264**	**139**	**106.2**	**72300**	**705**
Swab 3	7,218 – 7,234	6.93	817	987	896	2.01	6090	2.85	35600	192	155	115.1	78600	557

Table 2.1 Water chemistry of swabs 3-5 from Cutter.

2.2.3 Cutter experimental flow-through methods

In the summer of 2014, in collaboration with Drs. Susan Carroll and Megan Smith at Lawrence Livermore National Laboratories (LLNL), Livermore, CA, experimental flow-through investigations were completed utilizing a core plug from the Cutter KGS #1 well and collected formation water. The core required having both ends smooth and the entirety of the core void of large external vugs or large fractures as the confining

pressures could detrimentally destroy the core. The core was sanded down prior to experimental setup in order for the core to fit the ladder and to smooth both ends (original dimensions 1.5" D x 2.125" L, new dimensions 1.5" D x 1.961" L). The core was bandaged with PTFE tape and wrapped in a heat-shrinkable Viton® sleeve to prevent lateral flow of water into the core. The cased core was inserted into the ladder and placed into the reaction chamber, which had been filled with DI water (Figure 2.5).

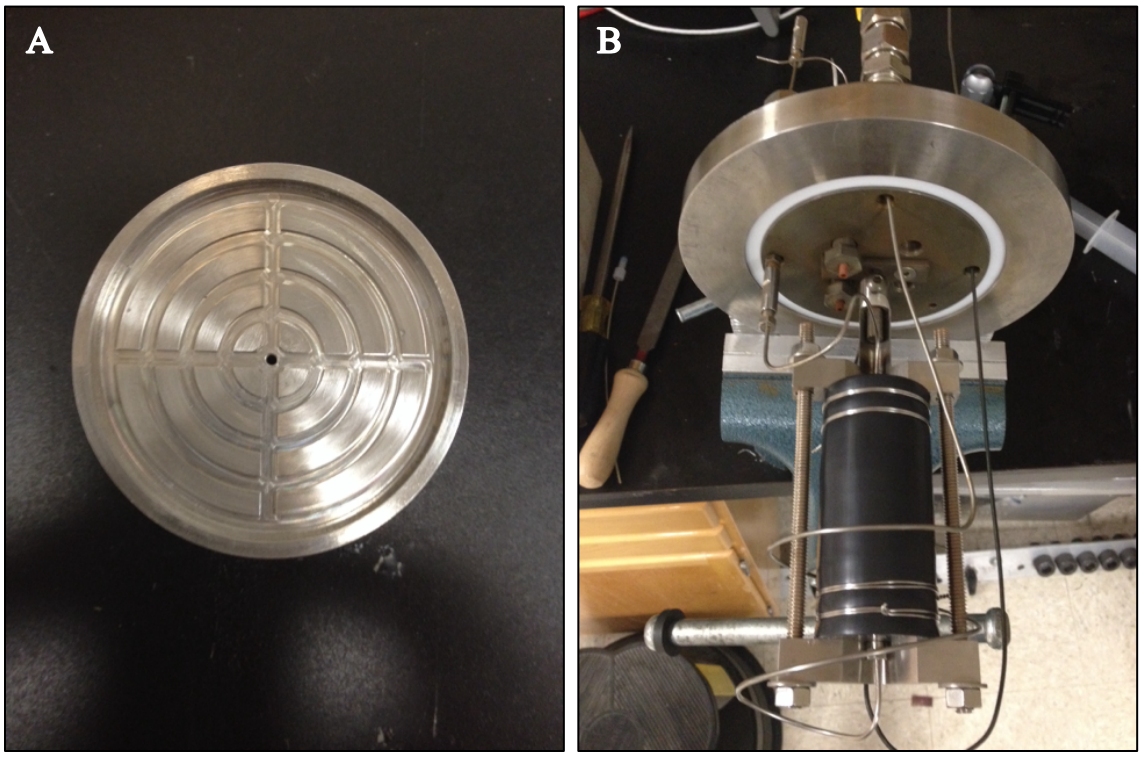


Figure 2.5 A) LLNL reactor end-cap. B) LLNL latter with black Viton® wrapped core. (Images courtesy of Lawrence Livermore National Laboratories).

The DI water was used to maintain the confining pressure. The core was allowed to saturate over night at 60°C with a confining pressure of 3,600 psi (~25 MPa). Since turbidity of the original unaltered brine was of concern, the sample was filtered using a peristaltic pump with a 0.45 μm filter. Brine and CO_2 were allowed to equilibrate, with equilibrium being reached when the pressure deferential diminished to a negligible

amount. Brine was equilibrated with desirable partial pressure (*p*CO2) of 3 MPa and was attained with injection of 99.9% CO_2 at a controlled temperature and pressure. Pressures and temperatures were chosen so that a comparison could be made to earlier experimental carbonates ran by LLNL. Once fully saturated, CO_2-free brine was injected into the core at a rate of 0.34 mL/min. A conservative tracer (potassium iodide (KI)) test was injected utilizing and was chosen based upon the high ionic strength and individual concentration of swab 4. Upon completion of the tracer test, CO_2 and tracer-free brine was run through the core to remove any residual KI. CO_2 flow was then initiated at a flow rate of 0.34 mL/min, and marked by the time = 0 days. The same initial temperature (60°C) and confining pressure (3,600 psi) was used and the outlet pressure was held at 1,800 psi (~12.4 MPa). A dual-cylinder pump was used and allowed for fluid injection to be continuous. As one cylinder injected CO_2 equilibrated brine, the other cylinder filled with CO_2 equilibrated brine. A customized computer program monitoring the injection and cylinder fluid-levels would automatically switch to the full cylinder as the other cylinder was nearing full evacuation, which allowed for continued fluid injection. Pressure transducers and thermocouples were utilized to monitor in-line pressure and temperature conditions and could be adjusted accordingly. Aqueous samples were collected with increasing intervals of time throughout the progression of the experiment. Samples were initially taken every 30 minutes due to the rapid change in the pressure differential. When the pressure stabilized, samples were taken progressively less often. When the inlet and outlet pressure becomes equal pressure breakthrough has occurred. The whole experiment lasted 17 days.

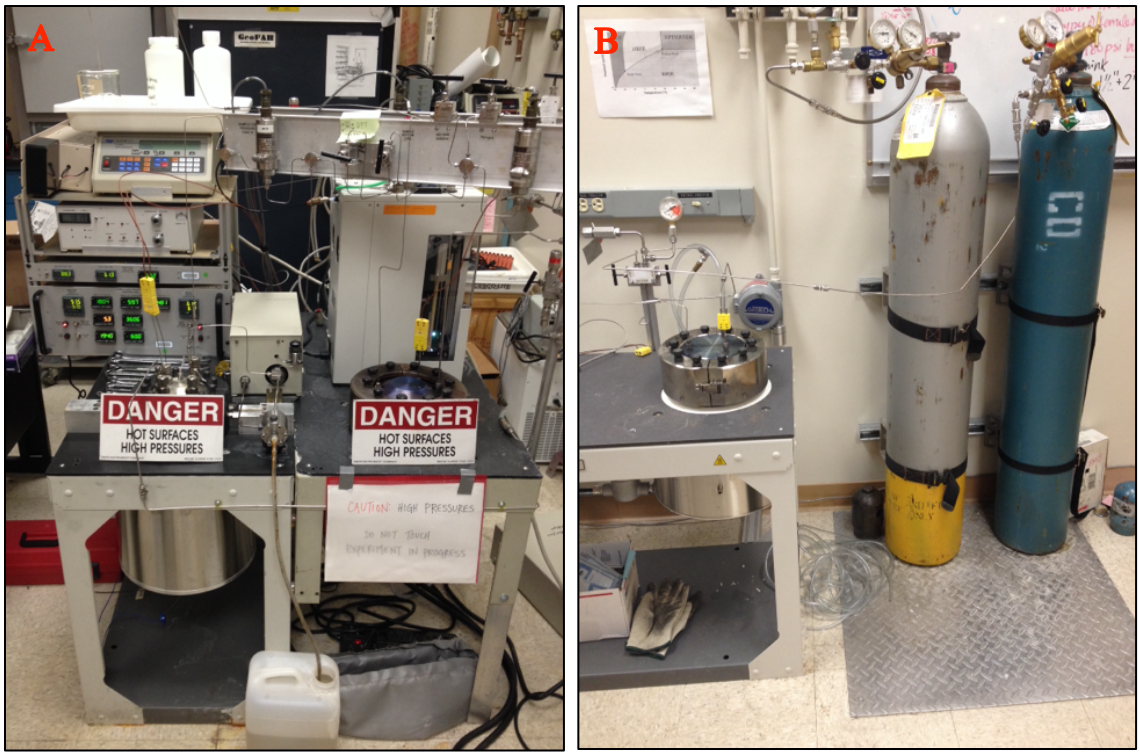


Figure 2.6 LLNL core flooding reactor experimental setup. (Images courtesy of Lawrence Livermore National Laboratories)

Four samples were taken over every sampling period for varying analyses and they included: IC for anions, ICP-OES for cations, Isotope analysis for $\delta^{2}H$, $\delta^{18}O$, $\delta^{13}C$ (DIC), and Total Inorganic Carbon (TIC). For IC and ICP-OES a single 50 mL syringe was allowed to be filled until enough sample was collected for each analysis. All samples except for isotopes were again filtered with a 0.20 µm filter. Sample containers were previously marked, weighed dry, weighed wet, and with the addition of the sample weighed for a third and final time.

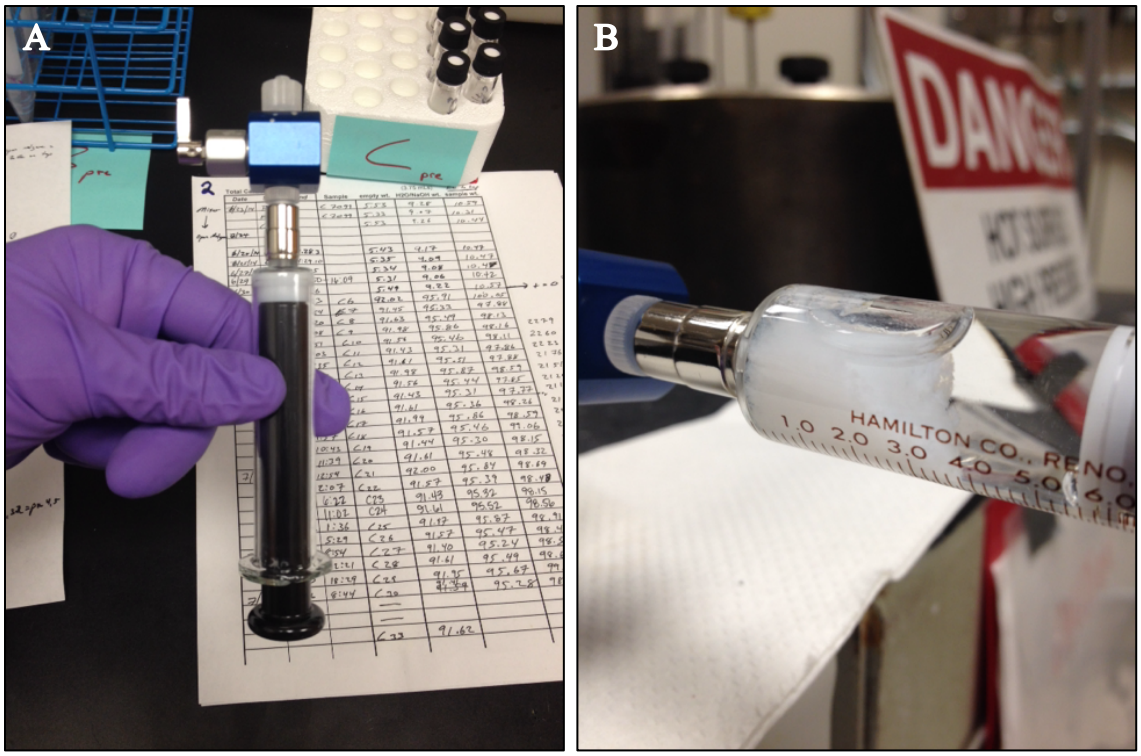


Figure 2.7 TIC analysis using a gastight glass syringe. (Images courtesy of Lawrence Livermore National Laboratories)

For IC analysis 15 mLs of MilliQ water was added for the wet phase, and then 0.5 mL of sample was added. IC analysis was analyzed at the Kansas Geological Survey using a Dionex® ICS-3000 Ion Chromatography System. ICP-OES analyses required 10 mLs of MilliQ water, and 1 mL of sample along with 0.15 mL (1.5 vol%) of ultrapure HNO_3. Acidification was done using JT Baker® ultrex II ultrapure reagent HNO_3 acid. ICP was performed at the University of Kanas. For isotopic analysis, 30 mLs of unfiltered sample was taken. Due to the large amount of sample needed and low flow rates isotope sample collection was limited for analysis of δ^2H, $\delta^{18}O$, and $\delta^{13}C$ (DIC). TIC samples were taken with a gas tight glass Hamilton Co.® 10 mL syringe. The syringe we pre-filled with 3.75 mL NaOH and then placed on the outlet spigot until ~8 mL of sample was collected. The syringe was shaken in order to dissolve any residual gaseous

CO_2. The sample was then filtered using a 0.20 μm syringe filter and injected into a 2 mL clear glass vial until there was no headspace. TIC samples were analyzed using an O-I-Analytical Aurora Model 1030 TOC with a 1088 Autosampler.

2.2.4 Cutter LLNL X-ray computed tomography analysis

Pre and post-experimental core-flood X-ray computed tomography scans (XRCT) scans were completed for Cutter core 20-9. The cores were scanned at the University of Texas, Austin, TX. An Xradia® MicroXCT-400 scanner utilizing the macro objective for the pre and post scans. The core was scanned at the top and bottom with the resulting volumes digitally stitched together. Each volume included 1,081 views with 360 degrees of rotation and was scanned at 2.5 seconds per view. The volumes were reconstructed with a beam-hardening correction of 0.05, byte scaling of -10, 575, and a low-contrast ring correction. A Hamamatsu® X-ray source operating at 110 kV and 10 W with a 2.1 mm SiO_2 pre-filter was utilized.

2.2.5 Processing of X-ray computed tomography scans

Pre and post scanned images were analyzed using the image software package FIJI®. Pre and post images were aligned in order to straighten the images so that further processing could take place. Both stacks were registered to one another, and due to the smoothing of the core, the post XRCT images were less than the pre stack images and so images were deleted from the pre stack to match and align with the post stack. Utilizing the post stack, a mask was created highlighting the pore space. Due to the subjectivity of distinguishing pore space from mineral, a high and low threshold was created to highlight different threshold values for pore space identification. The voxel size of the image could hide possible pore space if the threshold is underestimated, and could include non-pore

space if overestimated. The high threshold, 40, is a possible overestimation of pore space (Figure 2.8). A low threshold, 30, was chosen because it represented the distinguishing porosity, and overlooked what could be either mineral or smaller pore space (Figure 2.8). The pre stack images were given a threshold of 30, and were created to represent before reaction images of pre-existing pore space. Full size images are included in Appendix B.

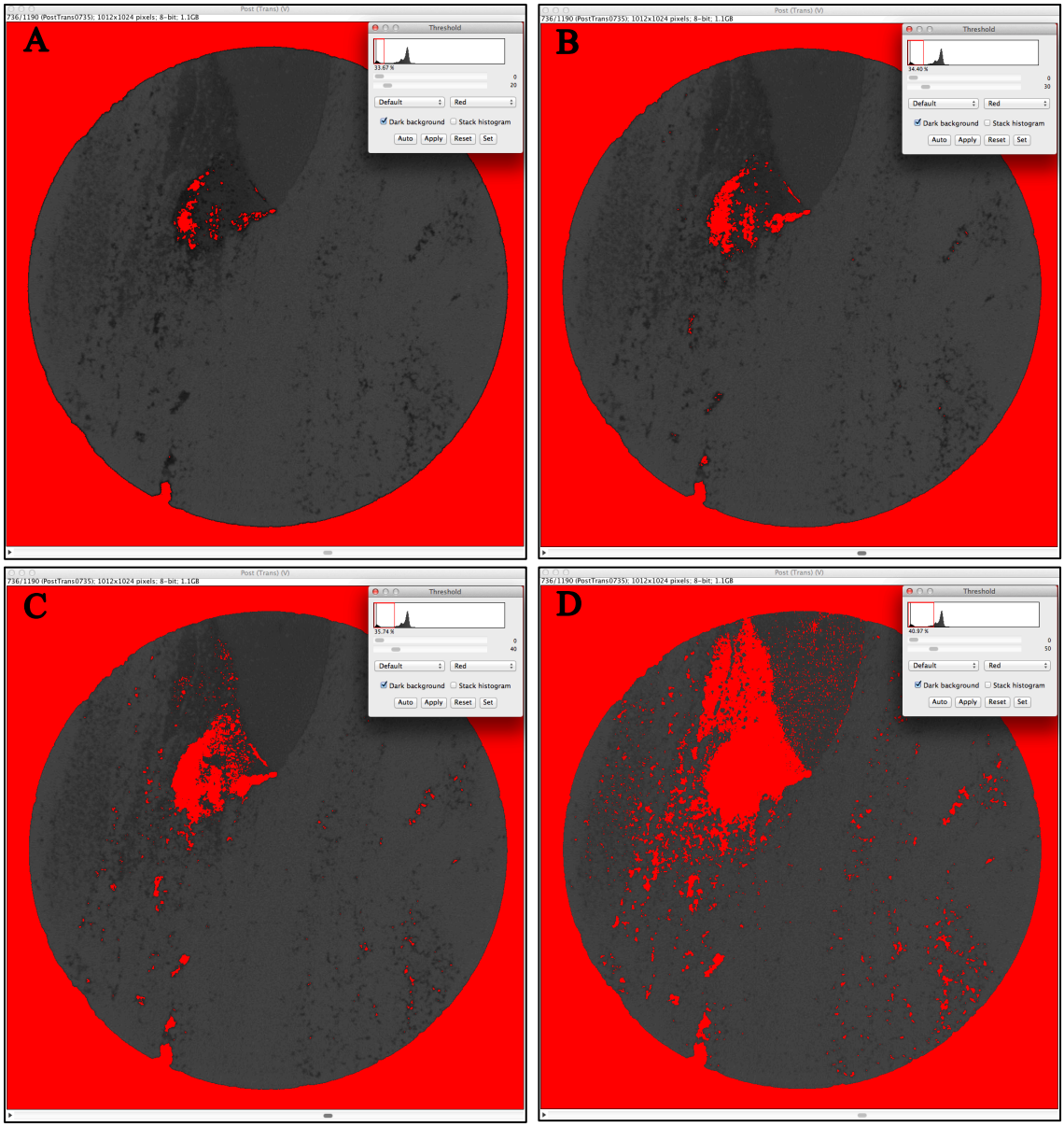


Figure 2.8 Cutter LLNL threshold differences indicating porosity. Images show differentiation between threshold values. Threshold values are: A=20, B=30, C=40, and D=50. All thresholds were taken from the same image slice.

Post stack images were added to the pre stack images and a new threshold was added to indicate newly dissolved mineral. The pre and post stacks were added together for both the high and low threshold examples. Using the plugin, 3D viewer, the high and low stacks were converted into 3D images, with the high stack being purple, the low stack being blue, and the pre reaction stack being white (Figure 2.8).

2.3 Results

2.3.1 Cutter Flow-through analysis results

Eluent flow-through samples were analyzed for cation and anions. Cations analyzed include: Ca^{2+}, K^{+}, Mg^{2+}, Na^{+}, Cu^{2+}, Fe, Li^{+}, Mn, Sr^{2+}, Ba^{2+}, Mo, Pb^{2+}, and Zn^{2+}(Table 2.2). Anions analyzed include: Cl^{-}, Br^{-}, SO_4^{2-}, and NO_2^{-} (Table 2.3). δ^2H, $\delta^{18}O$, $\delta^{13}C$ (DIC), and total inorganic carbon (TIC) were selectively measured at different times throughout the experiment (Table 2.4). Tables only include elements that were above detection limits.

Time (days)	Analyte	Ca^{2+} (mg/L)	K^{+} (mg/L)	Mg^{2+} (mg/L)	Na^{+} (mg/L)	Cu (mg/L)	Fe (mg/L)	Li (mg/L)	Mn (mg/L)	Sr^{2+} (mg/L)
0	**A1**	5700.8	729.3	881.0	34880.3	9.0	2.5	13.2	7.2	161.3
0.29	**A2**	5049.7	646.4	779.1	30878.8	6.8	2.9	11.8	6.5	143.1
2.23	**A3**	5114.4	827.0	794.2	31273.1	6.5	3.6	12.1	6.6	145.3
4.28	**A4**	5642.3	784.5	875.1	34608.1	5.2	2.3	13.3	7.1	158.1
5.07	**A5**	4748.3	632.3	732.3	29073.6	5.6	2.9	11.0	6.0	133.7
5.11	**A6**	4734.2	658.1	744.2	29632.2	9.6	2.5	11.2	7.5	139.0
5.14	**A7**	5710.3	874.1	838.7	32893.3	19.2	1.4	12.2	16.1	155.9
5.16	**A8**	5869.7	925.7	878.4	34236.1	14.3	4.2	12.9	15.0	161.0
5.19	**A9**	5770.0	752.4	884.3	34496.9	9.0	4.7	13.0	11.3	159.7
5.22	**A10**	5441.7	709.9	838.7	32743.8	7.9	3.8	12.4	9.5	153.1
5.27	**A11**	5135.4	693.7	800.2	31030.8	6.3	3.2	12.0	8.2	146.1
5.33	**A12**	5842.9	749.7	907.4	35415.3	6.4	3.2	13.6	8.9	164.6
5.37	**A13**	5745.4	759.9	908.8	34804.4	6.1	3.1	13.3	8.6	161.0
5.42	**A14**	5988.6	813.0	941.2	36342.3	6.2	3.1	13.8	8.9	167.3
5.44	**A15**	5489.1	740.1	862.7	33196.9	5.7	2.9	12.6	8.1	152.4
5.46	**A16**	5536.4	734.3	862.2	33547.8	5.8	2.9	13.0	8.3	155.8
5.49	**A17**	6135.9	786.1	961.5	37104.6	6.0	3.0	13.8	9.0	174.1
5.51	**A18**	5964.5	774.2	937.3	36053.7	5.9	3.0	14.0	8.8	167.8
5.55	**A19**	6102.9	800.4	952.9	36893.5	5.7	2.9	13.8	8.8	173.0
5.58	**A20**	5550.3	716.0	864.5	33509.1	5.2	2.7	12.8	8.1	158.6
5.64	**A21**	5929.5	764.2	930.0	35794.5	5.5	2.8	13.6	8.6	168.8
5.69	**A22**	5651.7	752.8	882.6	34128.1	5.2	2.7	13.0	8.2	160.5
5.86	**A23**	6408.8	823.7	1009.3	38759.7	5.6	2.8	14.4	9.0	179.3
6.06	**A24**	6340.7	830.1	996.6	38291.9	5.8	2.8	15.0	9.3	178.8
6.17	**A25**	5398.0	683.0	843.1	32546.1	4.7	2.4	12.7	7.8	153.0
6.33	**A26**	6165.7	790.9	976.7	37248.5	5.3	2.5	14.4	8.8	172.7
6.97	**A27**	4949.8	651.8	776.9	29755.1	4.3	2.2	11.8	7.2	140.9
7.11	**A28**	6121.4	790.5	960.4	36921.6	5.1	2.4	14.1	8.7	173.1
7.37	**A29**	5888.4	747.4	976.1	34811.5	4.8	2.3	13.1	8.1	162.0
7.96	**A30**	5545.7	720.1	876.0	33410.6	4.6	2.2	13.0	7.9	156.0
8.19	**A33**	4810.4	617.1	758.5	28944.1	3.9	1.9	11.0	6.8	136.0
9.28	**A34**	5716.8	725.8	898.1	34473.7	4.5	2.0	12.8	7.8	160.6
11.00	**A35**	5325.3	672.0	838.8	32115.5	4.4	1.9	13.0	7.9	151.4
11.97	**A36**	5653.1	720.2	884.2	34080.9	3.1	2.8	13.0	14.8	158.3
13.96	**A 39**	5722.3	712.2	894.1	34473.8	2.9	2.8	13.5	15.4	162.5
15.96	**A40**	5955.2	738.8	931.5	35897.3	3.0	2.7	14.1	16.0	167.4
18.93	**A41**	5615.7	694.7	876.8	33891.1	2.6	2.8	13.2	16.8	159.0
21.12	**A42**	5653.4	698.9	877.0	33844.1	2.4	2.7	13.1	16.8	159.3
	Apre1	5610.9	706.0	858.6	34325.2	5.7	2.4	13.2	8.1	157.5
	Apre2	5471.3	694.6	845.0	33424.1	5.7	2.3	13.3	8.1	155.4
	Apre3	5133.8	646.7	781.8	31367.5	8.0	3.6	11.9	6.8	146.5
	Apre4	5563.4	707.4	855.2	34028.4	6.1	2.4	13.0	7.3	158.8
	Apre5	5613.7	714.1	866.8	34316.5	5.5	3.8	12.8	14.8	157.0
	Apre6	5197.4	656.4	798.7	31749.2	5.6	3.7	11.9	14.0	147.8
	Amq	-35.2	-10.1	-11.5	-183.0	0.0	0.6	-0.2	-0.2	-0.7
	Apost 1	4970.4	624.2	768.7	30148.6	4.0	1.4	12.5	7.4	140.3
	Apost2	5494.9	692.7	847.5	33313.5	4.1	1.4	12.9	7.6	155.7
	Apost3	5537.5	692.2	847.4	33611.0	2.6	2.1	12.9	14.8	156.6
	Apost4	5674.2	701.6	868.6	34385.7	2.7	2.1	13.4	15.3	161.1
	Aextra2	58.0	15.6	8.0	403.9	1.1	1.5	0.0	0.5	2.0
	A37 pre7	6050.3	752.0	924.4	36659.8	5.2	4.1	14.0	17.7	172.6
	A38 pre 8	5883.0	726.5	893.4	35778.3	5.1	4.0	13.7	17.3	168.5

Table 2.2 Cutter LLNL cation analysis of pre and post experimental flow through eluent. CO_2 started at day 5.11, sample A6. Apre1-2 is from the first brine-mixing vessel. Apre 3-4 is from the open Nalgene/pre-CO_2 flow. Apre5-6 is from the second brine-mixing vessel. Amq is MilliQ water. Apost 1-2 is from the first brine-mixing vessel. Apost 3-4 is from the second brine-mixing vessel. Aextra is from the reactor vessel confining water. Apre 7-8 is from the third brine-mixing vessel.

Time (days)	Analyte	Cl (mg/L)	NO_2 (mg/L)	SO_4 (mg/L)	Br (mg/L)
0	**B1**	62567.6	2241.9	606.9	91.0
0.29	**B2**	52027.0	2404.4	362.4	67.6
2.23	**B3**	41333.2	1748.3	289.2	92.8
4.28	**B4**	64260.7	2044.7	502.3	94.2
5.07	**B5**	50140.4	2162.6	347.5	65.9
5.11	**B6**	35802.4	1779.6	259.3	51.6
5.14	**B7**	22787.4	1216.7	161.8	55.6
5.16	**B8**	49135.3	2067.0	359.8	96.3
5.19	**B9**	51445.3	2148.7	367.3	82.2
5.22	**B10**	43057.4	1550.1	309.9	55.1
5.27	**B11**	50748.5	1826.4	356.5	76.1
5.33	**B12**	50554.4	2055.4	366.0	71.0
5.37	**B13**	50711.8	1945.1	365.6	88.7
5.42	**B14**	38941.9	1509.0	286.3	70.8
5.44	**B15**	51973.5	2116.1	388.6	62.3
5.46	**B16**	40745.8	1617.2	301.2	58.6
5.49	**B17**	38087.3	1852.1	282.3	45.6
5.51	**B18**	48227.7	909.3	368.8	51.2
5.55	**B19**	42168.2	874.5	317.6	50.9
5.58	**B20**	44994.7	949.3	342.2	67.0
5.64	**B21**	26634.1	1398.8	190.3	52.5
5.69	**B22**	32686.3	1702.0	186.9	73.0
5.86	**B23**	54565.1	1919.5	338.5	67.1
6.06	**B24**	65114.0	2466.5	394.1	104.5
6.17	**B25**	41378.1	2092.2	246.4	54.7
6.33	**B26**	37782.6	1901.5	214.3	69.2
6.97	**B27**	34459.2	1663.0	205.0	57.7
7.11	**B28**	46623.9	1972.3	327.0	68.9
7.37	**B29**	51829.6	1927.8	334.5	137.6
7.96	**B30**	52419.3	2297.9	362.5	81.3
8.19	**B33**	46042.2	2363.5	321.2	71.1
9.28	**B34**	40917.9	1943.7	281.2	61.7
11.00	**B35**	35494.0	1684.7	237.6	49.9
11.97	**B36**	52755.5	2616.8	357.2	61.5
13.96	**B39**	58618.1	2671.4	423.6	78.2
15.96	**B40**	114779.6	3425.3	788.7	158.0
18.93	**B41**	64719.4	2945.4	463.0	65.1
21.12	**B42**	59638.9	2913.3	417.6	81.9
	Bpre1	47987.0	2460.6	357.2	49.7
	Bpre2	0	0	0	0
	Bpre3	40916.7	2344.0	296.4	47.2
	Bpre4	53911.6	0	296.3	56.5
	Bpre5	52728.0	0	283.2	104.9
	Bpre8	68328.7	0	389.6	116.7
	Bmq	67.5	0	0	0
	Bpost1	64206.2	3018.5	460.8	89.1
	Bpost3	62366.4	0	361.0	103.3
	Bpost5	115916.1	0	734.5	186.5
	B1xtr2	339.4	0	24.4	0.0

Table 2.3 Cutter LLNL anion analysis of pre and post experimental flow through formation water. CO_2 started at day 5.11, sample B6. Bpre1-2 is from the first brine-mixing vessel. Bpre 3-4 is from the open Nalgene/pre-CO_2 flow. Bpre5,8 is from the second brine-mixing vessel. Bmq is MilliQ water. Bpost 1 is from the first brine-mixing vessel. Bpost 3 is from the second brine-mixing vessel. Bpost 5 is from the third brine-mixing vessel. B1xtr2 is from the reactor vessel confining water.

Time (days)	Analyte	TIC (mg/L C)	Analyte	δ^2H H_2O (‰)	$\delta^{18}O$ H_2O (‰)	$\delta^{13}C$ DIC (‰)
0	**BCC1**	7.1				
0.29	**BCC2**	7.3	**D2**	-50.8	-6.54	-22.2
2.23	**BCC3**	6.8	**D3**	-49.6	-6.14	-21.6
4.28	**BCC4**	6.0				
5.07	**BCC5**	6.3	**D5**	-50.3	-6.51	-20.8
5.11	**C6**	431.9				
5.14	**C7**	651.3				
5.16	**C8**	748.1	**D8**	-49.1	-6.91	-23.3
5.19	**C9**	760.1				
5.22	**C10**	756.5				
5.27	**C11**	848.0				
5.33	**C12**	798.7				
5.37	**C13**	889.1				
5.42	**C14**	835.6				
5.44	**C15**	842.0				
5.46	**C16**	924.8				
5.49	**C17**	867.9				
5.51	**C18**	998.6				
5.55	**C19**	875.6				
5.58	**C20**	908.4				
5.64	**C21**	960.2				
5.69	**C22**	954.6				
5.86	**C23**	925.3				
6.06	**C24**	964.0	**D24**	-49.4	-6.89	-23.1
6.17	**C25**	1136.6				
6.33	**C26**	929.3				
6.97	**C27**	1031				
7.11	**C28**	980.3	**D28**	-48.7	-7.22	-23.5
7.37	**C29**	1035				
7.96	**C30**	960.9				
8.19	**C33**	954.5	**D33**	-48.6	-7.49	-24.2
9.28	**C34**	1067	**D34**	-49.1	-7.73	-24.4
11.00	**C35**	932.6				
11.97	**C36**	1499				
13.96	**C39**	962.5	**D39**	-49.8	-7.22	-21.9
15.96	**C40**	1178	**D40**	-49.3	-7.87	-22.3
18.93	**C41**	863.0	**D41**	-47.9	-7.00	-22.3
21.12	**C42**	798.8				
	BCCpre1	7.34	**Dpre 1**	-49.7	-6.42	-22.9
	BCCpre2	7.36	**Dpost 3**	-48.5	-7.99	-21.5
			Dpost 4	-48.6	-7.83	-22.0

Table 2.4 Cutter LLNL analysis total inorganic carbon (TIC), δ^2H, $\delta^{18}O$, and $\delta^{13}C$ (DIC). CO_2 flow started at day 5.11, sample C6. BCCpre1-2 is from the first brine-mixing vessel.

Figures 2.7-2.24 shows changes in water chemistry with time. Initial fluctuations until CO_2 injection was due to tracer tests and tracer washout flooding. At day 11, pressure failure occurred and subsequent time measurements and water samples were from CO_2 injection pressure climbing back to original preset injection pressure. Pressure failure is distinctly different than pressure break-through. Pressure failure occurred after

switching to the secondary reactor mixer vessel, pressure break-through occurred before pressure failure (Figure 2.9). Pressure breakthrough, if it can be indicated by a 20 psi difference in the inlet and outlet pressures, occurred at 255 hours. Pressure failure occurred at 265 hours into the experiment.

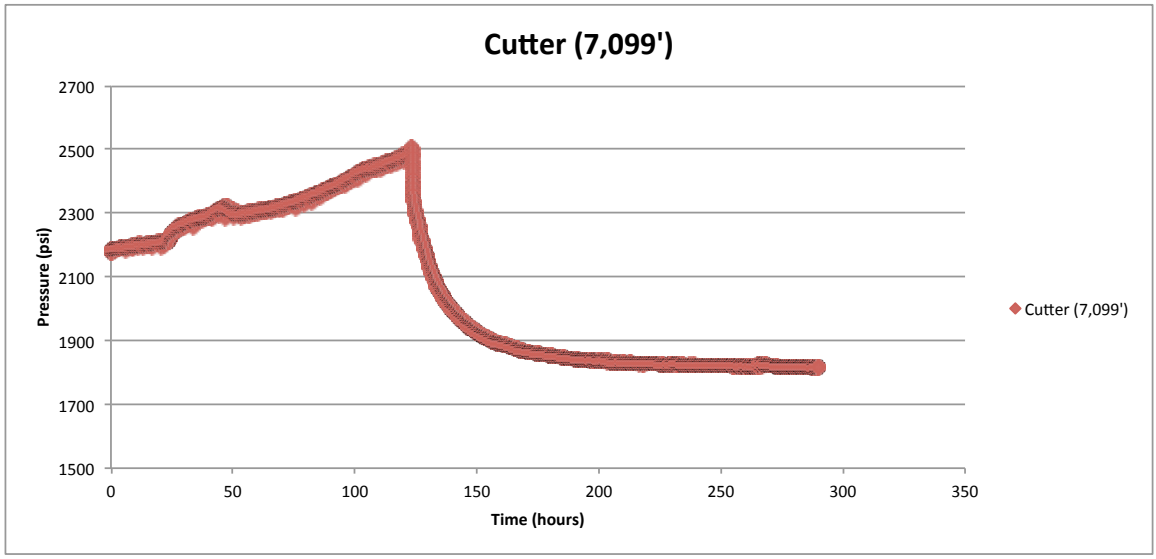


Figure 2.9 Cutter LLNL pressure change through time.

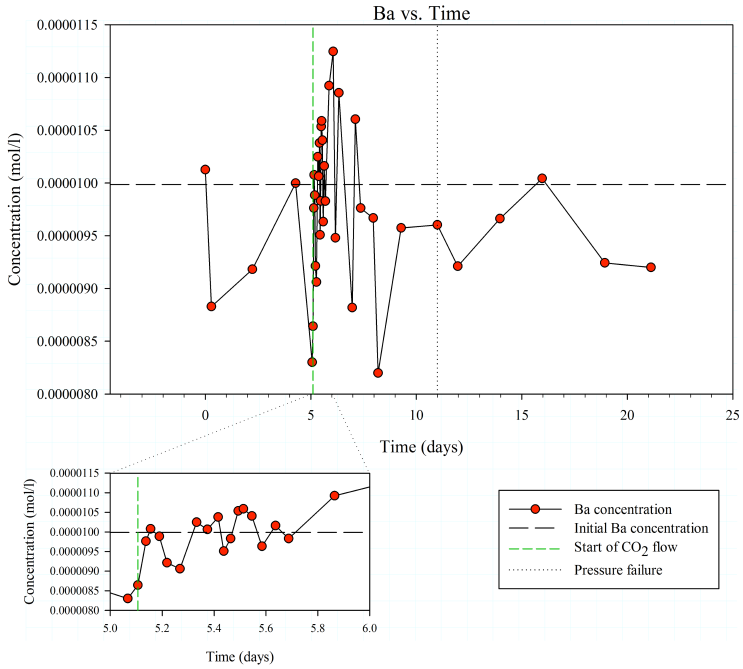


Figure 2.10 Variation of Ba^{2+} concentration through time.

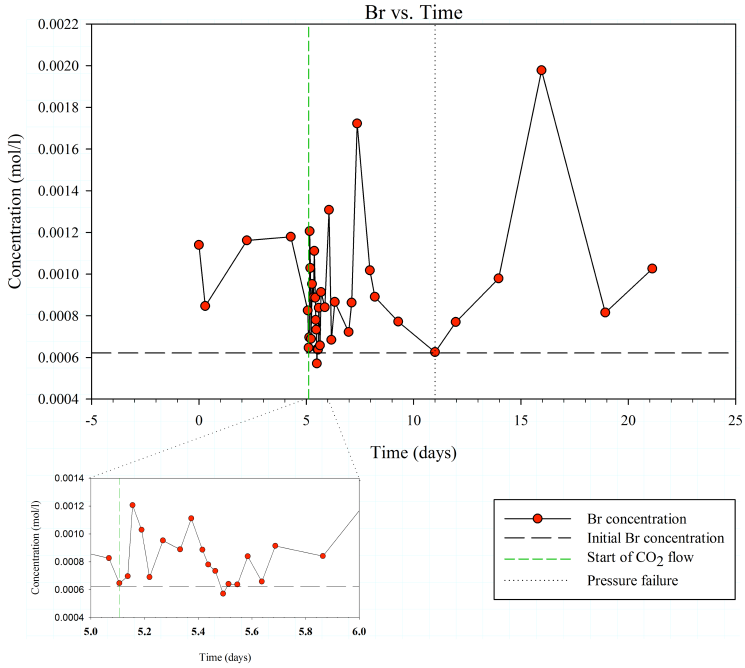


Figure 2.11 Variation of Br^- concentration through time.

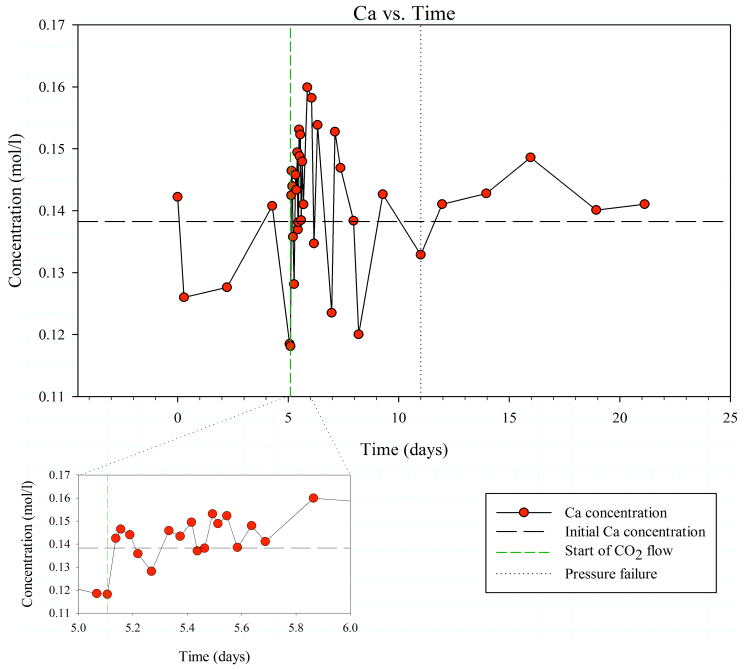


Figure 2.12 Variation of Ca^{2+} concentration through time.

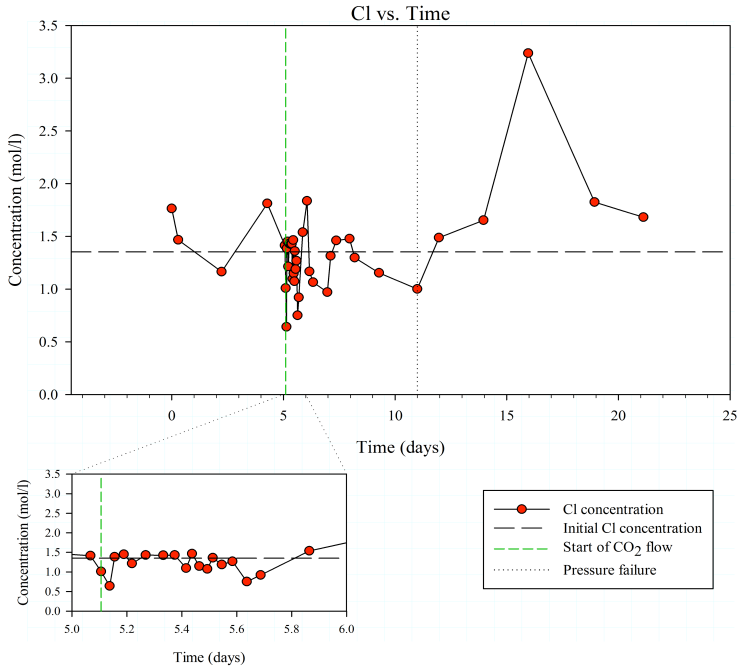


Figure 2.13 Variation of Cl^- concentration through time.

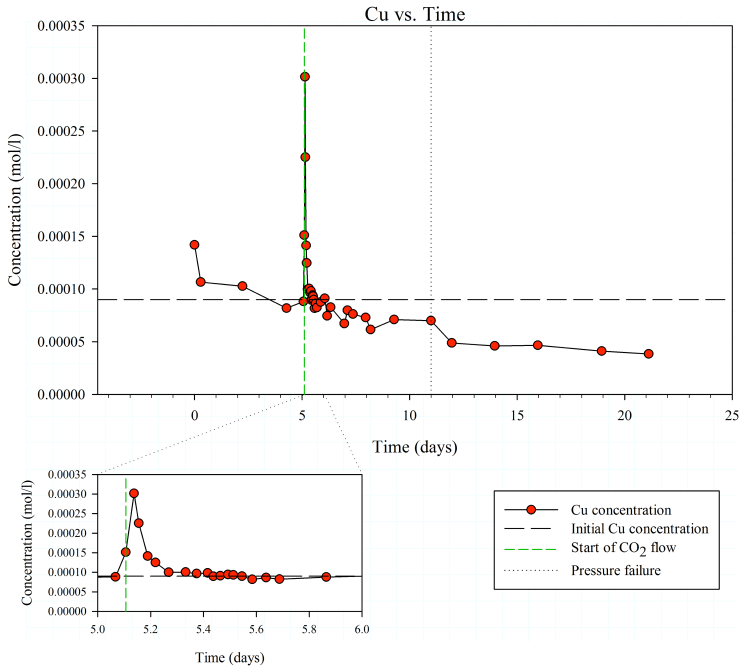


Figure 2.14 Variation of Cu^{2+} concentration through time..

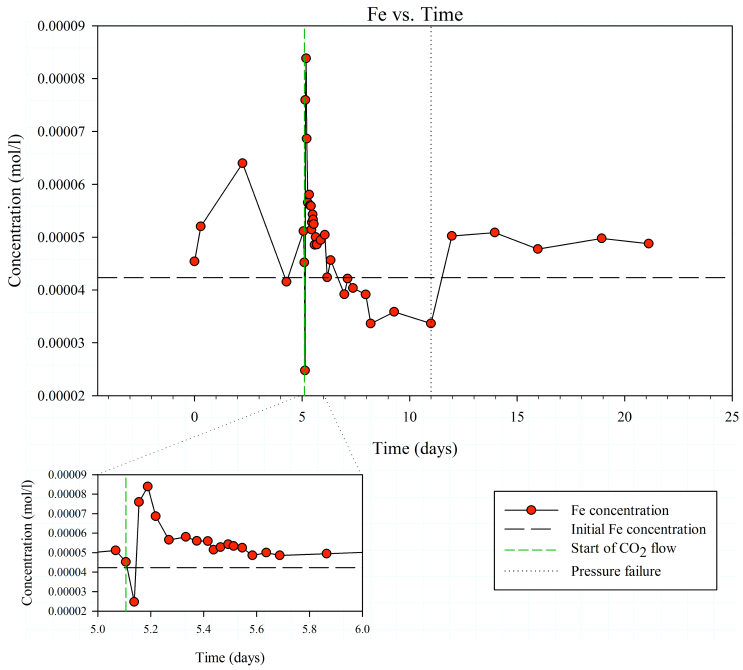


Figure 2.15 Variation of Fe concentration through time.

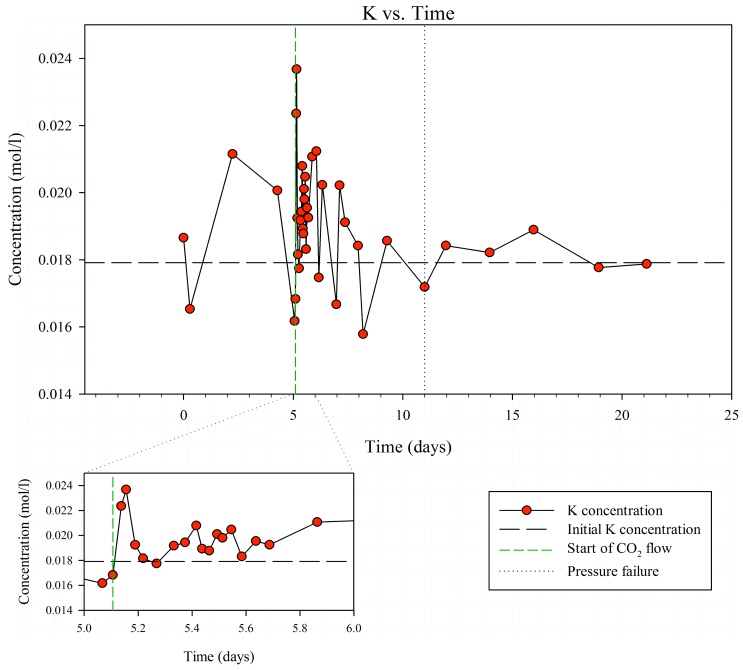


Figure 2.16 Variation of K^+ concentration through time.

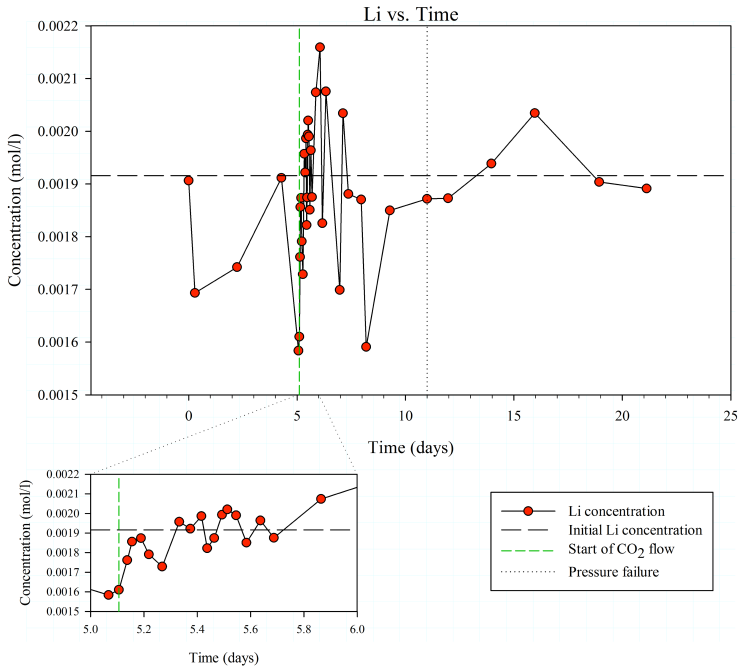


Figure 2.17 Variation of Li^+ concentration through time.

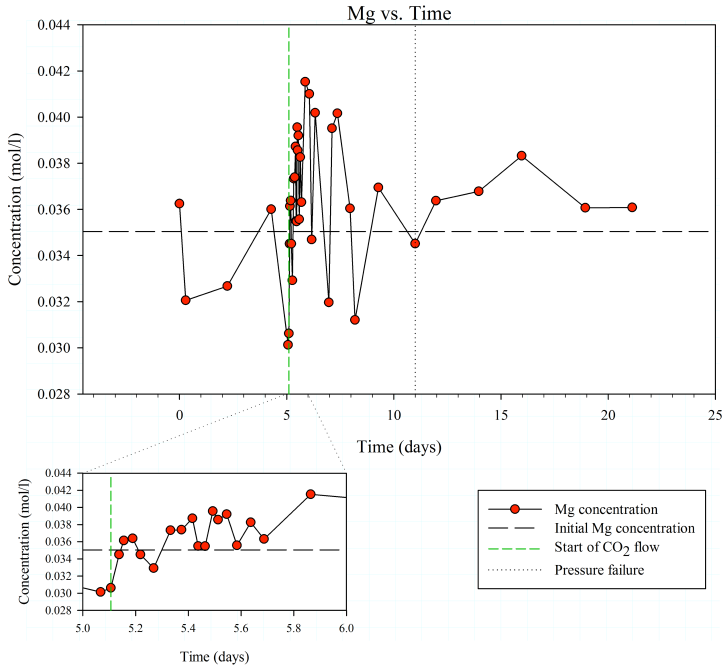


Figure 2.18 Variation of Mg^{2+} concentration through time.

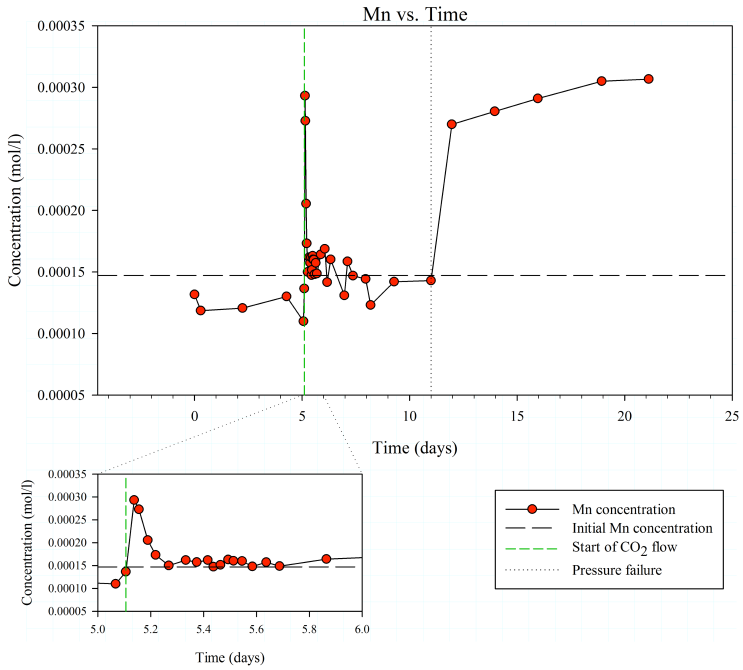


Figure 2.19 Variation of Mn concentration through time.

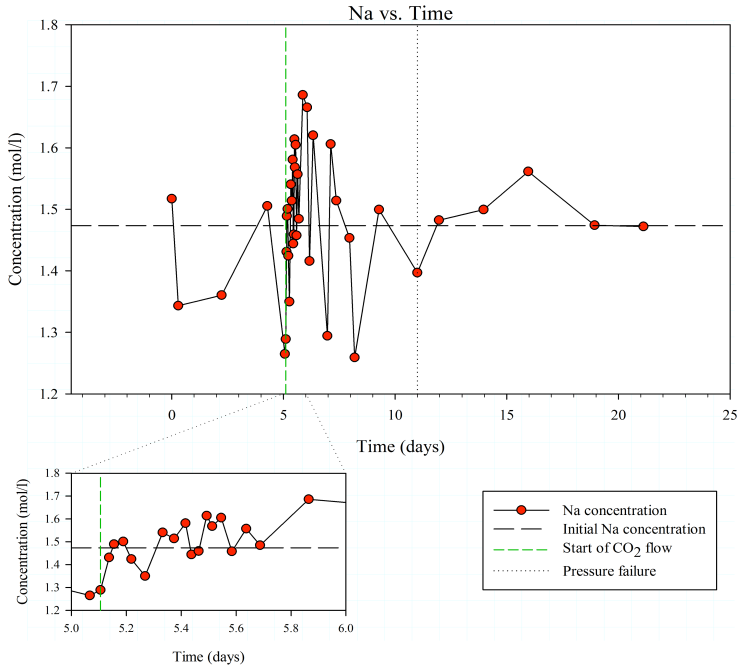


Figure 2.20 Variation of Na^+ concentration through time.

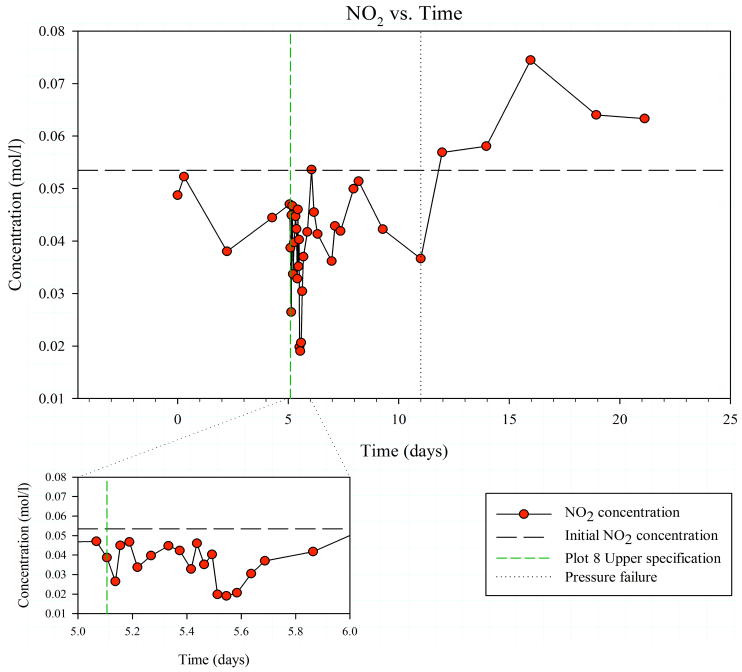


Figure 2.21 Variation of NO_2^- concentration through time.

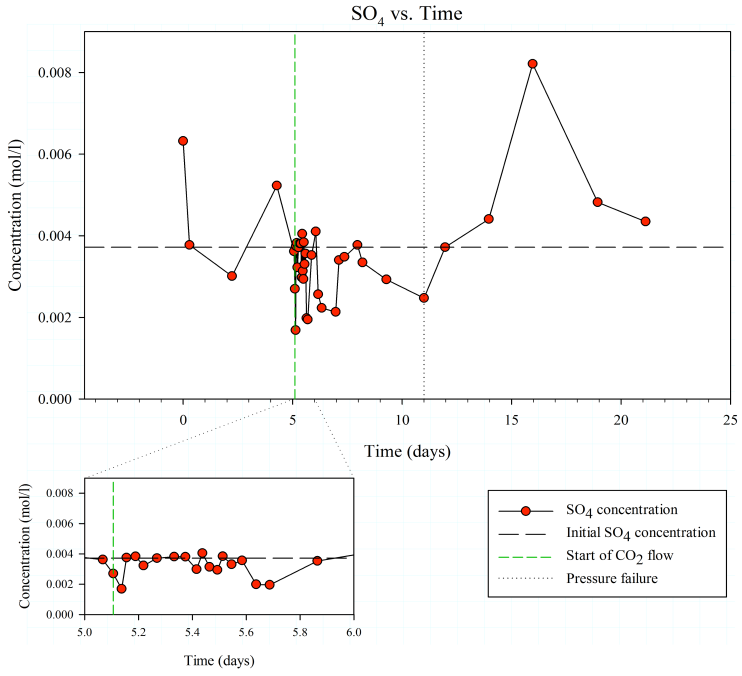


Figure 2.22 Variation of SO_4^{2-} concentration through time.

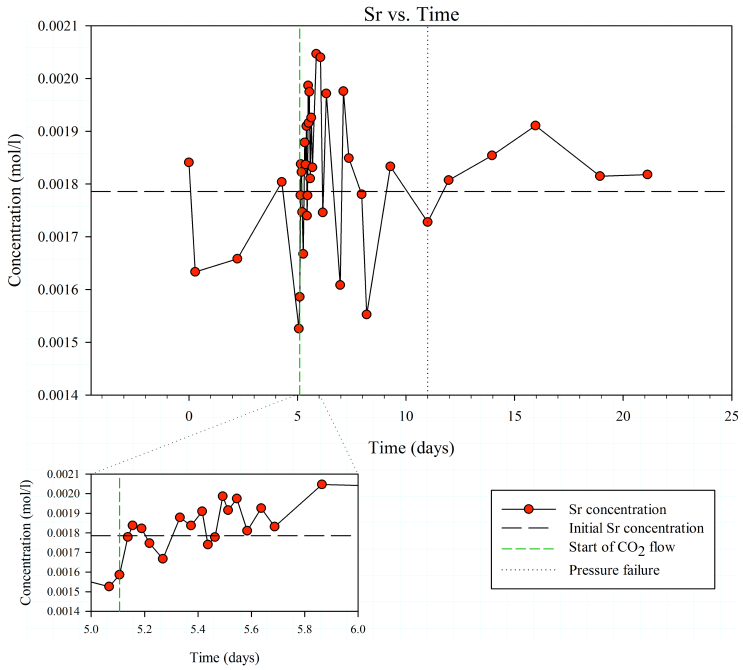


Figure 2.23 Variation of Sr^{2+} concentration through time.

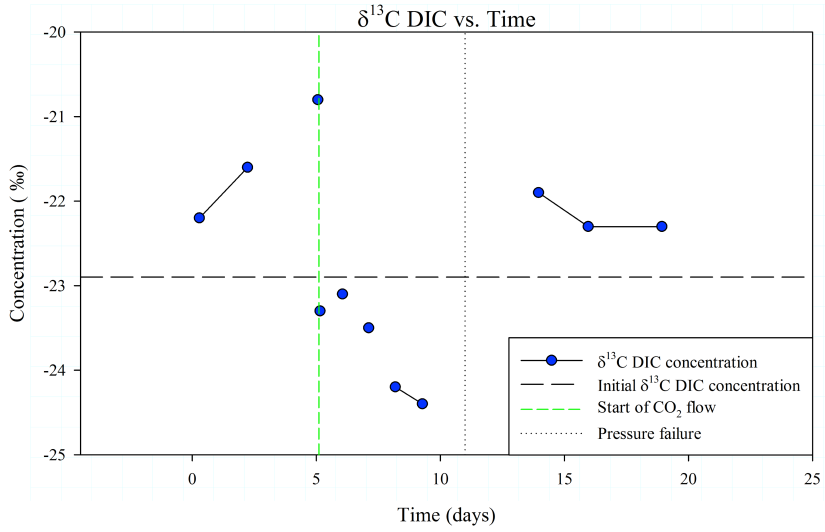


Figure 2.24 Variation of $\delta^{13}C$ (DIC) concentration through time.

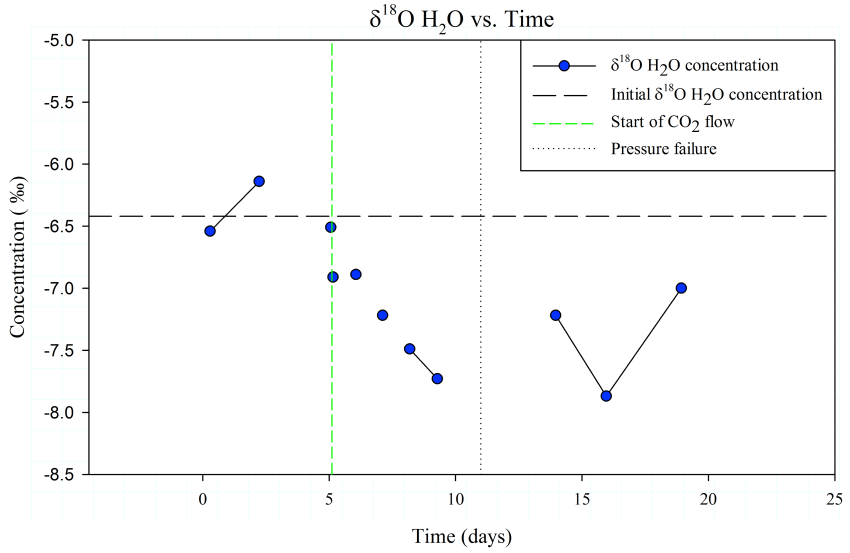


Figure 2.25 Variation of $\delta^{18}O$ concentration through time.

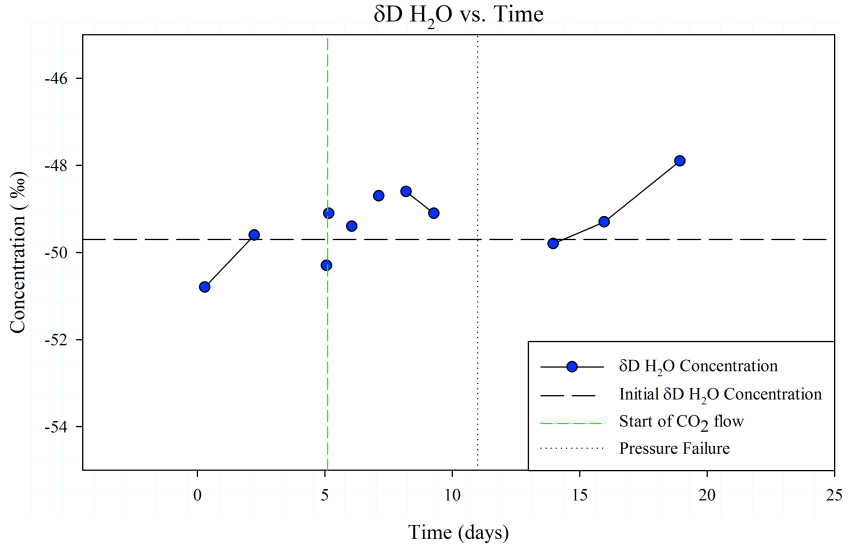


Figure 2.26 Variation of $\delta^{2}H$ concentration through time.

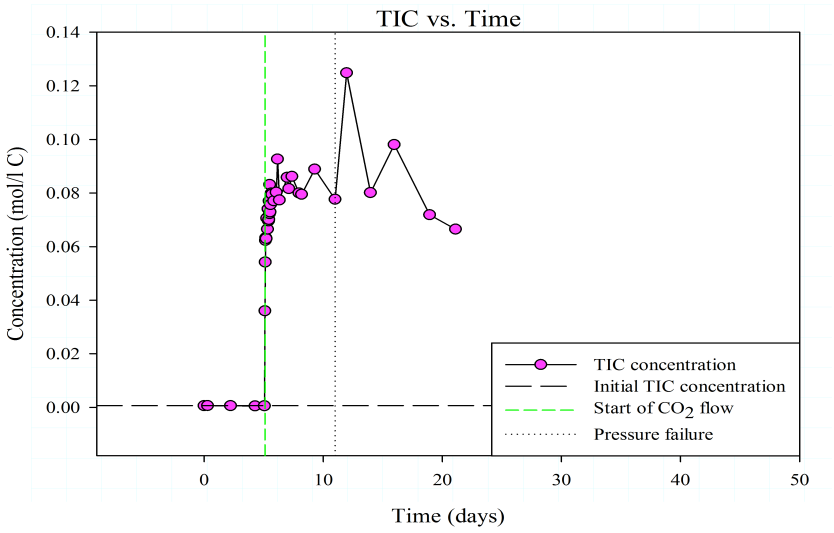


Figure 2.27 Variation of total inorganic carbon (TIC) concentration through time.

Ca^{2+}, Mg^{2+}, Na^{+}, Li^{+}, Sr^{2+}, Mn, Cl^{-}, SO_4^{2-}, Br^{-}, NO_2^{-}, δ^2H and TIC all show a general increase in dissolved concentrations (Figure 2.12, Figure 2.18, Figure 2.20, Figure 2.17, Figure 2.23, Figure 2.19, Figure 2.13, Figure 2.22, Figure 2.11, Figure 2.21, Figure 2.26, Figure 2.27), while K^{+}, Fe, $\delta^{18}O$, $\delta^{13}C$ (DIC) show an overall decrease in dissolved concentrations with Ba^{2+} showing no overall change (Figure 2.16, Figure 2.15^{+}, Figure 2.25, Figure 2.24). All cations, except Fe, show initial increases in dissolved concentrations upon the introduction of CO_2 flow. Fe decreases over the first 30 minutes with the start of CO_2 flooding, and then drastically increases in dissolved concentrations for the next hour. Fe and Mn both show a similar reactive trend after the first 30 minutes of CO_2 flow, and then steadily stabilized out. At pressure failure, T = 11 days (265 hours), there is a drastic increase again in dissolved concentrations for both species.

All anions, except Br^{-}, decrease over the first 30 minutes, then increase in concentration and vary over the rest of the experiment. Total Inorganic Carbon shows a very quick increase in dissolved concentrations and steadily increases through time

(Figure 2.27). With sampling being sparser for isotopes, trends become more difficult to detect. $\delta^{18}O$, and $\delta^{13}C$ (DIC) both show initial increases in depletion followed by enrichment with time (Figure 2.25, Figure 2.24). $\delta^{13}C$ (DIC) shows much faster depletion in relation to $\delta^{18}O$. $\delta^{2}H$ shows enrichment upon CO_2 injection followed by very slight depletion (Figure 2.26).

Pressure failure that occurred during the experiment had a significant effect on all the anions and a few cations (Fe, Mn) along with $\delta^{2}H$, and TIC. All of these species, except Fe, experienced the highest concentrations following pressure failure. Cation concentrations did increase over the course of injection, however these concentrations did not vary as significantly as other species did at pressure failure.

Pressure breakthrough can be inferred in two general ways. The first way is when the inlet injection pressure equals the outlet pressure. The second way is when the outlet pressure is close to the inlet pressure and does not change for a long period of time. If a 20 psi difference can be representative of pressure breakthrough then the first time the outlet pressure was within 20 psi of 1,800 psi was on 07/05/14 at 11:50 pm.

2.3.2 Cutter X-ray computed tomography analysis

In Figure 2.28 compares the pre reaction stacks (first column) to the low threshold stacks (middle column) and to the high threshold stacks (last column). Full-size and additional pictures of the scans are included in Appendix B. Photos of the core plug are presented at the top of Figure 2.28 to show reaction pathways and chert nodule locations. Pre-reaction tomography scans indicate dominant porosity occurring between mineral boundaries. This is seen on the outlet side as a “V” shape, which is within the chert nodule. Porosity is highlighted on the scans as occurring between the chert nodule

and the dolomite. Figure 2.29 shows the inlet side of the core and the dominant fluid pathway that formed. As the chert nodule fades, on the inlets side, and diminishes inside the core, the apparent pre reaction porosity increases through the core. The low threshold example (blue images, middle column) indicates a dominant wormhole, or preferential pathway, occurring along the mineral boundary. The high threshold example shows the same preferential wormhole, but due to the higher threshold indicating additional pore space the wormhole is less visible as it is hidden behind the additional pore space.

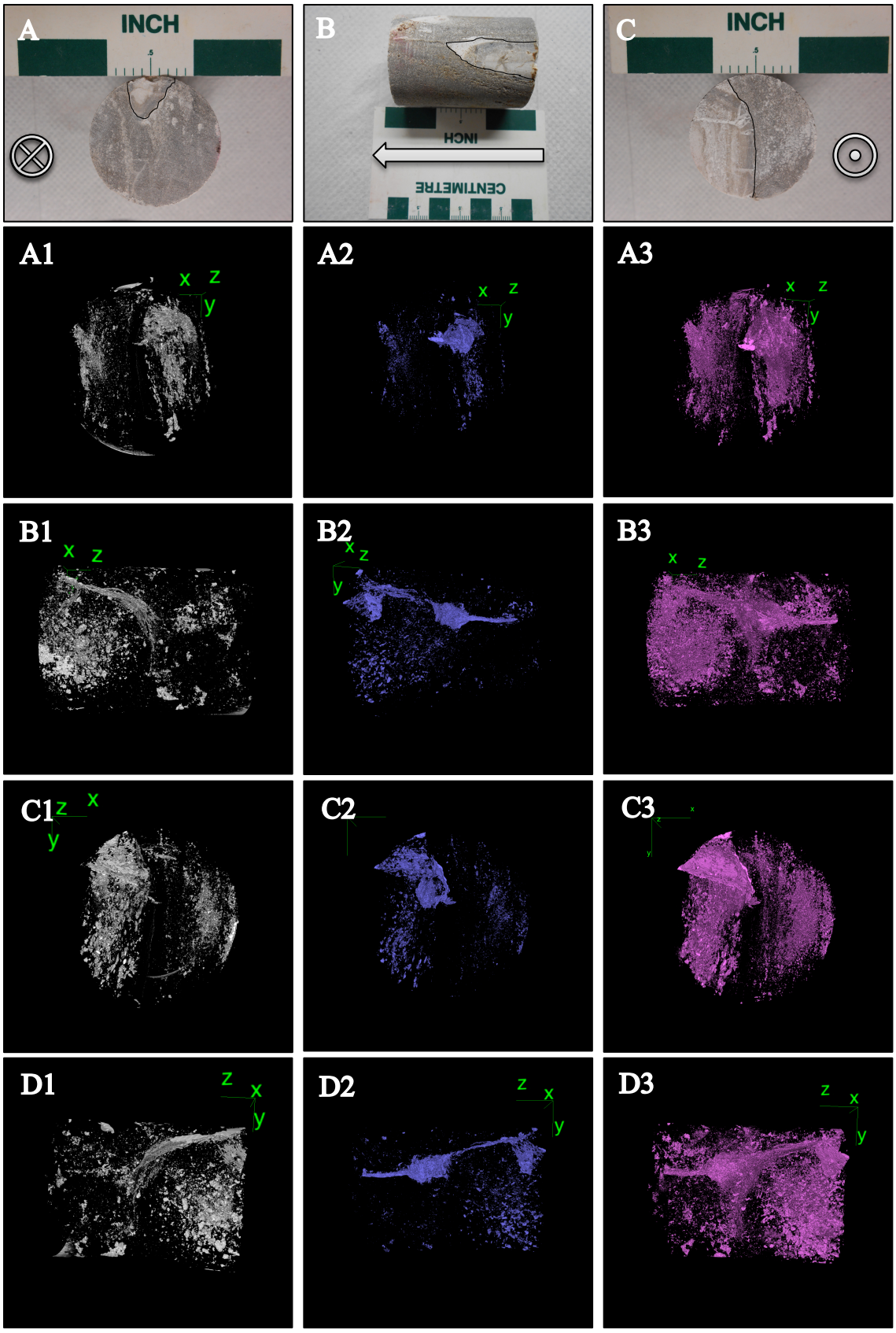

A
INCH
B
INCH
CENTIMETRE
C
INCH
A1
x z
y
A2
x z
y
A3
x z
y
B1
x z
B2
x z
y
B3
x z
C1
z x
y
C2
C3
D1
z x
y
D2
z x
y
D3
z x
y

Figure 2.28 Cutter 20-9 core and 3D XRCT images. All (A) pictures indicate inlet side, all (B) pictures indicate same point of view along with flow direction, all (C) images indicate outlet side, and all (D) images indicate backside of (B). All x1 images indicate pre-injection pore space, all x2 images indicate low threshold pore space, and all x3 images indicate high threshold pore space. The chert is outlined in black in photos A, B, and C.

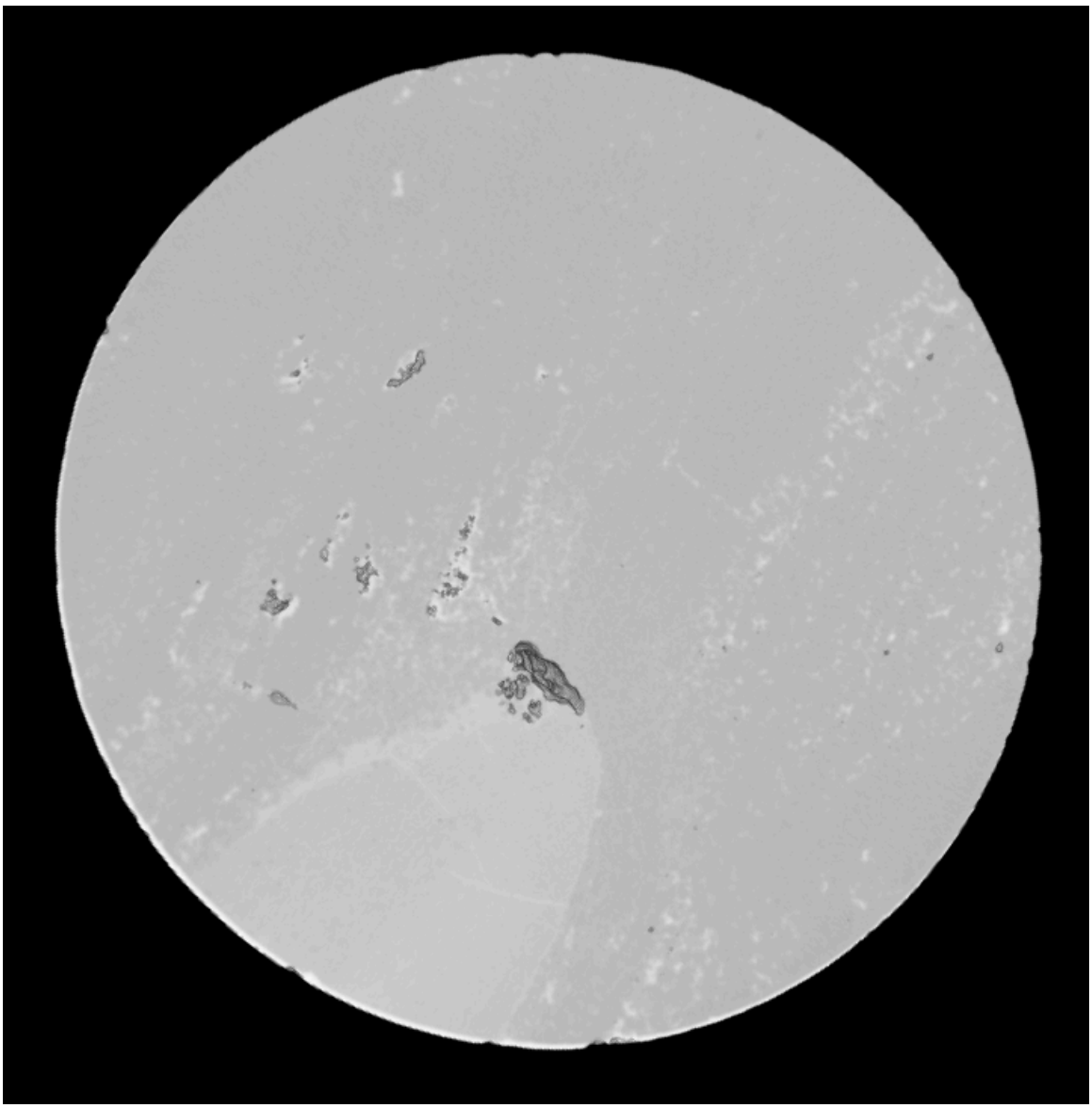


Figure 2.29 Post XRCT image of the inlet side of the core. Fluid flow preferentially followed the darker gray areas, especially between mineral boundaries as can be seen in the center of the image. Chert is the lighter of the gray colors and occurs in the bottom right of the image in a half oval outline.

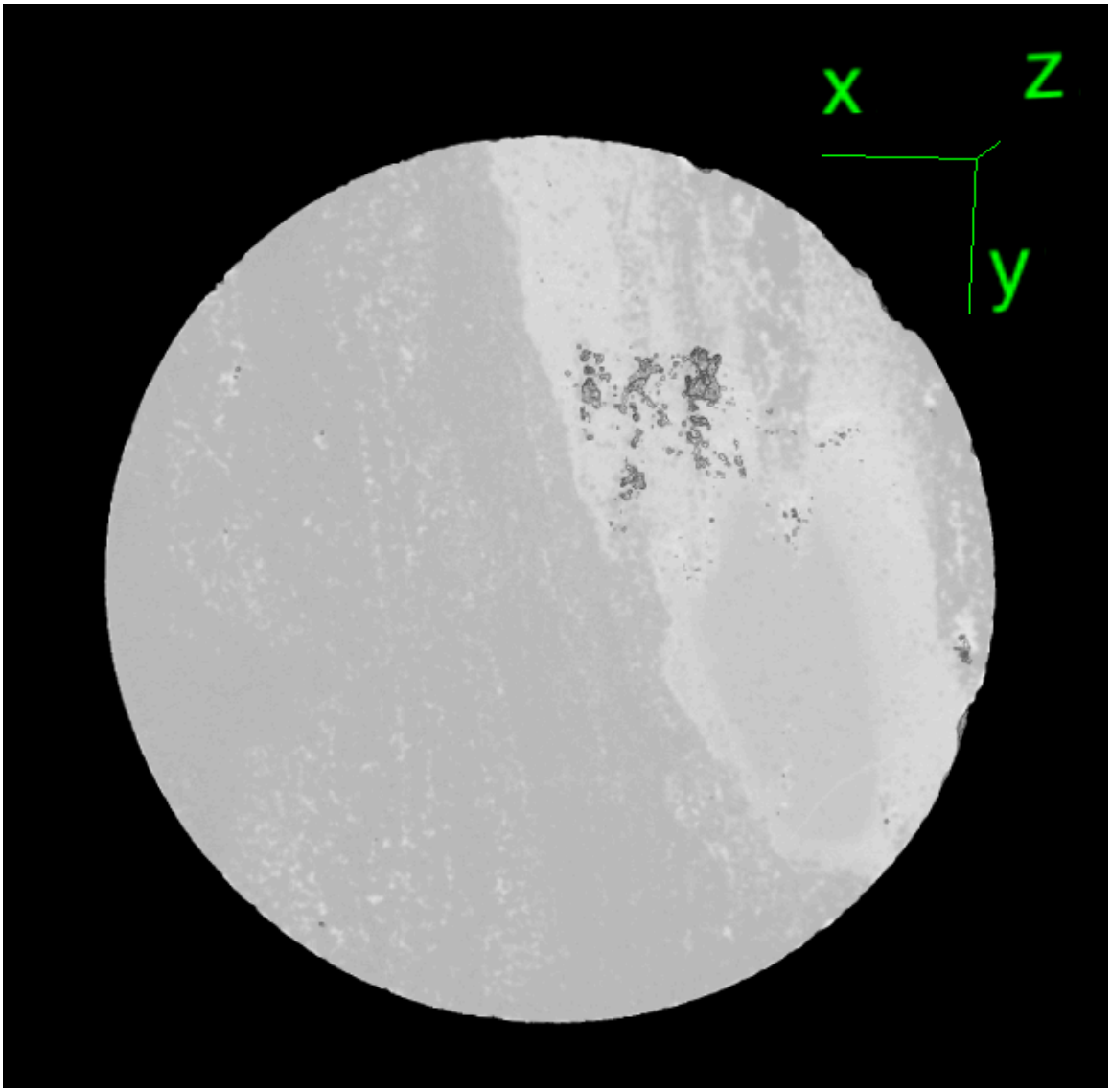


Figure 2.30 Post XRCT image of a middle slice of core looking towards the outlet. Chert is outlined as the lighter color occurring in the right half of the image.

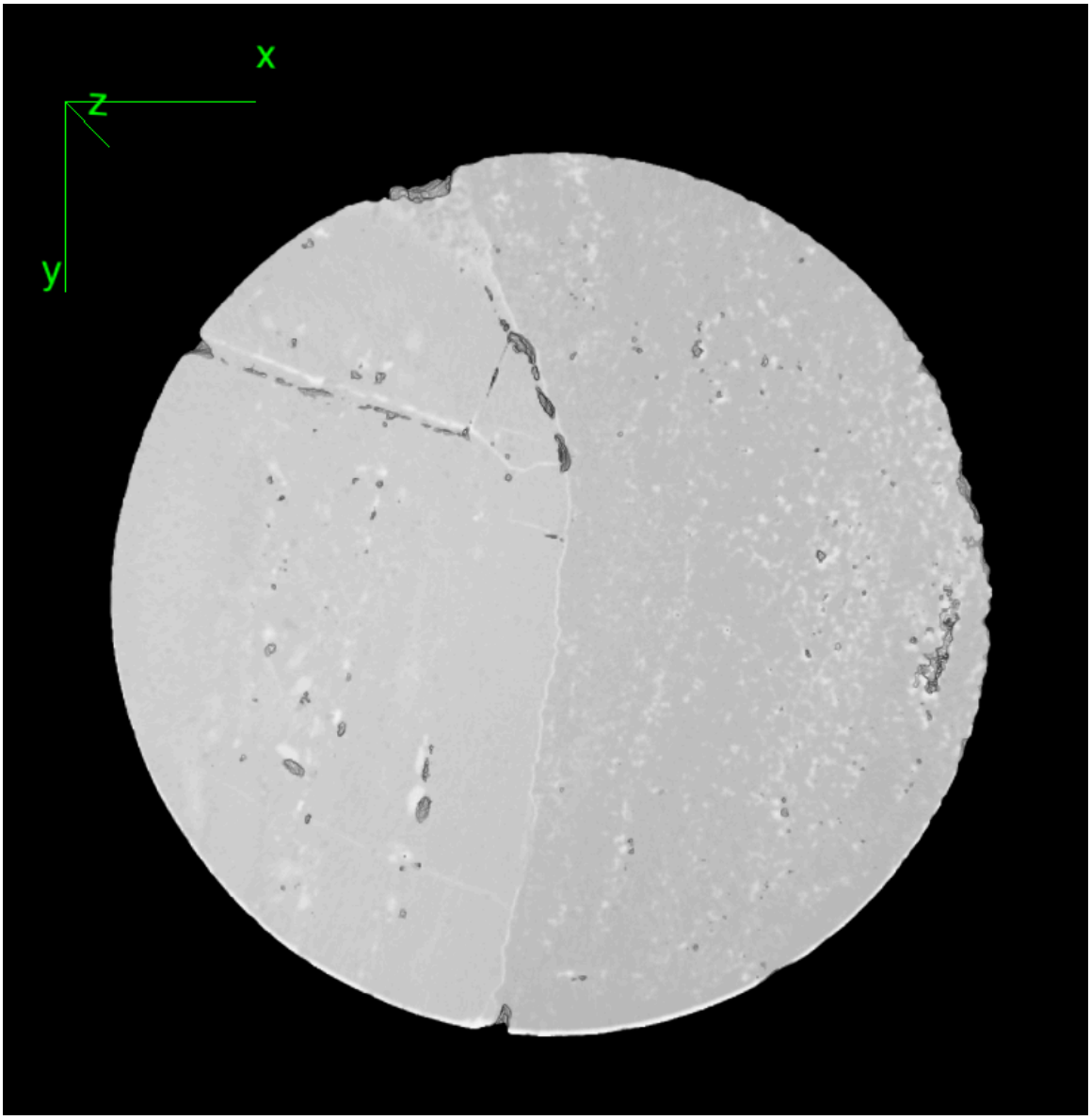


Figure 2.31 Post XRCT image of the outlet side of the core. Chert is outlined as the lighter color occurring in the left side of the image.

2.4 Discussion

2.4.1 Flow-through experiment

Original brine from swab 4 was sampled twice post filtration; once before CO_2 saturation phase, and once post-CO_2 saturation phase. These values were used to establish baseline concentrations for pre-CO_2 flow (Figures 2.8-2.21). During the start of CO_2 flow

and for the first two samples taken (starting at 5.14 days (123.30 hrs.), an increase in all cation concentrations was noted, except Fe, which showed an initial decrease. All anions show an initial decrease in concentration with time (starting at 5.14 days (123.30 hrs.), except for Br^-, which showed an initial increase in concentration. TIC concentration showed an increase at the start of CO_2 flow and remained relatively constant (average 917 mg/l C) through the whole experiment until the pressure failure occurred at day 11 (Figure 2.27). Initial increases in dissolved concentration of Ca and Mg is expected due to the decrease in pH that is caused by the injection of CO_2, which sequentially allows for the dissolution of the dolomitic core plug.

Wang et. al., 2013 investigated the reactivity of dolomite with H_2O-saturated supercritical carbon dioxide to varying temperatures, pressures, and time periods. The study differs from this study in that reservoir conditions were studied at both 55-110°C, 25 MPa and 220°C, 25 MPa, while this study used reservoir conditions of 60°C and 3 MPa. Experimental time also differed in that Wang et. al., used reaction times of 96 and 164 hours, while this study was concluded at 290 hours. Wang et. al. found that dolomite was unreactive to anhydrous supercritical carbon dioxide, but was dissolved and mineral precipitation occurred with H_2O-saturated supercritical carbon dioxide. The main drivers of dissolution and precipitation were found to be temperature and reaction time. These factors controlled the extent of mineral re-precipitation along with the composition and morphology. Relative permeability and the permeability of the Arbuckle along with the contact line between phases and contact angle of the CO_2 could be affected by the amount of dissolution and mineral re-precipitation that occurs.

Redox sensitive species all show variation throughout the experiment. These species generally only showed high initial change variability with the introduction of CO_2, however showed little and decreased reactivity until pressure failure occurred. One study found alkalinity and divalent metal cations dissolved from silicate minerals to be the rate limiting steps in carbonate precipitation (Worden, 2006; Pauwels et al., 2007; Kampman et al., 2014). Some redox species only show initial change in concentration following the start of CO_2 (Cu, Zn), while others show substantial variation at both the start of CO_2 flow and at the pressure failure (e.g. Mn, Fe_{Total}). This variation seen with some ionic species could indicate further beneficial chemical reactions occurring if injection is discontinuous. If important carbonate precipitating species shows heightened or renewed reactivity to CO_2 injection then alternating flow of the CO_2, similar to water-alternating-gas (WAG) techniques used for secondary and tertiary hydrocarbon recovery, could allow for increased preferential dissolution and eventual precipitation of these species.

Iron and SO_4 are both potentially important species for mineral trapping, and can form siderite. Siderite precipitation depends on the amount of sulfide and iron or oxyhydroxides present, along with bicarbonate. The reductive dissolution rate of iron (Fe^{3+} to Fe^{2+}) could determine the amount of siderite precipitation (Lammers et al, 2011). If a sufficient amount of iron is present, addition of a reducing agent such as SO_2 can be injected along with CO_2. This common flue gas byproduct has been shown to sufficiently reduce iron and allow for siderite to form (Palandri et al., 2005; Garcia et al., 2012). With this experiment Fe shows an initial decrease in concentration (5.11 – 5.14 days) followed by a rapid increase (5.14 – 5.19 days), and thereafter shows little reactivity until

pressure failure (11 days). SO_4 shows an initial decrease in concentration (5.11 – 5.14 days), followed by an increase in concentration (5.14 – 5.19 days), and thereafter shows variability with a significant increase in concentration at pressure failure (11 days). During field sampling there was no H_2S detected or measured at Cutter, but there was H_2S detected at Wellington. The rapid increase in the concentration of Fe (5.14 days – 5.16 days) and small increase in the concentration of SO_4 over the same time period could indicate oxidation of H_2S, released from the dissolution of pyrite. While no pyrite was visibly seen on the exterior of the Cutter core, possible small amounts of pyrite could be found within the core and explain the Fe and SO_4 trends (Figure 2.15, Figure 2.22). Pyrite was possibly observed within fractures of the XRCT scans of the Cutter core at the depth of 7,110 ft., and this core is only 12 ft. deeper than the experimental core used. With the presence of pyrite or H_2S gas within the formation of injection it could allow Fe (III) to be reduced into Fe (II) in order to precipitate siderite.

The greatest variability in species concentrations, excluding pressure failure, coincides with the sharpest decrease in injection pressure. This is especially true for the redox-sensitive species, and may indicate that these species will have the greatest reactivity following the front of the outward progressing CO_2 plume. From these experimental results the highest reactivity could be seen by the redox species as the plume migrates both vertically and horizontally, but this reactivity will not be as great within the plume itself. This is inversely related to all the species that showed a smaller and more stable reactivity change to the CO_2, e.g., Ca, Mg, Sr, Na, Ba, Li, where these elemental species would exhibit the greatest reactivity within the plume and on a much longer time scale. Carbonate minerals will still show the greatest change in response to

CO_2 injection within the Arbuckle, yet the quickest relative change in concentrations might be best seen with the redox-sensitive species. These redox species, however may only exhibit high initial change followed by little reactivity. Transport and dissolution rates of CO_2 will determine the reactivity of many species. While surface area of the minerals is unknown, the reactivity and dissolution or precipitation will further depend on how much surface area of the mineral comes in contact with the acidified brine. Precipitation via ionic trapping will also be limited by the transport and diffusion of the CO_2 into the brine, along with the rates of CO_2 flow and dissolution (Kampman et al., 2014).

Initial post XRCT scans show that dissolution took place predominantly along the dolomite/chert boundary (Figure 2.28, Figure 2.29, Figure 2.30, Figure 2.31). Injection occurred on the side with the smaller chert nodule with XRCT scans showing a possible preferential pathway developing along this mineral boundary and continuing vertically along the same path throughout the core. Injected brine could preferentially prefer these mineral boundaries as pathways through the core. Smith et al. (2012) mentions that on the microscale, brine will exploit preexisting or constructed fractures present as preferential dissolution pathways. These pathways are preferred due to the ease of dissolution and their higher permeability. Precipitation and dissolution can alter these flow pathways and initiate new flow regimes. Renewed reactivity seen occurring at the pressure failure could indicate reactivation of secondary flow channels, or the creation of new ones. Initial fluid flow could have created a wormhole that follows the mineral boundary with smaller channels or fingers forming off the main chute. These smaller fingers, which eventually terminate, increased the available surface area for CO_2-brine-

rock interactions to occur. As the main channel and fingers formed, redox sensitive species reacted quickly; however with no new channels created, the reactivity of these species decreased. When pressure failure occurred, it could have allowed for precipitation within the pore throats at the origins of these fingers. As pressure was ramped back to the normal injection rate, new fingers or channels could have been created, and accounted for the sometimes-drastic increase in dissolved concentrations of certain species. If alternating pressure of injection can allow for new channel creation and thus increased mineral surface area interactions, it could allow for increased CO_2 trapping to occur.

Three-dimensional renderings of the XRCT stacks do show a dominant preferential pathway that developed along the mineral boundary of the chert and dolomite. The inlet and start of the wormhole can be seen in Figure 2.29. This wormhole followed the first chert mineral boundary till the chert faded into dolomite about half way through the core (Figure 2.29). This mineral transgression caused the CO_2 to exploit pore space within the dolomite and chert mesh. Once the injected CO_2 found the backside chert nodule the flow pathways merged and formed a dominant fluid path within the chert.

In a similar experiment investigating evaporates Smith et al., (2012) showed that preferential dissolution of the dolomitic core occurred and allowed for a localized channel to develop providing an overall increase in bulk permeability. Porosity and microfractures drove this channel creation. Anhydrite found within the core was unreactive to the injected CO_2 brine. Dissolution of the reactive dolomite allowed for the release and transport of the unreactive anhydrite, contributing to the increase in porosity and permeability. Fracture orientation and formation mineralogy need to be well

characterized in order to understand the creation and progression of these localized channels.

Our experiment showed pressure breakthrough occurring around 255 hours. Pressure breakthrough exhibits little reactivity with the elemental constituents, and was defined by a 20psi pressure differential from the injection and outlet pressures. A pressure failure occurred when the computer program dropped the injection pressure from 1800 psi to 165 psi. This was not planned, however water samples were taken pre and post failure and show increased dissolved concentrations with most species. Pressure failure can also be related to the renewal of CO_2 injection. As pressure was increased back to 1800 psi, elemental species began to react. Reactions especially seen with redox sensitive species have implications for alternating injection, meaning start-stop-start CO_2 injection. Depending on the species of interest for mineral trapping or dissolution, along with the formation mineralogy, alternating injection could allow for renewed activity of redox sensitive species. Without alternation these species will only showed reactivity with the introduction of the CO_2, followed by diminished reactivity. These species will only be active on the CO_2 plume front, and will not be reactive within the plume itself. Depending on the speed of the plume migration, little to no reactivity within the plume means that little dissolution or reactivity will occur with the redox sensitive species. This is important if these species are of interest for CO_2 storage. Major elemental species, with the exception of sulfate and chloride, showed continual reactivity throughout the progression of the experiment. Some species showed slight increase in dissolved concentrations, but not to the extent of the redox species. This means that the major elements will be reactive within the plume and not show preference with either continual

or alternating injection. These elements, Ca and Mg, are the two most important for carbonate precipitation. The renewal in activity seen with all elemental species could be due to new channel creation or dissolution of precipitates that formed after the decrease in pressure. With the pressure failure or decrease in pressure it allowed for a calmer environment to exist within the core. This could have allowed for dissolved species to precipitate out. With the ramping back up of pressure this precipitate could have dissolved and accounted for the increase in dissolved concentrations. This precipitate could have also blocked the preexisting flow pathways and caused new channel development to occur. With new channels, the fluid would be able to interact with unreacted minerals elsewhere within the core and could account for the increased in dissolved elemental concentrations. CO_2 pressure failure caused a degassing of the CO_2 from the brine. Since the fluid injection rate was held constant and the pressure below the pCO_2 needed to keep the gas within the brine only the brine was flowing through the core. As pressure was increased residual gaseous CO_2 that was trapped due to degassing, allowed for an increased pH environment. This over acidification allowed for greater dissolution of the carbonate core. The increased amount of dissolution allowed for unreacted minerals to come in contact with the acidified brine. This could have attributed to the increase seen with the concentration of dissolved species. Depending on the species of interest along with the formation mineralogy careful experimentation needs to be done to determine if continual or alternating injection would allow for the greatest amount of trapping to occur.

2.5 Conclusion

The extent of carbonate dissolution was investigated utilizing cored rock and formation brine from the Arbuckle injection zone in Kansas. Hydrochemical analysis of brine collected post injection showed that the major ions (Ca, Mg, K, Li, Na, Sr, SO_4, Cl) reacted initially and displayed continual reactivity throughout the experiment. These ions would exhibit continual reactivity as the plume migrated and the CO_2 was continually injected. As seen with the pressure failure, the majority of these ions showed renewed reactivity and in many cases exhibited the highest concentrations post pressure failure. The renewal in activity could allow for greater solubility trapping and CO_2-water-rock interactions to occur if CO_2 injection was discontinuous or intermittent. Redox sensitive ions generally showed high reactivity with CO_2 injection followed by a general decrease in activity up to pressure failure (Cu, Fe, Mn). This behavior could indicate that the greatest reactivity of these redox sensitive species could occur at the forefront of the CO_2 plume, with little reactivity occurring within the plume. These species showed the greatest renewal in reactivity after the pressure failure. This rejuvenation of species reactivity again supports the idea of altering CO_2 injection into the Arbuckle.

XRCT scans indicate that CO_2 flow preferentially preferred mineral boundaries as dissolution pathways. The Arbuckle is dominantly dolomitic with intermittent chert layers and this core is believed to be representative of the entire injection interval. The preference for the boundary between chert and dolomite for fluid flow is due to the weaker matrix and greater porosity present between these minerals. Three-dimensional renderings of the XRCT scans show that a wormhole developed and followed the dolomite-chert boundary until the chert discontinued half way through the core. With the

absence of the mineral boundaries the flow pathways transitioned into a stable dissolution front exploiting other areas of increased porosity and permeability. As the CO_2 flow encountered the other larger chert nodule on the back or outlet side of the core, some of the fluid pathways merged and reformed the wormhole. Varying thresholds show differences in inferred porosity. The lower threshold clearly shows the wormhole as it progresses through the core. The higher threshold, representing greater perceived porosity, still shows the wormhole but additionally shows an initial dissolution front occurring in the first half of the core. Pre injection scans show the increased porosity in the first half of the core only.

Inferring porosity based off of XRCT scans can be difficult distinguishing porosity from rock due to the closeness in colors. Image voxel size can also overlook micro-porosity and underestimate fluid pathway development. Heterogeneity of the proposed injection interval could partially determine if a stable dissolution front or preferential pathway is the preferred mode of CO_2 transport.

Acknowledgements and Disclaimer

This work was performed under the U.S. Department of Energy and National Energy Technology Laboratory Contract #FE0002056. Experimental work and analysis was conducted at Lawrence Livermore National Laboratory. Further analysis was completed at Kansas State University, University of Kansas, and the Kansas Geological Survey.

A version of this Chapter is intended for publication in the journal Environmental Science and Technology.

Chapter 3 Conclusion

Geologic carbon storage is potentially one of the most feasible methods to decrease the global atmospheric concentration of anthropogenic carbon dioxide. The dependence on fossil fuels will continue to grow with the ever-increasing world population. While green energy and some renewables are still in their infancy, they have yet to become efficient enough to detract from the commanding use of fossil fuels. Developing countries that have some of the largest growing populations and economies will not be initially concerned with greenhouse emissions, nor will they be able to afford the more expensive alternatives to fossil fuels. Carbon storage within deep geologic repositories could allow for the net decrease of carbon dioxide emissions, if progressive development and enhancement of green or renewable alternatives continue. As part of the Department of Energy's regional carbon sequestration partnership, Kansas is being investigated to develop the technology and to determine the feasibility for CO_2 storage within the regional saline Arbuckle aquifer. Sedimentary basins and their commonly associated saline aquifers hold the potential for the greatest amount of CO_2 storage, as so far discussed in various scientific reports and literatures. The high permeability, porosity, salinity, and total dissolved solids can allow for the necessary chemical reactions to occur that safely trap the injected CO_2. The depth and thickness of the Arbuckle along with other qualifiers make CO_2 storage within the unit exceedingly plausible. Geochemical and hydrochemical analysis of the area needs to be well understood. Vertical connectivity, formation brine history, and an in depth characterization of the formation water through ionic and isotopic analysis can help determine the potential for CO_2 injection. Flow-through experiments can simulate a small-scale injection by recreating an

in-situ environment that can be monitored and assessed. These flow-through experiments can provide crucial information of how the system will react to CO_2 injection by injecting CO_2-equilibrated formation brine into a cored rock from within the formation. This work is both a cross comparison of the hydrochemistry of Cutter and Wellington, along with an investigation of a core-flooding experiment done with core plug and brine from Cutter.

Within Wellington the low porosity baffle zone that was confirmed by nuclear magnetic resonance logs, porosity measurements, and hydrochemical analysis could impede the upward migration of the CO_2 when it is injected into the lower Arbuckle. Cl^- vs. Cl/Br ratios show separation and distinct groupings of the upper and lower Arbuckle. Isotopes, $\delta^{18}O$ and $\delta^{2}H$ confirm this separation of hydraulic connectivity both by ratio analysis between Cl^-, and depth wise variation. The Arbuckle as within Wellington is not well mixed and is due to this low porosity baffle zone. Molar ionic ratios show distinct grouping of the upper Arbuckle trending towards calcite recrystallization, while the lower Arbuckle shows a trend towards dolomitization. These distinct differences between the upper and lower Arbuckle will exhibit different chemical reaction upon the introduction of CO_2. The baffle zone will not only help impede the vertical flow of the CO_2 plume but will force it to move laterally. This lateral movement will allow for prolonged CO_2-water-rock interactions to occur and will aid in dissolution and mineral trapping of the vertically buoyant gas. Even if the acidified brine dissolves and permeates this baffle zone there will still be a couple hundred feet of Arbuckle to interact with before it reaches the much less permeable and highly resistant overlying caprock.

Within Cutter there appears to be no distinct low porosity zone and instead the waters within the area are well mixed. Hydrochemical data showed no distinct groupings

of depth to indicate vertical separation. However swabs 7 and 10 could be the exception. Both of these intervals plot as distinct outliers in the majority of the figures as depicted in details in the first chapter. These intervals could have different flow regimes, or be anomalous due to sampling conditions. A well-mixed zone would allow for the injected CO_2 to move freely, all though on varying time scales, within the area upon injection. Both Cl^- vs. Cl/Br and isotopic analysis show groupings or separation based on depth. Swabs 7 and 10 plot as distinct outliers, however none of the other swabs can be grouped together based on depth. Molar ionic ratios of Cutter indicate that the upper intervals trend towards calcite recrystallization, swab 7 is distinctly trending towards dolomitization, while the rest of the samples indicate no trend.

The overall conclusion of the comparison of these two locations is that within Wellington a vertical separation exists that impedes the overall connectivity within the Arbuckle, while within Cutter there is no vertical separation and a well-mixed system is in place. Isotopic analysis of $\delta^{18}O$ vs. $\delta^{2}H$ show that Wellington has a greater range of variability with distinct zones, and Cutter has a tighter variation with no distinct zones.

Experimental core-flooding results concluded that preferential flow pathways developed along dolomite/chert mineral boundaries. Flow pathways followed the weakly bound fracture network that existed between the two mineral phases (dolomite and amorphous silica). Experimental modeling of the development of these fluid channels will depend on the inferred parent porosity of the host rock. Pressure of injection showed the largest constraint on hydrochemical change through time. Alternating injections of water and gas, or doing discontinuous CO_2 injection could allow for the development and creation of new channel formation. An increase in the surface area that comes in contact

with the acidified brine will allow for greater solubility and dissolution of the host rock to occur, thereby allowing for greater dissolution trapping and would allow for an increased number of dissolved ionic species to interact and re-precipitate with the CO_2 as carbonates. Redox sensitive species exhibited the greatest variability upon initial injection. If these species, such as Fe, were being targeted for mineral trapping then alternating the injection process would allow for the greatest amount of reactivity. These species would show the greatest reactivity at the CO_2 plume front, but would exhibit diminished activity within the plume itself. Increasing the fluid channel network through these altering of injections or injectate, would allow for the greatest reactivity and overall trapping of the CO_2.

References

Bachu, S., 2003. Screening and ranking of sedimentary basins for sequestration of CO_2 in geological media in response to climate change. Environmental Geology, 44: 277-289.

Barker, R., 2012. Geochemical and mineralogical characterization of the Arbuckle aquifer: studying mineral reactions and its implications for CO_2 sequestration. Thesis, Kansas State University.

Benson, S., and Cole, D., 2008. CO_2 Sequestration in Deep Sedimentary Formations. Elements, Vol. 4: 325-331.

Benson, S., and Cook, P., 2005. Underground geologic storage. IPCC special report on carbon dioxide capture and storage. Prepared by Working Group III of the IPCC [Metz, B., Davidson, O., Coninck, H., Loos, M., Meyer, L., (Eds.)]. Cambridge University Press: 195-276.

Black, J., Carroll, S., Haese, R., 2014. Rates of mineral dissolution under CO_2 storage conditions. Chemical Geology, In-Press.

Burnside, N., and Naylor, M., 2014. Review and implications of relative permeability of CO_2/brine systems and residual trapping of CO_2. International Journal of Greenhouse Gas Control, 23: 1-11.

Carpenter, A. 1978. Origin and Chemical Evolution of Brines in Sedimentary Basins. Oklahoma Geological Survey, Circular 79: 60-77.

Carey, J., 2013. Geochemistry of wellbore integrity in CO_2 sequestration: Portland cement-steel-brine-CO_2 interactions. Reviews in Mineralogy & Geochemistry, 77: 505-539.

Carr, J., McGovern, H., Gogel, T., 1986. Geohydrology of and potential for fluid disposal in the Arbuckle Aquifer in Kansas. USGS Open-File Report, 86-491.

Carr, T., Merriam, D., Bartley, J., 2005. Use of relational databases to evaluate regional petroleum accumulation, groundwater flow, and CO_2 sequestration in Kansas. AAPG Bulletin, v. 89, no. 12: 1607-1627.

Dubacq, B., Bickle, J., Evans, K., 2013. An activity model for phase equilibria in the H_2O-CO_2-NaCl system. Geochim. Cosmochim. Acta 110: 229-252.

Fontes, J., and J. Matray, 1993. Geochemistry and origin of formation brines from the Paris Basin, France: 2. Saline solutions associated with oil-fields. Chemical Geology, v. 109(1-4): 177-200.

Franseen, K., A. P. Byrnes, et al., 2003. Geological Controls of Variable Character of Arbuckle Reservoirs in Kansas: An Emerging Picture. Kansas Geological Survey Open-file report. Lawrence, KS, Kansas Geological Survey**:** 11.

Garcia, S., Rosenbauer, R., Palandri, J., Maroto-Valer, M., 2012. Sequestration of non-pure carbon dioxide streams in iron oxyhydroxides-containing saline repositories. International Journal of Greenhouse Gas Control, 7: 89-97.

Golubev, S., Bénézeth, P., Schott, J., Dandurand, J., Castillo, A., 2009. Siderite dissolution kinetics in acidic aqueous solutions from 25 to 100 ˚C and 0 to 50 atm pCO_2. Chemical Geology, 265: 13-19.

Hill, B., Hovorka, S., Melzer, S., 2013. Geologic carbon storage through enhanced oil recovery. Energy Procedia, 1-23

Hofmann, H., and Cartwright, I., 2013. Using hydrochemistry to understand inter-aquifer mixing in the on-shore par of the Gippsland Basin, southeast Australia. Applied Geochemistry, 33: 84-103.

Humez, P., Lagneau, V., Lions, J., Negrel, P., 2013. Assessing the potential consequences of CO_2 leakage to freshwater resources: A batch-reaction experiment towards an isotropic tracing tool. Applied Geochemistry, 30: 178-190.

IPCC, 2005. IPCC special report on carbon dioxide capture and storage. Prepared by Working Group III of the IPCC [Metz, B., Davidson, O., Coninck, H., Loos, M., Meyer, L., (Eds.)]. Cambridge University Press, 442 pp.

Jorgensen, D. G., 1989. Paleohydrology of the Anadarko Basin, Central United States. Oklahoma Geological Survey, Circular 90: 179-193.

Jorgensen, D., Helgesen, J., Imes, J., 1989. Regional aquifers in Kansas, Nebraska, and Parts of Arkansas, Colorado, Missouri, New Mexico, Oklahoma, South Dakota, Texas, and Wyoming – Geohydrologic Framework. U.S. Geological Survey Professional Paper: 1414—B.

Kampman, N., Bickle, M., Wigley, M., Dubacq, B., 2014. Fluid flow and CO_2-fluid-mineral interactions during CO_2-storage in sedimentary basins. Chemical Geology, 369: 22-50.

Kharaka, Y., Thordsen, J., Hovorka, S., Nance, H., Cole, D., Phelps, T., Knauss, K., 2009. Potential environmental issues of CO_2 storage in deep saline aquifers: Geochemical results from the Frio-I Brine Pilot test, Texas, USA. Applied Geochemistry, 24: 1106-1112.

Lammers, K., Murphy, R., Riendeau, A., Smirnov, A., Schoonen, M., Strongin, D., 2011. CO_2 Sequestration through Mineral Carbonation of Iron Oxyhydroxides. Environmental Science and Technology, 45: 10422-10428

Leung, D., Caramanna, G., and Maroto-Valer, M., 2014. An overview of current status of carbon dioxide capture and storage technologies. Renewable and Sustainable Energy Reviews, 39: 426-443.

McIntosh, J., Walter, L., Martini, A. 2004. Extensive Microbial Modification of formation water Geochemistry: Case Study from the Midcontinent Sedimentary basin, United States. Geological society of America Bulletin. 116, No 5-6: 743-759.

Merriam, D., The Geologic History of Kansas: State Geological Survey of Kansas, Bulletin 162. University of Kansas Publications. Lawrence KS, 1963. P146-151.

Michael, K., Golab, A., Shulakova, V., Ennis-King, J., Allinson, G., Sharma, S., Aiken, T., 2010. Geological storage of CO_2 in saline aquifers – A review of the

experience from existing storage operations. International Journal of Greenhouse Gas Control, 4: 659-67.

Musgrove, M., Banner, J., 1993. Regional Ground-Water Mixing and the Origin Of Saline Fluids: Midcontinent, United States. Science, 259 No. 5103: 1877-1882.

Ott, H., Roels, S., Kloe, K., 2015. Salt precipitation due to supercritical gas injection: I. Capillary-driven flow in unimodal sandstone. International Journal of Greenhouse Gas Control, In-Press.

Palandri, J., Rosenbauer, R., Kharaka, Y., 2005. Ferric iron in sediments as a novel CO_2 mineral trap: CO_2-SO_2 reaction with hematite. Applied Geochemistry, 20: 2038-2048.

Pauwels, H., Gaus, I., le Nindre, Y.M., Pearce, J., Czernichowski-Lauriol, I., 2007. Chemistry of fluids from a natural analogue for a geological CO_2 storage site (Montmiral, France): lessons for CO_2-water-rock interaction assessment and monitoring. Appl. Geochem. 22 (12), 2817-2833

Peysson, Y., André, L, Azaroual, M., 2014. Well injectivity during CO_2 storage operations in deep saline aquifers—Part 1: Experimental investigation of drying effects, salt precipitation and capillary forces. International Journal of Greenhouse Gas Control, 22: 291-300.

Romanak, K., Harmon R., Kharaka, Y., 2013. Geochemical Aspects of Geologic Carbon Storage, Editorial. Applied Geochemistry, 30: 1-3.

Scheffer, A., 2012. Geochemical and Microbiological Characterization of the Arbuckle Saline Aquifer, a Potential CO_2 Storage Reservoir; Implications for Hydraulic Separation and Caprock Integrity. Thesis. University of Kansas.

Smith, M., Sholokhova, Y., Hao, Y., and Carroll, S., 2013. Evaporite Caprock Integrity: An Experimental Study of Reactive Mineralogy and Pore-Scale Heterogeneity during Brine-CO_2 Exposure. Environmental Science and Technology, 47: 262-268.

Song, J., and Zhang, D., 2012. Comprehensive Review of Caprock-Sealing Mechanisms for Geologic Carbon Sequestration. Environmental Science & Technology, 47: 9-22.

Stueber, A. M., and L. M. Walter, 1991. Origin And Chemical Evolution Of Formation Waters From Silurian-Devonian Strata In The Illinois Basin, USA. Geochimica Et. Cosmochimica Acta, 55 (1): 309-325.

USDOE, 2010. Carbon Utilization and Storage Atlas. U.S. Department of Energy, National Energy Technology Laboratory, fourth ed., 130 pp.

Wang, X., Alvarado, V., Swoboda-Colberg, N., Kaszuba, J., 2013.Reactivity of dolomite in water-saturated supercritical carbon dioxide: Significance for carbon capture and storage and for enhanced oil and gas recovery. Energy Conversion and Management, 65: 564-573.

Wilson, T. P., and D. T. Long, (1993). Geochemistry And Isotope Chemistry Of Ca-Na-Cl Brines In Silurian Strata, Michigan Basin, USA. Applied Geochemistry 8 (5): 507-524.

Wollenweber, J., Alles, S., Busch, A., Krooss, B., Stanjek, H., Littke, R., 2010. Experimental investigation of the CO_2 sealing efficiency of caprocks. International Journal of Greenhouse Gas Control, 4: 231-241.

Worden, R.H., 2006. Dawsonite cement in the Triassic Lam Formation, Shabwa Basin, Yemen: a natural analogue for a potential mineral product of subsurface CO_2 storage for a greenhouse gas reduction. Mar. Pet. Geol. 23 (1), 61-77.

Zekri, A., Shedid, S., Almehaideb, R., 2009. Investigation of supercritical carbon dioxide, aspheltenic crude oil, and formation brine interactions in carbonate formations. Journal of Petroleum Science and Engineering, 69: 63-70

Appendix A

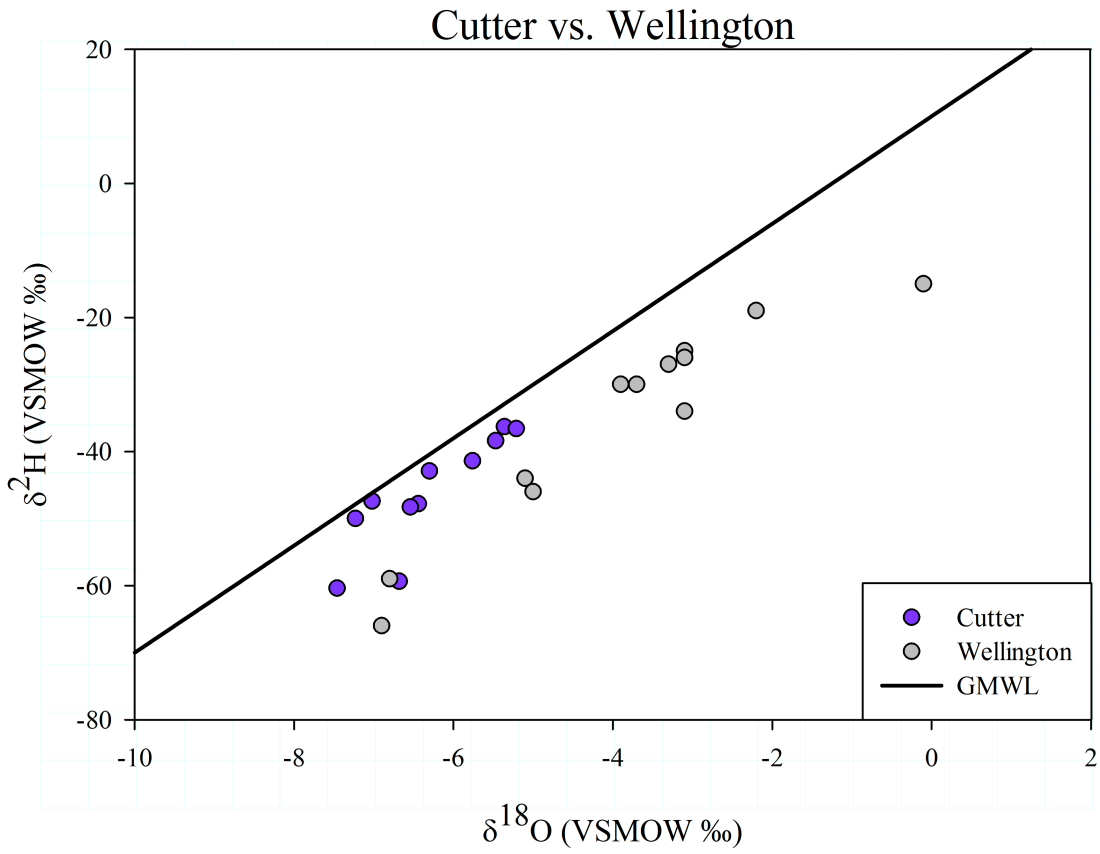
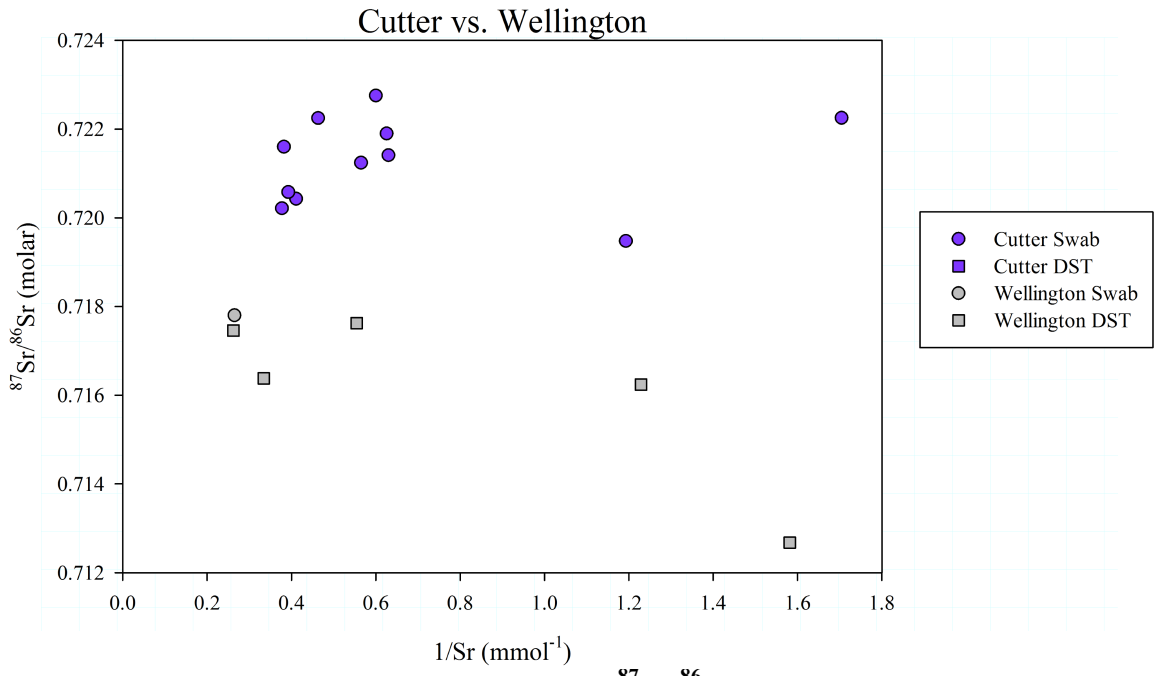
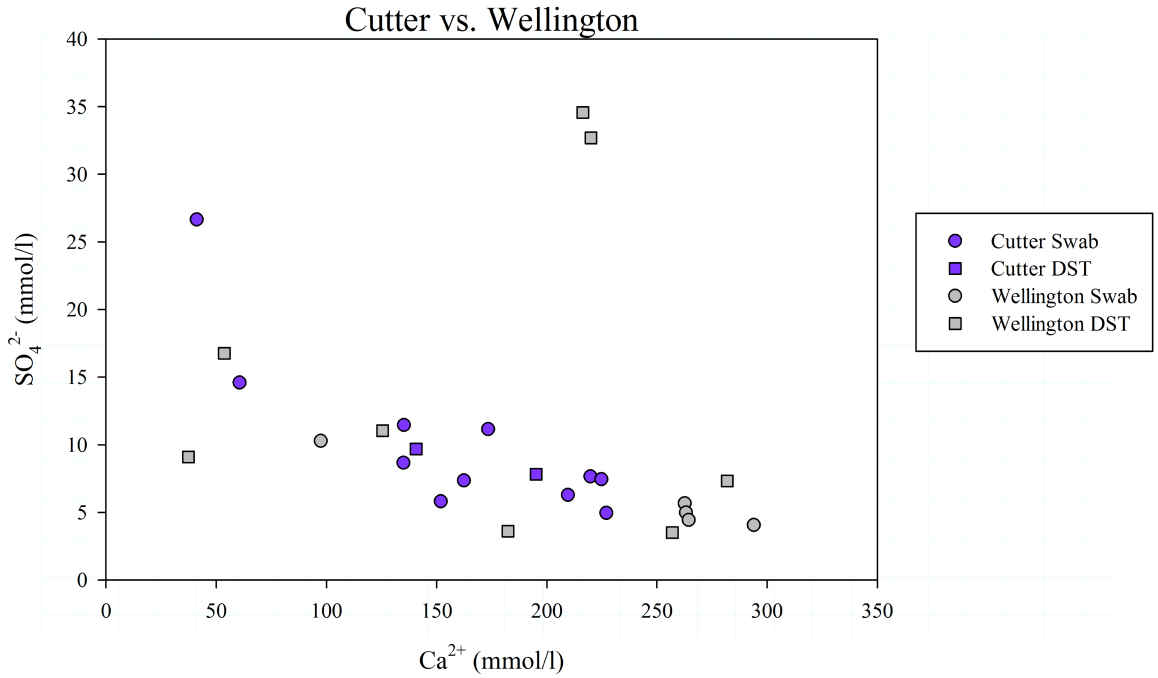


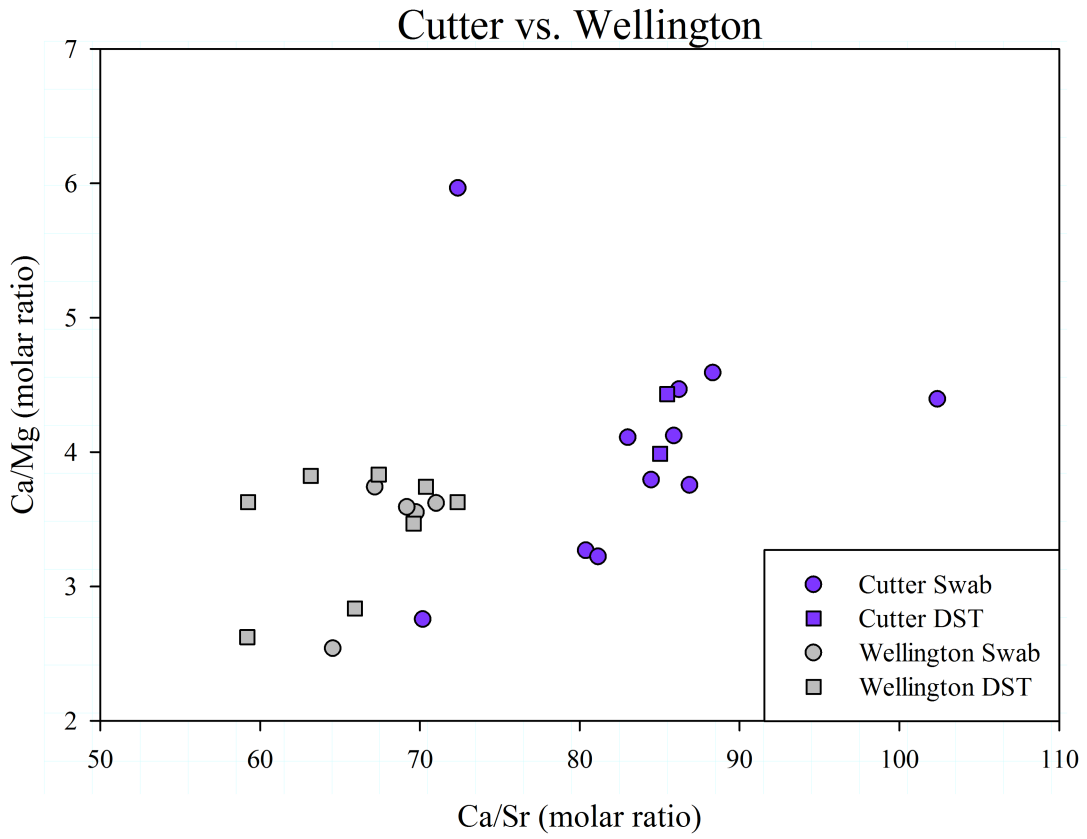
Figure A.3.1 Cutter vs. Wellington comparison of $\delta^{18}O$ vs. $\delta^{2}H$.



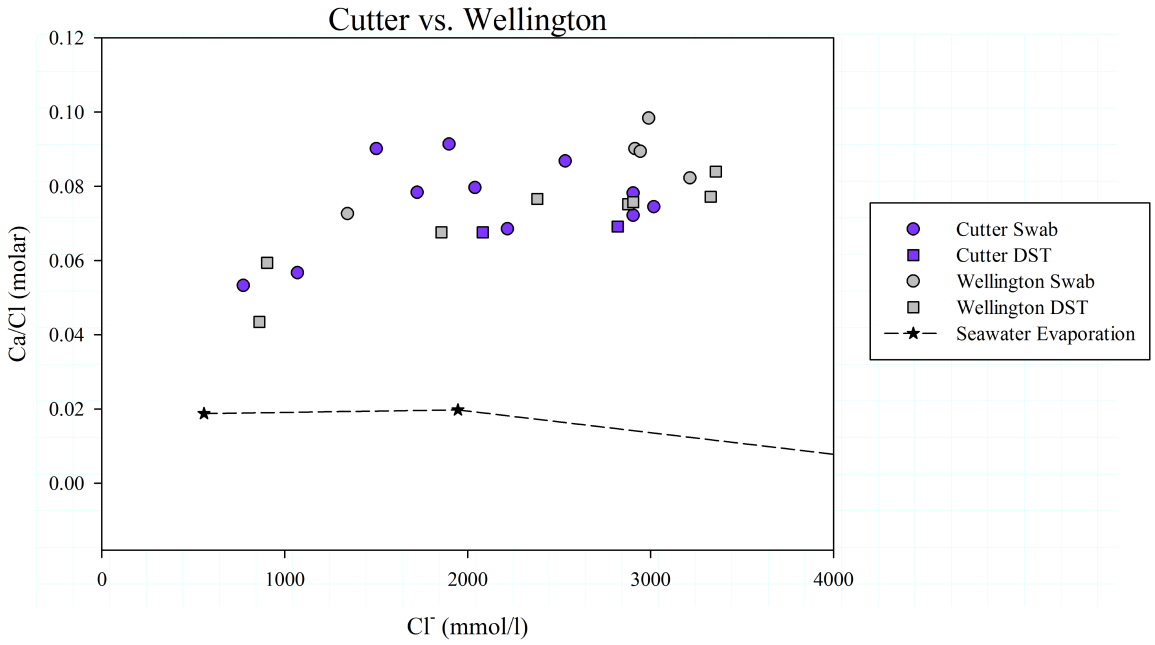
Cutter vs. Wellington comparison of 1/Sr vs. $^{87}Sr/^{86}Sr$.



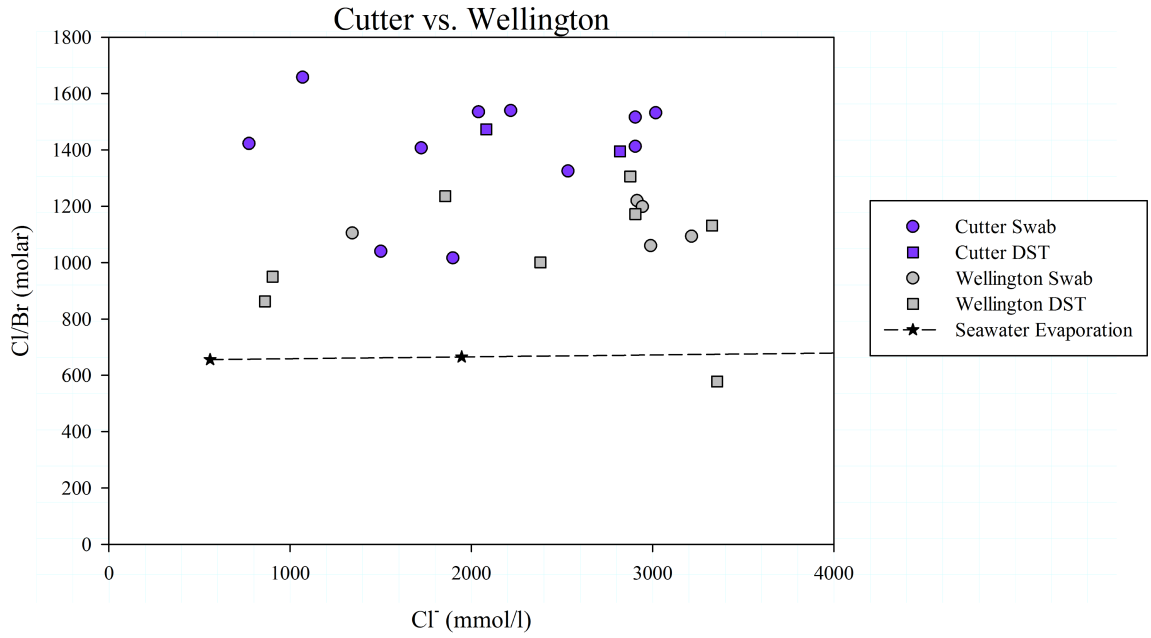
Cutter vs. Wellington comparison of Ca^{2+} vs. SO_4^{2-}.



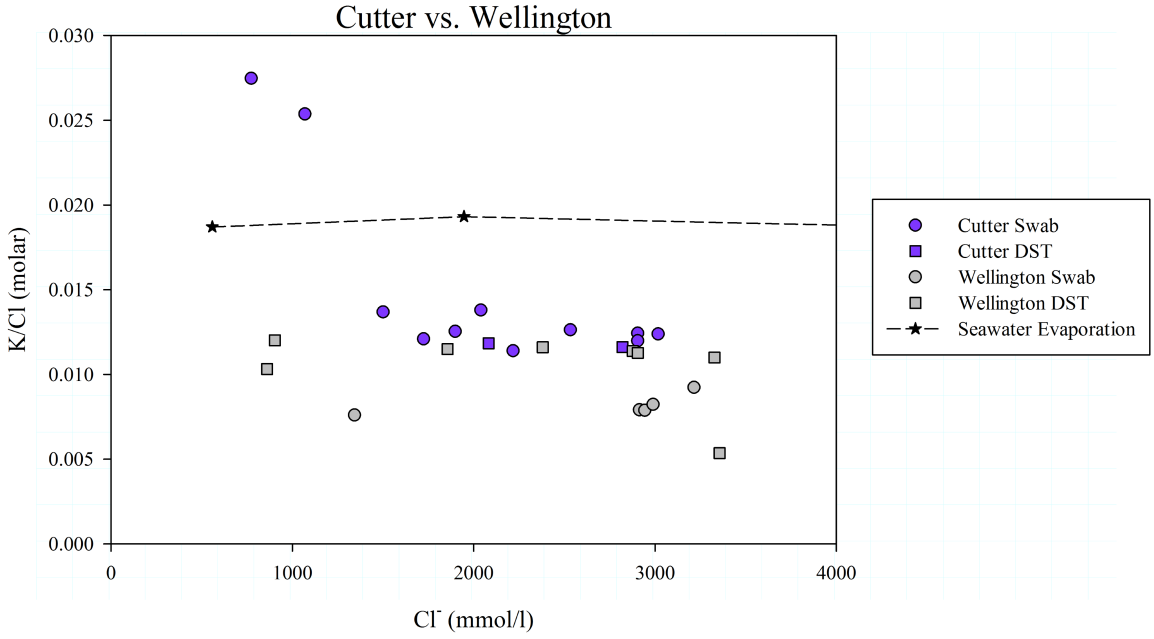
Cutter vs. Wellington comparison of Ca/Sr vs. Ca/Mg.



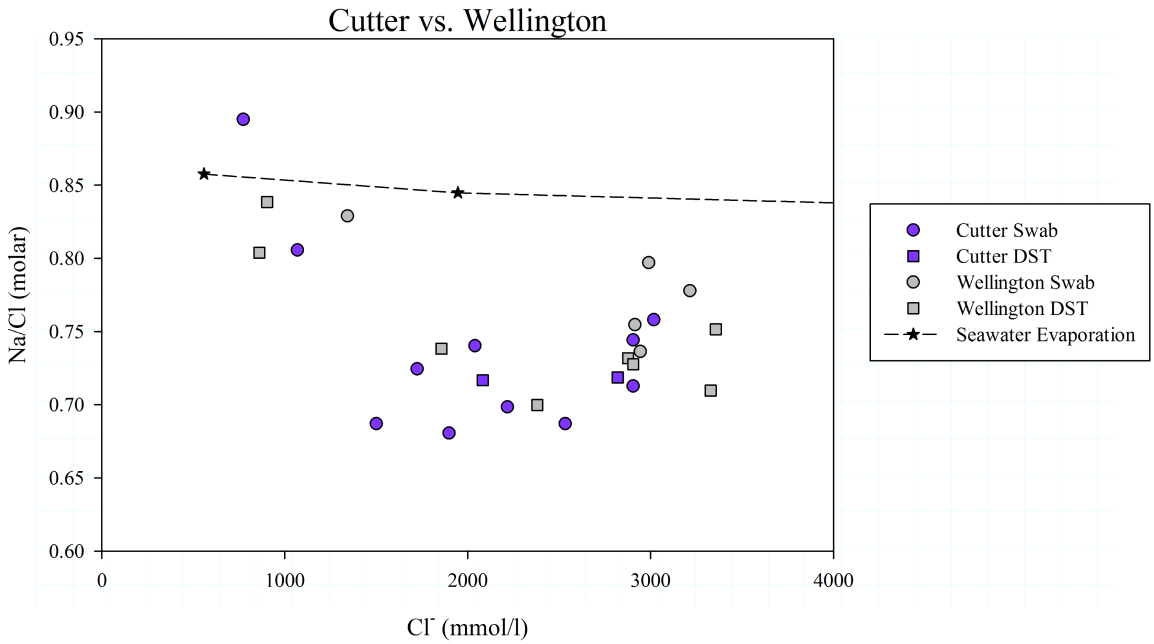
Cutter vs. Wellington comparison of Cl^- vs. Ca/Cl.



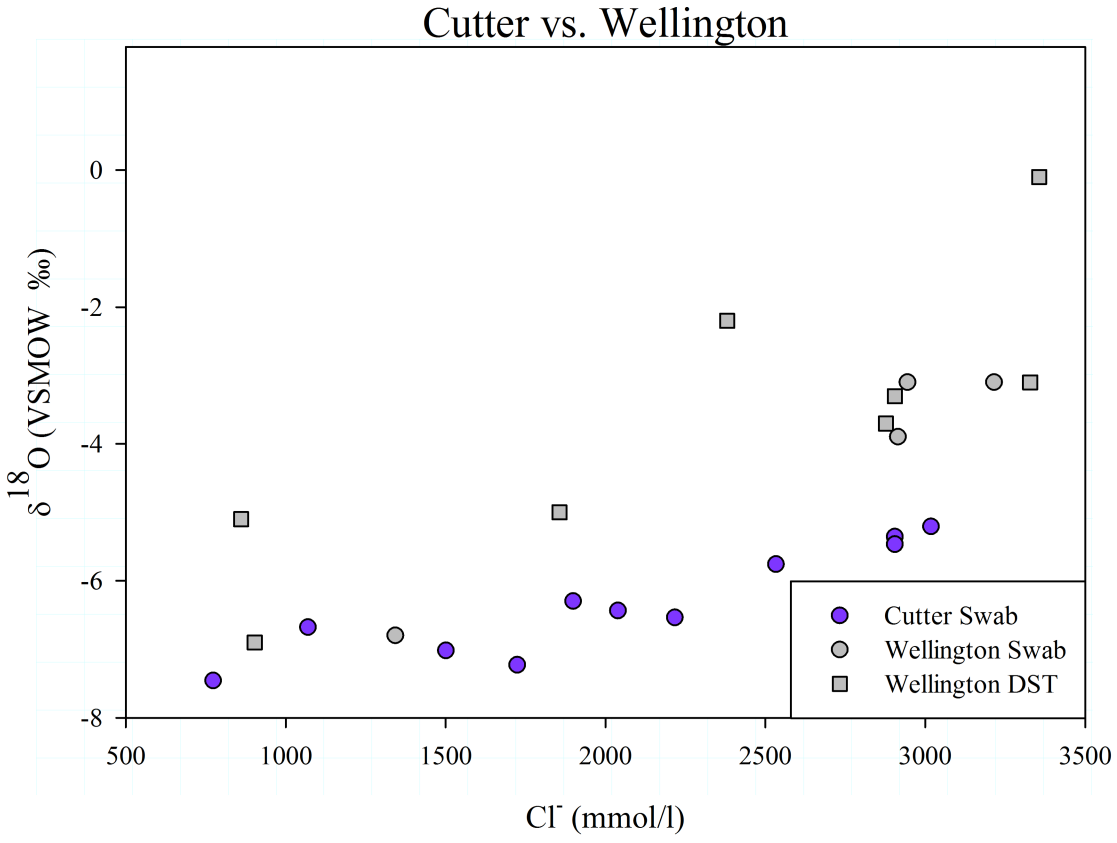
Cutter vs. Wellington comparison of Cl^- vs. Cl/Br.



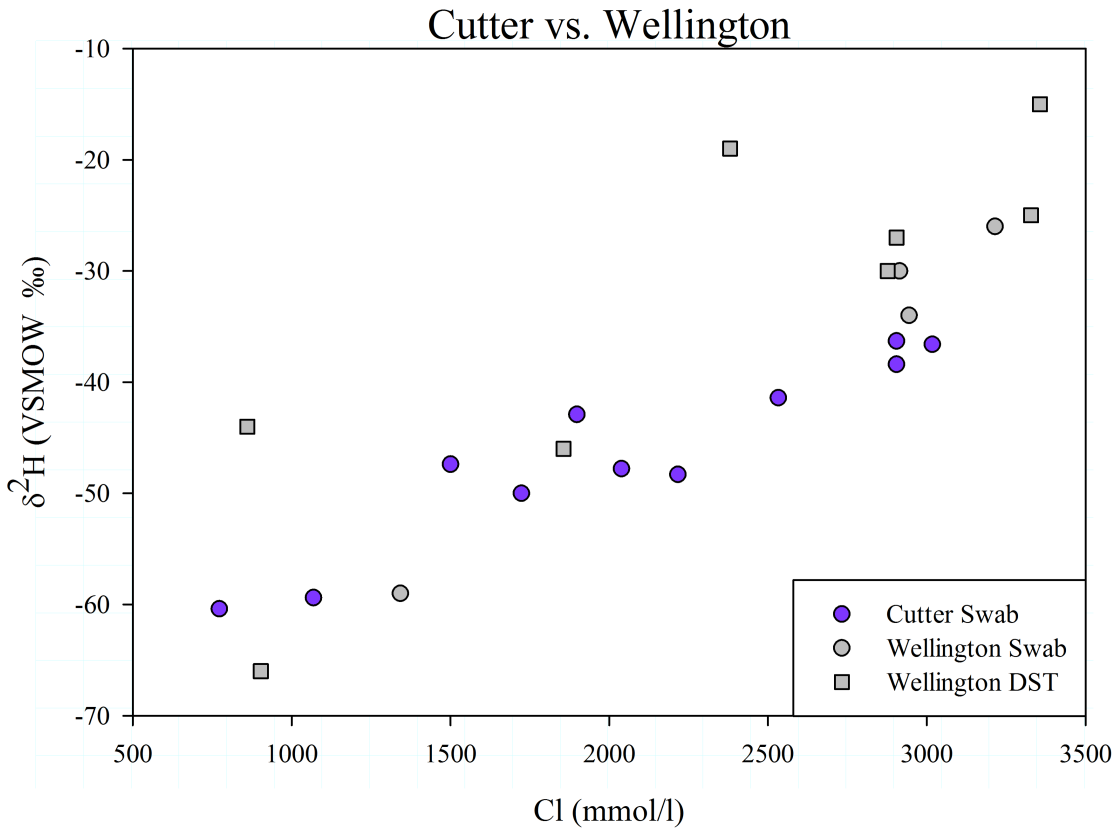
Cutter vs. Wellington comparison of Cl^- vs. K/Cl.



Cutter vs. Wellington comparison of Cl^- vs. Na/Cl.



Cutter vs. Wellington comparison of Cl^- vs. $\delta^{18}O$.



Cutter vs. Wellington comparison of Cl^- vs. δ^2H.

Appendix B

Time	Time		Analyte Name	Ca 396.847	K 766.490	Mg 285.213	Na 589.592	Cu 327.393	Fe 239.562
minutes	days			mg/L	mg/L	mg/L	mg/L	mg/L	mg/L
0	0		**A1**	5700.83	729.26	880.99	34880.2	9.02	2.54
7.02	0.29		**A2**	5049.67	646.36	779.14	30878.7	6.77	2.91
53.60	2.23		**A3**	5114.40	827.01	794.18	31273.1	6.52	3.57
102.67	4.28		**A4**	5642.30	784.48	875.13	34608.0	5.20	2.32
121.62	5.07		**A5**	4748.33	632.32	732.30	29073.6	5.60	2.86
122.55	5.11	Start of CO2 flow	**A6**	4734.22	658.07	744.22	29632.1	9.60	2.53
123.30	5.14		**A7**	5710.26	874.05	838.74	32893.3	19.16	1.38
123.73	5.16		**A8**	5869.67	925.72	878.36	34236.1	14.31	4.24
124.53	5.19		**A9**	5770.02	752.41	884.28	34496.9	8.97	4.68
125.25	5.22		**A10**	5441.71	709.94	838.65	32743.7	7.92	3.83
126.45	5.27		**A11**	5135.43	693.69	800.16	31030.8	6.33	3.16
127.98	5.33		**A12**	5842.92	749.69	907.35	35415.3	6.38	3.24
128.98	5.37		**A13**	5745.44	759.86	908.79	34804.4	6.13	3.13
129.98	5.42		**A14**	5988.65	813.02	941.15	36342.3	6.23	3.12
130.50	5.44		**A15**	5489.14	740.06	862.66	33196.9	5.68	2.87
131.13	5.46		**A16**	5536.36	734.28	862.25	33547.8	5.77	2.95
131.83	5.49		**A17**	6135.95	786.14	961.46	37104.5	5.98	3.03
132.32	5.51		**A18**	5964.47	774.22	937.31	36053.7	5.91	2.98
133.10	5.55		**A19**	6102.91	800.41	952.85	36893.5	5.71	2.93
134.03	5.58		**A20**	5550.35	716.03	864.55	33509.1	5.19	2.71
135.28	5.64		**A21**	5929.53	764.17	929.99	35794.5	5.48	2.79
136.50	5.69		**A22**	5651.71	752.76	882.58	34128.1	5.23	2.71
140.75	5.86		**A23**	6408.77	823.74	1009.35	38759.6	5.56	2.76
145.42	6.06		**A24**	6340.73	830.15	996.56	38291.9	5.79	2.82
147.97	6.17		**A25**	5398.00	682.95	843.14	32546.1	4.73	2.37
151.87	6.33		**A26**	6165.71	790.95	976.71	37248.4	5.25	2.55
167.28	6.97		**A27**	4949.82	651.82	776.91	29755.0	4.27	2.19
170.73	7.11		**A28**	6121.43	790.48	960.36	36921.6	5.07	2.35
176.85	7.37		**A29**	5888.45	747.42	976.14	34811.4	4.84	2.25
191.12	7.96		**A30**	5545.69	720.10	875.99	33410.5	4.63	2.19
196.62	8.19		**A33**	4810.44	617.06	758.48	28944.0	3.90	1.88
222.80	9.28		**A34**	5716.83	725.80	898.06	34473.6	4.51	2.00
264.02	11.00	Pressure Failure	**A35**	5325.35	671.95	838.84	32115.5	4.44	1.88
287.23	11.97		**A36**	5653.12	720.22	884.16	34080.8	3.10	2.80
335.13	13.96		**A 39**	5722.26	712.16	894.09	34473.7	2.92	2.84
383.15	15.96		**A40**	5955.20	738.78	931.53	35897.2	2.96	2.67
454.42	18.93		**A41**	5615.68	694.66	876.76	33891.1	2.61	2.78
506.95	21.12		**A42**	5653.35	698.86	877.03	33844.1	2.44	2.72
			Analyte Name	**Ca 396.847**	**K 766.490**	**Mg 285.213**	**Na 589.592**	**Cu 327.393**	**Fe 239.562**
			Apre1	5610.88	705.97	858.60	34325.19	5.70	2.43
			Apre2	5471.32	694.58	845.02	33424.10	5.74	2.30
			Apre3	5133.81	646.66	781.83	31367.51	7.95	3.61
			Apre4	5563.42	707.43	855.19	34028.35	6.15	2.37
			Apre5	5613.75	714.11	866.77	34316.51	5.47	3.82
			Apre6	5197.36	656.38	798.72	31749.18	5.58	3.68
			Amq	-35.18	-10.08	-11.54	-183.02	0.00	0.60
			Apost 1	4970.37	624.21	768.66	30148.58	4.01	1.44
			Apost2	5494.95	692.69	847.46	33313.49	4.13	1.42
			Apost3	5537.47	692.20	847.43	33610.96	2.64	2.12
			Apost4	5674.23	701.65	868.63	34385.66	2.67	2.13
			Aextra2	58.04	15.62	8.00	403.86	1.12	1.48
			A37 pre7	6050.34	751.96	924.37	36659.76	5.22	4.14
			A38 pre 8	5882.96	726.49	893.40	35778.31	5.07	4.02

Cutter LLNL cation analysis of pre and post experimental flow through eluent. CO_2 started at day 5.11, sample A6. Apre1-2 is from the first brine-mixing vessel. Apre 3-4 is from the open Nalgene/pre-CO_2 flow. Apre5-6 is from the second brine-mixing vessel. Amq is MilliQ water. Apost 1-2 is from the first brine-mixing vessel. Apost 3-4 is from the second brine-mixing vessel. Aextra is from the reactor vessel confining water. Apre 7-8 is from the third brine-mixing vessel.

Time	Time		Analyte Name	Li 670.784	Mn 259.372	Sr 407.771	Ba 455.403	Mo 202.031	Pb 220.353	Zn 213.857
Minutes	Days			mg/L	mg/L	mg/L	mg/L	mg/L	mg/L	mg/L
0	0		**A1**	13.23	7.23	161.30	1.39	1.48	1.41	5.90
7.02	0.29		**A2**	11.75	6.51	143.12	1.21	1.37	0.28	3.95
53.60	2.23		**A3**	12.09	6.63	145.28	1.26	0.97	0.28	3.27
102.67	4.28		**A4**	13.27	7.14	158.06	1.37	0.44	0.42	3.05
121.62	5.07		**A5**	10.99	6.04	133.69	1.14	0.33	0.35	2.56
122.55	5.11	Start of CO2 flow	**A6**	11.18	7.49	138.96	1.19	0.19	0.21	8.72
123.30	5.14		**A7**	12.23	16.10	155.86	1.34	1.27	0.96	21.52
123.73	5.16		**A8**	12.89	14.98	161.02	1.38	1.42	1.28	19.61
124.53	5.19		**A9**	13.01	11.29	159.70	1.36	1.84	0.68	11.13
125.25	5.22		**A10**	12.43	9.51	153.06	1.27	1.85	0.45	6.95
126.45	5.27		**A11**	12.00	8.24	146.08	1.24	1.67	0.44	5.00
127.98	5.33		**A12**	13.59	8.89	164.60	1.41	1.63	0.75	4.74
128.98	5.37		**A13**	13.34	8.65	160.95	1.38	1.64	0.58	4.34
129.98	5.42		**A14**	13.79	8.88	167.32	1.43	1.67	0.76	4.31
130.50	5.44		**A15**	12.65	8.09	152.44	1.31	1.57	0.45	3.79
131.13	5.46		**A16**	13.01	8.32	155.81	1.35	1.49	0.33	3.97
131.83	5.49		**A17**	13.84	8.96	174.08	1.45	1.62	0.86	4.19
132.32	5.51		**A18**	14.02	8.80	167.85	1.45	1.68	0.66	4.05
133.10	5.55		**A19**	13.81	8.78	173.03	1.43	1.72	0.45	4.05
134.03	5.58		**A20**	12.85	8.13	158.63	1.32	1.52	0.92	3.61
135.28	5.64		**A21**	13.63	8.64	168.75	1.40	1.69	0.50	3.80
136.50	5.69		**A22**	13.02	8.16	160.48	1.35	1.62	0.66	3.59
140.75	5.86		**A23**	14.39	9.02	179.34	1.50	1.65	0.57	3.88
145.42	6.06		**A24**	14.99	9.27	178.75	1.54	1.51	0.20	4.02
147.97	6.17		**A25**	12.67	7.78	152.99	1.30	1.23	0.57	3.24
151.87	6.33		**A26**	14.41	8.80	172.74	1.49	1.18	0.55	3.71
167.28	6.97		**A27**	11.79	7.19	140.92	1.21	0.84	0.85	2.95
170.73	7.11		**A28**	14.12	8.71	173.12	1.46	0.90	0.55	3.54
176.85	7.37		**A29**	13.06	8.07	162.00	1.34	0.72	0.38	3.30
191.12	7.96		**A30**	12.98	7.92	156.00	1.33	0.63	0.09	3.26
196.62	8.19		**A33**	11.04	6.76	136.03	1.13	0.52	0.50	2.60
222.80	9.28		**A34**	12.84	7.80	160.63	1.31	0.50	0.46	3.21
264.02	11.00	Pressure Failure	**A35**	12.99	7.85	151.40	1.32	0.41	0.42	3.19
287.23	11.97		**A36**	13.00	14.83	158.35	1.26	0.39	0.58	1.21
335.13	13.96		**A 39**	13.46	15.40	162.45	1.33	0.32	0.48	1.32
383.15	15.96		**A40**	14.12	15.98	167.42	1.38	0.33	0.78	1.56
454.42	18.93		**A41**	13.22	16.75	159.02	1.27	0.25	0.48	0.84
506.95	21.12		**A42**	13.13	16.85	159.29	1.26	0.22	0.61	0.83
			Analyte Name	**Li 670.784**	**Mn 259.372**	**Sr 407.771**	**Ba 455.403**	**Mo 202.031**	**Pb 220.353**	**Zn 213.857**
			Apre1	13.25	8.07	157.53	1.38	0.25	0.54	3.38
			Apre2	13.35	8.10	155.41	1.36	0.21	0.70	3.35
			Apre3	11.87	6.75	146.54	1.24	0.26	0.59	3.12
			Apre4	13.05	7.32	158.76	1.36	0.26	0.54	3.47

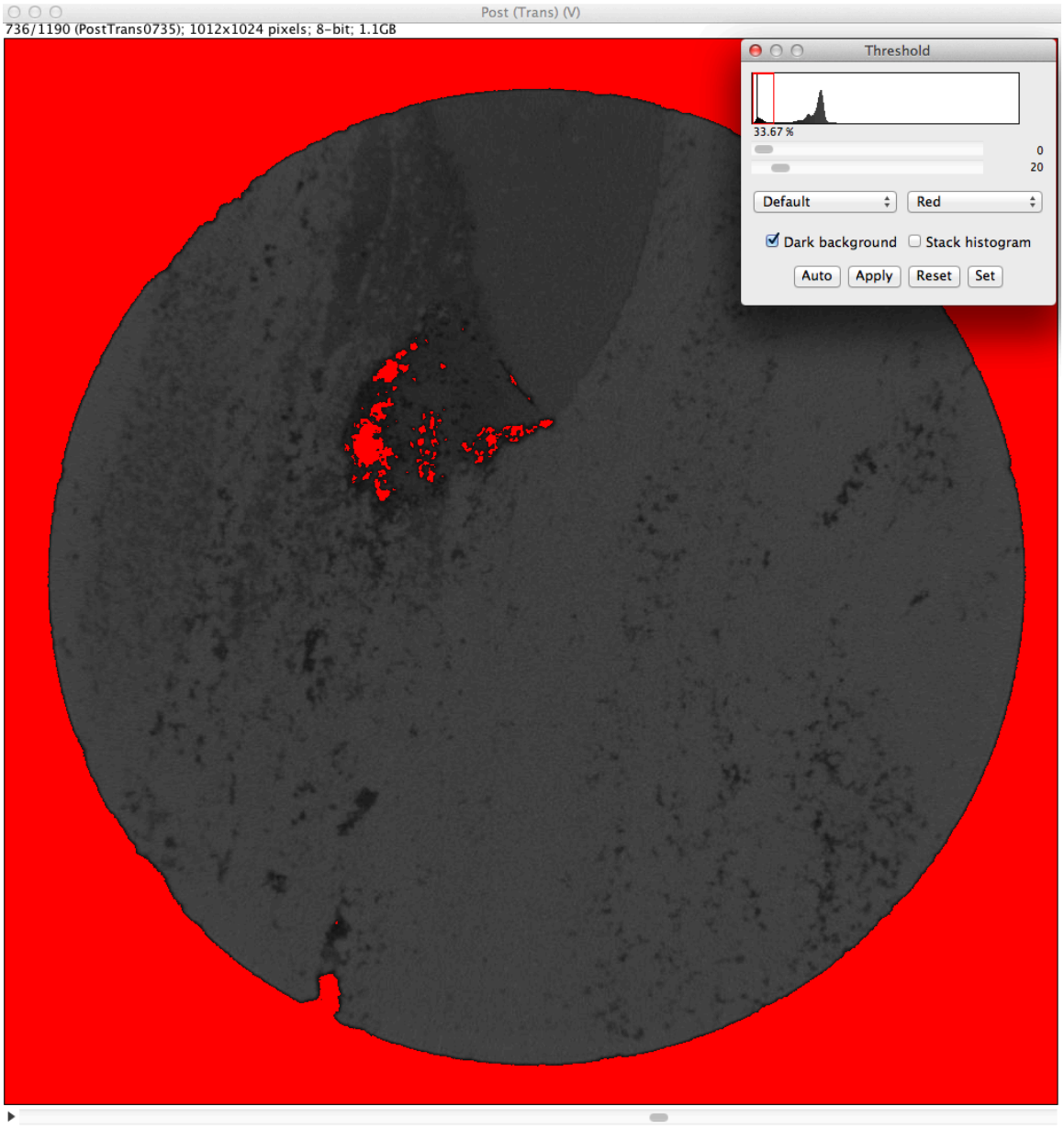
			Apre5	12.76	14.82	157.01	1.26	0.02	0.35	1.23
			Apre6	11.87	14.05	147.84	1.14	0.22	0.96	1.12
			Amq	-0.24	-0.16	-0.67	-0.06	0.14	0.37	-0.49
			Apost 1	12.45	7.41	140.30	1.26	0.25	0.50	2.95
			Apost2	12.92	7.64	155.75	1.31	0.30	0.64	3.10
			Apost3	12.94	14.78	156.56	1.25	0.14	0.71	1.27
			Apost4	13.39	15.25	161.13	1.30	0.05	0.86	1.30
			Aextra2	0.02	0.48	2.01	0.04	0.14	0.06	2.09
			A37 pre7	13.97	17.70	172.65	1.34	0.08	0.64	0.84
			A38 pre 8	13.72	17.28	168.54	1.33	0.17	0.36	0.82

Cutter LLNL cation analysis of pre and post experimental flow through eluent. CO_2 started at day 5.11, sample A6. Apre1-2 is from the first brine-mixing vessel. Apre 3-4 is from the open Nalgene/pre-CO_2 flow. Apre5-6 is from the second brine-mixing vessel. Amq is MilliQ water. Apost 1-2 is from the first brine-mixing vessel. Apost 3-4 is from the second brine-mixing vessel. Aextra is from the reactor vessel confining water. Apre 7-8 is from the third brine-mixing vessel.

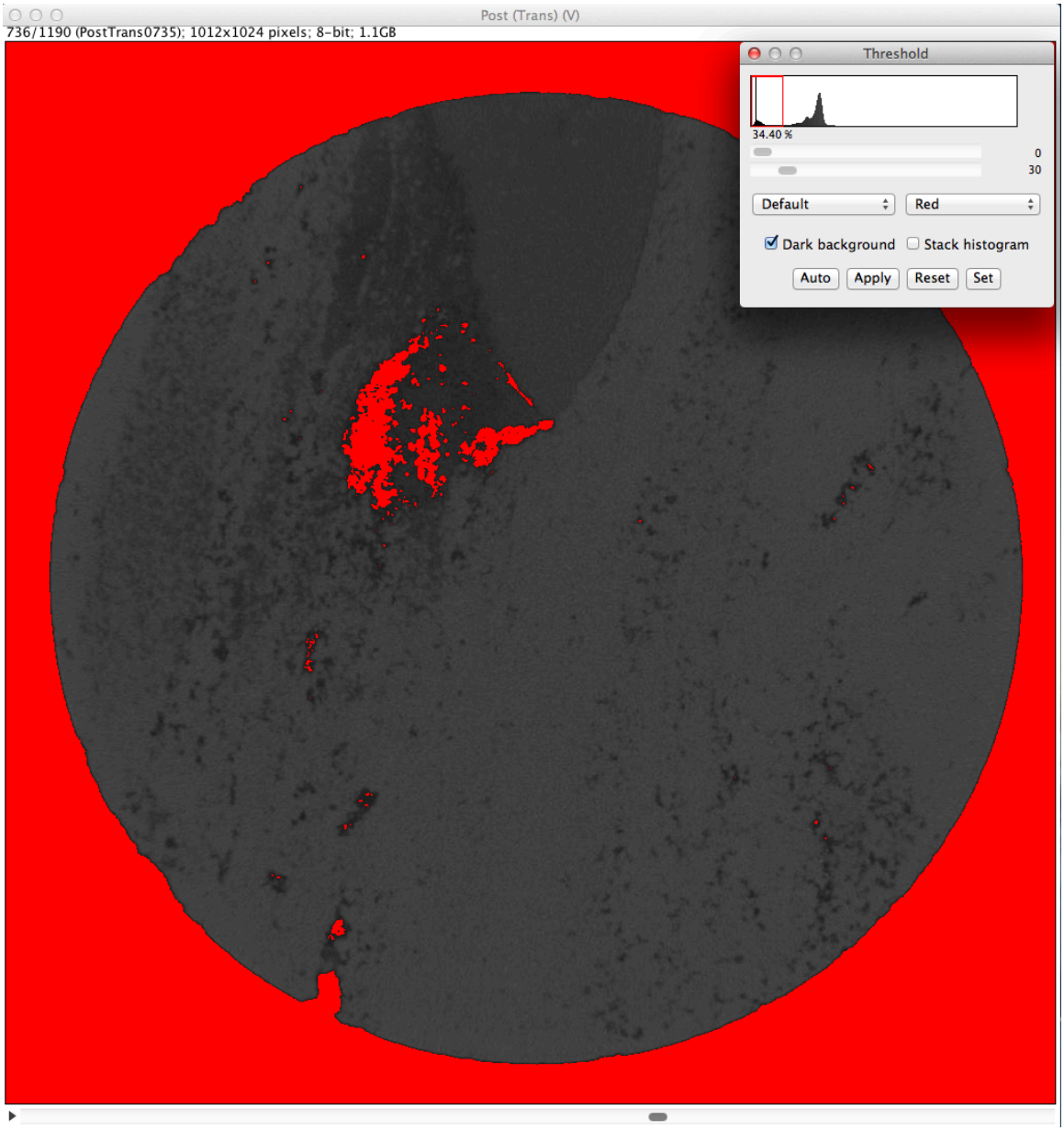
Time (minutes)	**Time (days)**	**Analyte**	**Cl (mg/L)**	**NO_2 (mg/L)**	**SO_4 (mg/L)**	**Br (mg/L)**
0	0	**B1**	62567.6	2241.9	606.9	91.0
7.02	0.29	**B2**	52027.0	2404.4	362.4	67.6
53.60	2.23	**B3**	41333.2	1748.3	289.2	92.8
102.67	4.28	**B4**	64260.7	2044.7	502.3	94.2
121.62	5.07	**B5**	50140.4	2162.6	347.5	65.9
122.55	5.11	**B6**	35802.4	1779.6	259.3	51.6
123.30	5.14	**B7**	22787.4	1216.7	161.8	55.6
123.73	5.16	**B8**	49135.3	2067.0	359.8	96.3
124.53	5.19	**B9**	51445.3	2148.7	367.3	82.2
125.25	5.22	**B10**	43057.4	1550.1	309.9	55.1
126.45	5.27	**B11**	50748.5	1826.4	356.5	76.1
127.98	5.33	**B12**	50554.4	2055.4	366.0	71.0
128.98	5.37	**B13**	50711.8	1945.1	365.6	88.7
129.98	5.42	**B14**	38941.9	1509.0	286.3	70.8
130.50	5.44	**B15**	51973.5	2116.1	388.6	62.3
131.13	5.46	**B16**	40745.8	1617.2	301.2	58.6
131.83	5.49	**B17**	38087.3	1852.1	282.3	45.6
132.32	5.51	**B18**	48227.7	909.3	368.8	51.2
133.10	5.55	**B19**	42168.2	874.5	317.6	50.9
134.03	5.58	**B20**	44994.7	949.3	342.2	67.0
135.28	5.64	**B21**	26634.1	1398.8	190.3	52.5
136.50	5.69	**B22**	32686.3	1702.0	186.9	73.0
140.75	5.86	**B23**	54565.1	1919.5	338.5	67.1
145.42	6.06	**B24**	65114.0	2466.5	394.1	104.5
147.97	6.17	**B25**	41378.1	2092.2	246.4	54.7
151.87	6.33	**B26**	37782.6	1901.5	214.3	69.2
167.28	6.97	**B27**	34459.2	1663.0	205.0	57.7
170.73	7.11	**B28**	46623.9	1972.3	327.0	68.9
176.85	7.37	**B29**	51829.6	1927.8	334.5	137.6
191.12	7.96	**B30**	52419.3	2297.9	362.5	81.3
196.62	8.19	**B33**	46042.2	2363.5	321.2	71.1
222.80	9.28	**B34**	40917.9	1943.7	281.2	61.7
264.02	11.00	**B35**	35494.0	1684.7	237.6	49.9
287.23	11.97	**B36**	52755.5	2616.8	357.2	61.5
335.13	13.96	**B39**	58618.1	2671.4	423.6	78.2

383.15	15.96	**B40**	114779.6	3425.3	788.7	158.0
454.42	18.93	**B41**	64719.4	2945.4	463.0	65.1
506.95	21.12	**B42**	59638.9	2913.3	417.6	81.9
		Bpre1	47987.0	2460.6	357.2	49.7
		Bpre2	0	0	0	0
		Bpre3	40916.7	2344.0	296.4	47.2
		Bpre4	53911.6	0	296.3	56.5
		Bpre5	52728.0	0	283.2	104.9
		Bpre8	68328.7	0	389.6	116.7
		Bmq	67.5	0	0	0
		Bpost1	64206.2	3018.5	460.8	89.1
		Bpost3	62366.4	0	361.0	103.3
		Bpost5	115916.1	0	734.5	186.5
		B1xtr2	339.4	0	24.4	0.0

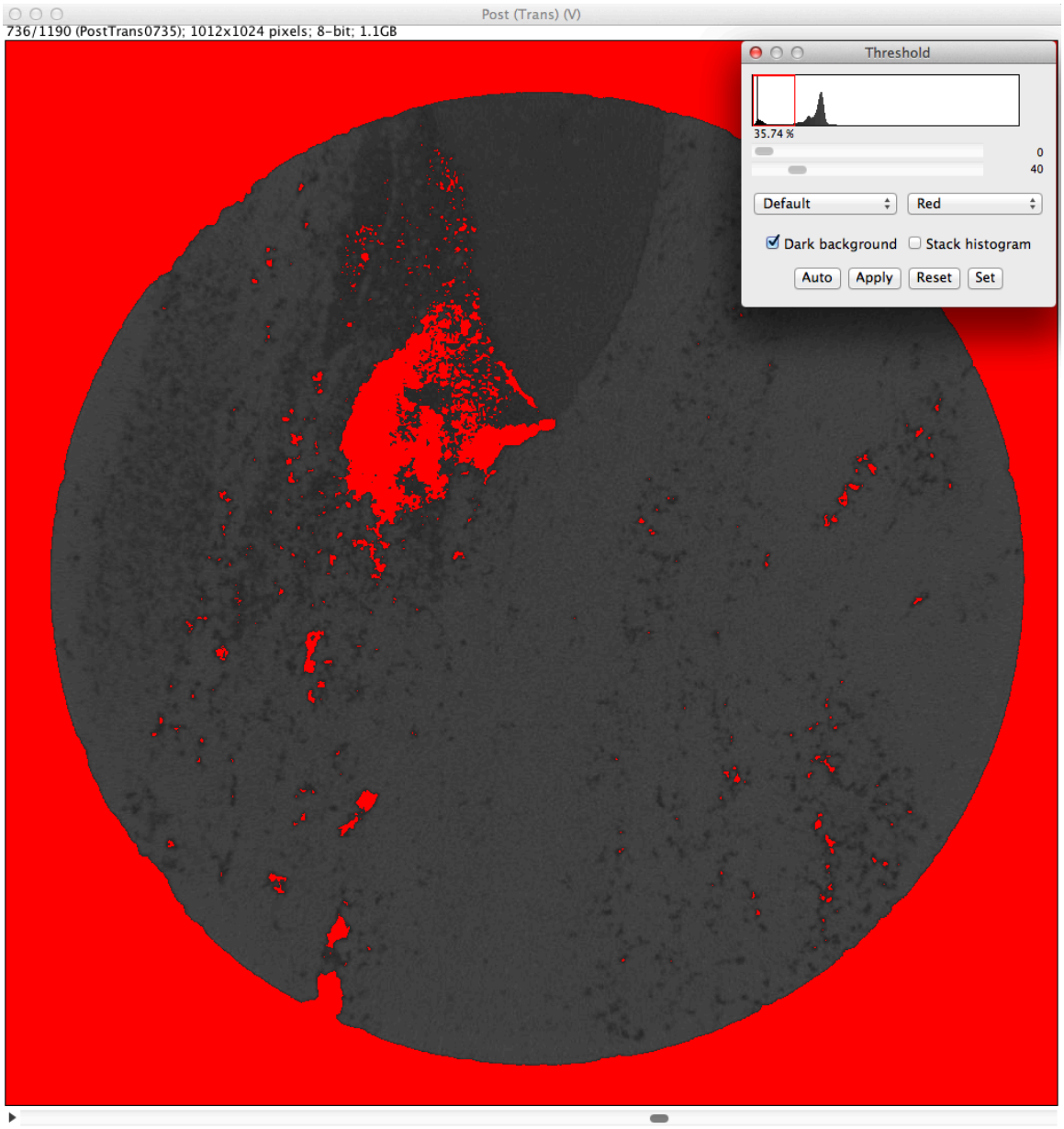
Cutter LLNL anion analysis of pre and post experimental flow through formation water. CO_2 started at day 5.11, sample B6. Bpre1-2 is from the first brine-mixing vessel. Bpre 3-4 is from the open Nalgene/pre-CO_2 flow. Bpre5,8 is from the second brine-mixing vessel. Bmq is MilliQ water. Bpost 1 is from the first brine-mixing vessel. Bpost 3 is from the second brine-mixing vessel. Bpost 5 is from the third brine-mixing vessel. B1xtr2 is from the reactor vessel confining water.



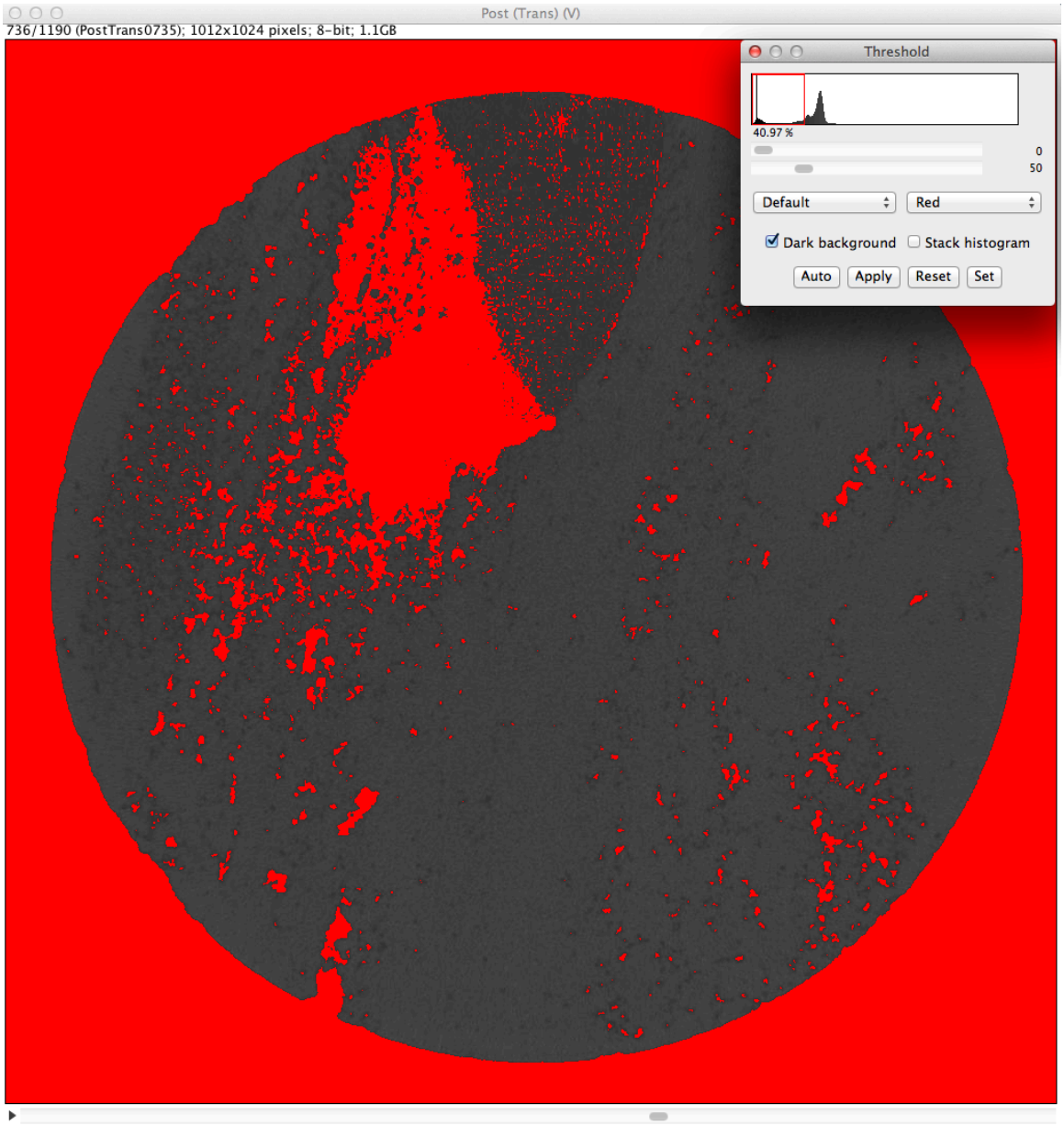
Full-scale XRCT scan showing a threshold value of 20. Porosity is indicated by the red space within the core, Cutter 20-9.



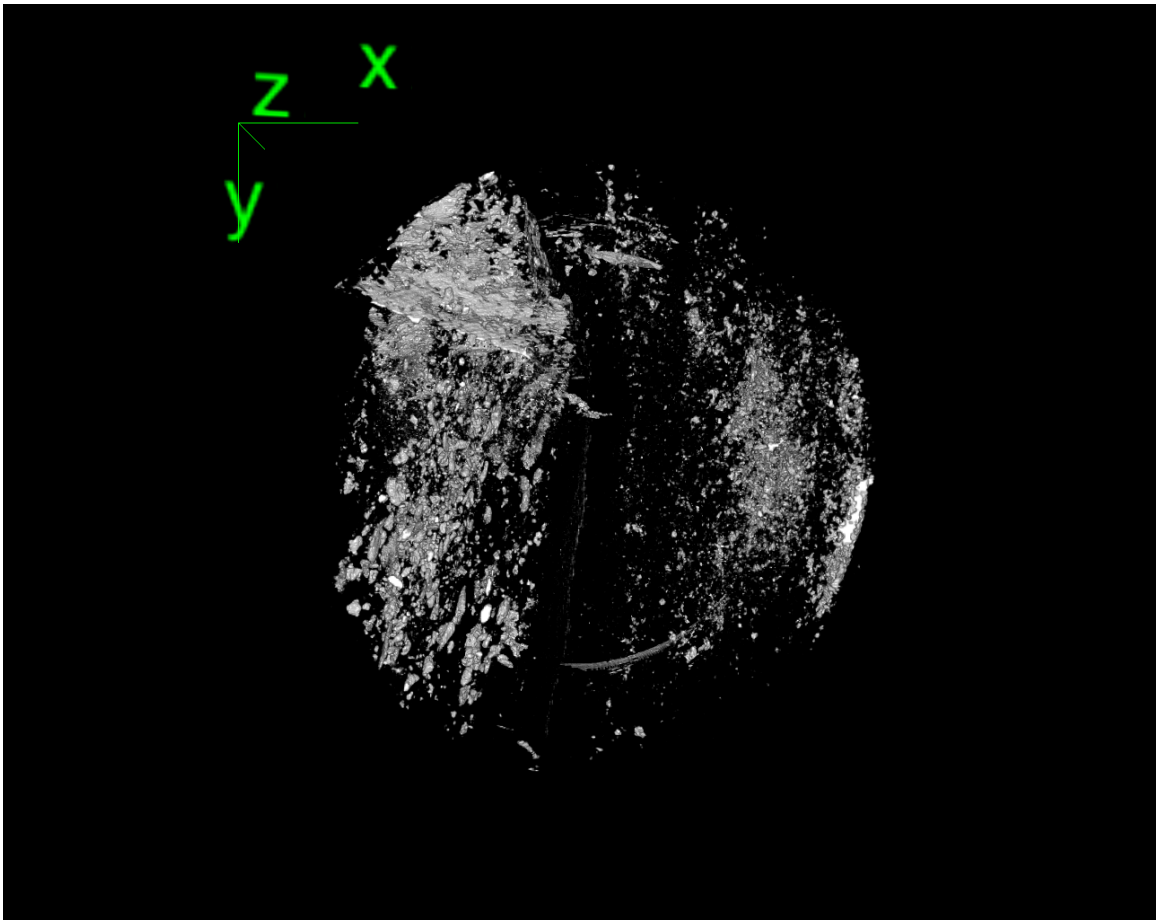
Full-scale XRCT scan showing a threshold value of 30. Porosity is indicated by the red space within the core, Cutter 20-9.



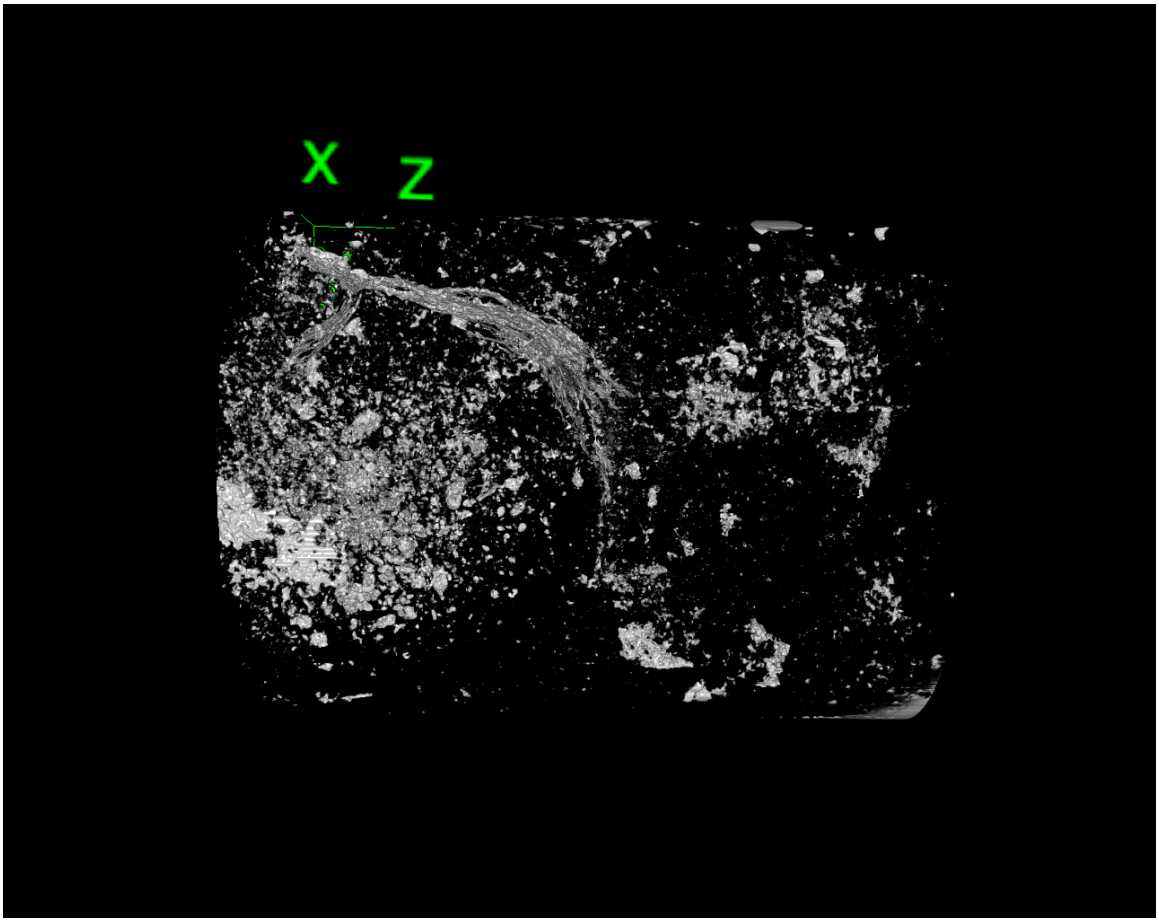
Full-scale XRCT scan showing a threshold value of 40. Porosity is indicated by the red space within the core, Cutter 20-9.



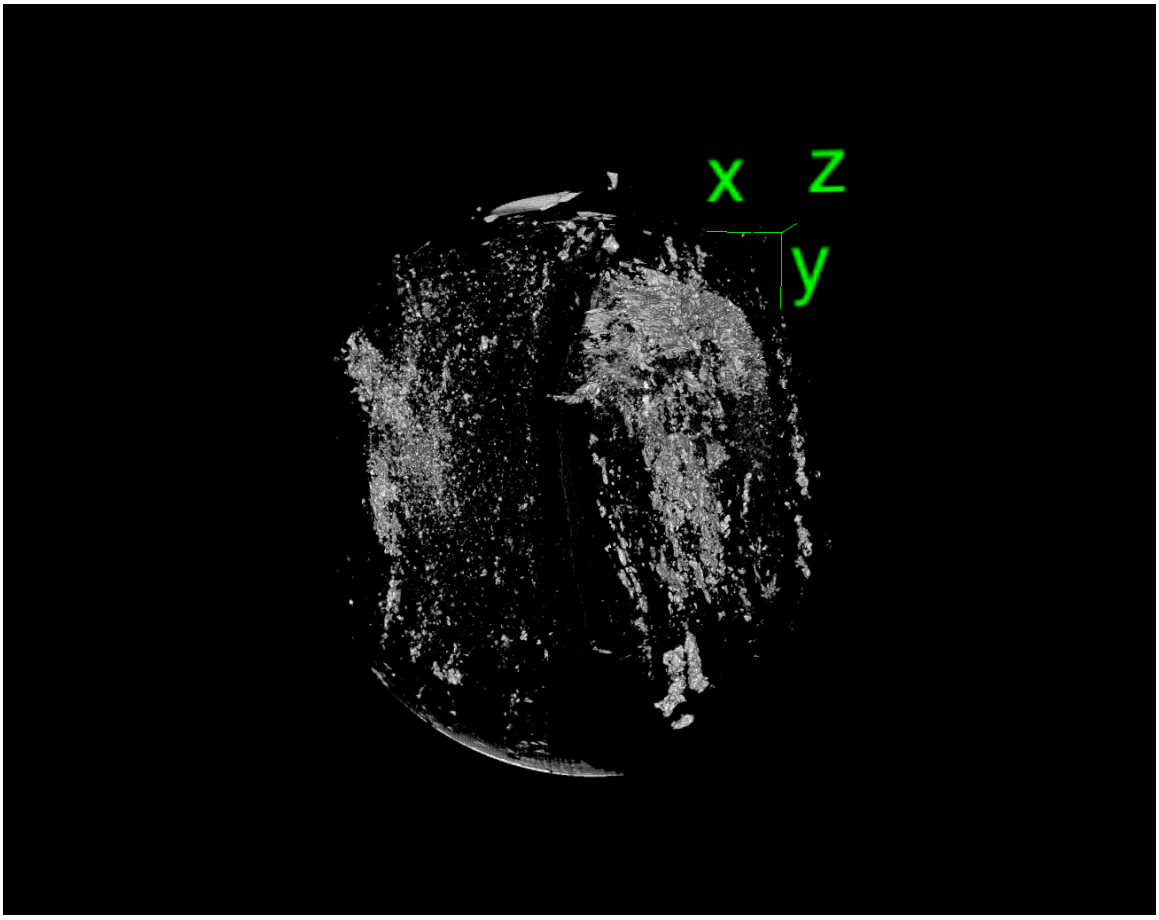
Full-scale XRCT scan showing a threshold value of 50. Porosity is indicated by the red space within the core, Cutter 20-9.



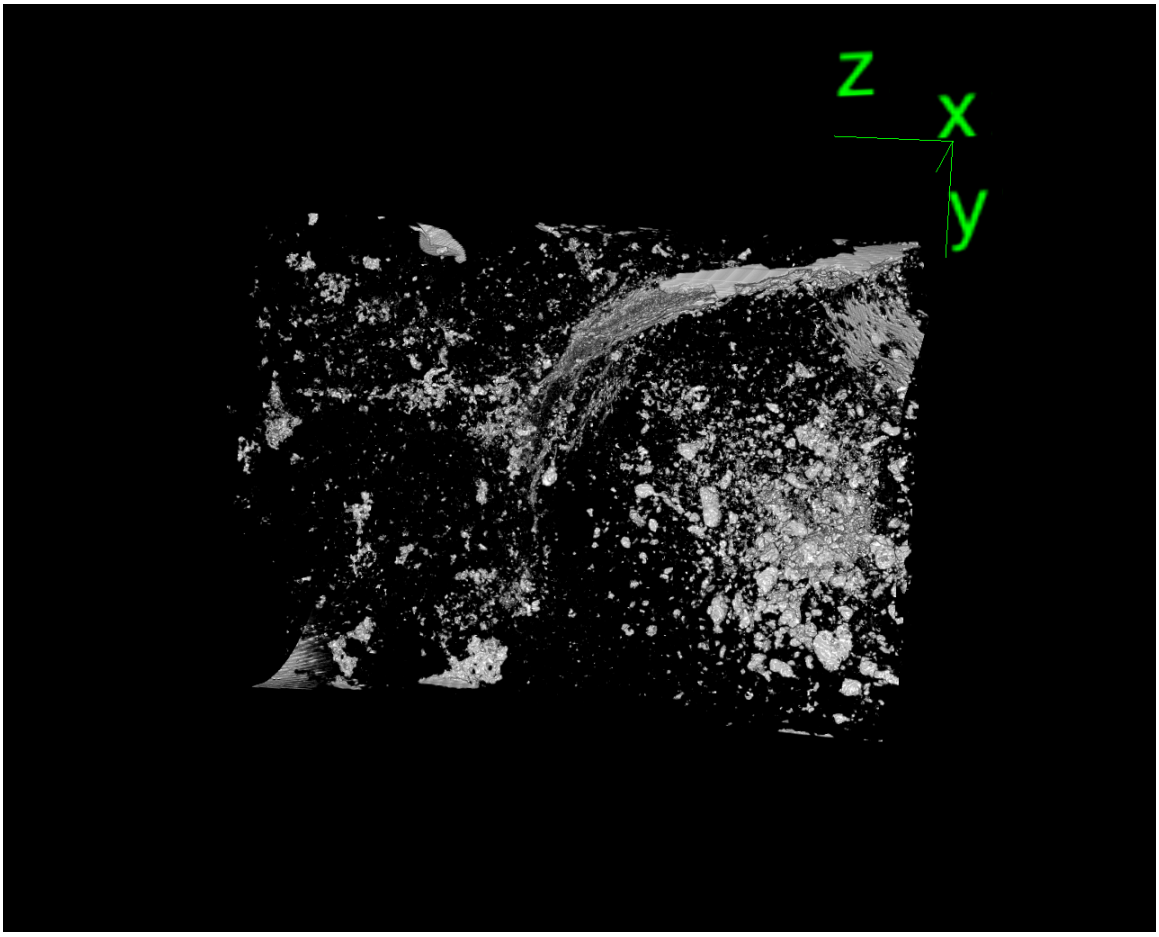
3D XRCT image of pre reaction pore space looking at the outlet side, Cutter 20-9.



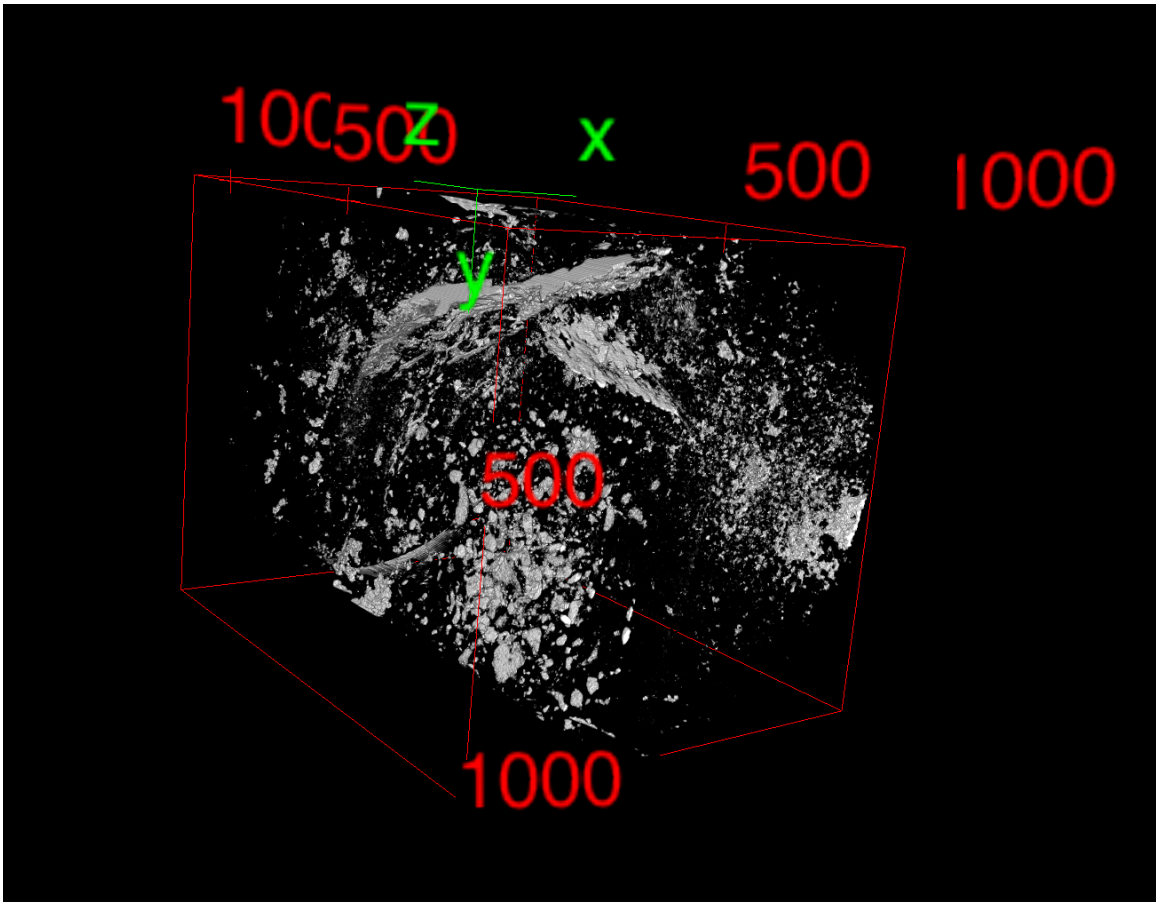
3D XRCT image of pre reaction pore space, side profile, Cutter 20-9.



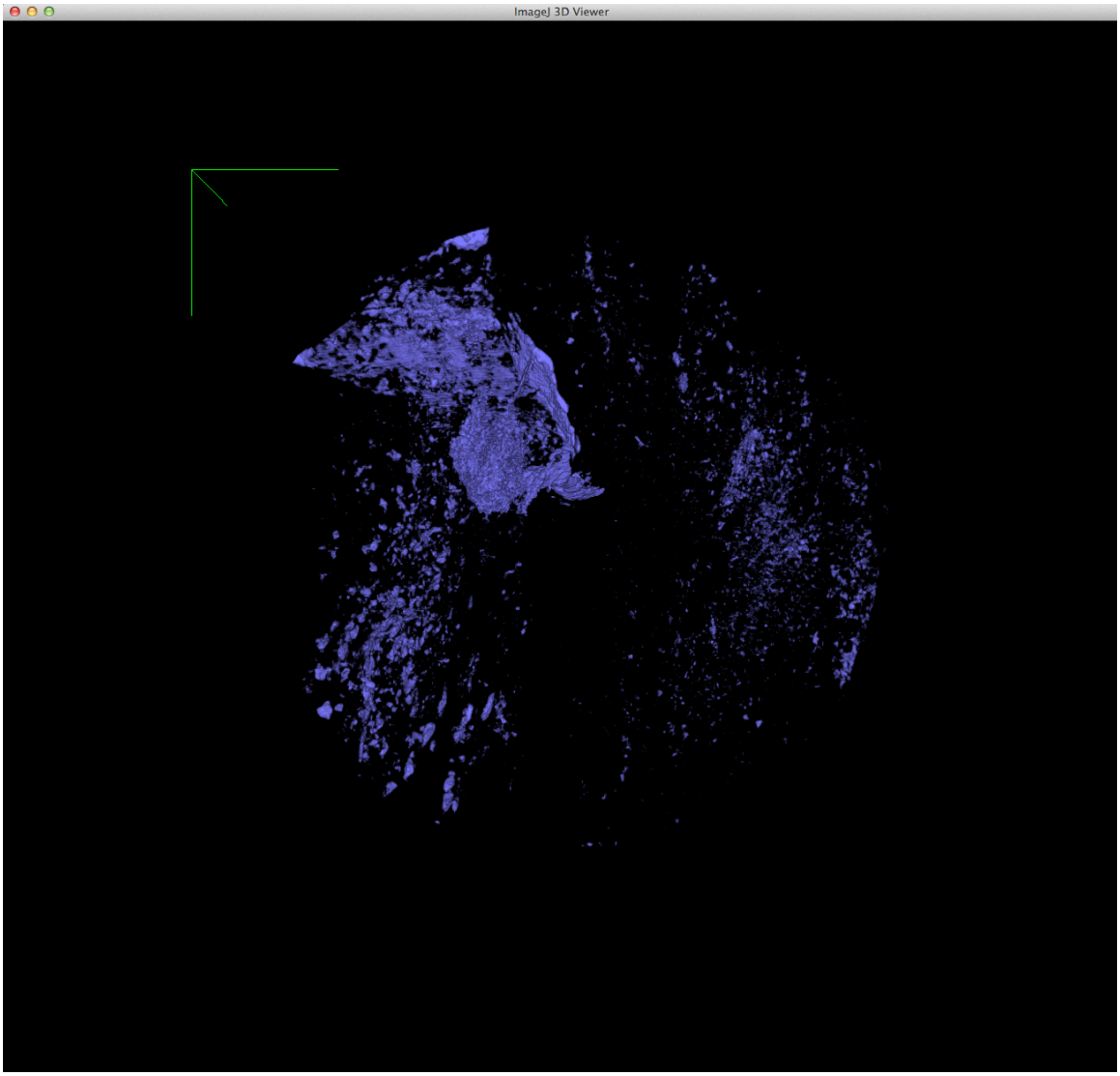
3D XRCT image of pre reaction pore space looking at the inlet side, Cutter 20-9.



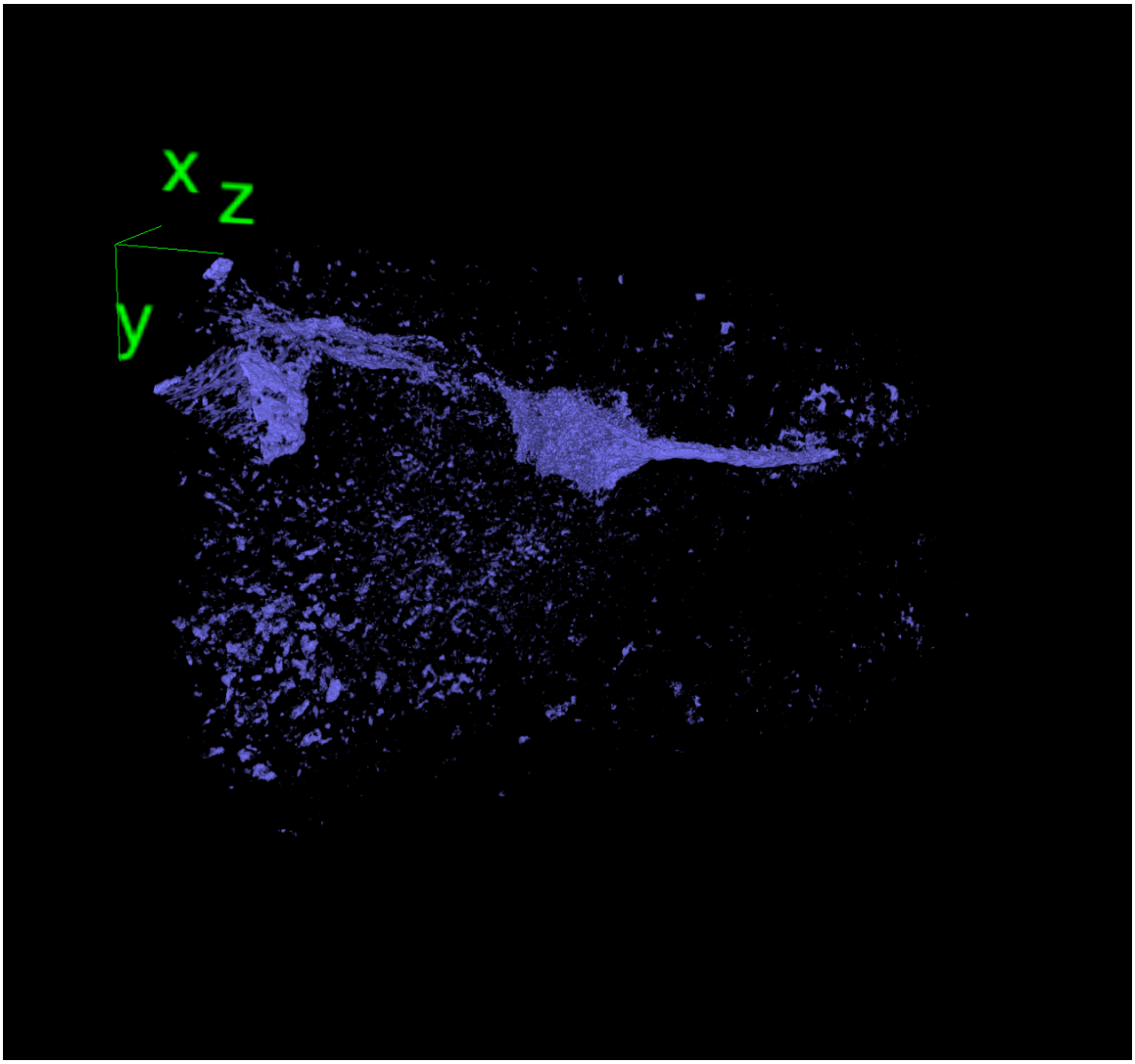
3D XRCT image of pre reaction pore space, side profile, Cutter 20-9.



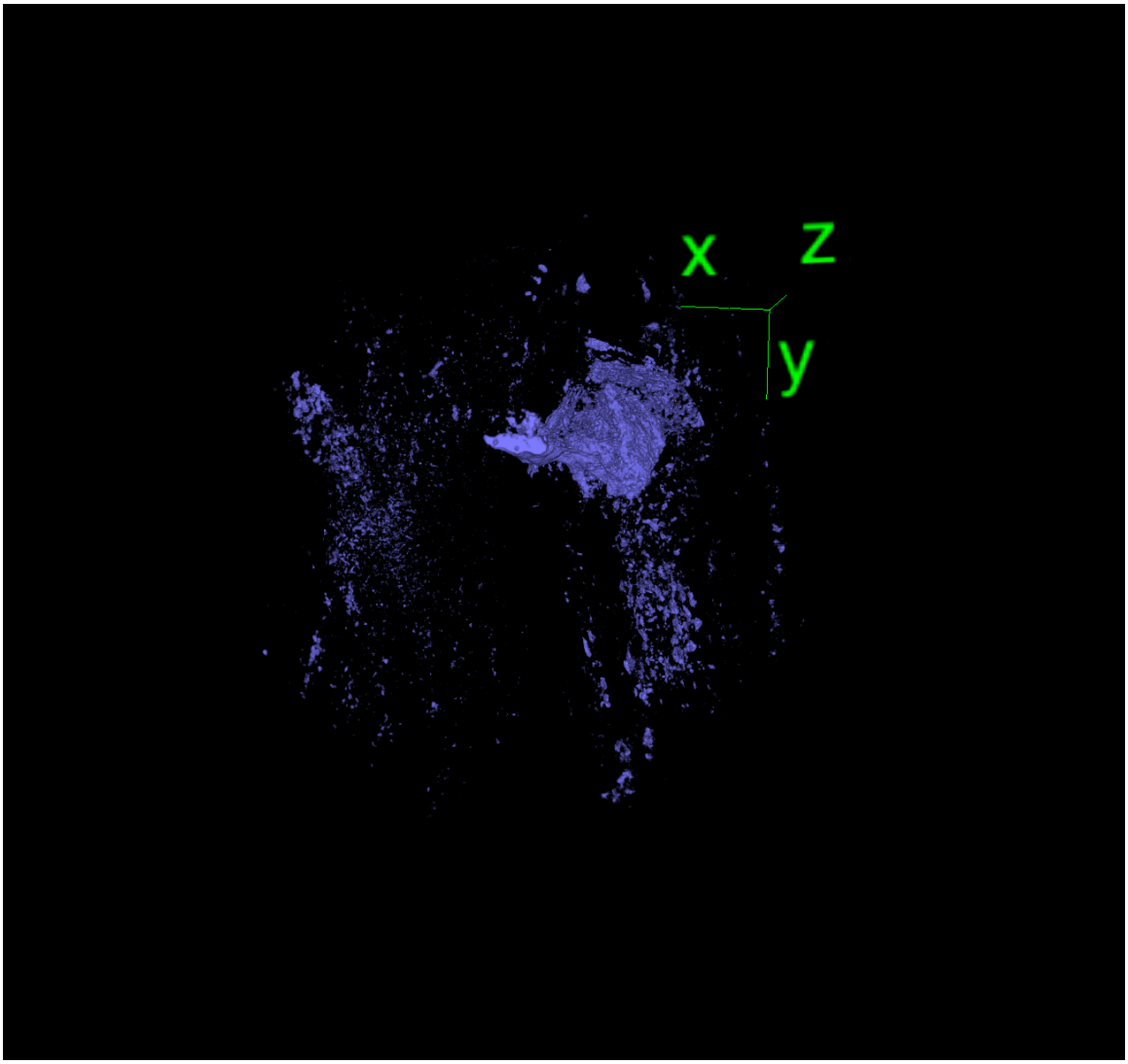
3D XRCT image of pre reaction pore space, additional profile, Cutter 20-9.



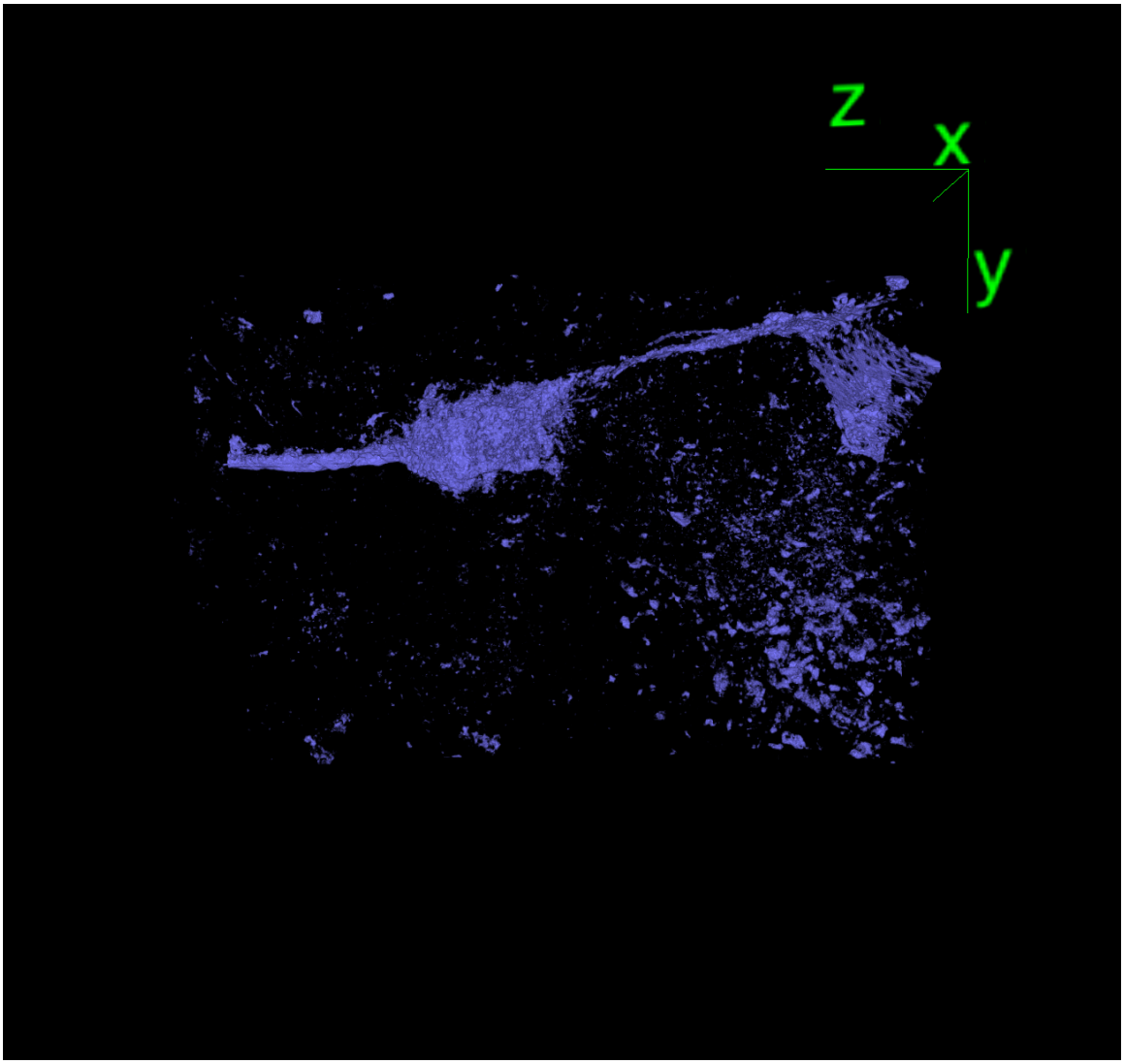
3D XRCT image of low threshold pore space looking at the outlet side, Cutter 20-9.



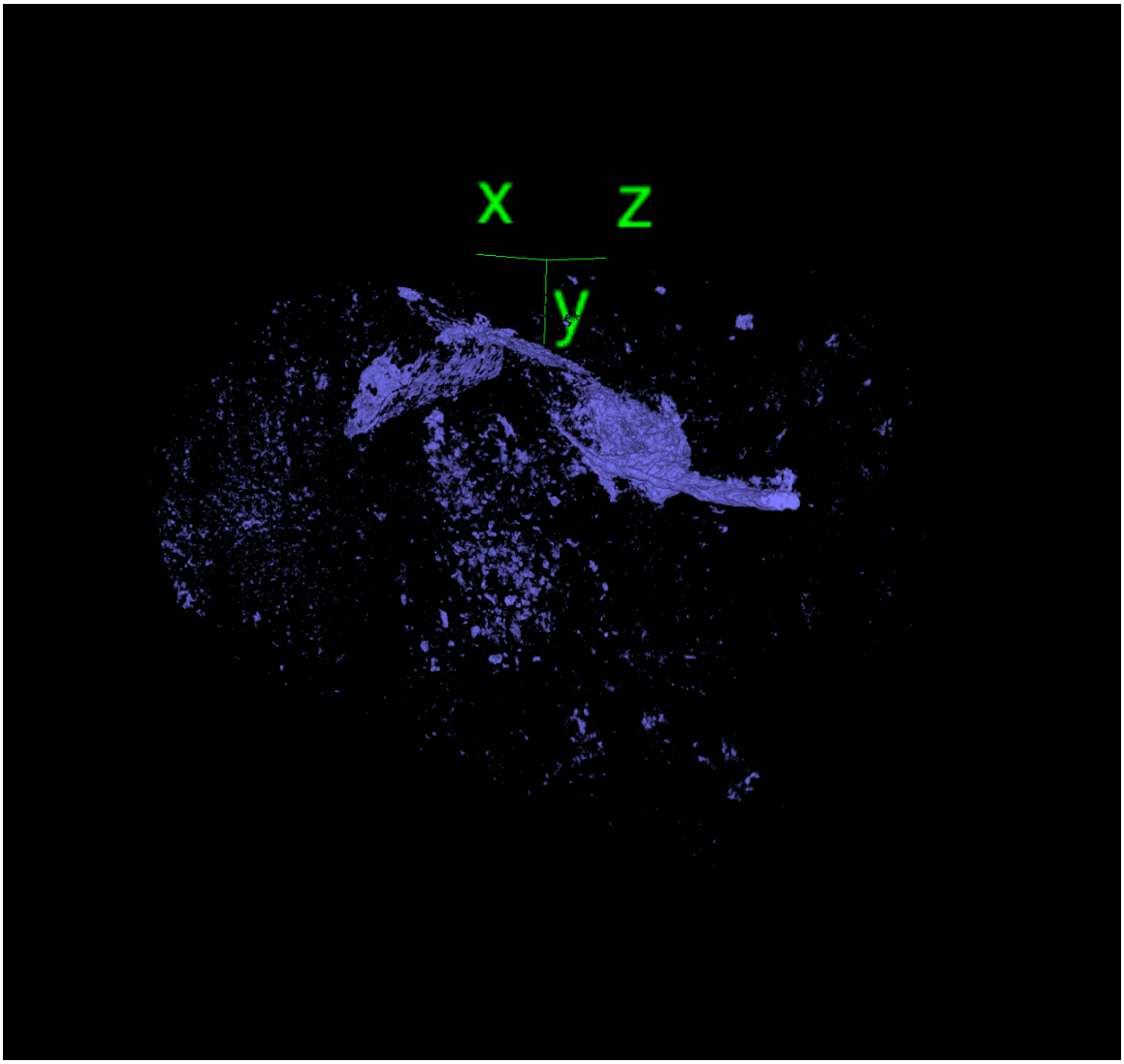
3D XRCT image of low threshold pore space, side profile, Cutter 20-9.



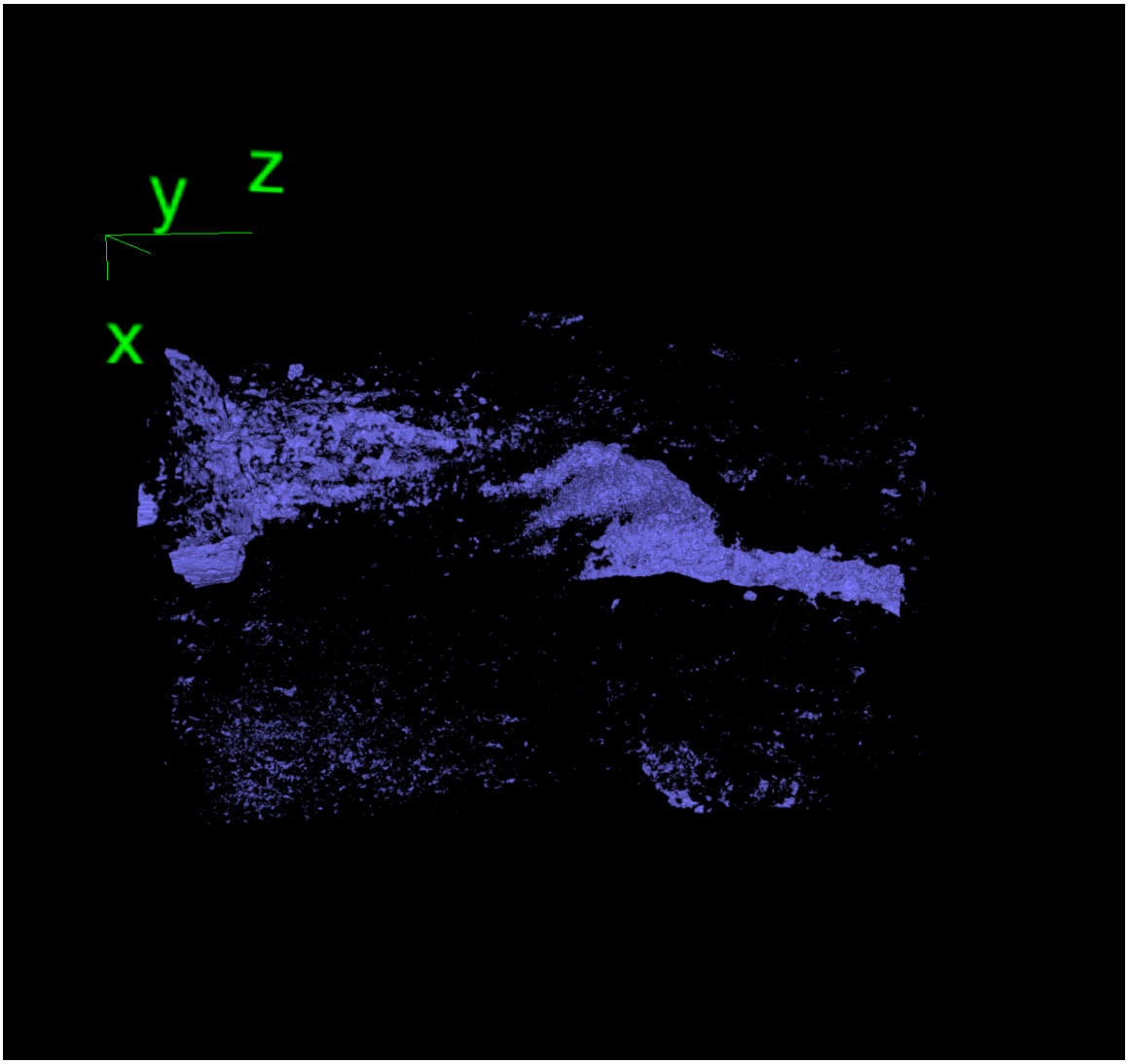
3D XRCT image of low threshold pore space looking at the inlet side, Cutter 20-9.



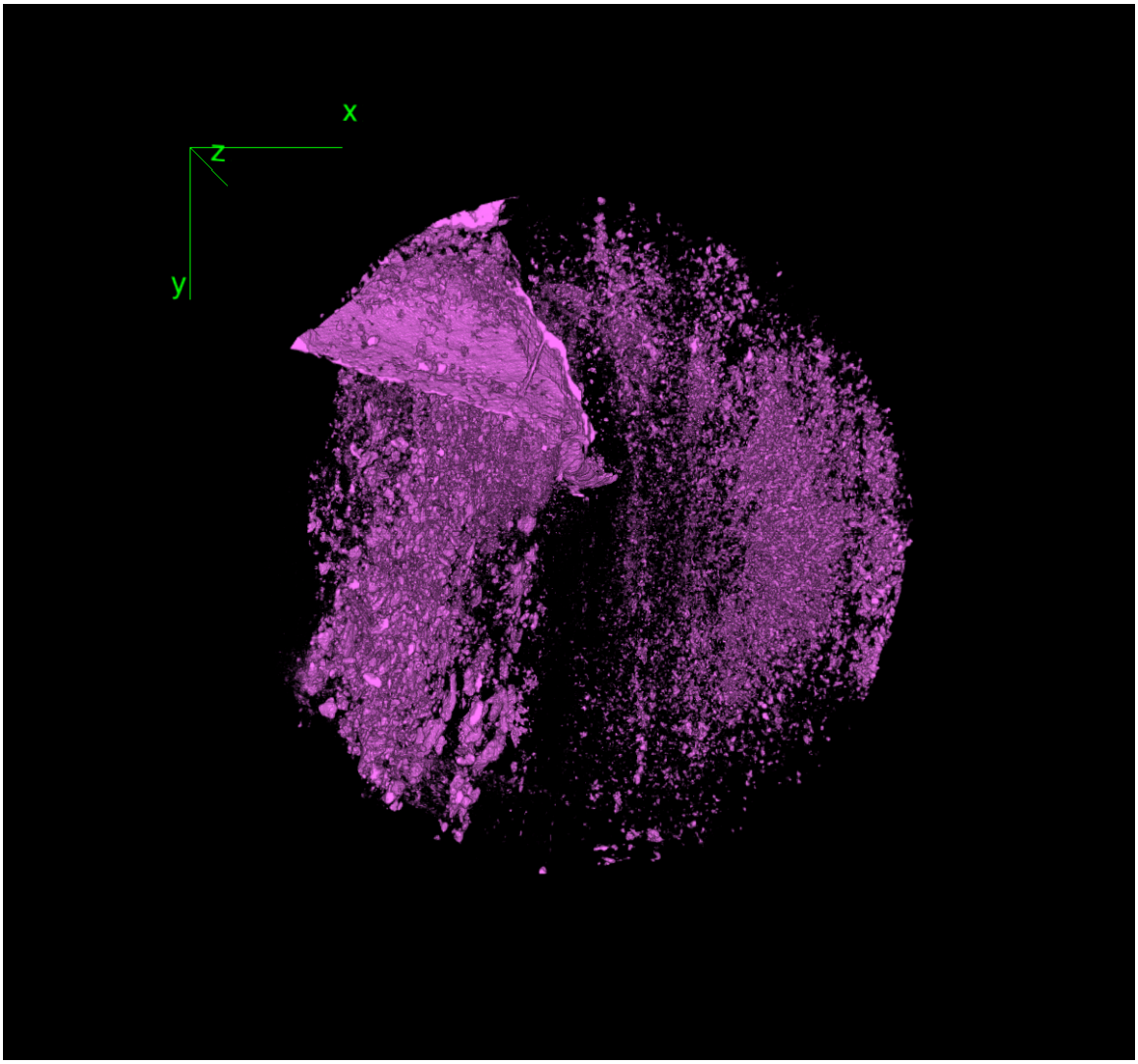
3D XRCT image of low threshold pore space, side profile, Cutter 20-9.



3D XRCT image of low threshold pore space, additional profile, Cutter 20-9.

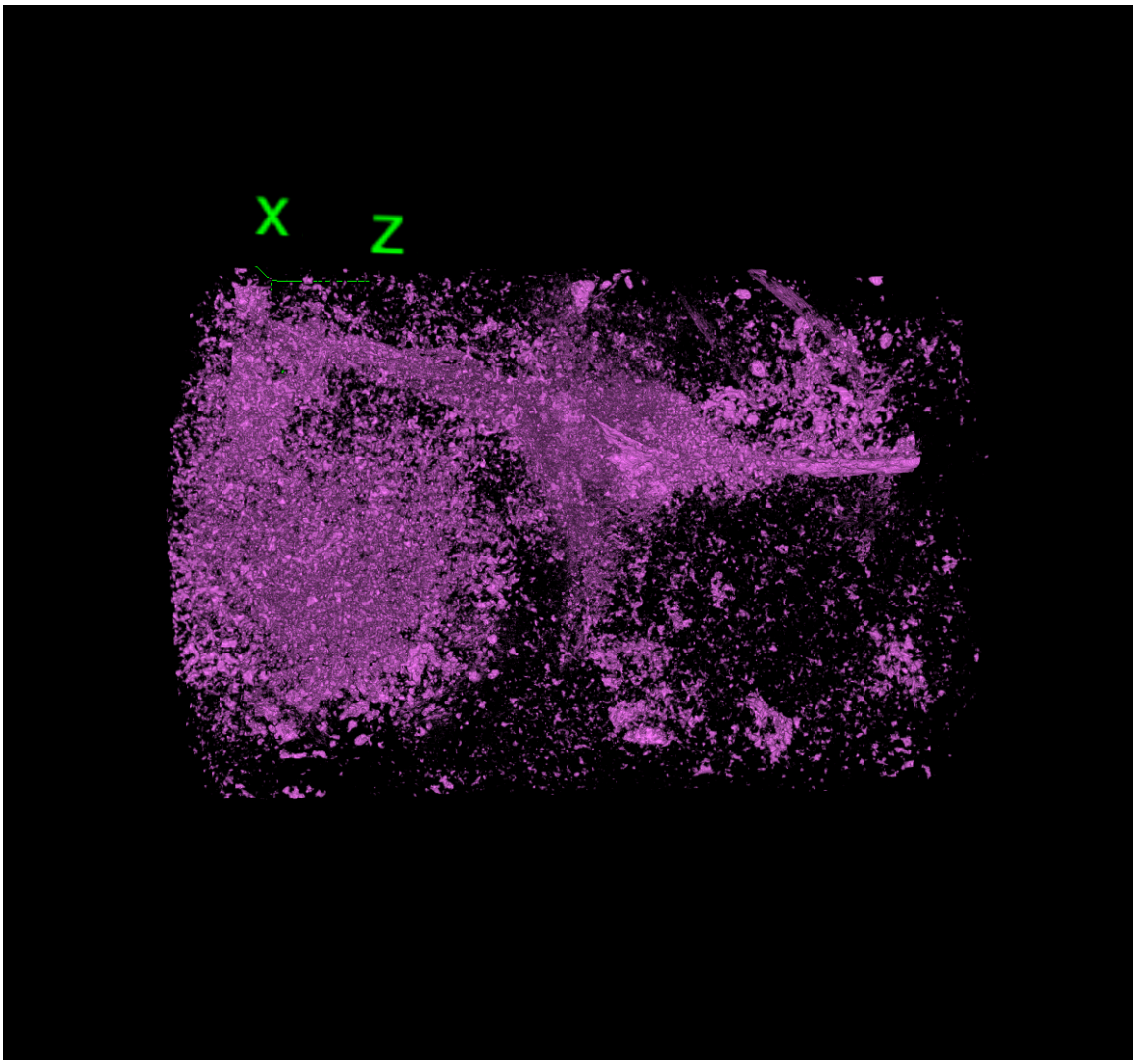


3D XRCT image of low threshold pore space, additional profile, Cutter 20-9.

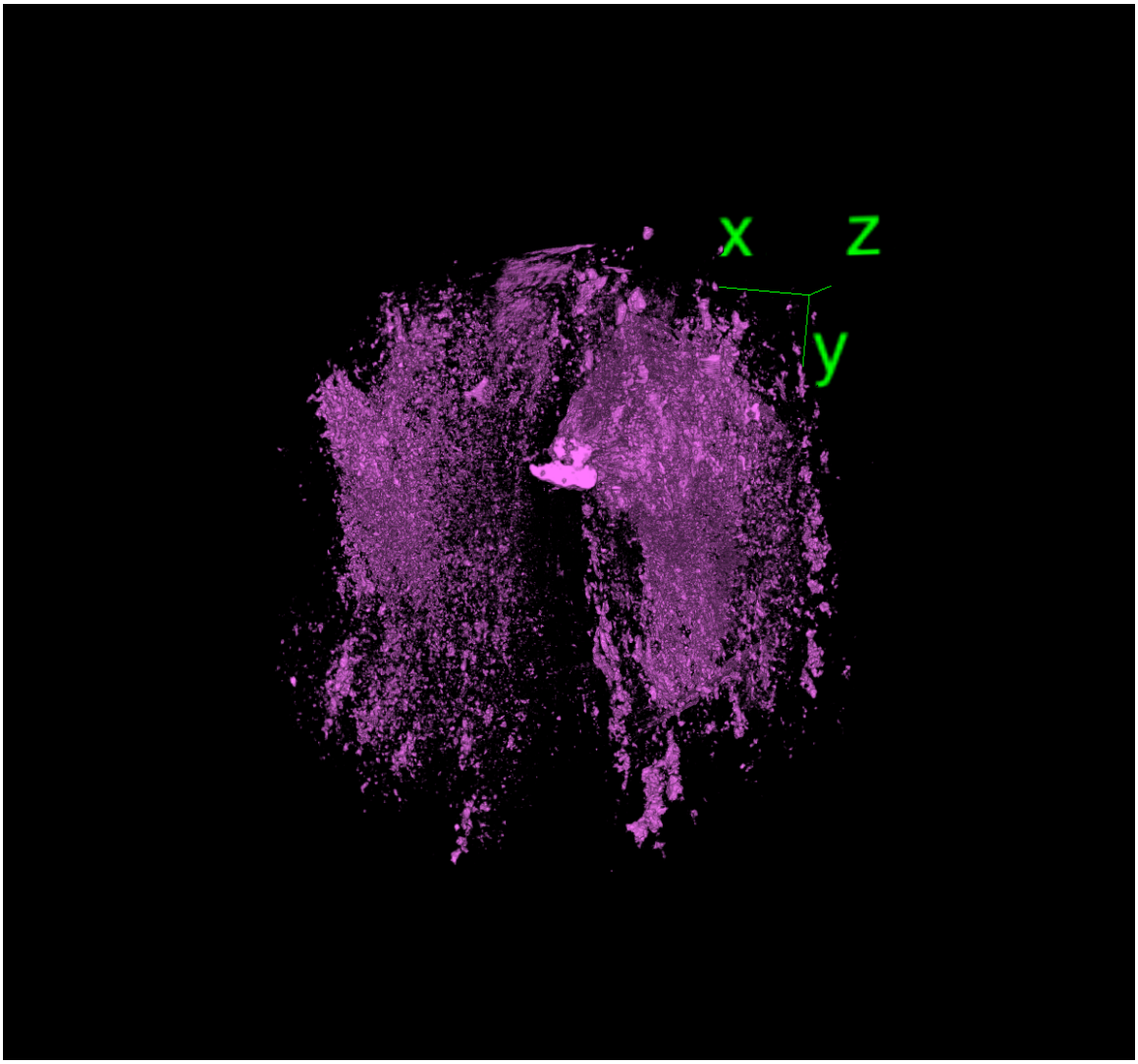


3D XRCT image of high threshold pore space looking at outlet side, Cutter 20-9.

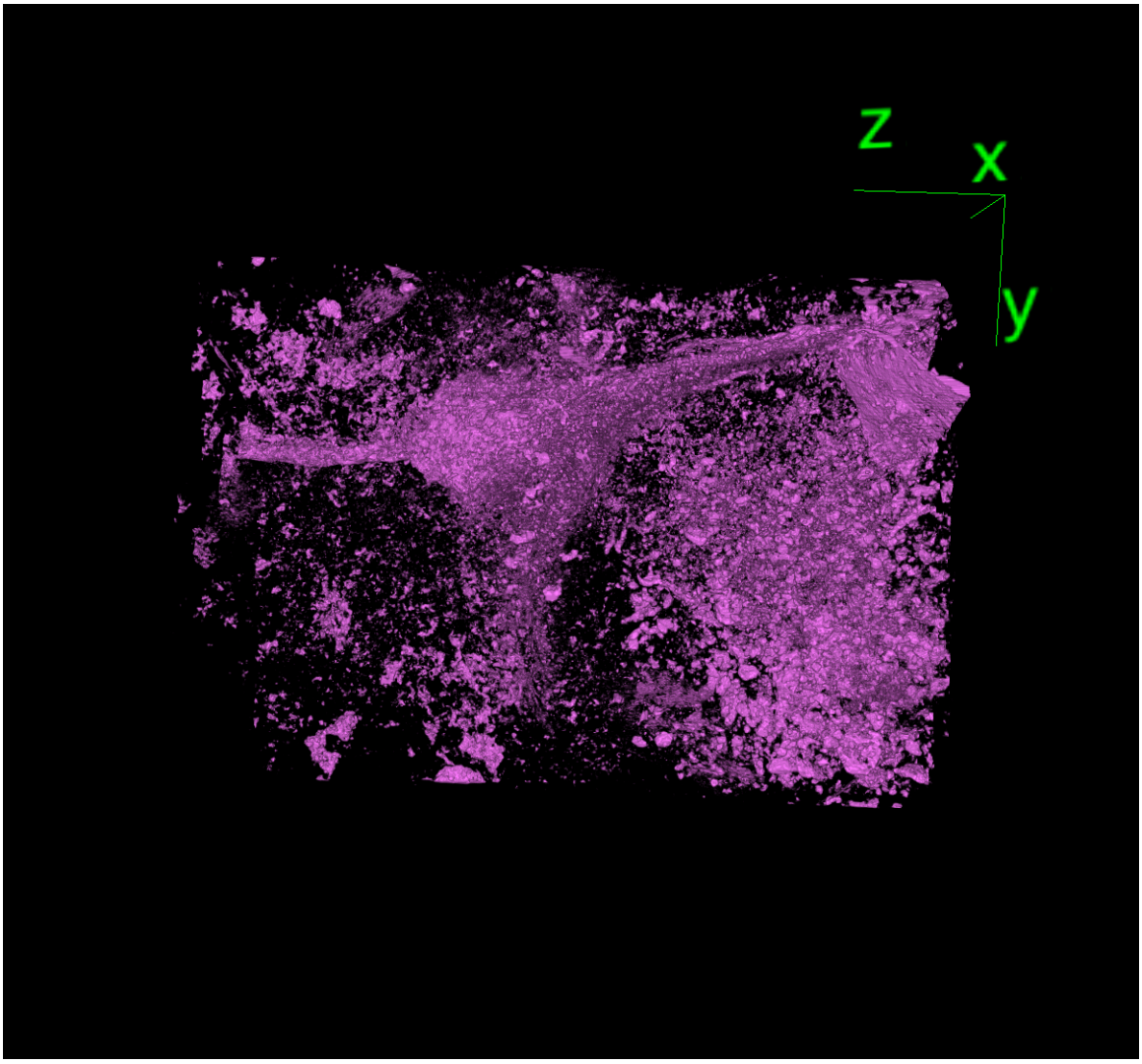
f



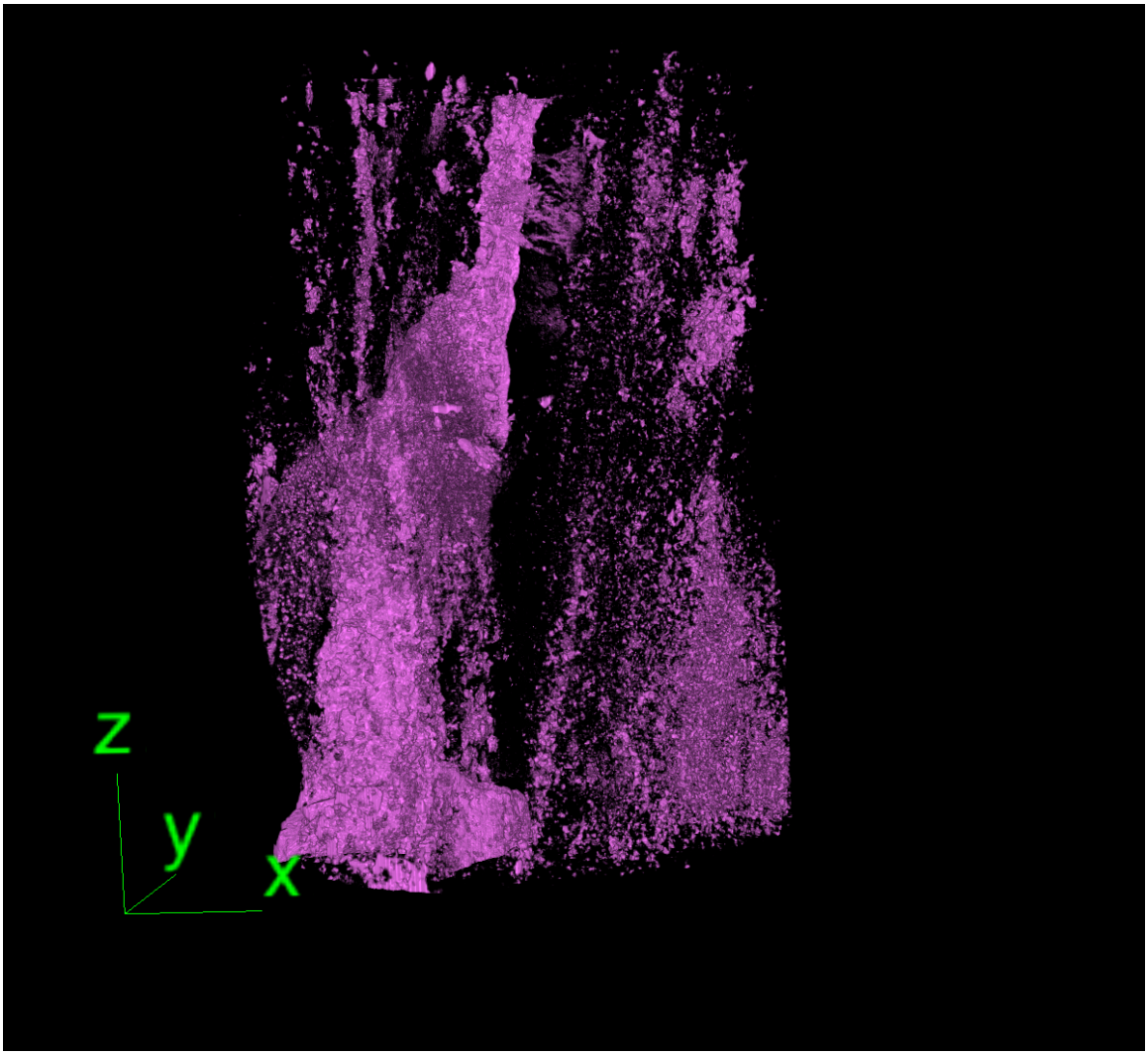
3D XRCT image of high threshold pore space, side profile, Cutter 20-9.



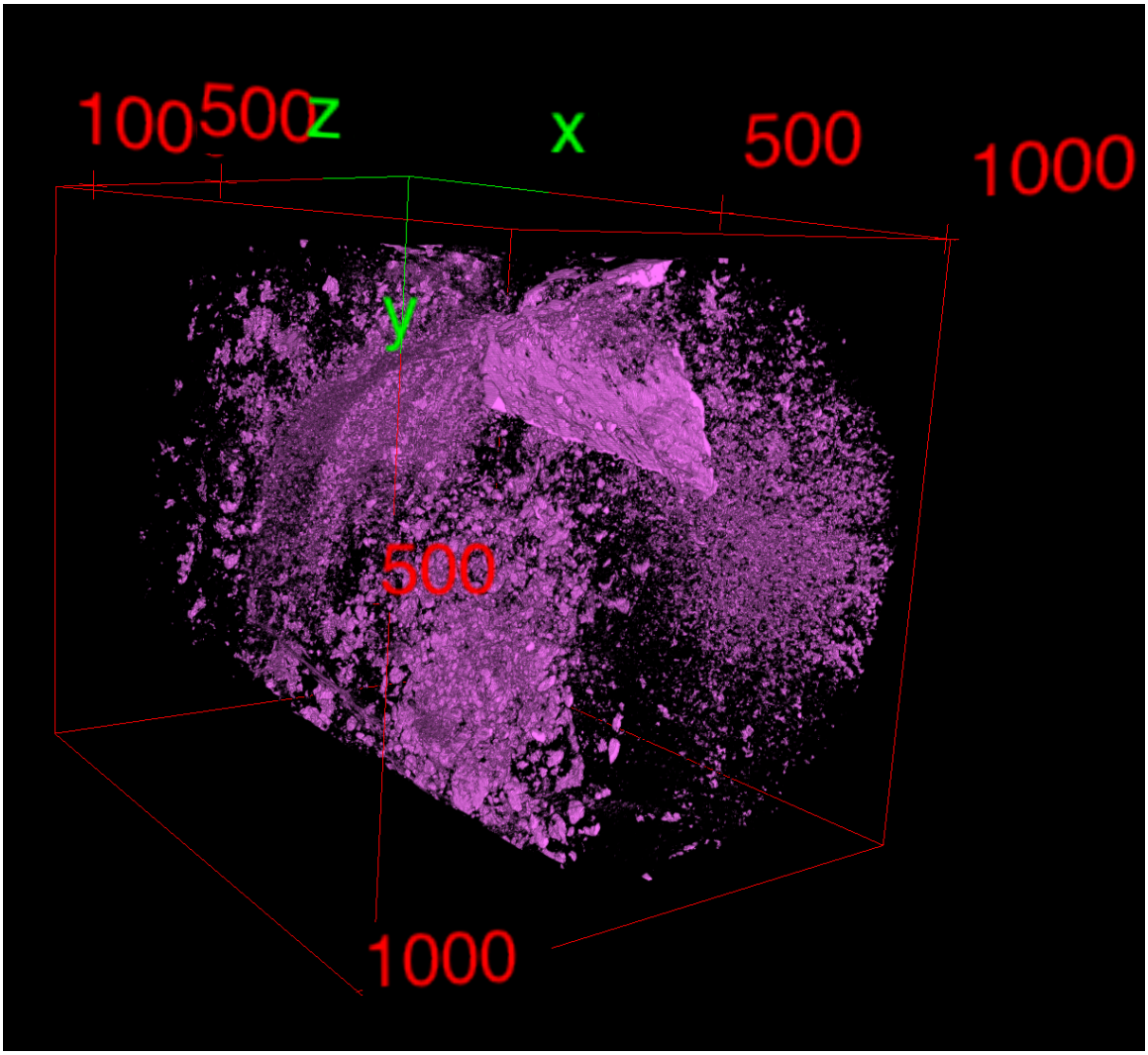
3D XRCT image of high threshold pore space looking at inlet side, Cutter 20-9.



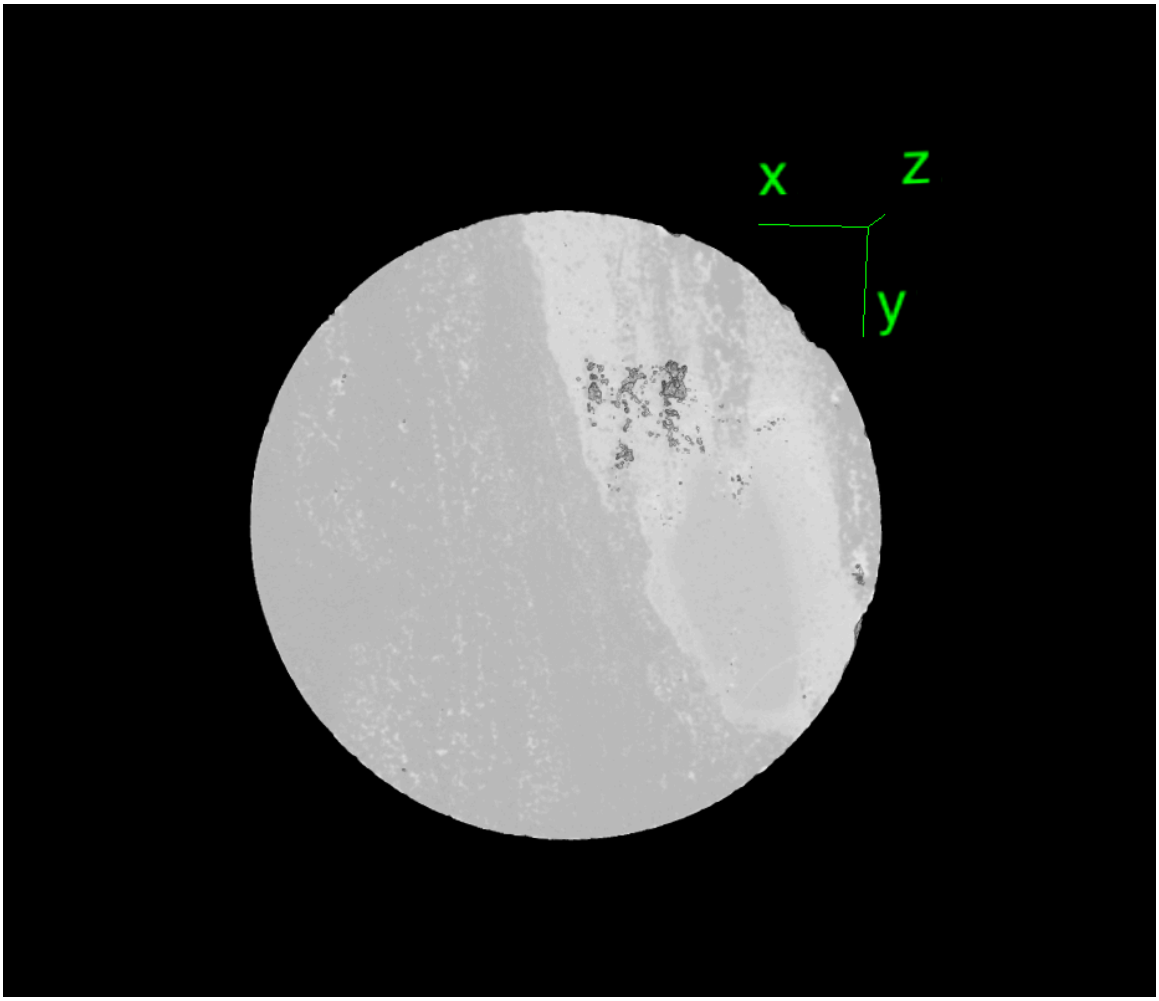
3D XRCT image of high threshold pore space, side profile, Cutter 20-9.



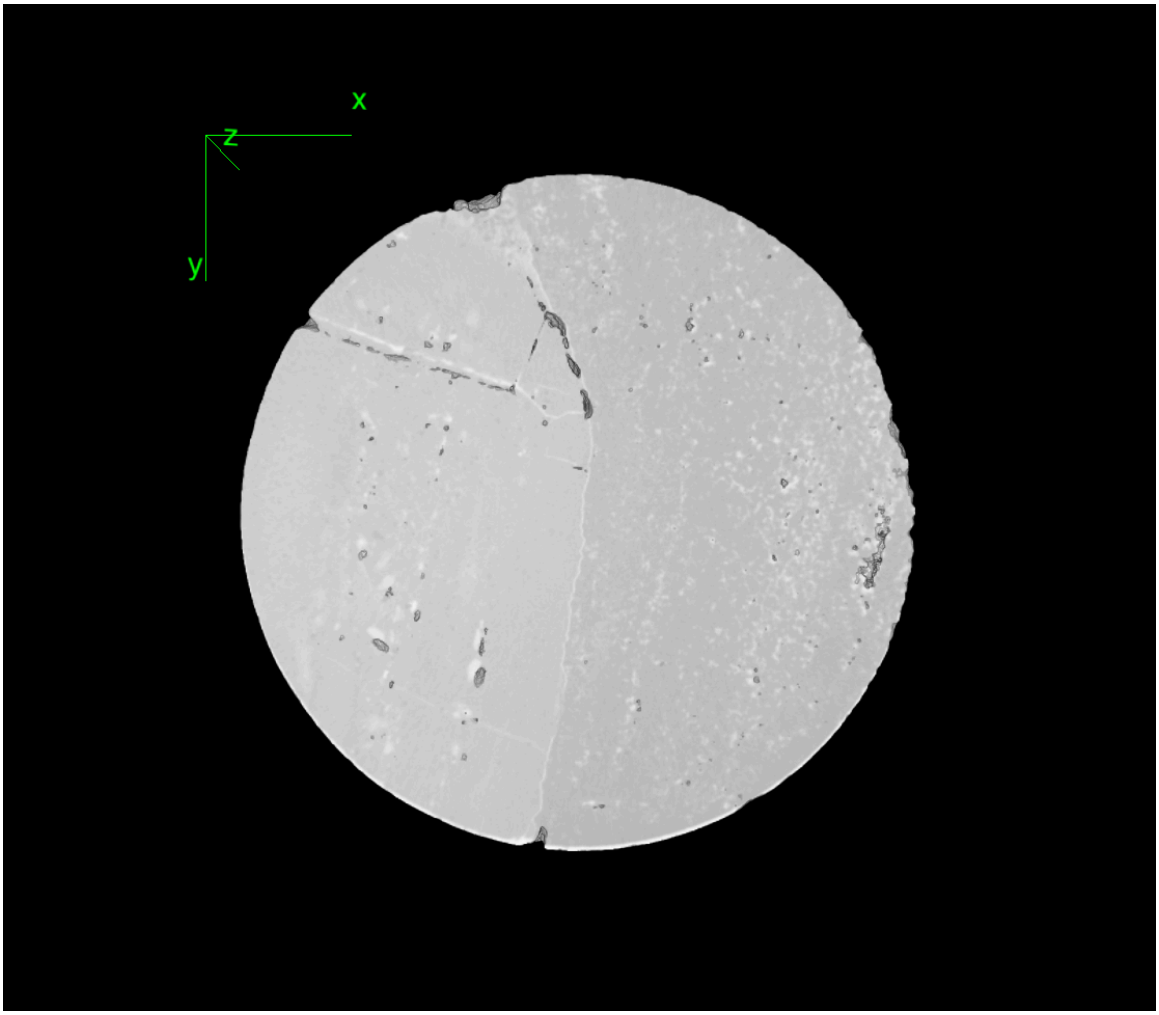
3D XRCT image of high threshold pore space, additional profile, Cutter 20-9.



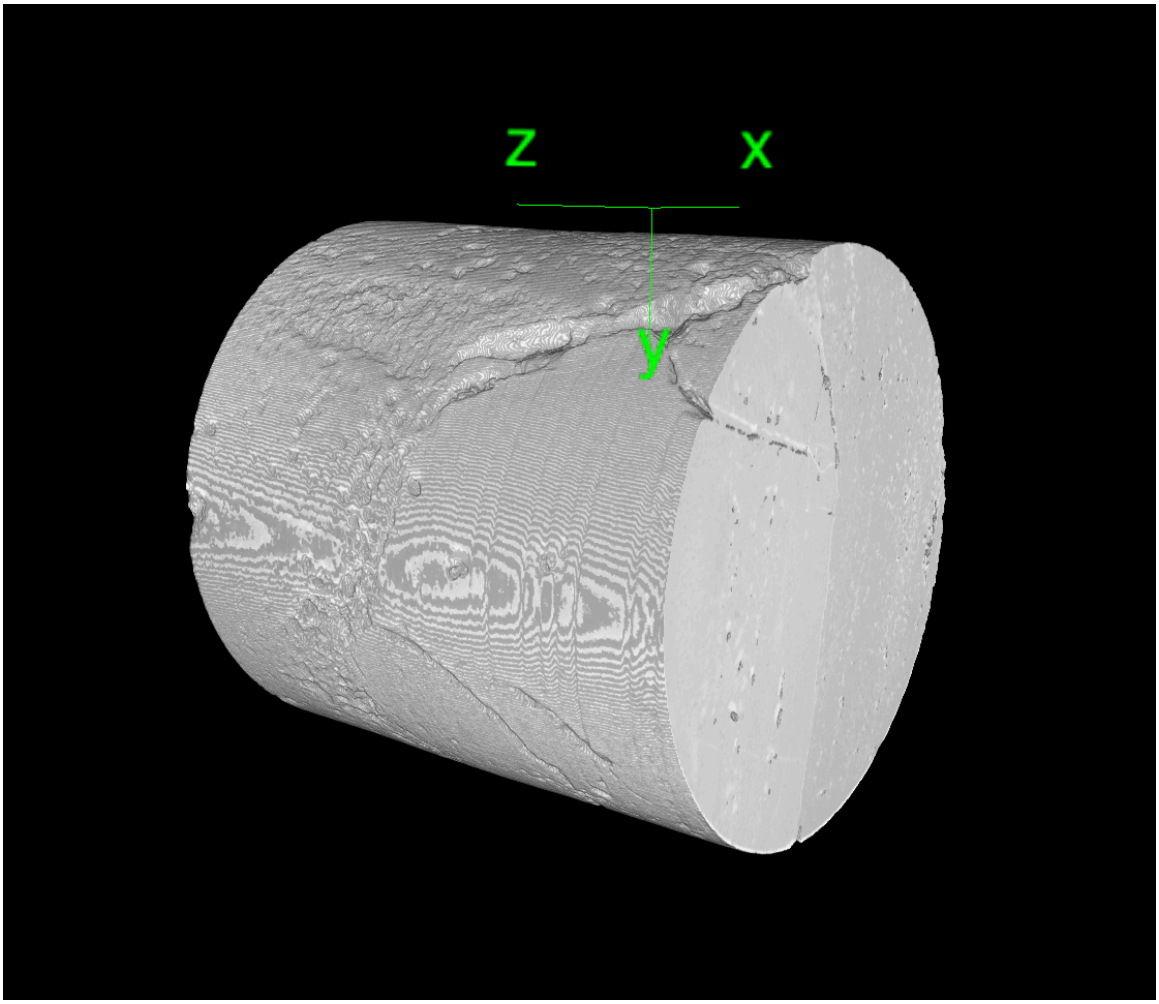
3D XRCT image of high threshold pore space, additional profile, Cutter 20-9.



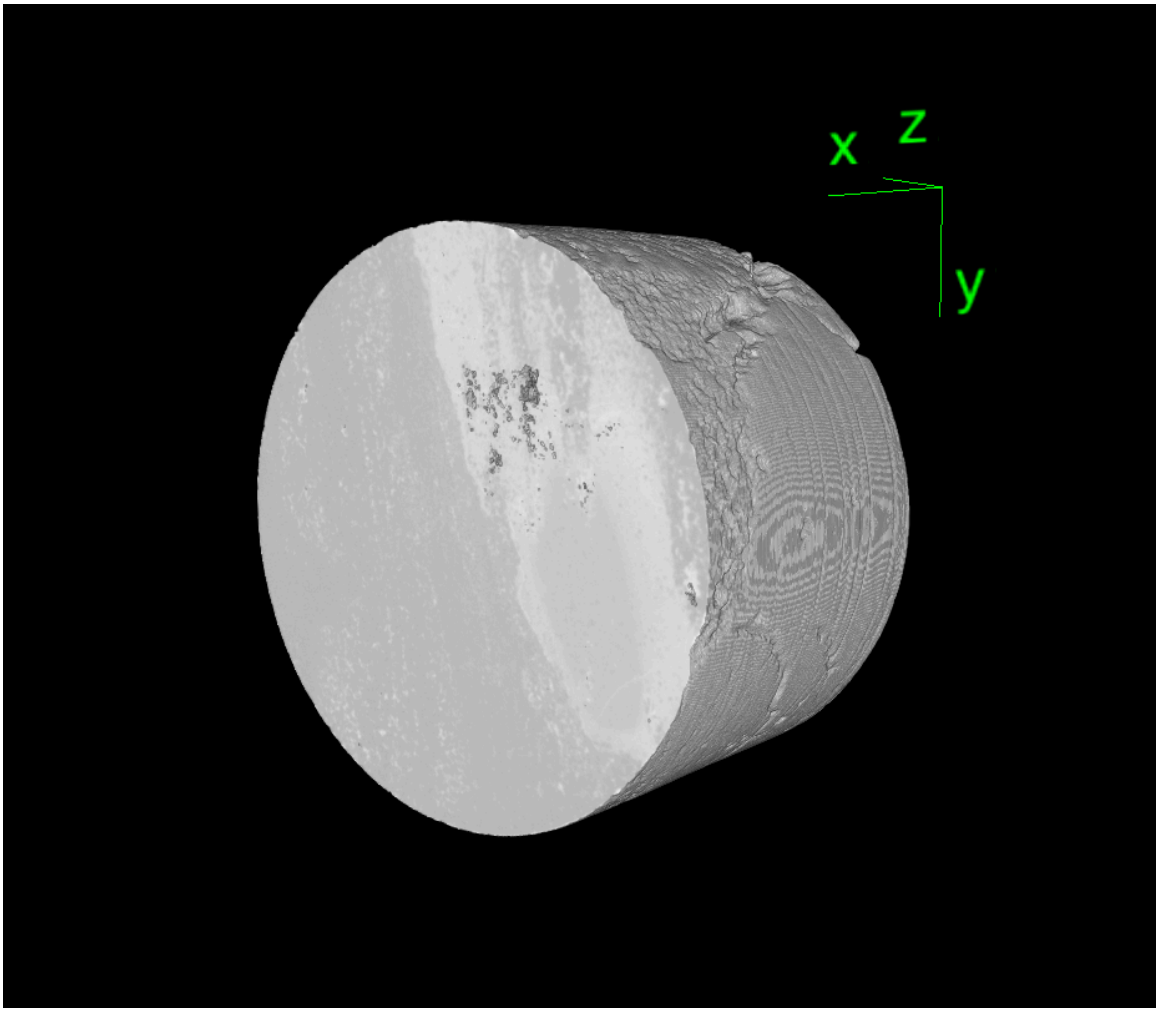
3D XRCT image of halfway through the core, looking towards outlet, Cutter 20-9.



3D XRCT image of the core looking at the outlet side, Cutter 20-9.



Partial 3D XRCT image of the core, outlet side is on the right, Cutter 20-9.



Partial 3D XRCT image of halfway through the core (595 image slices), Cutter 20-9.

LLNL – C20-9 ICP-OES	Dry Container (empty wt. oz.)	10mL MeQ (water wt. oz.)	Brine Sample 1mL (sample wt. oz.)	Acid 0.15 mL (Total wt. oz.)
Apre1	6.40	16.36	17.45	17.66
Apre2	6.50	16.49	17.59	17.80
Amq	6.42	16.41	17.27	17.48
Apre3	6.42	16.43	17.41	17.60
Apre4	6.36	16.35	17.45	17.65
Apre 5	6.43	16.40	17.46	17.67
Apre 6	6.47	16.46	17.43	17.64
Apre 7	6.42	16.38	17.50	17.70
Apre 8	6.35	16.29	17.38	17.57
Apost 1	6.44	16.47	17.51	17.69
Apost 2	6.47	16.48	17.54	17.75
Apost 3	6.52	16.52	17.55	17.76
Apost 4	6.44	16.43	17.50	17.51
Arxtr2	6.40	n/a	17.38	17.59
A1	6.40	16.40	17.52	17.71
A2	6.51	16.51	17.47	17.69
A3	6.45	16.43	17.42	17.62
A4	6.48	16.46	17.56	17.77
A5	6.43	16.42	17.32	17.52
A6	6.42	16.41	17.34	17.54
A7	6.44	16.39	17.40	17.62
A8	6.33	16.26	17.33	17.54
A9	6.44	16.37	17.45	17.65
A10	6.36	16.31	17.35	17.56
A11	6.39	16.32	17.33	17.53
A12	6.47	16.40	17.54	17.74
A13	6.39	16.34	17.47	17.66
A14	6.36	16.29	17.45	17.64
A15	6.47	16.42	17.47	17.67
A16	6.38	16.33	17.40	17.61
A17	6.44	16.37	17.53	17.74
A18	6.46	16.39	17.55	17.76
A19	6.44	16.37	17.52	17.74
A20	6.44	16.38	17.45	17.65
A21	6.43	16.37	17.50	17.72
A22	6.44	16.24	17.30	17.50
A23	6.44	16.38	17.58	17.78
A24	6.46	16.34	17.57	17.79
A25	6.46	16.41	17.46	17.66
A26	6.44	16.35	17.53	17.73
A27	6.46	16.44	17.41	17.62
A28	6.44	16.39	17.57	17.77
A29	6.51	16.49	17.56	17.77
A30	6.43	16.40	17.47	17.68
A33	6.35	16.33	17.22	17.43
A34	6.45	16.43	17.50	17.70
A35	6.43	16.39	17.45	17.65
A36	6.36	16.34	17.38	17.57
A39	6.36	16.33	17.40	17.62
A40	6.42	16.35	17.49	17.68
A41	6.47	16.38	17.41	17.61
A42	6.31	16.33	17.38	17.58

LLNL sample recording sheet for ICP-OES analysis of major cations.

LLNL – C20-9 IC	Dry Container (empty wt. oz.)	15mL MeQ (water wt. oz.)	Brine Sample 0.5mL (sample wt. oz.)
Bpre1	6.44	21.41	21.80
Bpre2	6.43	21.40	21.75
Bmq	6.43	21.45	n/a
Bpre3	6.40	21.36	21.70
Bpre 4	6.39	21.36	21.79
Bpre 5	6.47	21.46	21.89
Bpre 8	6.39	21.36	21.91
Bpost 1	6.48	21.47	22.00
Bpost3	6.37	21.38	21.89
Bpost 5	6.44	21.44	22.36
Brxtr2	6.43	n/a	22.04
B1	6.40	21.40	21.93
B2	6.36	21.32	21.74
B3	6.43	21.39	21.73
B4	6.45	21.44	21.98
B5	6.51	21.48	21.89
B6	6.44	21.39	21.69
B7	6.44	21.38	21.56
B8	6.42	21.37	21.77
B9	6.35	21.29	21.71
B10	6.44	21.36	21.71
B11	6.42	21.36	21.78
B12	6.38	21.29	21.72
B13	6.38	21.39	21.82
B14	6.39	21.34	21.66
B15	6.42	21.34	21.75
B16	6.39	21.30	21.63
B17	6.37	21.26	21.56
B18	6.37	21.27	21.65
B19	6.45	21.36	21.70
B20	6.46	21.37	21.73
B21	6.47	21.38	21.62
B22	6.45	21.38	21.64
B23	6.52	21.46	21.91
B24	6.40	21.33	21.87
B25	6.47	21.40	21.74
B26	6.37	21.29	21.61
B27	6.38	21.31	21.59
B28	6.39	21.32	21.70
B29	6.28	21.27	21.69
B30	6.40	21.40	21.83
B33	6.43	21.40	21.77
B34	6.53	21.50	21.84
B35	6.41	21.40	21.68
B36	6.48	21.45	21.88
B39	6.42	21.38	21.85
B40	6.37	21.34	21.81
B41	6.39	21.37	21.87
B42	6.46	21.45	21.93

LLNL sample recording sheet for IC analysis of major anions.

LLNL – C20-9 Total Carbon	Dry Container (empty wt. oz.)	3.75mL NaOH (NaOH wt. oz.)	Brine Sample 0.5mL (sample wt. oz.)
Pre 1	5.53	9.28	10.59
Pre 2	5.33	9.07	10.31
Cmq	5.53	9.26	10.44
C1	5.43	9.17	10.47
C2	5.35	9.09	10.47
C3	5.34	9.08	10.47
C4	5.31	9.06	10.42
C5	5.49	9.22	10.57
C6	92.02	95.91	100.05
C7	91.45	95.33	97.88
C8	91.63	95.49	98.13
C9	91.98	95.86	98.16
C10	91.56	95.46	98.11
C11	91.43	95.31	97.86
C12	91.61	95.51	97.88
C13	91.98	95.87	98.59
C14	91.56	95.44	97.85
C15	91.43	95.31	97.77
C16	91.61	95.36	98.26
C17	91.99	95.86	98.59
C18	91.57	95.46	99.06
C19	91.44	95.30	98.15
C20	91.61	95.48	98.32
C21	92.00	95.84	98.69
C22	91.57	95.39	98.48
C23	91.43	95.32	98.15
C24	91.61	95.52	98.56
C25	91.97	95.87	98.91
C26	91.57	95.47	98.44
C27	91.40	95.24	98.53
C28	91.61	95.49	98.61
C29	91.95	95.67	99.08
C30	91.41	95.28	98.29
C33	91.62	95.51	98.57
C34	91.97	95.84	99.52
C35	91.55	95.40	98.30
C36	91.39	95.27	98.37
C39	91.59	95.48	97.91
C40	91.96	95.84	99.01
C41	91.55	95.75	98.85
C42	91.38	95.16	97.38

LLNL sample recording sheet for Total Carbon analysis of total inorganic carbon.